Control of meiotic progression through cyclin-dependent kinase complexes in *Arabidopsis thaliana*

Dissertation with the aim of achieving a doctoral degree at the

Faculty of Mathematics, Informatics and Natural Sciences

Department of Biology

University of Hamburg

Submitted by

Kostika Sofroni

2020 in Hamburg, Germany

Supervisor: Prof. Dr. Arp Schnittger

First Examiner: Prof. Dr. Arp Schnittger

Second Examiner: Dr. Magdalena Weingartner

Date of oral defence: 28. 08. 2020

INDEX

ABSTRACT

Precise control of cell cycle progression is of key importance in maintaining genome stability in dividing cells. The cell cycle consists of a faithful order of events coordinating chromosome dynamics with cytoskeleton behavior to achieve cell growth and the formation of new daughter cells. In sexually reproducing organisms a special type of cell division, i.e. meiosis, is needed to keep the cellular DNA content stable over generations. In meiosis, a single round of DNA replication is followed by two rounds of chromosome segregation events, which result in a reduction of the genomic content by half. After meiosis, gametes can be formed which fuse in the process of fertilization to restore the original DNA amount in the offspring. Any deviations from normal meiosis could impair gamete function and thus compromise the future progeny. Hence, the control of the meiotic cell cycle program is of fundamental interest.

Major regulators of cell cycle progression are cyclin-dependent kinase complexes. In this study I could show that the Arabidopsis central cell cycle regulator CDKA;1 together with the cyclin co-factor CYCB3;1 are key regulators of the microtubule cytoskeleton in meiosis. For full CDKA;1 activity, not only cyclin binding but also phosphorylation by Cdk-activating kinases (CAKs), i.e CDKD kinases is required. Combination of *CAK* mutants with a weak loss-of-function mutant in *CDKA;1* revealed a plethora of phenotypes, including defects in chromosome segregation and microtubule organization during meiosis. Interestingly, a moderate reduction of CDKA;1 activity converted the simultaneous cytokinesis normally seen at the end of male meiosis in Arabidopsis into a successive cytokinesis as found in maize and other monocotyledonous species, where two cell division events, i.e. after meiosis I and after meiosis II occur. Additionally, live cell imaging upon treatment with the microtubule depolymerizing drug oryzalin revealed a novel function of CYCB3;1 in organizing microtubule arrays during meiosis.

I was further involved in analyses, showing that the activity of CDKA;1 is central to meiosis-specific events taking place during prophase. First we could show that the CDKA;1-mediated phosphorylation of ASYNAPTIC 1 (ASY1) is required for chromosome axis formation. Second we provided evidence that, the phosphorylation of a cohesin regulator SWITCH 1/DYAD (SWI1) at late prophase is mediated by

Cdk-cylin complexes corroborating the presence of a prophase pathway of cohesion removal in plants.

Furthermore, the here generated fluorescent protein fusions of components of Cdk-cyclin complexes can be used as imaging tools to investigate stress response or to quantify cell cycle progression. This is exemplified by the specific localization of CDKA;1 under heat stress in structures called stress granules and by the time course of CYCB3;1 localization in combination with nuclear markers as a first attempt to establish a cell cycle hallmark system for live cell imaging in plants.

Taken together, this work gives insights on understanding the role of Cdk-cyclin complexes during meiosis and moreover provides new tools to investigate cell cycle progression in plants.

ZUSAMMENFASSUNG

Die genaue Kontrolle des Zellzyklus ist von großer Bedeutung für die Genomstabilität in sich teilenden Zellen. Der Zellzyklus besteht aus bestimmten Ereignissen, die unteranderem durch das Verhalten des Zytoskeletts und die Chromosomendynamik, das Zellwachstum und die Bildung von Tochterzellen sichern. Bei Organismen mit sexueller Fortpflanzung ist eine besondere Form der Zellteilung, die Meiose, für die stabile Aufrechterhaltung des DNA Gehalts über mehrere Generationen verantwortlich. Zu Beginn der Meiose wird die DNA repliziert und in zwei darauffolgenden Schritten halbiert. Im anschließenden Prozess der Fertilisierung wird der ursprüngliche DNA Gehalt wieder hergestellt. Jede Veränderungen in der Meiose können die Funktion der Gameten verändern und zukünftige Nachkommen beeinträchtigen. Daher ist die Kontrolle des meiotischen Zellzyklus von besonderem Interesse.

Wichtige Regulatoren des Zellzyklus sind Cyclin-abhängige Kinasen (CDK). In dieser Arbeit konnte ich zeigen, dass der Zellzyklusregulator CDKA;1 zusammen mit dem Cyclin CYCB3;1 die Organisation des Mikrotubuli-Zytoskelett in der Meiose reguliert. Für die komplette CDKA;1 Aktivierung ist nicht nur die Bindung eines Cyclins nötig, sondern auch die Phosphorylierung durch Cdk- aktivierende Kinasen (CAKs), wie zum Beispiel durch CDKD. Durch die Kombination von CAK Mutanten mit schwachen loss-of function CDKA;1 Mutanten konnten unterschiedliche Phänotypen beobachtet werden. Beispielsweise zeigen Mutanten Defekte in der Chromosomenteilung und den Mikrotubuli. Besonders interessant ist, dass eine moderate Reduktion der CDKA;1 Aktivität, die simultane Zytokinese, die am Ende der männlichen Meiose stattfindet, in eine sukzessive Zytokinese umwandelt. Eine sukzessive Zytokinese ist charakteristisch für monokotyledone Pflanzen bei denen jeweils eine Zellteilung nach der ersten und zweiten meiotischen Teilung stattfinden.

Darüberhinaus war ich an der Analyse beteiligt, die die zentrale Rolle von CDKA;1 für Ereignisse in der meiotischen Prophase 1 identifiziert hat. Als erstes haben wir gezeigt, dass CDKA;1 das Protein ASYNAPTIC1 (ASY1) phosphoryliert und damit für die Bildung der Choromosomachse unerlässlich ist. Zweitens konnten wir den Nachweis erbringen, dass die Phosphorylierung des Cohesin-Regulators SWITCH1/DYAD (SWI1) in der späten Prophase 1 durch Cdk-Cyclin Komplexe

vermittelt wird. Diese Entdeckung führte zu der Schlussfolgerung, dass auch in Pflanzen ein Prophase Pathway zur Cohesin Entfernung existiert.

Die in dieser Arbeit generierten Fluoreszenz Proteinreporter Fusionen der Cdk-Cyclin Komplexe, konnten bereits zur Analyse von pflanzliche Reaktion auf Stress und zur Quantifizierung des Zellzyklusablaufs verwendet werden. So konnte beispielsweise durch die mikroskopische Analyse von CDKA;1 unter Hitzestress gezeigt werden, dass CDKA;1 in Strukturen, die Stress Granula genannt werden, lokalisiert. Des weiteren konnte mit einer Zeitreihe des CYCB3;1 Reporters in Kombination mit anderen Zellmarkern die ersten Versuche zur Etablierung eines Kennzeichensystems für den Zellzyklus, der auf der mikroskopischen Lebendzellanalyse in Pflanzen basiert, unternommen werden.

Zusammenfasend vermittelt diese Arbeit neue Erkenntnisse über die Funktion der Cdk-Cyclin Komplexe in der Meiose und stellt neue Methoden zur Erforschung des Zellzyklusablaufs in Pflanzen bereit.

INTRODUCTION

General introduction

The majority of dividing cells undergo a mitotic cell cycle in which one round of DNA replication is followed by a single chromosome segregation event, giving rise to two identical nuclei, which then are separated by cell division. Different from mitosis, meiosis is a special type of division exclusively occurring in sexually reproducing organisms. It is composed of a first reductional division where homologous chromosomes are separated and a second equational division where sister chromatids are separated as in mitosis, the result being four genetically different gametes with half of the chromosome set. The full DNA content will be restored after the fusion of male and female gametes, i.e. upon fertilization. Moreover meiosis is the driving force of genetic diversity, since chromosomes of different parental origin are randomly sorted into two homologous groups in meiosis I and at the same time recombination between homologous chromosomes takes place, creating an even bigger genetic diversity among the gametes.

Achieving a successful meiotic division program relies on precise coordination of cytoskeleton dynamics with chromosome behaviour. First, during meiotic prophase, nuclear dynamics allowing homologous chromosome pairing and synapsis are supported by the microtubule cytoskeleton. This is exemplified by the telomere bouquet, a special interconnection between centromeres, nuclear envelope and microtubules and more specifically dynein promoting nuclear rotations to facilitate centromere pairing and clustering (Christophorou et al., 2015; Blokhina et al., 2019). Second the formation of the division spindle is required for the faithful separation of homologues since their segregation relies on spindle-generated forces to correctly position the two pools of chromosomes. Similarly to mitosis, the sister chromatid separation at the second meiotic division is dependent on the organization of the second spindle. Third, the execution of cytokinesis, the final event of cell division relies on a plant specific structure containing precisely organized antiparallel microtubule bundles and membrane compartments called phragmoplast .It allows cell plate formation, extension and fusion with the surrounding cell walls to physically separate the new nuclei into daughter cells. Interestingly, in some plant species post meiotic cytokinesis is uncoupled from the chromosome segregation events as the cell

wall is deposited only after the second and not already the first nuclear division. This is known as simultaneous cytokinesis, in contrast to the successive type in which cell wall is deposited after the first and after the second chromosome segregation events.

Cdk activity drives cell cycle progression, mitosis and meiosis

Actively dividing eukaryotic cells undergo a precise cycle of events leading to the formation of daughter cells. This cycle encompasses four sequential ordered phases including the replication of DNA (S phase), the segregation of chromosomes (M phase) and two gap (G) phases (Figure 1). The G1 and G2 phases are crucial in preparing the cellular machinery needed to accomplish the S or M phase and in ensuring that the previous phase has been correctly executed to succeed to the next one. Cells that are not dividing remain in a quiescent state called G0. The genome integrity and the correct order of cell cycle events are under strict surveillance of control mechanisms called checkpoints. For instance there are three major known checkpoints: the G1/S checkpoint, where DNA damage is the main indicator to restrict entry into S phase; G2/M checkpoint ensuring that cells don't initiate mitosis until DNA is correctly repaired and replicated and the metaphase to anaphase or spindle assembly checkpoint assuring that all chromosomes are correctly aligned and under bipolar tension prior to sister chromatid segregation (Figure 1).
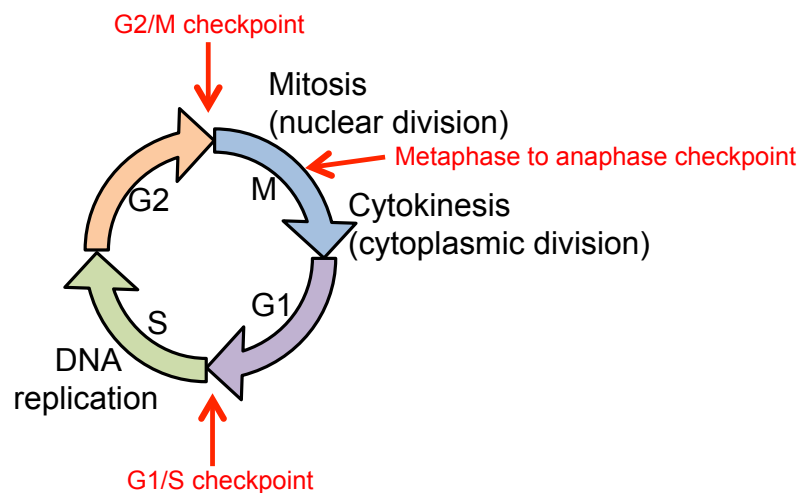
Figure 1: Overview of cell cycle progression.

The major regulators of the cell cycle are a special class of serine-threonine protein kinases named cyclin-dependent kinases (Cdks). In higher eukaryotes there are multiple Cdks having different roles in the cell cycle. The *Arabidopsis* homolog of

the human Cdk1/Cdk2, CDKA;1 is the main cell cycle regulator and its activity is tuned at multiple levels: interaction via the typical PSTAIRE domain with a cyclin co-factor, activation by phosphorylation by Cdk-activating kinases (CAKs), inhibition by phosphorylation by WEE1 kinase (under debate) or the binding of inhibitor proteins (Kip-related proteins (KRPs)) (Figure 2). CDKA;1 is the only PSTAIRE kinase in Arabidopsis and null mutants are viable but display defects in S phase and stem cell maintenance, thus making their functional study challenging (Nowack et al., 2012; Shimotohno et al., 2006). Phosphorylation of a canonical threonine (Thr161) in the T-loop of this kinase is essential for its function as a phospho-mimicry T161D substitution restored the primary defects of *cdka;1* null mutants, but resulted in dramatically reduced kinase activity with plants displaying various developmental abnormalities (Dissmeyer et al., 2007). Interestingly, in metazoans P-loop phosphorylation of the major cell cycle Cdks is found to be crucial when the nuclear DNA is damaged (Yata and Esashi, 2009). However in Arabidopsis the situation seems different. While *in vitro* experiments showed that WEE1 could phosphorylate the P-loop of CDKA;1 and block its activity (Shimotohno et al., 2006) WEE1-mediated DNA damage response was found to act independently of P-loop phosphorylation *in vivo* (Dissmeyer et al., 2009).
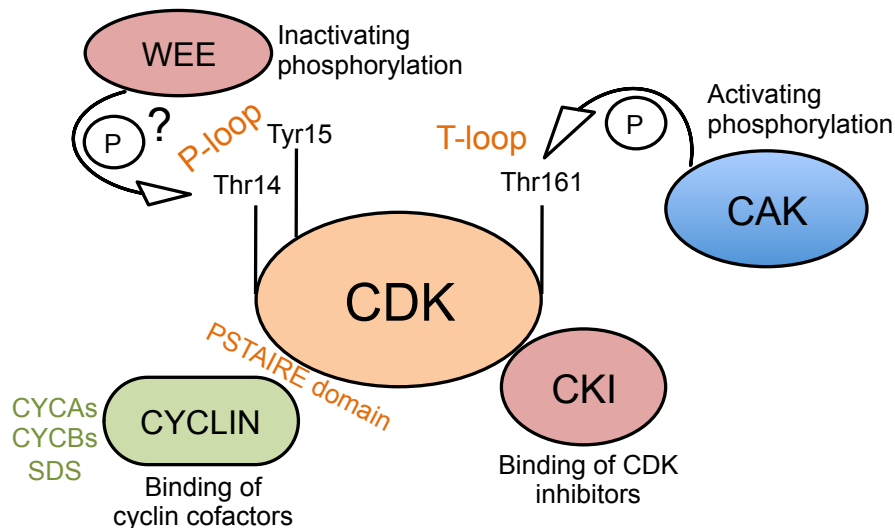
Figure 2: *Multiple layers of Cdk regulation: P-loop phosphorylation via WEE1 (still in question), T-loop phosphorylation via CAK, cyclin or inhibitor binding.*

Progression through the entire cell cycle is promoted by oscillating the activity of the Cdk core complex: low kinase levels are required for the licensing of DNA

replication, moderate levels to pursue DNA replication in S-phase and high levels for the correct chromosome segregation at M phase followed by again low kinase levels to exit mitosis and start another cell cycle (Stern and Nurse, 1996; Wijnker and Schnittger, 2013) (Figure 3). The decrease of Cdk activity at the onset of anaphase is largely due to the activation of the anaphase-promoting complex/cyclosome (APC/C) targeting the degradation of cyclins (Figure 3A). Several cyclins and one to several Cdks have evolved in different organisms, acting in different combinations at different time-points of the cell cycle. Interestingly however, in fission yeast a single artificially fused Cdk-cyclin complex is sufficient to drive mitosis and meiosis albeit with some deficiencies (Coudreuse and Nurse, 2010; Gutiérrez-Escribano and Nurse, 2015).

Meiosis is a specialized type of nuclear division in which two rounds of chromosome segregation (meiosis I and meiosis II) follow a single round of DNA replication (Figure 3B). This results in a reduction of the chromosome content by half, needed to maintain genome size in sexually reproducing organisms. The full chromosome content will be restored after male and female gamete fusion called fertilization. Meiosis is characterized by a long prophase during which meiosis-specific events such as recombination between homologous chromosomes, synaptonemal complex assembly and prophase pathway of cohesin removal take place (for more information on these processes see introductions of the publications in Chapter 2). After prophase I the fully paired and condensed chromosomes align in the equatorial plane in metaphase I and the homologues segregate at the opposite poles of the cell in anaphase I (Figure 3B). During interkinesis, chromosomes shortly decondense and a second segregation event, separating the sister chromatids, takes place ultimately resulting in the formation of four genetically different daughter cells. These events rely on different amounts of Cdk activity (Figure 3B). An hypothetical model described by (Wijnker and Schnittger, 2013) suggests that Cdk activity decreases after meiosis I to a level that allows to start a second meiotic division but not low enough for a second round of replication (Figure 3B). In Arabidopsis male meiosis, sufficiently high Cdk activity after meiosis I seems needed to prevent premature cytokinesis, indicated by a hypomorphic *cdka;1* mutant that shows cell wall deposition after only one division (Dissmeyer et al., 2007). Also the localization of active CDKA;1 complexes at the organellar band that separates the two newly formed nuclei after meiosis I fits a model, where high local CDKA;1 activity acts as a

barrier to prevent early cytokinesis (d'Erfurth et al., 2010; Bulankova et al., 2010; Dissmeyer et al., 2007). Additionally, mutants in the APC/C inhibitor *OSD1/GIG1* resulted in the termination of meiosis after the first division in Arabidopsis, indicating that the level of CDKA;1 activity after meiosis I might be controlled by cyclin availability (d'Erfurth et al., 2009).
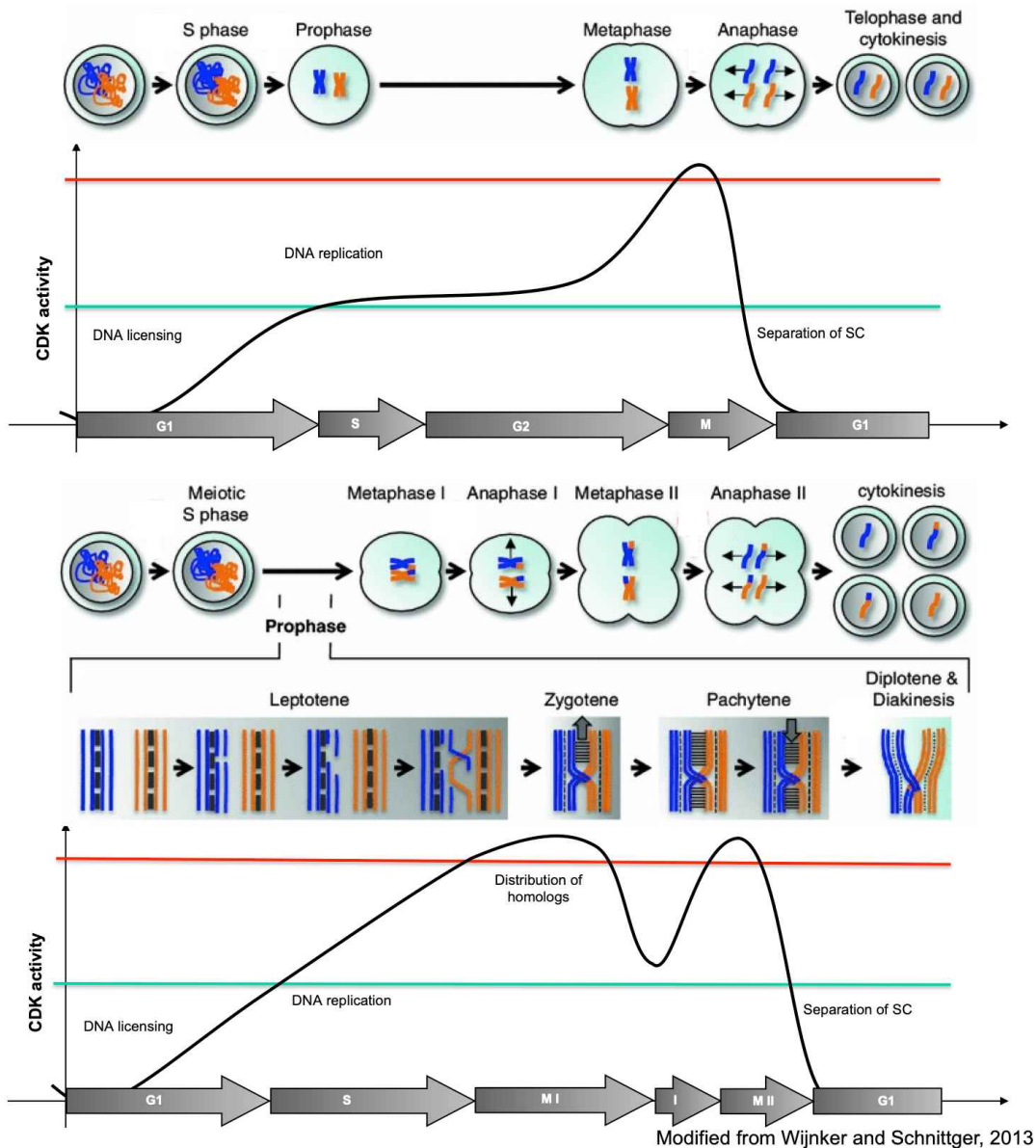
Figure 3: *Cdk activity promotes the progression of (A) mitotic and (B) meiotic cell cycle.*

Only one pair of homologous chromosomes is shown in orange and blue and each line represents one chromatid. During S phase chromatids duplicate, condense at prophase and segregate at anaphase. After telophase, two identical daughter cells are formed. Note the progressive increase of Cdk activity (black line on the graph), culminating at M phase. Putative threshold of S phase activity is represented by the green line and for M phase the red line. Specific events take place during the prophase of meiotic cell cycle: at leptotene double strand break formation (dotted orange and blue lines) and single

strand invasion, at zygotene progression of recombination and initiation of synapsis between the chromosomes (small black lines), at pachytene manifestation of crossovers and full synapsis of chromosomes and at diplotene/diakinesis chromosomes condense and crossovers remains at regions called chaismata. The homologues chromosomes segregate at anaphase I and sister chromatids at anaphase II, similar to mitosis. In the end, four genetically different gametes are formed. The hypothetical Cdk activity during meiotic cell cycle is shown in the last panel: note the two pics of Cdk activity needed for the first and second meiotic division and the decrease of Cdk activity after meiosis I does not reach the S phase threshold.

Modified from Wijnker and Schnittger, 2013.

Overview of meiotic cyclins

Cyclin-dependent kinases are regulated at multiple levels, of key importance being the type and the amount of the cyclin partner (Pines, 1995). Beside at least five central cell cycle Cdks (CDKA;1, CDKB1;1, CDKB1;2, CDKB2;1 and CDKB2;2) there are more then 30 cyclins in Arabidopsis (Vandepoele et al., 2002; Wang et al., 2004a). The first two cyclins shown to have a meiotic function are the A-type cyclin TAM (CYCA1;2) and SOLO DANCERS (SDS), an atypical cyclin, showing similarities with both A- and B-type cyclins and being necessary for crossover (CO) formation (Azumi et al., 2002; Harashima and Schnittger, 2012; Bulankova et al., 2013). TAM (TARDY ASYNCHRONOUS MEIOSIS) is needed for entry and progression through meiosis I as null mutants in *TAM* exit the meiotic program after the first division (Wang et al., 2004b; d'Erfurth et al., 2010; Bulankova et al., 2010).

Interestingly, single mutants of the closely related CYCA1;1 did not exhibit any meiotic phenotype, nor an enhanced phenotype when combined with *tam* mutants (Cromer et al., 2012). Also, most of the other A-type cyclins including CYCA2;2, CYCA3;2, CYCA3;3 and CYC3;4 are expressed in early meiotic prophase, but neither single nor double mutants of these cyclins showed any particular meiotic phenotype (Bulankova et al., 2013). Interestingly, although CYCA2;3 and CYCA2;4 were not found to be expressed in meiocytes, the triple mutant *cyca2;2 cyca3;2 cyca2;4* showed defects in chromosome segregation and condensation (Bulankova et al., 2013). This strongly suggests a partially redundant role of A-type cyclins in meiosis.

Among B-type cyclins only CYCB3;1 has been found to be expressed during meiosis, i.e. in metaphase I and II, marking both the first and second meiotic spindle as revealed by a GUS reporter line (Bulankova et al., 2013). Single mutants of

16

cycb3;1 were characterized by a premature formation of cell wall-like structures, a phenotype that was enhanced in combination with *sds* mutants (Bulankova et al., 2013). The question, which cyclins are involved in meiosis and how or when they interact with the core kinase proteins seems very complex given the diverse expression patterns and partial redundancy at different meiotic stages.

CAKs – a way to activate Cdks by T-loop phosphorylation

For the full activation of the Cdk complex, not only the binding of a cyclin cofactor is needed, but also Cdk-activating kinase (CAK)-mediated phosphorylation is of key importance (Morgan, 1997) (Figure 2). The phosphorylation of the activating Threonine 160/161 within Cdk T-loop is highly conserved among species and lies at the heart of Cdk activation (Dissmeyer et al., 2007; Shimotohno et al., 2003). In plants two classes of CAKs have been identified: CDKDs that are functionally related to vertebrate-type CAKs and CDKF, a plant specific CAK with unique features and dispensable for Cdk activation, as *cdkf* mutants showed post-embryonic development defects without alteration of kinase activity of the core Cdk complex (Takatsuka et al., 2009; Umeda et al., 2005).

There are three CDKD genes in the Arabidopsis genome: CDKD;1, CDKD;2 and CDKD;3 (Umeda et al., 2005; Shimotohno et al., 2003) (Figure 2). CDKDs control both Cdk activation and basal transcription as CDKD;2 and CDKD;3 display kinase activity towards the carboxy-terminal domain (CTD) of the largest subunit of RNA polymerase II. In vitro, the Cdk-kinase activity of CDKD;3 is higher than the one of CDKD;2 and CDKD;1 expressed in insect cells didn't phosphorylate neither Cdk nor CTD substrates (Takatsuka et al., 2015; Shimotohno et al., 2003). Mutations in single CDKD genes did not exhibit any particular phenotype but *cdkd;1 cdkd;2* and *cdkd;2 cdkd;3* double mutants showed dwarfism in post-embryonic development (Hajheidari et al., 2012). In the *cdkd;1 cdkd;3* double mutant, mitosis in male and female gametogenesis was severely defective (Takatsuka et al., 2015). Whether CDKDs have a role during plant meiosis is up to now not understood. However, Cdk7 a mammalian CAK is required for meiotic progression of oocytes (Brown et al., 1994; Fujii et al., 2011).

The microtubule cytoskeleton in mitosis and meiosis

The cytoplasm of eukaryotic cells is spatially organized by a network of protein filaments including actin, microtubules and intermediate filaments and thus constituting the cytoskeleton. Whereas the presence of intermediate filaments in plants is under debate, actin filaments and microtubules are crucial players in plant cell cycle and division. Actin filaments are required for the correct positioning of the nucleus, for distributing Golgi throughout the cortical cytoplasm and for reorganizing microtubule structures in different cell types (Kost and Chua, 2002). On the other side microtubules adopt different functional organizations in plant cell growth and division (Hashimoto, 2015).

During plant cell cycle progression, four major microtubule-based structures are present: the cortical array, a tight association of microtubules with the plasma membrane at interphase, the pre-prophase band, a plant-specific, microtubule dense, ring-like structure, displaying the same microtubule orientation as the cortical array and marking the site of later cell division, the mitotic spindle, a structure needed to move the chromatids to opposite poles of the cell and the phragmoplast, a molecular platform relevant for the execution of cytokinesis, i.e the cell wall deposition between the two new daughter nuclei (Wasteneys, 2002; de Keijzer et al., 2014) (Figure 4A).

The microtubule cytoskeleton is also a major player during the meiotic cell division program. Several studies have shown that microtubules promote nuclear rotations and thus pairing of homologous chromosomes during prophase (Christophorou et al., 2015). This is exemplified by the formation of a telomere bouquet, a hub where the occurrence of meiotic double-strand breaks, synapsis and stable homolog juxtaposition are coordinated and supported by the microtubule cytoskeleton in zebrafish (Blokhina et al., 2019). In yeast, meiotic spindle defects were observed in mutants of the telomere bouquet formation (Tomita and Cooper, 2007). After prophase I, the correct positioning of bivalents and their segregation rely on spindle-generated forces during meiosis I and chromatid segregation is supported by the two spindles during meiosis II (Brownfield et al., 2015). During the second metaphase in Arabidopsis male meiosis, when spindles share the same cytoplasm, it is crucial to prevent close physical proximity of these microtubule structures as a mingling might result in chromosome segregation and ploidy defects. While it is still unclear how exactly distancing is brought about, mutant analyses reveal the first players involved in positioning of the spindle. Loss of *Parallel Spindle 1 (PS1)* or *Jason (JAS)* for example results in altered spindle arrangements in male meiocytes

and defective meiotic products i.e triads (two reduced and one unreduced cell) or dyads (two unreduced cells) (Brownfield et al., 2015). The co-localization of JAS with endomembrane markers suggests that JAS-containing vesicles are required to maintain the positions of membrane bound organelles and thus restricting the possible spindle orientation to perpendicular to each other (Brownfield et al., 2015).

The study of microtubules is very complex due to their many functions and dynamic changes throughout cell cycle progression. A recent live cell imaging technique of whole anthers in Arabidopsis nicely revealed the spatiotemporal dynamics of microtubule configurations during meiosis (Prusicki et al., 2019) (Figure 4B). At the onset of meiosis microtubules are equally distributed in the cytoplasm changing to an arc-like structure called *half-moon* in early prophase. Similar to mitosis, a *full-moon*-like microtubule structure surrounds the nucleus later in prophase and when the nuclear envelope breaks down, microtubules are rapidly re-arranged to form the first meiotic spindle (Figure 4B). After anaphase I, microtubules persist in the mid-zone until late interkinesis. During the second meiotic division, two spindles within the meiocyte sustain sister chromatid segregation and tetrad formation. The regulation of these specific microtubule arrays observed in meiosis is up to now still largely a mystery.

A Microtubule arrays throughout the mitotic cell cycle

Pre-prophase band | Mitotic spindle | Early phragmolast | Late phragmoplast | Cortical microtubules

In green, microtubules
In blue, chromosomes

Modified from Wasteneys, 2002

B Microtubule arrays throughout the meiotic cell cycle

Cortical microtubules | *Half-moon* configuration | *Full-moon* configuration

Meiotic spindle I | Mid-zone microtubules | Meiotic spindle II | Tetrad

In red, microtubules
In green, REC8

Modified from Prusicki et al., 2019

Figure 4: Comparison between the mitotic (A) and meiotic (B) microtubule arrays during cell cycle in plants. (A) Four microtubule arrays shown in green alternate during the mitotic cell cycle: cortical microtubules, pre-prophase band, spindle and phragmoplast. (B) Microtubule arrays that characterize meiosis: half-moon, full-moon, mid-zone, the first and the two second spindles, shown in red.

However, studies from mitosis have shown that microtubule dynamics are controlled by many factors: on one side by microtubule-associated proteins (MAPs) of different nature and on the other side by Cdk-cyclin complexes and Aurora kinases (Dumitru et al., 2017; DeLuca et al., 2018; Vavrdová et al., 2019). Some MAPs, including MAP65-3 can stabilize microtubules against disassembly via filament bundling and cross-linking (Ho et al., 2012) and they might be targets of several protein kinases through cascades of phosphorylation (Vavrdová et al., 2019). Another subclass of MAPs are the motor proteins i.e. kinesins transporting various cargos such as membranous organelles. Many plant kinesins are involved in mitosis and meiosis for example AtNACK1 and AtNACK2 are essential for the completion of cell plate and tetrad formation, OsPSS1 controls male meiotic chromosomal dynamics and

gametogenesis (Li et al., 2012). Interestingly, MAPs in cortical microtubules contribute to the regulation of plasma membrane interacting proteins i.e. phospholipase D or actin-binding proteins (for more see review from (Krtková et al., 2016)).

Microtubule networks are also regulated by protein kinases. Several studies of mitosis have shown that Cdks localize to both nucleus and cytoplasm in pre-mitotic cells as well as to the pre-prophase band and to the spindle in a microtubule-dependent manner. Additionally, application of Cdk inhibitors resulted in the loss of spindle polarity (Colasanti et al., 1993; Weingartner et al., 2001, 2004). Recent data implicated the meiotic A-type cyclin TAM in the coordination of spindle formation with nuclear processes in *Arabidopsis*, since premature spindle/phragmoplast-like structures are formed in *tam* mutants before the meiotic nuclear envelope breakdown (Prusicki et al., 2019).

Aurora kinases A and B are known to regulate mitotic entry, spindle assembly and chromosome segregation as their altered expression resulted in aneuploidy and polyploidization (Demidov et al., 2014). However, little is known on how these kinases regulate meiotic microtubules.

Cytokinesis in plant meiosis

In mitotically dividing cells, cytokinesis marks the physical separation of the two new daughter nuclei. Although across all organisms cell division is regulated by the cytoskeleton and the membrane trafficking machinery, there is a high variability in how this process is accomplished in plants versus other eukaryotic organisms (Guertin et al., 2002). In animal cells, a cleavage furrow is formed at the division site, which is in most cases located at the cell equator. The major components of the furrow are actin and myosin, structured together in a contractile ring called the actomyosin ring. During anaphase the ring assembles beneath the plasma membrane and gradually contracts centripetally. At the same time the fusion of intracellular vesicles with the plasma membrane inserts new membrane adjacent to the ring. At the end, the cleavage furrow narrows to form the midbody, as a tether between the two new daughter cells containing the remains of the central spindle. When ring contraction is completed, membrane insertion and fusion fill the gap between the daughter cells (Guertin et al., 2002). In contrast, plants engage microtubules and actin to build a dense structure called phragmoplast. Microtubule-attached vesicles containing cell

wall components are transported within the phragmoplast towards the plane of cell division and fusion of these vesicles allows the inside-out extension of the phragmoplast, forming and enlarging a membranous structure called the cell plate (Müller and Jürgens, 2016). Finally, the fusion of the cell plate with the parental cell wall concludes the formation of two new daughter cells.

In the mitotic cell division, segregation of chromosomes is mostly followed by the formation of a cell plate (Figure 5A). In plant male meiosis, two different timings of cell plate formation are observed: successive and simultaneous cytokinesis (De Storme and Geelen, 2013; Müller and Jürgens, 2016) (Figure 5A). During successive cytokinesis, observed in male meiosis of most monocotyledonous species i.e maize, rice and wheat, a first cell plate is formed immediately after the first meiotic division, leading to a transitory dyad and after the second meiotic division a tetragonal, T-shaped or linear tetrad is formed by additional cytokinetic events (Furness and Rudall, 1999; Shamina et al., 2007) (Figure 5A,B). In contrast, in male meiosis of dicotyledonous species such as Arabidopsis or Tabaco, cell plate formation is uncoupled from chromosome segregation as cytokinesis occurs only when both meiotic divisions have been accomplished (Figure 5A). This simultaneous cytokinesis will result in tetragonal, rhomboidal or tetrahedral tetrad configurations (De Storme and Geelen, 2013) (Figure 5B).

Although the successive cytokinesis in male meiosis of many monocots resembles the conventional mitotic cytokinesis, recent studies in maize and rice have indicated specific alterations in microtubule dynamics (Shamina et al., 2007; De Storme and Geelen, 2013). First, there is no pre-prophase band marking the region of later cell plate attachment as observed in mitosis, but rather remaining midzone microtubules of the meiotic spindles determine the future cell wall positions. Second, the enhanced curvature of phragmoplast microtubule fibres as driving force of meiotic phragmoplast extension is due to the polymerization of new microtubules and not to microtubule recycling within the phragmoplast as observed in mitosis (Jürgens, 2005; Shamina et al., 2007). However the centrifugal phragmoplast extension and the inside-out direction of cell wall deposition is conserved in both cases (Figure 5A). Strikingly different from the above-mentioned mechanisms of cell plate formation in mitosis and successive-type meiosis, the simultaneous cytokinesis is characterized by a cell wall deposition occurring in an outside-in mode. Starting from the parental cell wall the centripetal ingrowth of the cell plate is mediated by a phragmoplast-like

structure also named radial microtubule arrays (RMAs) originating from the microtubule organizing centres (MTOCs) of telophase II nuclei (Otegui and Staehelin, 2004) (Figure 5A). A similar microtubule dynamics is observed in endosperm development, where at first, successive cycles of nuclear divisions take place without cytokinesis and then, at the moment of cellularization, RMA-based cell plate formation simultaneously occurs between all nuclei (Otegui and Staehelin, 2000).

Modified from De Storme and Geelen, 2013
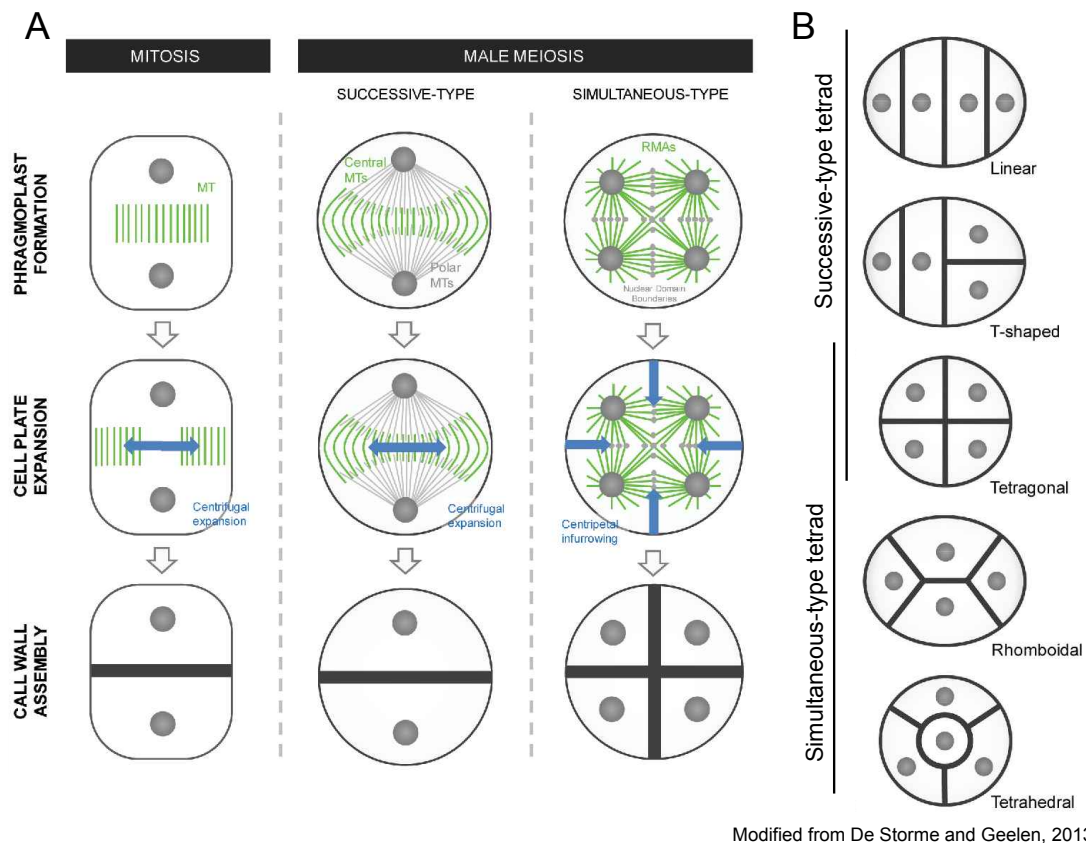
Figure 5: Overview of cytokinesis in plants.

(A) Comparison of mitotic and meiotic cytokinesis: during mitosis the phragmoplast is formed in the mid-zone and expands centrifugally allowing an inside-out directed cell plate growth. This mechanism seems conserved in the successive-type cytokinesis seen for example in male meiosis of Maize. During the simultaneous type cytokinesis of Arabidopsis thaliana, Nicotiana tabacum, Luzula male meiocytes the cell wall is deposited centripetally, i.e. from outside-in leading to a separation of all four gametes at the same time. In green microtubules and in blue the direction of cell wall deposition. (B) Configurations of meiotic products after successive cytokinesis (linear, T-shaped and tetragonal) and simultaneous cytokinesis (tetrahedral, rhomboidal and tetragonal). For more see review from De Storme and Geelen, 2013

The molecular mechanisms of cell plate formation during plant meiosis remain unclear and most of the actual knowledge comes from studies in mitosis. One of the first proteins identified to be relevant for cell plate formation in Arabidopsis was the syntaxin KNOLLE (Lauber et al., 1997), a membrane associated protein involved in vesicle fusion. KNOLLE has been found in the plane of cell division in mitotically dividing cells including roots, floral meristems, ovules and endosperm, but not in male meiocytes (Lauber et al., 1997; Lukowitz et al., 1996). This suggests that the molecular machinery of cell plate formation during meiotic cytokinesis differs, at least partially from the one in mitotic cytokinesis. Nevertheless, genetic screens in Arabidopsis have revealed mutants specifically affecting cytokinesis in plant meiosis. The *STUD/TETRASPORE/NACK2* gene is specifically required for cytokinesis of male meiocytes and its absence results in tetranucleate microspores due to the absence of cell wall deposition (Hülskamp et al., 1997; Spielman et al., 1997). Similar phenotypes were observed in *mpk4* mutants, involved in the mitogen-activated kinase signalling pathway (MAPK) (Takahashi et al., 2010; Zeng et al., 2011). The MAPK pathway results in phosphorylation of members of the MAP65 protein family, microtubule associated proteins specifically located to the phragmoplast (Boruc et al., 2017; Ho et al., 2012; Smertenko et al., 2006). Phosphorylated MAP65s increase microtubule instability at the phragmoplast mid-zone, thus allowing the cell plate extension (Müller et al., 2004). If similar mechanisms of cell plate extension are relevant for meiotic cytokinesis is still unknown.

Additionally, exterior factors such as temperature and hormones influence cytokinesis in male meiosis. Low temperature stress leads to the production of diploid male gametes in Arabidopsis by destabilizing the post-meiotic radial microtubule arrays and thus inhibiting cytokinesis (Liu et al., 2017; Storme et al., 2012). Recently, it has been shown that high temperature stress on the other side affects not only crossover designation but also male meiotic cell division and cell wall deposition in Arabidopsis (Storme and Geelen, 2020). Although we are starting to better understand the regulation of meiotic cytokinesis in plants, it is still challenging to dissect the differences between species in terms of diversity of meiotic products and pathways regulating successive or simultaneous cytokinesis. Even in the most studied model plant Arabidopsis, we lack many essential actors of cell plate formation, components of the meiotic phragmoplast and their regulators.

SIMOULTANEOUS CYTOKINESIS in *Arabidopsis*

Prophase I	Metaphase I	Interkinesis	Metaphase II	Telophase II	Tetrad

SUCCESSIVE CYTOKINESIS in *Maize*

Prophase I	Metaphase I	Interkinesis	Metaphase II	Telophase II	Tetrad
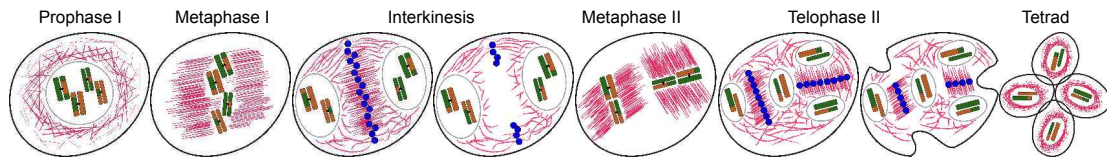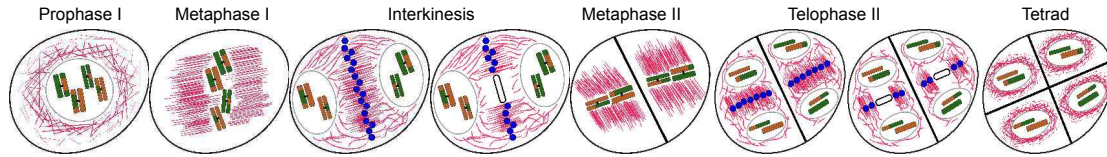
——	Cell wall
——	Nuclear envelope
——	Microtubules
▮▮▮	Chromosomes
●	Hypothetical meiotic phragmoplast

Summery of microtubule dynamics and cytokinesis during meiosis in Arabidopsis (simultaneous cytokinesis) and maize (successive cytokinesis) as representative examples.

Research aim and chapter overview/thesis structure

Meiosis is essential for sexually reproducing organisms through the reduction of chromosome numbers and the generation of genetic diversity via recombination. The behaviour of chromosomes is highly regulated and tightly coordinated with the cytoskeleton dynamics. The spatiotemporal order of events taking place during meiosis is of key importance in generating haploid gametes. Any deviations i.e premature termination after the first meiotic division or missegregation of chromosomes can have dramatic effects on the next generation. Hence, multiple levels of regulation govern meiotic progression.

Among the major cell cycle regulators, the activity of cyclin-dependent kinase complexes is crucial in promoting mitotic divisions. However, up to now little is known about the role of these complexes during the meiotic cell cycle progression.

The major aim of my thesis was to investigate the major cell cycle cyclin-dependent kinase in Arabidopsis, CDKA;1 during meiosis at two different levels. First, the requirement of Cdk-Activating Kinases (CAKs), i.e. CDKDs in activating CDKA;1 and thus promoting chromosome segregation, microtubule organization and cytokinesis during meiosis. Second, the role of CYCB3;1, a cyclin partner of CDKA;1, in regulating meiotic microtubules by using a modified live cell imaging protocol to follow meiocytes under drug treatment. These data will be presented in Chapter 1.

The second aim of my thesis was to better understand the role of CDKA;1 during meiotic prophase. I contributed to the analysis of CDKA;1 in controlling axis assembly (Chapter 2.1) and on how Cdk-cyclin activity affects the sister chromatid cohesion at late prophase (Chapter 2.2).

Finally I had particular interest in extending the importance of Cdks/cyclins beyond meiosis by using them as molecular tools to investigate stress response (Chapter 3.1) and quantify cell cycle progression in Arabidopsis roots (Chapter 3.2).

CHAPTER 1: Cdk complexes promote meiotic progression

1.1 CDKD-dependent activation of CDKA;1 controls microtubule dynamics and cytokinesis during meiosis

The following manuscript has been accepted for publication the 4th of May 2020 at the Journal of Cell Biology and is currently in press production with the identification **DOI: 10.1083/jcb.201907016**.

While I am responsible for most of the work presented, the co-authors contributed the following experiments:

- Hirotomo Takatsuka: initial cloning of *CDKD;1, CDKD;2* and *CDKD;3* reporter lines
- Chao Yang: generation of *CYCB3;1:GFP* reporter line and kinase assays of CDKA;1 and CYCB3;1 (Figure 8C)
- Nico Dissmeyer: generation of the *VFD cdka;1* construct and kinase assays of *VF cdka;1* and *VFD cdka;1* (Figure 3)
- Shinichiro Komaki: generation of *GFP:MAP65-3* reporter line
- Lev Böttger: root growth assay under oryzalin treatment (Figure S5A)

Details of specific author contributions are highlighted on figure legends.

CDKD-dependent activation of CDKA;1 controls microtubule dynamics and cytokinesis during meiosis

Condensed title: Control of meiotic microtubules by CDKA;1

Kostika Sofroni[1], Hirotomo Takatsuka[2,3], Chao Yang[1], Nico Dissmeyer[4], Shinichiro Komaki[2], Yuki Hamamura[1], Lev Böttger[1], Masaaki Umeda[2] and Arp Schnittger[1,*]

[1] University of Hamburg, Department of Developmental Biology, Ohnhorststr. 18, D-22609 Hamburg, Germany

[2] Nara Institute of Science and Technology, Graduate School of Science and Technology, Nara, Japan

[3] Present address: School of Biological Science and Technology, College of Science and Engineering, Kanazawa University, Kakuma-machi, Kanazawa, 920-1192 Japan

[4] Department of Plant Physiology, University of Osnabrück, Barbarastrase 11, D-49076 Osnabrück, Germany

[*] For correspondence: arp.schnittger@uni-hamburg.de, Phone: +49 40 428 16 502, Fax: +49 40 428 16 503

Summary

CDKA;1, the Arabidopsis ortholog of Cdk1 and Cdk2, controls microtubule organization in meiosis. Reducing CDKA;1 activity converts the simultaneous cytokinesis, separating all four meiotic products concomitantly, into two successive cytokineses after the first and second meiotic division as found in many crop species.

Abstract

Precise control of cytoskeleton dynamics and its tight coordination with chromosomal events are key to cell division. This is exemplified by formation of the spindle and execution of cytokinesis after nuclear division. Here, we reveal that the central cell cycle regulator CYCLIN DEPENDENT KINASE A;1 (CDKA;1), the Arabidopsis homolog of Cdk1 and Cdk2, partially in conjunction with CYCLIN B3;1 (CYCB3;1), is a key regulator of the microtubule cytoskeleton in meiosis. For full CDKA;1 activity, the function of three redundantly acting CDK-activating kinases (CAK), CDKD;1, CDKD;2 and CDKD;3, is necessary. Progressive loss of these genes in combination with a weak loss-of-function mutant in *CDKA;1* allowed a fine-grained dissection of the requirement of cell-cycle kinase activity for meiosis. Notably, a moderate reduction of CDKA;1 activity converts the simultaneous cytokinesis in Arabidopsis, i.e. one cytokinesis separating all four meiotic products concurrently, into two successive cytokineses with cell wall formation after the first and second meiotic division as found in many monocotyledonous species.

Introduction

Meiosis is a specialized type of cell division in which two rounds of chromosome segregation events, meiosis I and meiosis II, follow a single round of DNA replication resulting in a reduction of the DNA content by half. By this, meiosis maintains genome size in sexually reproducing organisms from one generation to the next since the full DNA content of an organism is restored after the fusion of the female and male gametes. Moreover, meiosis is a driving force for genetic diversity. First, homologous chromosomes exchange DNA segments during early prophase I through crossing-over, thus creating novel composition of genetic alleles. Second, all homologous chromosome pairs are randomly separated at the end of meiosis I, thereby forming new, yet complete, chromosome sets in daughter cells.

Both processes, the reduction in ploidy and meiotic recombination, require an elaborate behavior of chromosomes. For instance, homologous chromosomes must recognize each other in early prophase I and undergo pairing while they need to be separated and equally distributed to opposite cell poles later in meiosis I. A key component facilitating homology search and pairing of chromosomes by promoting nuclear rotations, and separation of chromosomes by building the spindles, as well as many other aspects of meiosis, is the microtubule cytoskeleton (Ding et al., 1998; Yoshida et al., 2013; Tapley and Starr, 2013; Christophorou et al., 2015). Consistent with their many functions, microtubule assemblies undergo dramatic changes during meiosis as revealed by live cell imaging (Mogessie et al., 2018; Prusicki et al., 2019). However, much of our understanding of the regulation of microtubules during cell division comes from studies of mitosis and despite of their importance, it is far from understood how microtubule dynamics are controlled in meiosis.

A paradigm for the role of microtubules in mitosis is the formation of the phragmoplast in plants. The phragmoplast is a microtubule-based structure that serves to establish the new cell wall (cell plate) between the separated nuclei during plant cell division (Jürgens, 2005; Müller and Jürgens, 2016; Smertenko et al., 2017). Notably, some plant species skip phragmoplast formation and hence lack cytokinesis after the first meiotic division (meiosis I). Instead, four cell walls are concurrently formed after the second meiotic division (De Storme and Geelen, 2013). This type of cytokinesis, called simultaneous cytokinesis, which is characteristic for male meiosis in many dicotyledonous species, e.g. in the model plant *Arabidopsis thaliana* (De

Storme and Geelen, 2013). In contrast, maize, rice and wheat male meiocytes, representative for the majority of monocotyledonous plants, undergo cytokinesis after each division, referred to as successive cytokinesis (Furness and Rudall, 1999; Jürgens, 2005; Shamina et al., 2007). How the different cytokinesis programs are brought about is up to now not understood.

The dynamics of microtubules are controlled by many factors, especially kinases. Next to Aurora kinases and MAPKs, especially CDK-cyclin complexes have been found to regulate the microtubule cytoskeleton in mitosis (Dumitru et al., 2017; DeLuca et al., 2018; Vavrdová et al., 2019). CDKA;1, the major cell cycle CDK in Arabidopsis and the homolog of the animal kinase Cdk1 and Cdk2 (Nowack et al., 2012), was found to localize to several microtubule arrays in mitotic cells, especially to the pre-prophase band (Colasanti et al., 1993; Weingartner et al., 2001). Conversely, application of CDK inhibitors resulted in the loss of spindle polarity, and the expression of a non-degradable cyclin B1 version disrupted phragmoplast organization and caused cytokinetic defects (Binarová et al., 1998; Weingartner et al., 2004).

While the regulation of microtubules by CDKA;1 in meiosis has not been studied so far, recent data implicated the meiotic A-type cyclin TARDY ASYNCHRONOUS MEIOSIS (TAM) in the coordination the microtubule cytoskeleton with nuclear processes in Arabidopsis. In *tam* mutants, ectopic anti-parallel microtubule bundles are formed that resembled the microtubule organization in the spindle and the phragmoplast. Notably, these structures appeared prior to nuclear envelope breakdown (NEB) and are after NEB rapidly incorporated into the first meiotic spindle (Prusicki et al., 2019).

TAM has been earlier found to build an active complex with CDKA;1 (Harashima and Schnittger, 2012; Cromer et al., 2012). Mutants with lowered CDKA;1 activity levels have reduced fertility and suffer from multiple defects in meiosis, including an altered meiotic recombination pattern (Dissmeyer et al., 2007, 2009; Wijnker et al., 2019). Consistent with its many functions, CDKA;1 is present throughout female and male meiosis (Bulankova et al., 2010; Zhao et al., 2012; Yang et al., 2020).

The dissection of the role of CDK-cyclin complexes in plants is complex since besides TAM there are over 30 cyclins present in the Arabidopsis genome (Wang et al., 2004a). Among them, seven A- and B-type cyclins have been found to be

expressed in male meiocytes, examples in addition to TAM being SDS (SOLO DANCERS) and CYCB3;1 (Bulankova et al., 2013). While SDS has been found to play an important role in meiotic recombination (Azumi et al., 2002; Girard et al., 2015) not much is known about CYCB3;1 and single mutants of *CYCB3;1* did not exhibit any obvious growth defect. However, ectopic and premature cell wall formation in meiocytes were found in the double mutants of *sds* and *cycb3;1* (Bulankova et al., 2013).

Besides the interaction with cyclin co-factors, CDKs are regulated by the binding of inhibitors and by phosphorylation (Morgan, 1997). Phospho-control of CDKs works at two levels in animals and yeast, i.e. by an inhibitory phosphorylation in the P-loop and activatory phosphorylations in the T-loop (Morgan, 1997). However, there seem to be variations to this general scheme since at least in Arabidopsis, CDKA;1 appears to be only regulated by T-loop not by P-loop phosphorylation (Harashima et al., 2007; Dissmeyer et al., 2007, 2009; Bulankova et al., 2010).

T-loop phosphorylation of CDKA;1 is catalyzed by another class of CDKs, i.e. CDK-activating kinases (CAKs), e.g. the monomeric kinase CAK1 in budding yeast and Cdk7-cyclin H complexes in vertebrates (Kaldis, 1999). CAK activity is represented by the D-type CDKs in Arabidopsis that build a small gene family with three members, CDKD;1, CDKD;2, and CDKD;3 of which all form active complexes with the Arabidopsis cyclin H homolog (Shimotohno et al., 2003; Umeda et al., 2005). Single mutants in *CDKDs* do not show any obvious alterations from the wildtype. However, double mutants *cdkd;1 cdkd;2* and *cdkd;2 cdkd;3* are reduced in growth and fertility while the double mutant *cdkd;1 cdkd;3* is gametophytic lethal (Takatsuka et al., 2015; Hajheidari et al., 2012). Consequently, the triple mutant *cdkd;1 cdkd;2 cdkd;3* could also not be recovered. However, *cdkd;1 cdkd;2* could be combined with a weak loss-of-function allele of *CDKD;3*, named *cdkd3-2*, and resulted in miniature plants that in addition showed defects in gametophyte development (Hajheidari et al., 2012).

Here, we have analyzed the function of CDKDs in meiosis. Removing CDKDs in a step-wise fashion allowed us to dissect their role in a very fine-grained manner. In particular, we found that microtubule organization is controlled by CDKA;1 in a CDKD-activation dependent mode. Strikingly, we observed that a slight reduction of CDKA;1 activity converted the simultaneous meiosis of Arabidopsis into

a successive meiosis, indicating that small differences in CDKA;1 activity are fully sufficient to drastically alter meiotic progression.

Results

CDKDs are expressed during the entire meiosis and co-localize with CDKA;1 in the nucleus

To understand the role of CDKDs in meiosis, we first analyzed their localization pattern in male meiocytes. For this purpose, we generated genomic reporters in which the coding sequence of mVenus as a fluorescent marker was added directly before the stop codon of the three *CDKD* genes. Since single mutants in each of the *CDKD* genes do not lead to a mutant phenotype, we transformed these genomic constructs into the two double mutants *cdkd1/- cdkd3/+* and *cdkd2/- cdkd3/-*, which show reduced growth and have fertility defects (Hajheidari et al., 2012). Expression of these reporter lines completely rescued the *cdkd1/- cdkd3/+* and *cdkd2/- cdkd3/-* double mutant phenotypes and we conclude that these reporters are fully functional (Figure S1A-E).

Since CDKD;2 was previously found to have high kinase activity against Cdk2 and since CDKA;1 and Cdk2 are homologous kinases (Shimotohno et al., 2006; Dissmeyer et al., 2007), we generated a genomic *CDKA;1* reporter fused to mTurquoise2 (*PRO$_{CDKA;1}$CDKA;1:mTurquoise2*) to allow the concomitant analysis of CDKDs and CDKA;1. We judged the *PRO$_{CDKA;1}$CDKA;1:mTurquoise2* to be fully functional since it complemented the severe somatic growth reduction of *cdka;1/-* null mutants (Nowack et al., 2012), and restored the meiotic defects previously observed in weak loss-of-function *cdka;1/-* mutants (Dissmeyer et al., 2007; Wijnker et al., 2019; Yang et al., 2020) (Figure S1F-G).

All three CDKDs localized to the nuclei of meiocytes (Figure S2). As a representative example and for reasons presented below, we focused our analysis on CDKD;3. Figure S2A-F shows the accumulation pattern of CDKD;3 and CDKA;1. During pre-meiosis, both CDKD;3 and CDKA;1 abundance levels were low (Figure S2A). In prophase I, accumulation of CDKD;3 increased and it co-localized with the nuclear portion of CDKA;1 (Figure S2B-D). As revealed by co-localized pixel maps and scatter plot analyses, the level of co-localization is stage dependent: high at early

and middle prophase I (R_{coloc}=0.915 and 0.893, respectively) and low at late prophase I (R_{coloc}=0.726). This dynamics is at least in part due to a simultaneous increase of the cytoplasmic and a decrease of the nuclear portion of CDKA;1 as revealed by a recent ratiometric quantification of CDKA;1 abundance during meiosis (Yang et al., 2020). Later, CDKD;3 accumulated together with CDKA;1 in the newly formed nuclei after meiosis I (in interkinesis) and after meiosis II (in tetrads) (Figure S2E,F). A very similar accumulation pattern was found for CDKD;1 and CDKD;2 (Figure S2G,H). Thus, CDKDs are present throughout meiosis and the high level of co-localization is consistent with an *in vivo* interaction between CDKA;1 and all CDKDs in the nuclei of meiocytes, especially during prophase I.

Double mutants in *CDKD* genes have severe meiotic defects
The accumulation patterns of CDKDs suggested that all three proteins function in meiosis. To assess their role, we analyzed chromosome spreads of male meiocytes of single *cdkd* mutants in comparison with the wildtype (Figure 1, Figure S3A,B).

Since none of the single *cdkd* mutants showed any obvious alteration from the wildtype, consistent with no obvious reduction in fertility and growth of *cdkd* single mutants, we next studied double mutants. Neither *cdkd;1/- cdkd;2/-* nor *cdkd;2/- cdkd;3/-* homozygous double mutants showed an apparent difference in meiosis to the wildtype (Figure S3C,D).

As the double homozygous mutant of *cdkd;1/-* and *cdkd;3/-* is gametophytic lethal (Takatsuka et al., 2015), we analyzed the combination of these mutants by keeping one of them in a heterozygous state. First defects of *cdkd;1 cdkd;3* combinations became notable in metaphase I when in the wildtype and single *cdkd* mutants, five fully condensed bivalents are visible and are physically kept together by chiasmata as a result of crossing-over (Figure 1A, first and second row). In *cdkd;1/- cdkd;3/+* and *cdkd;1/+ cdkd;3/-* double mutants, we observed univalents, indicating a failure of crossover formation between homologous chromosomes in these plants (red arrows Figure 1A and red circles Figure 1B). While two pools of equally distributed chromosomes are visible in interkinesis of wild-type plants, we found unbalanced pools having a 6:4 or a 8:2 chromosome segregation in the *cdkd;1 cdkd;3* double mutants (39% of meiocytes with unbalanced chromosome pools in *cdkd;1/- cdkd;3/+*; 43% in *cdkd;1/+ cdkd;3/-*) that persisted in metaphase II (Figure 1C,D). Additionally, chromosomes were still connected in form of DNA bridges (white

arrows) at late stages of the second meiotic division (telophase II) after sister chromatids were already separated (Figure 1A,E). Notably, a wild-type phenotype was restored in the double *cdkd;1/- cdkd;3-* mutants when the genomic *CDKD;1:mVenus* reporter construct was present (Figure S3E), confirming the functionality of this construct and corroborating that the meiotic defects seen in plants of *cdkd;1 cdkd;3* double mutant combinations were due to the absence/reduction of CDKD activity.

Taken together, these data demonstrate that CDKD;1 and CDKD;3 have a largely redundant role in crossover formation and chromosome segregation with CDKD;3 being more important than CDKD;1.
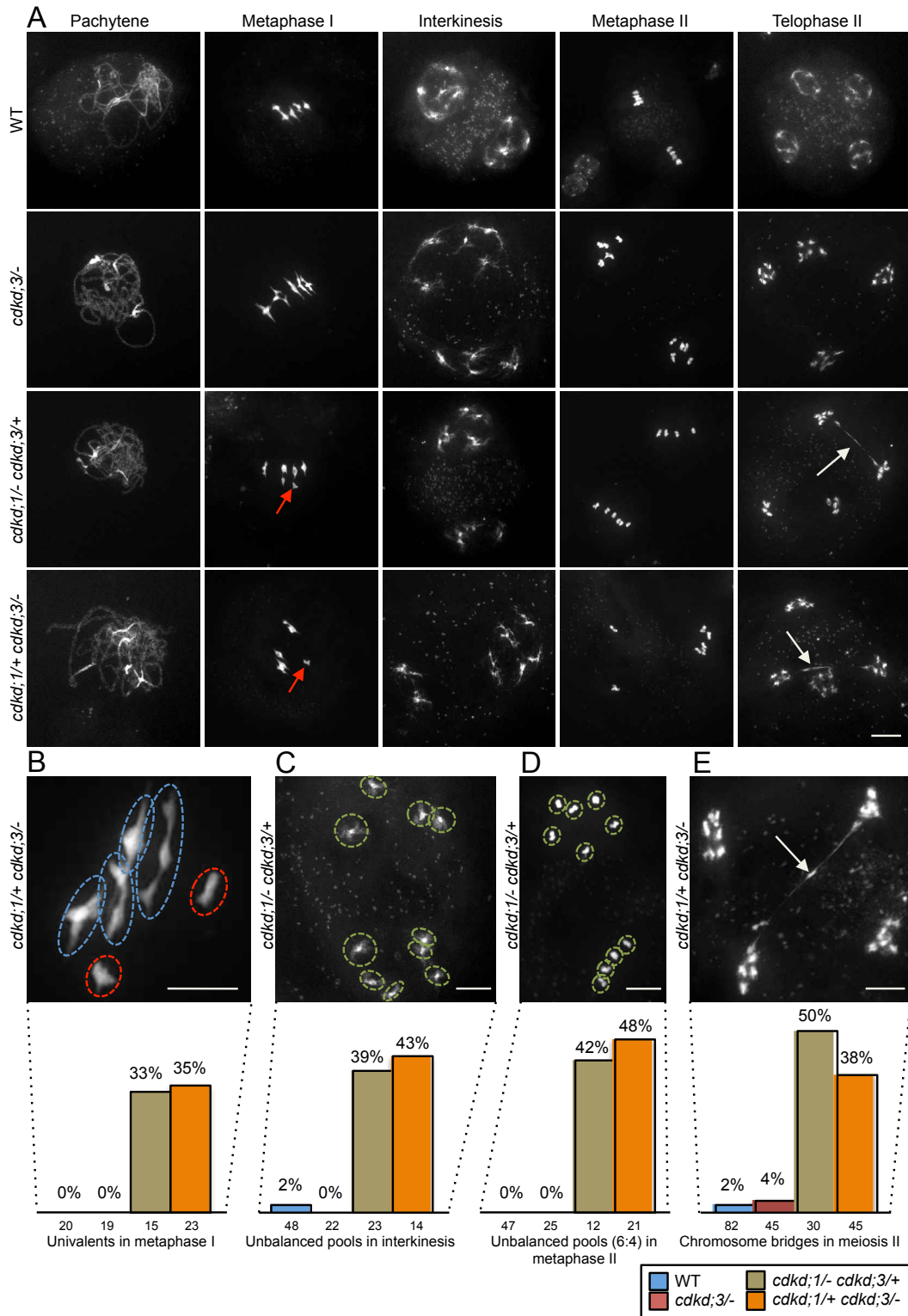
Figure 1. Analysis of meiotic defects in *cdkd* mutants. (A) Chromosome spread analysis of male meiocytes in the wildtype (WT) versus single *cdkd;3* mutants and two different double *cdkd;1 cdkd;3* mutant combinations during pachytene, metaphase I, interkinesis, metaphase II, and telophase II. Red arrows indicate univalents in metaphase I and white arrows designate chromosome bridges in telophase II. (B) Close up of chromosomes with missing chiasmata in metaphase I of *cdkd;1/+ cdkd;3/-*. Red circles highlight univalents and blue circles bivalents. (C) Unbalanced chromosome pools in

interkinesis, and (D) in metaphase II, (E) a chromosome bridge in telophase II in *cdkd;1/+ cdkd;3/-* double mutants. In the last row, quantification of meiotic defects observed in *cdkd;3/-* (n=66), *cdkd;1/- cdkd;3/+* (n=50) and *cdkd;1/+ cdkd;3/-* (n=58) versus the wildtype (n=115). The numbers under every column indicate the meiocytes found per stage. Scale bar 10 μm.

Combined reduction of CDKD and CDKA activity results in a strongly enhanced mutant phenotype

A likely target of CDKD action, which could be responsible for the observed meiotic defects in *cdkd* mutants, is the major cell-cycle kinase CDKA;1 in Arabidopsis (Shimotohno et al., 2006; Nowack et al., 2012). One possibility to test this is by substituting in CDKA;1 the residue that is usually phosphorylated by CDKDs, i.e. Thr 161 with an amino acid that mimics phosphorylation, i.e. with a negative charge such as Asp or Glu (Dissmeyer et al., 2007; Harashima et al., 2007), and expressing this variant in the *cdkd* double mutants (Dissmeyer and Schnittger, 2011). However, such substitutions were previously generated and did not fully mimic T-loop phosphorylation of CDKA;1 resulting in CDKA;1 variants with reduced kinase activity (Dissmeyer et al., 2007; Harashima et al., 2007).

To assess the nature of a possible functional interaction between the two genes, we undertook a double mutant analysis. To this end, we used a previously described *CDKA;1* allele, called *CDKA;1$^{T14V;Y15F}$*, or short hereupon *VF*, in which a *cdka;1* null mutant carries the mutated *CDKA;1* expression construct resulting in a kinase variant with slightly reduced activity (Dissmeyer et al., 2009). While *cdka;1* mutants with very little kinase activity have severe meiotic defects making it difficult to observe any possible enhancement of the mutant phenotype (Dissmeyer et al., 2007, 2009; Yang et al., 2020), *VF cdka;1/-* plants follow a meiotic course, which is, at least qualitatively, similar to that in the wildtype (compare the first row of Figure 1A and 2B). Next, we combined *VF cdka;1/-* mutants with single mutants in *CDKD;1* and *CDKD;3*. The resulting double mutants displayed a progressive increase of meiotic defects depending on the degree of expression reduction (heterozygous versus homozygous) of the respective genes (Figure 2, Figure S4).
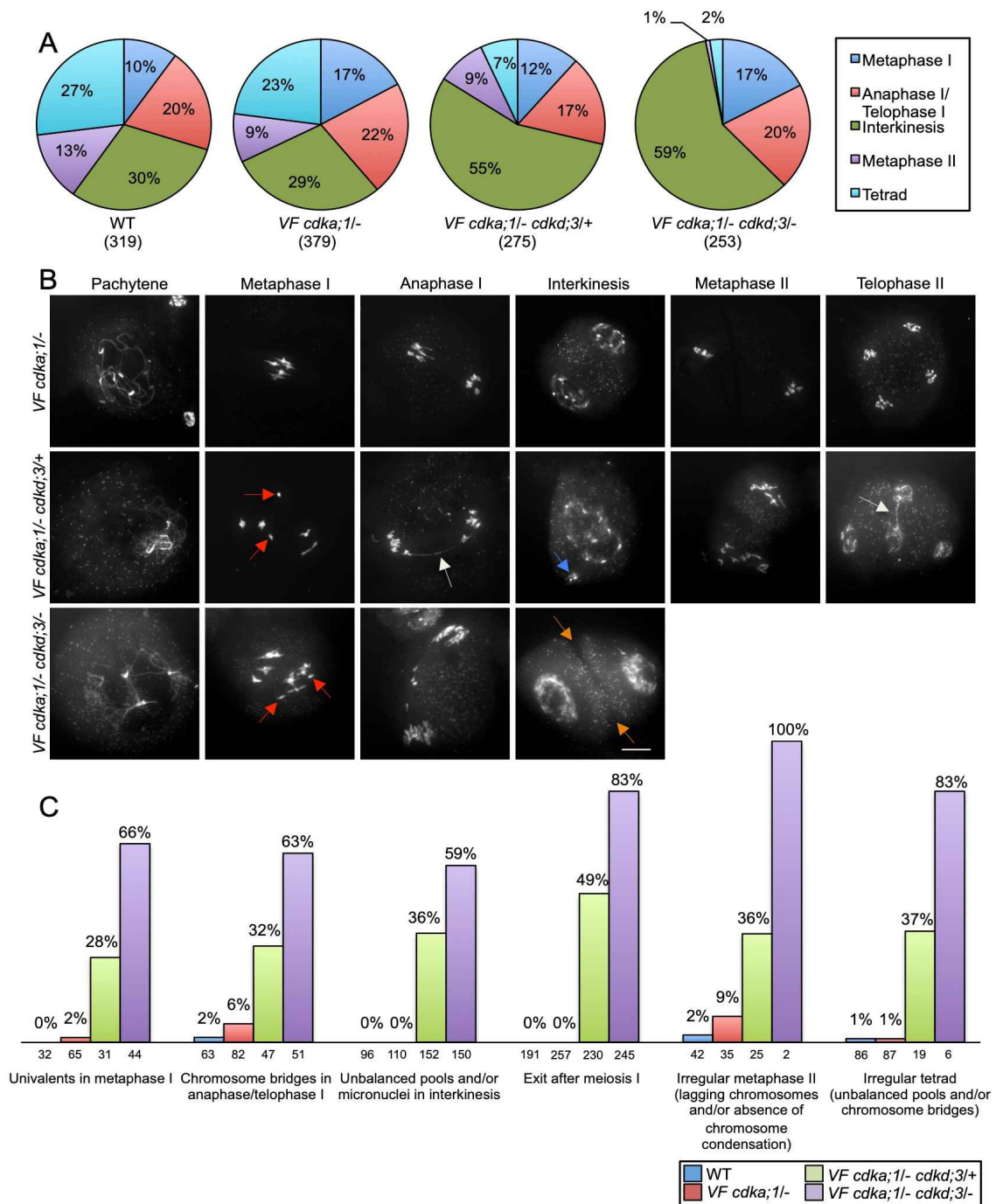
Figure 2. Analysis of meiotic defects in *VF* and *VF cdkd;3* double mutant combinations. (A) Repartition of meiotic stages within one single flower bud undergoing meiosis from metaphase I to telophase II/tetrad stage in the wildtype (WT) (n=319), *VF cdka;1/-* (n=379), *VF cdka;1/- cdkd;3/+* (n=275) and *VF cdka;1/- cdkd;3/-* (n=253). (B) Chromosome spreads of male meiocytes in *VF cdka;1* and *VF cdka;1 cdkd;3* double mutants. Red arrows indicate univalents/fragments in metaphase I, white arrows pinpoint chromosome bridges in anaphase I and/or telophase II, blue arrows highlight micronuclei in interkinesis and orange arrows point to premature cell wall formation in interkinesis. Scale bar 10 μm. (C) Quantification of meiotic defects observed in *VF cdka;1 cdkd;3* double mutants versus the wildtype given in percent of the meiocytes of one genotype that show the respective feature. The numbers under every column indicate the meiocytes found per stage.

When quantifying meiotic stages from metaphase I onwards, as a rough estimate for the course of meiosis, we observed in the wildtype that 10% of the meiocytes are in metaphase I, 20% in anaphase I/telophase I, 30% in interkinesis, 13% metaphase II, and 27% in tetrad stage (Figure 2A). A similar distribution was found in *VF cdka;1/-* single mutants (Figure 2A). However, in combination of *VF cdka;1/-* with heterozygous *cdkd;3/+* mutants (called *VF cdka;1/- cdkd;3/+*), 55% of the 275 analyzed meiocytes were in interkinesis and the number of cells undergoing the second meiotic division was strongly decreased (from 40% in the wildtype to 16% in the double mutant) (Figure 2A).

When *cdkd;3* was homozygous mutant in a *VF cdka;1/-* background (called *VF cdka;1/- cdkd;3/-*), meiocytes in the second meiotic division could not be found and the number of meiocytes in interkinesis increased even further (Figure 2A). Concomitantly, we observed in these mutants a significant increase in seed abortion (Figure S4A-B) and a drastic decrease in pollen viability (Figure S4C). Moreover, we saw that the size of viable pollen grains became enlarged (Figure S4D). Typically, pollen size correlates very well with nuclear DNA content (De Storme et al., 2007) and the observed increase in size of the viable pollen from *VF cdka;1/- cdkd;3* plants was similar to that observed in tetraploid wild-type plants (Figure S4D-E). Taken together, these results suggest that reduced CDKD activity results in diminished activation of CDKA;1 that leads to incomplete meiotic progression and ploidy defects in the progeny (as detailed below).

To test whether reduced T-loop phosphorylation of CDKA;1 in *cdkd* mutants could especially affect the activity of the CDKA;1 VF variant, we generated a triple mutated CDKA;1 (called *VFD* in the following) version in which we used the VF variant and substituted Thr161 with Asp that we knew from previous experiments cannot fully mimic a phosphorylated Thr residue in the context of the T-loop of CDKA;1 (CDKA;1 D variant; (Dissmeyer et al., 2007)). While *VF cdka;1/-* plants show no obvious reduction in growth and fertility, *D cdka;1/-* plants are stunted and completely sterile (Dissmeyer et al., 2007, 2009), *VFD cdka;1/-* plants were even more compromised than *D cdka;1/-* plants, resembling *cdka;1* null mutants with the exception of a root being formed in *VFD* but not in *cdka;1* null mutants (Figure 3A-C) (Nowack et al., 2012; Weimer et al., 2012). Kinase assays from *VFD cdka;1/-* plants revealed that this CDKA;1 variant has very low kinase activity consistent with the severe mutant phenotype of these plants (Figure 3D). Thus, although the structural

effects of the VFD mutations in CDKA;1 are not fully clear, the here-observed high sensitivity of CDKA;1 VF variant towards the presumptive reduction of T-loop phosphorylation in *cdkd* mutants is consistent with the strong defects of *VFD cdka;1/-* plants and further supports the idea that CDKA;1 is an *in vivo* target of CDKDs.
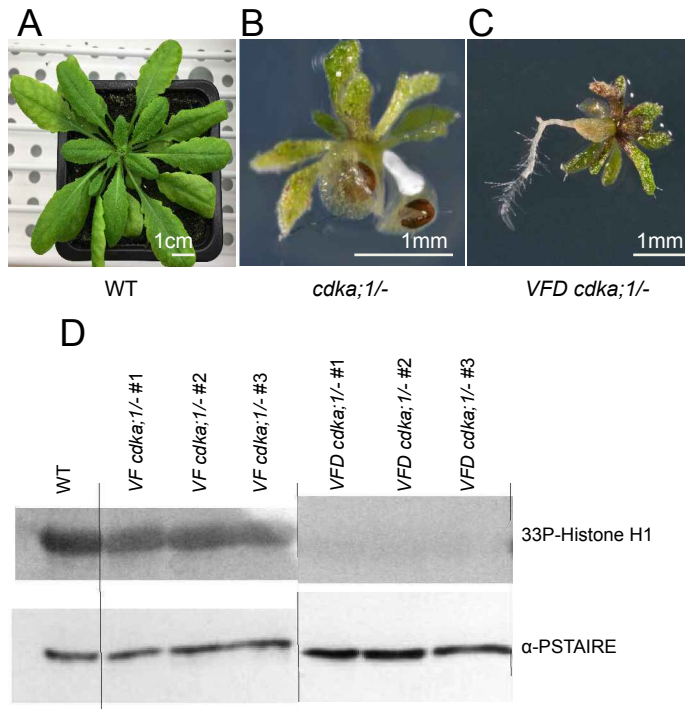
Figure 3. Characterization of the *VFD cdka;1* mutant. Comparison between a wild-type (WT) *Arabidopsis* plant (A), the *cdka;1/-* null mutant (B) and the *cdka;1/- VFD* mutant (C). The *cdka;1/- VFD* mutants are reduced in growth to a similar extent as the homozygous *cdka;1* mutant but develop a root. (D) Upper row, CDK-kinase assays with plant material of the wildtype, *VF cdka;1/-* , and *VFD cdka;1/-* using bovine histone H1 as a substrate. Lower row, CDKA;1 protein levels per kinase assay were visualized using an α-PSTAIRE antibody.

Nico Dissmeyer provided figure 3C, D and kinase assays in 3D.

To get a more detailed understanding of the mutant phenotypes of *VF cdkd* plants, we next performed chromosome spreads. In *VF*, meiotic progression was similar to the above-described chromosome spreads of the wildtype (compare the first row of Figure 1A and 2B). In *VF cdka;1/- cdkd;3/+*, chromosomes are paired at pachytene, but the presence of univalents (red arrows in Figure 2B) in 28% of cases in metaphase I indicated a reduction of crossover formation (Figure 2C). In anaphase I, we observed chromosome bridges indicating unresolved crossovers (Figure 2B,C). In addition, the organellar band, separating the two pools of chromosomes in interkinesis in the wildtype, was not found in *VF cdka;1/- cdkd;3/+* (Figure 2B). Furthermore, we

observed micronuclei at interkinesis-like stages (Figure 2B, blue arrow, Figure 2C). The second meiotic division was strongly affected as seen by very irregular chromosome figures in metaphase II, unbalanced segregation of chromosomes, and chromosome bridges in late meiosis (Figure 2B, second row, Figure 2C).

In *VF cdka;1/- cdkd;3/-* plants, where CDKD levels were further reduced, univalents at metaphase I and chromosome fragments at anaphase I were observed (Figure 2B, third row, Figure 2C). Premature cell wall formation (Figure 2B, orange arrows) and exit of meiosis after meiosis I were observed in 83% of the cells, presumably leading to meiotic products with a greater than the haploid nuclear DNA content consistent with our above-presented pollen size measurements (Figure 2B, third row, Figure 2C, Figure S4E).

Notably, the combined reduction/loss of CDKA;1 and CDKD3 activity went much beyond a simple additive mutant phenotype. For instance, while *cdkd3/-* mutants show no univalents in metaphase I and *VF cdka;1/-* plants have only in 2% of all metaphase cells univalents, 28% of all meiocytes in metaphase I of the mutant combination *VF cdka;1/- cdkd;3/+* have univalents (Figure 2C). This value even further increased in the *VF cdka;1/- cdkd;3/-* double mutant to 66% of all meiocytes. A similar dosage dependency and great enhancement much exceeding an additive effect were observed for all meiotic phenotypes quantified in *VF cdka;1 cdkd;3* combinations, i.e. chromosome bridges in anaphase I, unbalanced pools of chromosomes/micronuclei in interkinesis, exit after meiosis I, irregular metaphase II, and irregular tetrads (Figure 2C).

Additionally, we also analyzed the combinations *VF cdka;1/- cdkd;1/+* and *VF cdka;1/- cdkd;1/-* (Figure S4F,G). Whereas meiotic progression was not affected in *VF cdka;1/- cdkd;1/+* (Figure S4G, first row), double homozygous mutants showed premature cell wall formation (orange arrows) at interkinesis in 75% of cases (Figure S4G, second row). Taken together, the combined reduction of CDKA;1 and CDKD activity strongly enhanced the mutant phenotypes seen in hypomorphic *VF cdka;1* mutants indicating that CDKDs, especially CDKD;3, act as CDKA;1 activating kinases in meiosis.

CDKD;3 and CDKA;1 regulate microtubule organization in prophase I

To obtain further insights into the course of meiosis in *cdkd* mutants and their combination with *VF cdka;1/-*, we introgressed the KINGBIRD reporter line into *VF*

cdka;1/- and *VF cdka;1/- cdkd;3*. The KINGBIRD line holds a combination of two fluorescent reporters, one for the microtubule cytoskeleton, i.e. *PRO$_{RPS5A}$:TagRFP:TUA5*, and the other one for chromatin, by labeling the alpha kleisin subunit of the meiosis-specific cohesion complex, i.e. *PRO$_{REC8}$:REC8:GFP* (Prusicki et al., 2019).

We first focused on prophase I. In the wildtype, the nucleus moves to one side of meiocyte in zygotene and microtubules progressively accumulate around the nucleus starting from the side of the nucleus that faces the cytoplasm, giving rise to a *half-moon* like appearance (Figure 4A, light blue arrow) (Prusicki et al., 2019). In late prophase I, this process is completed and distinct arrays of microtubules embrace the entire nucleus (Figure 4B). After nuclear envelope breakdown (NEB) in diakinesis, the first spindle structures become visible (Figure 4C).

We found that the microtubule structures in *VF cdka;1/-* in combination with *cdkd3* were affected in a dosage-dependent manner. While the *half-moon* configuration of microtubules was less prominent in *VF cdka;1/- cdkd;3/+* than in the wildtype (Figure 4D), it appeared to be completely lost in *VF cdka;1/- cdkd;3/-* (Figure 4G). Similarly, the microtubule structure that embraces the whole nucleus in later prophase I progressively diminished as CDKD;3 levels were further reduced in the context of *VF cdka;1/-* (Figure 4E,H), i.e. tubulin displayed a less bundled localization pattern as quantified by line scan intensity plots in comparison with the wildtype (Figure 4B', E', H' and J).

In addition, *VF cdka;1/- cdkd;3/-* but not *VF cdka;1/- cdkd;3/+* mutants showed ectopic anti-parallel microtubule bundles at late prophase I, i.e. before NEB, resembling the microtubule organization in the phragmoplast and which were also recently seen in *tam* mutants (Prusicki et al. 2019). These structures are described in more detail below. Thus, the organization of microtubules in prophase I strongly depends on the dosage of CDKA;1 and CDKDs.
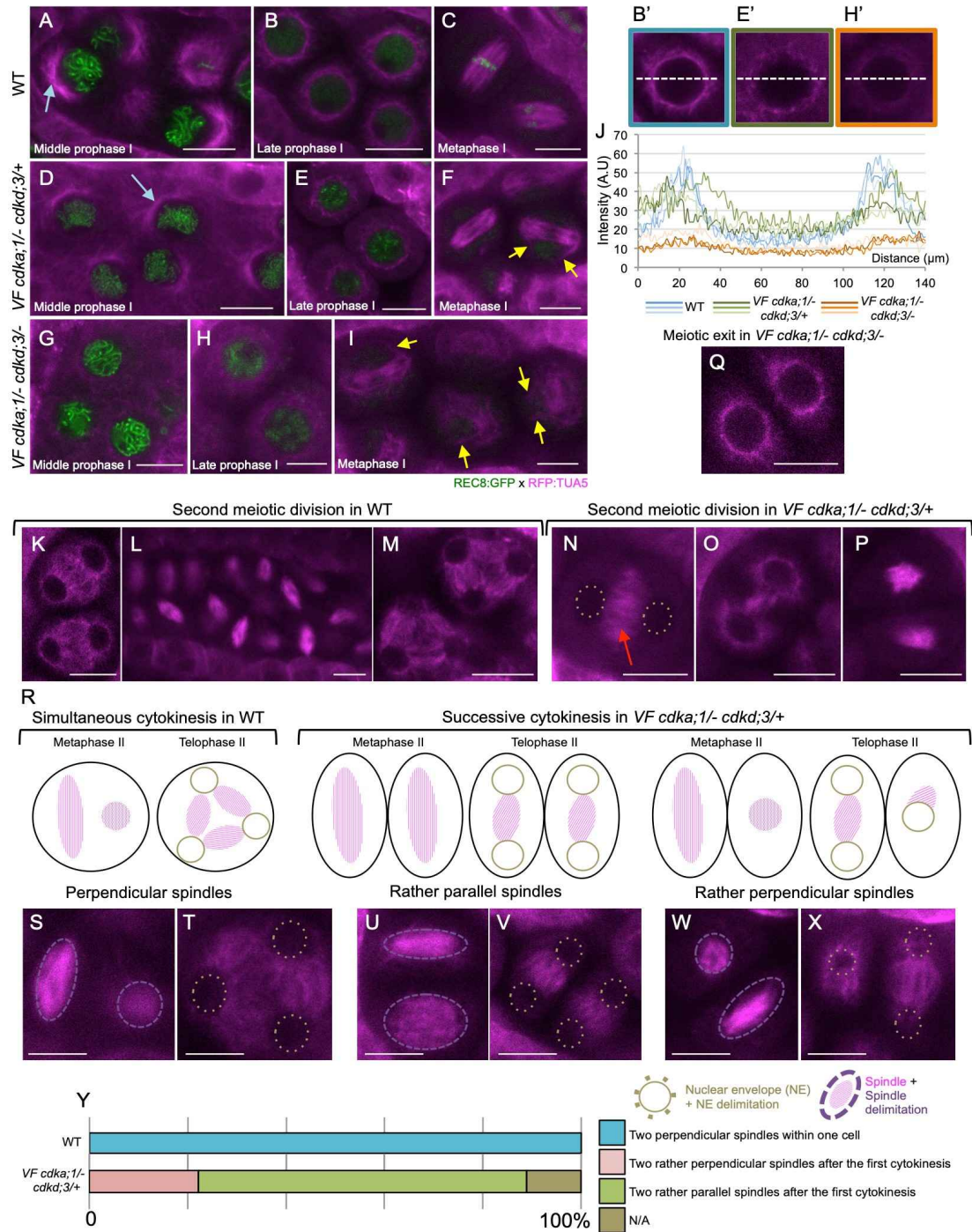
Figure 4. Microtubule arrays in the wildtype versus *VF cdka;1- cdkd;3* mutants. Confocal laser scanning micrographs of meiocytes expressing TagRFP:TUA5 (magenta) and REC8:GFP (green) from mid prophase I to metaphase I in the wildtype (WT) (A-C), *VF cdka;1- cdkd;3/+* (D-F), and *VF cdka;1- cdkd;3/-* (G-I). Light-blue arrows indicate the *half-moon* configuration of microtubules present in the wildtype, that is lost in *VF cdka;1- cdkd;3/-*. The yellow arrows highlight irregular spindles in metaphase I. (J) Pixel intensity quantification from 3 meiocytes at late prophase I in the wildtype (B' and blue lines), *VF cdka;1- cdkd;3/+* (E' and green lines) and *VF cdka;1- cdkd;3/-* (H' and orange lines) of a section going through the middle of the meiocyte (white dotted line). After metaphase I,

meiotic exit and dyad formation in *VF cdka;1/- cdkd;3/-* (Q), second meiotic division in the wildtype (K-M) and *VF cdka;1/- cdkd;3/+* (N-P). Red arrows indicate the mid-zone microtubule array. Schematic representation (R) of simultaneous cytokinesis in the wildtype that is characterized by two perpendicular spindles at metaphase II and a tetrahedral tetrad (S,T) versus successive cytokinesis in *VF cdka;1/- cdkd;3/+* mutant in which the predominant spindle configuration is parallel leading to a planar tetrad (U,V, W,X). (Y) Spindle orientation quantification for the wildtype (n=40) and *VF cdka;1/- cdkd;3/+* (n=36). Scale bar 10 μm.

The level of CDKD;3 and CDKA;1 determine the pattern of cytokinesis

Next, we investigated the microtubule localization after prophase I. In the wildtype, microtubules re-organize after diakinesis to form the first meiotic spindle in metaphase I (Figure 4C). After interkinesis (Figure 4K), microtubules rearrange to form two perpendicularly oriented spindles (Figure 4L,S) leading to the formation of a tetrahedral tetrad (Figure 4M,T). Strikingly different microtubule configurations were found in *VF cdka;1/-* mutants in combination with *cdkd3*. In the *VF cdka;1/-* plants with reduced CDKD;3 activity (*VF cdka;1/- cdkd;3/+* and *VF cdka;1/- cdkd;3/-*), unattached fibers and irregular spindle structures were found (Figure 4F,I yellow arrows). At later stages, consistent with our chromosome spread analysis (Figure 2B), premature exit after the first meiotic division leads to the formation of dyads in *VF cdka;1/- cdkd;3/-* as judged by the morphology and size of the cells (Figure 4Q).

Most interestingly, a different situation appeared in *VF cdka;1/- cdkd;3/+*, i.e. in plants with a moderate reduction of CDKD;3 activity. Here, microtubules bundled in interkinesis in the mid-zone (Figure 4N, red arrow) and progressively disappeared from outside to the inside of the meiocyte (Figure 4O). Subsequently, two rather parallel oriented spindles were formed in 67% of cases (Figure 4P,U,Y) giving rise to a planar tetrad (Figure 4V), while two rather perpendicularly positioned spindles, reflecting the wildtype-like spindle constellation and leading to a tetrahedral orientation of the tetrad, only appeared in 22% of cases (Figure 4W,X,Y).

This microtubule pattern suggested that there could be a cell division after the first meiotic division and hence, a transformation of the simultaneous into a successive cytokinesis in male meiosis of *VF cdka;1/- cdkd;3/+*. To test this hypothesis, we followed meiosis in the wildtype and *VF cdka;1/- cdkd;3* mutants by live cell imaging based on a recently developed protocol (Prusicki et al., 2019). To this end, we combined a tubulin marker (TagRFP:TUA5) with a plasma membrane marker (GFP:SYP132). SYP132 is a syntaxin (Qa-SNARE) known to mediate

membrane fusion, needed for example for secretion and building the cell plate during cytokinesis of somatic cells (Park et al., 2018).

In the wildtype, the reorganization of microtubules after diakinesis until metaphase II (as outlined above) is very fast and takes place in a largely concerted manner in all meiocytes within one anther (Figure 5A and Video 1A). At the end of telophase II, four spores are simultaneously formed after the invagination of the plasma membrane in an outside-in direction through simultaneous cytokinesis (Figure 5A, last column). The total duration of meiosis from diakinesis till telophase II in the wildtype was determined to be approximately 240 min (Figure 5E,I).

In *VF cdka;1/-*, similar to the wildtype, all meiocytes within one anther concertedly progressed through metaphase I, interkinesis, metaphase II and telophase II with no obvious alteration of microtubule organization patterns and no significant differences in the duration of the first meiotic division when compared to the wildtype, i.e. 73 min in the wildtype versus 80 min in the mutant (Video 1B, Figure 5F,I). However, meiocytes of *VF cdka;1/-* plants spent more time in interkinesis than wild-type plants (160 min versus 70 min) and metaphase II appeared to be slightly extended with 70 min in the wildtype versus 89 min in *VF cdka;1/-* (Figure 5F,I).

Remarkably, live cell imaging of *VF cdka;1/- cdkd;3/+* plants revealed cell wall deposition not only after anaphase II but also already after anaphase I (Figure 5B from Video 2, red arrows). Therefore, meiocytes did not exit meiosis after a premature cytokinesis after meiosis I as seen in mutants with a strong reduction of CDKD activity, i.e. *VF cdka;1/- cdkd;3/-* (see below). Instead, microtubules were rapidly organized in a ring-like structure around the nuclear envelope, similar to late prophase I. This microtubule configuration, unlike the wild-type situation, persisted for a while and was then followed by the formation of a second spindle, in spatial configurations matching our above-presented analysis (Figure 5 B from Video 2, Figure 4N-P,U-X). Consistent with an altered microtubule organization and precocious cell wall formation, we found that interkinesis is much longer in *VF cdka;1/- cdkd;3/+* plants with 260 min versus 70 min in the wildtype (Figure 5G,I).

Thus, a concomitant reduction of CDKD and CDKA activity converts the simultaneous cytokinesis of Arabidopsis male meiocytes into a successive cytokinesis, which is the predominant mode of division in male meiosis of monocotyledons (Furness and Rudall, 1999) and has been analyzed in detail for example in maize (Nannas et al., 2016). This finding can also explain the occurrence

of differently sized spores after meiosis in *VF cdka;1/- cdkd;3/+* plants (Figure S4D,E), i.e. one population of meiocytes that presumably terminates meiosis after the first division and a second class that undergoes a second cell division.

In *VF cdka;1/- cdkd;3/-* plants, which have the lowest level of CDKD activity, we observed defective spindles and premature microtubule removal at the spindle mid-zone followed by cell wall deposition (Figure 5C from Video 3, red arrows). Almost all meiocytes terminated meiosis after a long interkinesis, i.e. 250 min versus 70 min in the wildtype and no second division was observed (Figure 5H,I).

Interestingly, in both mutant combinations meiotic cell wall deposition still occurs in an outside-in direction (Figure 5D from Video 4, red asterisks). Thus, the here-observed successive cytokinesis as well as the premature cytokinesis followed by termination of meiosis after the first meiotic division display a similar mode of cleavage wall formation as observed for the simultaneous cytokinesis in the wildtype.
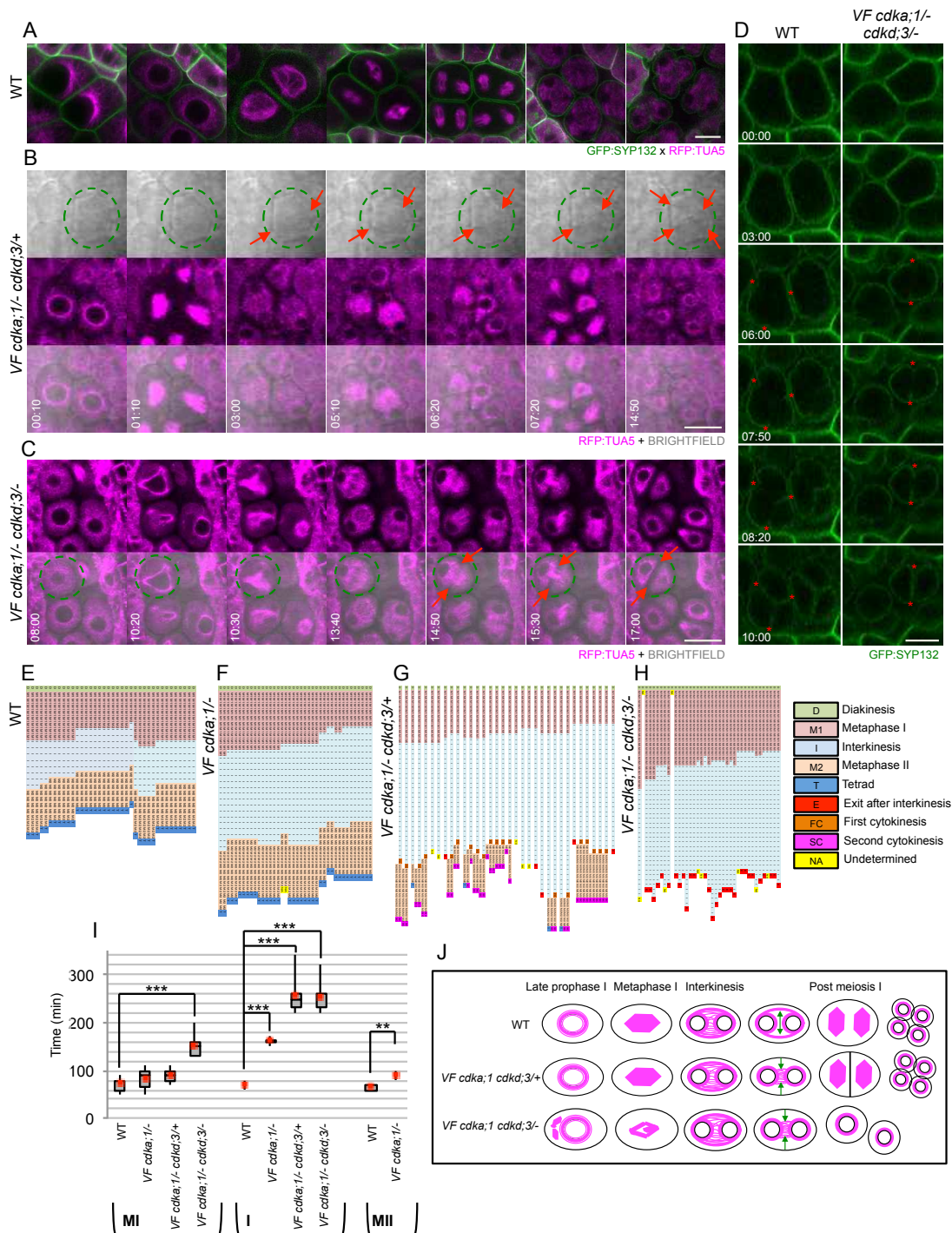
Figure 5. Analysis of the meiotic progression in the wildtype and *VF cdkd;3* mutants.

(A, see also Video 1A) Confocal laser scanning micrographs of male meiocytes expressing TagRFP:TUA5 (magenta) and GFP:SYP132 (green) during meiotic progression in the wildtype (WT) (time indicated with white numbers: h:min). (B from Video 2) Meiotic progression in *VF cdka;1/- cdkd;3/+* (time indicated with white numbers: h:min) showing the conversion of a simultaneous into a successive cytokinesis in one male meiocyte highlighted with a green circle. TagRFP:TUA5 in magenta and bright field in grey, overlay in the third row, cell wall deposition is marked with red arrows. (C from Video 3) Meiotic progression in one meiocyte (green circle) of *VF cdka;1/- cdkd;3/-* mutant expressing TagRFP:TUA5 (in magenta) and the respective overlay with the bright field in the

second row, showing microtubule dynamics and cell wall deposition (red arrows) from late prophase I to meiotic exit (time indicated with white numbers: h:min). (D from Video 4) Comparison of simultaneous cytokinesis in the wildtype versus meiotic exit in *VF cdka;1/- cdkd;3/-* using GFP:SYP132 (green) as plasma membrane marker. Red asterisks mark the initiation and the outside-in direction of cell wall deposition during cytokinesis time indicated with white numbers: h:min). Comparison of the duration of meiotic stages for single meiocytes between the wildtype (E), *VF cdka;1/-* (F), *VF cdka;1/- cdkd;3/+* (G) and *VF cdka;1/- cdkd;3/-* (H). Every line represents a single cell undergoing meiosis and every square a 10 minutes interval of a specific meiotic stage: diakinesis (D), metaphase I (M1), interkinesis (I), metaphase II (M2), and telophase II/tetrad (T). In some mutants, exit after interkinesis (E) or a first cytokinesis (FC) is observed. After the second meiotic division, a second cytokinesis (SC) will finally lead to the formation of meiotic products. Data aligned by taking a starting point 10 min before the first meiotic spindle is visible and as final time point 10 min after the spindle of the second meiotic division disappears. (I) Box plots of metaphase I, interkinesis and metaphase II duration in the wildtype (n=38), *VF cdka;1/-* (n=40), *VF cdka;1/- cdkd;3/+* (n=34) and *VF cdka;1/- cdkd;3/-* (n=37). Red dots represent the mean value. Level of significance (P<0.05*; P<0.01**;P<0.001***) is determined by a one-way ANOVA followed by Tukey's test. (J) Cartoons summarizing microtubule organization during meiotic progression in the wildtype versus *VF cdka;1 cdkd;3* mutant combinations. Green arrows represent the direction of microtubule removal in the midzone during late interkinesis. Scale bar in A,B, C, and D 10 μm.

The pattern of MAP65 localization depends on CDKA;1 and CDKD activity

To further characterize the microtubule defects, we introgressed the microtubule binding protein MAP65-3 into *VF cdka;1/-cdkd;3/-* mutants. MAP65-3 has been shown to act as a bundling factor of antiparallel microtubules near their plus ends (Ho et al., 2012). In the wildtype, MAP65-3 is clearly visible at late prophase I (Figure 6A) and localized together with tubulin in a *full-moon* like conformation surrounding the nucleus shortly before NEB. In interkinesis, MAP65-3 accumulated in the mid-zone between the two nuclei (Figure 6B), and, at the beginning of the second meiotic division, it is removed, following the pattern of microtubule removal, from the cell center to the side of the cell (Video1A, Figure 5J, Figure 6D from Video 5). After anaphase II, MAP65-3 is localized in the mid-zones between the four newly forming nuclei (Figure 6C,D from Video 5).

In *VF cdka;1/- cdkd;3/-* mutant plants, the MAP65-3 was generally more diffuse than in the wildtype (Figure 6E) consistent with the less organized microtubule pattern in the mutant as described above. At late prophase I, before NEB, bundled microtubules were decorated with MAP65-3 resembling a phragmoplast-like microtubule organization (Figure 6E-G, white asterisks). Live cell imaging revealed

that these structures persisted until metaphase I, where they rapidly disappeared and were apparently incorporated into the microtubules forming the meiotic spindle (Figure 6H, I from Video 6). Afterwards, MAP65-3 localized to the phragmoplast of the terminal cell division after meiosis I observed in *VF cdka;1/- cdkd;3/-* and was removed in an outside-in fashion, consistent with a centripetal formation of the new cell wall (see above).

Taken together these data show that CDKDs together with CDKA;1 are major regulators of the microtubule cytoskeleton and cytokinesis in meiosis. On the one hand, they appear to be necessary for the proper formation of distinct microtubule structures, such as the *half-moon* structure in prophase I or the meiotic spindle. On the other hand, they are important for repression of untimely microtubule configurations in prophase I, and also prevent cytokinesis after meiosis I. Remarkably, a moderate reduction of CDKA;1 activity and premature cell wall formation is compatible with entry into a second meiotic division for which sufficient CDKA;1 activity is needed again.
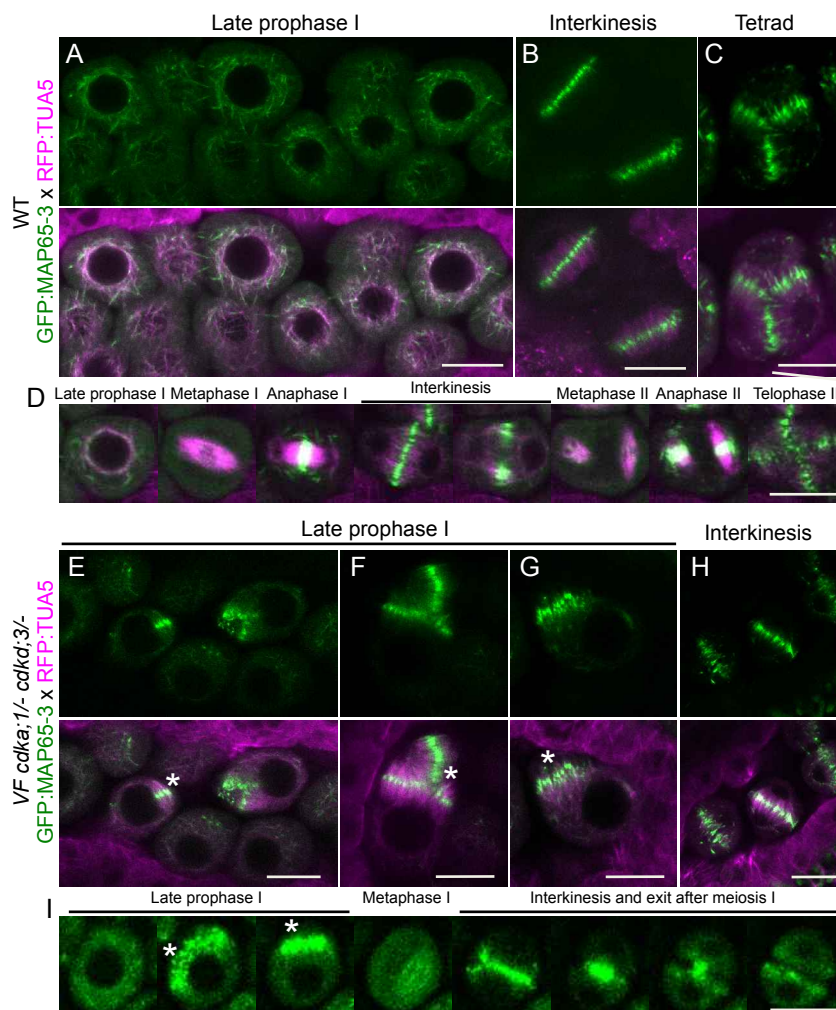
Figure 6. Formation of premature phragmoplast-like structures in plants with low CDKA;1 activity. Confocal laser scanning micrographs of meiocytes expressing TagRFP:TUA5 (magenta) and GFP:MAP65-3 (green) at late prophase (A), interkinesis (B) and tetrad (C) in the wildtype (WT). (D from Video 5) Time course of TagRFP:TUA5 and GFP:MAP65-3 from late prophase to telophase II in the wildtype. Confocal micrographs of meiocytes expressing TagRFP:TUA5 (magenta) and GFP:MAP65-3 (green) at late prophase (E-G) and interkinesis (H) in *VF cdka;1/- cdkd;3/-*. (I from Video 6) Time course of TagRFP:TUA5 and GFP:MAP65-3 from late prophase to exit after meiosis I in *VF cdka;1/- cdkd;3-* . White asterisks highlight the premature phragmoplast formation. Scale bar 10 µm.

Shinichiro Komaki generated the MAP65-3 reporter line.

CDKA;1 and TUA5 co-localize at the spindle during metaphase I and II

To explore the dynamics of CDKA;1 with respect to the microtubule cytoskeleton, we combined plants expressing TagRFP:TUA5 with our functional CDKA;1 reporter line (*PRO_{CDKA;1}CDKA;1:mVenus*) (Yang et al., 2020) and with plants expressing *PRO_{CDKA;1}:mVenus* as a negative control. Free mVenus was expected to localize to both the cytoplasm and the nucleus. While we found this pattern in tapetum cells, mVenus was predominantly localized to the nucleus in meiocytes for unknown reasons. None-the-less, as described below, the construct could serve as a negative control when compared to the CDKA;1:mVenus fusion during the course of meiosis.

We first analyzed a possible co-localization pattern in late prophase I when microtubules are localized in a ring-like structure around the nucleus, (Figure 7A,B first row). The profile plots of signal intensities from a line going through the meiocyte revealed no overlap between free mVenus and tubulin (Figure 7C, first panel). Whether CDKA;1:mVenus specifically co-localized with tubulin could not be unambiguously decided since CDKA;1:mVenus is also strongly present everywhere in the cytoplasm at this stage (Figure 7D, first panel). Shortly before NEB, when the microtubule structures start to rearrange to form the first spindle, both free mVenus and the CDKA;1:mVenus fusion protein are still surrounded by microtubules and, similar to the stage before, a clear co-localization pattern of CDKA;1:mVenus with microtubules could not be unambiguously confirmed (Figure 7A,B second rows).

After NEB, however, when the spindle is fully assembled at metaphase I, CDKA;1:mVenus is enriched in the region of the spindle microtubules (Figure 7B, third row) and the signal intensities overlap (Figure 7D, third panel), whereas the free mVenus signal, albeit weak after NEB (Figure 7A, third row), was not found to be

enriched at spindle fibers (Figure 7C, third panel). Similarly, at metaphase II both spindles are slightly enriched with CDKA;1:mVenus (Figure 7B, last row, 7D, last panel), but not with free mVenus (Figure 7A, last row, 7C, last panel). Together with the spindle defects observed before, we conclude that CDKA;1 is an important regulator of the meiotic spindle and likely directly acts on the spindle fibers and/or associated factors although we cannot rule out that spindle defects are at least partially caused in an indirect manner, e.g. from an effect of low CDKA;1 activity on cortical microtubules.
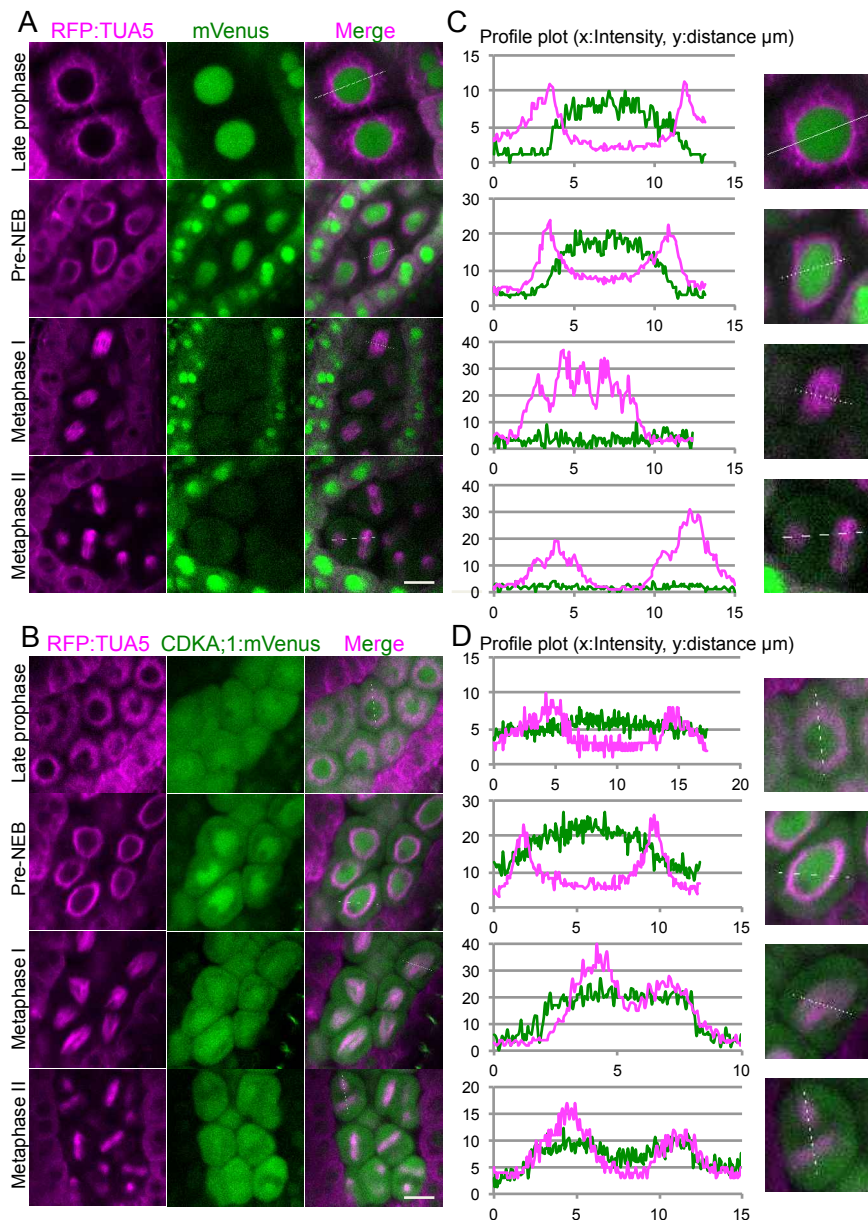
Figure 7. CDKA;1 co-localizes with the spindle in metaphase I and metaphase II.

(A) Confocal laser scanning micrographs showing the localization of TagRFP:TUA5 (magenta, first column) expressed from the PRO$_{RPS5A}$ promoter and mVenus (green, second column) expressed from

the PRO_{CDKA;1} promoter in late prophase, shortly before NEB, metaphase I and metaphase II. Third column represents the merge of the two channels. (C) Signal intensity plot profile of a section (white line) through one meiocyte shown in panel A (close up in second column). (B) Confocal laser scanning micrographs showing the localization of Tag:RFP:TUA5 (magenta, first column) expressed from the PRO_{RPS5A} promoter and a CDKA:mVenus (green, second column) fusion proteins expressed from the PRO_{CDKA;1} promoter in late prophase, shortly before NEB, metaphase I and II. Third column represents the merge of the two channels. (D) Signal intensity plot profile of a section (white line) through one meiocyte (close up in second column). Scale bar 10 μm.

CYCB3;1 functions together with CDKA;1 to regulate microtubule organization during meiosis

Essential for the activation of CDKA;1 is not only the phosphorylation by CDKDs, but also the binding of a cyclin cofactor. Since a GUS fusion to CYCB3;1 was previously found to localize to both meiotic spindles, we suspected that CYCB3;1 could be a regulator of MT in meiosis (Bulankova et al., 2013). Previous mutant analyses revealed a function of CYCB3;1 in repressing premature cell wall deposition and assuring the accuracy of cell wall formation (Bulankova et al., 2013). To address a possible function of CYCB3;1 in microtubule organization, we first monitored root growth of *cycb3;1* mutants on agar plates containing the microtubule depolymerizing reagent oryzalin. As a positive control we used mutants in the central spindle assembly checkpoint component *MITOTIC ARREST DEFICIENT 1* (*MAD1*), which are hypersensitive to this drug (Komaki and Schnittger, 2017). Indeed, the growth of *cycb3;1/-* mutants was as strongly reduced as *mad1/-* on oryzalin in comparison to the wildtype pinpointing to a function of CYCB3;1 in regulating the microtubule cytoskeleton (Figure S5A).

To understand then the role of CYCB3;1 during meiosis, we first generated a genomic *CYCB3;1* reporter, in which the ORF for *GFP* was inserted right before the stop codon of *CYCB3;1* (*PRO_{CYCB3;1}:CYCB3;1:GFP*). This reporter fully rescued the oryzalin sensitivity of root growth found in *cycb3;1/-* mutants and we hence conclude that it is functional (Figure S5A). CYCB3;1 was then found to accumulate in the cytoplasm of meiocytes throughout prophase I and appeared to be associated with the spindle at metaphase I while it was not present in metaphase II in contrast to a previous report (Bulankova et al., 2013) (Figure 8A). The spindle localization of *CYCB3;1:GFP* was confirmed by live cell imaging in plants co-expressing the *TagRFP:TUA5* reporter (Figure 8B from Video7). Currently, we cannot explain the

discrepancy between the previously used GUS fusion with CYCB3;1 that indicated the presence of CYCB3;1 at the second meiotic spindle and our reporter. Possibly, the GUS tag interfered with the degradation of CYCB3;1 and hence making it available when the second meiotic spindle is formed.
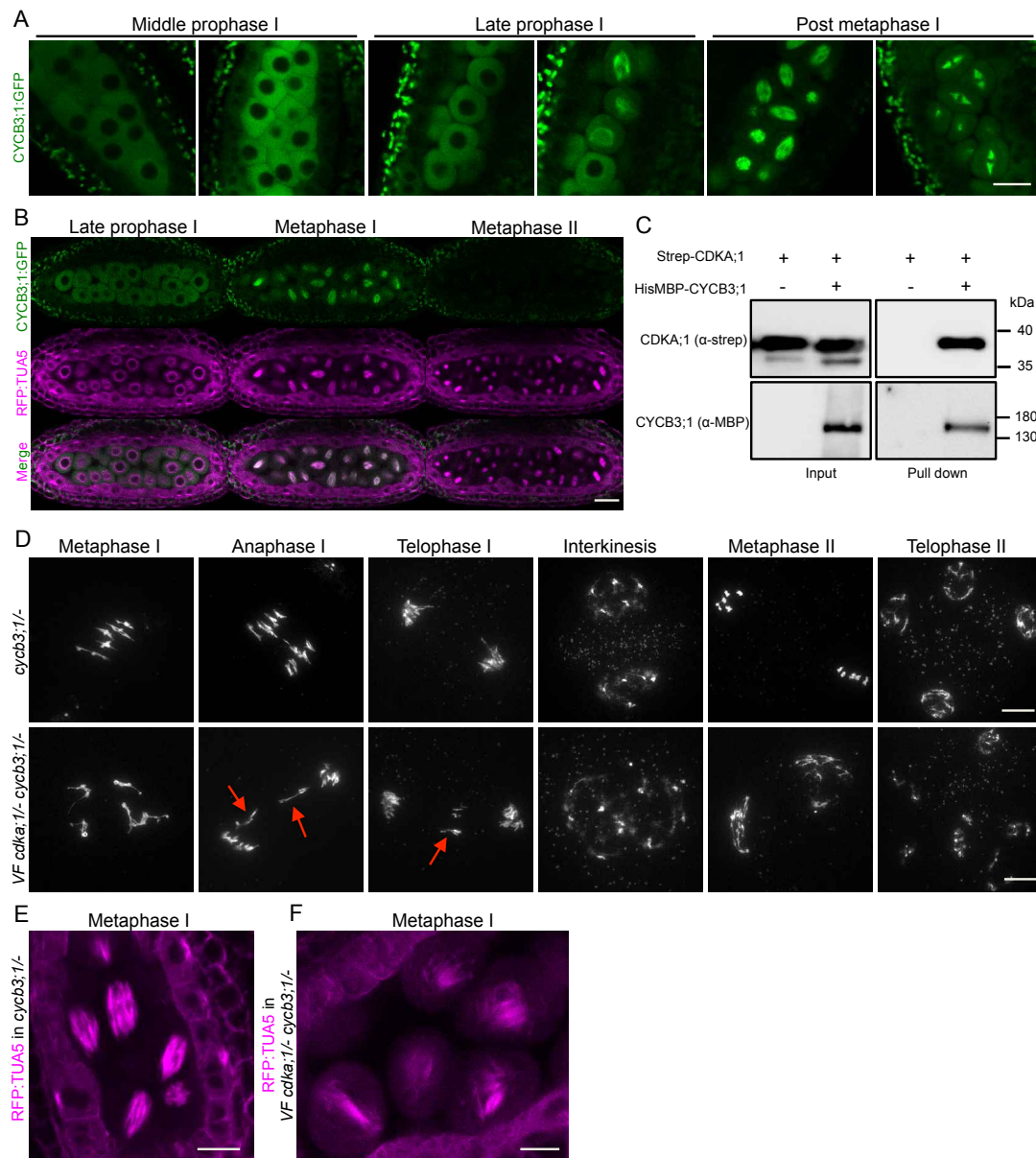
Figure 8. Characterization of CYCB3;1 in meiosis. (A) Confocal laser scanning micrographs showing the localization of a functional reporter for CYCB3;1 (CYCB3;1:GFP in green) throughout meiosis. Scale bar 10 μm. (B from Video 7) Confocal micrographs of TagRFP:TUA5 (magenta) and CYCB3;1:GFP (green) at late prophase, metaphase I and II. CYCB3;1 co-localize with the first but not the second spindle. Scale bar 20 μm. (C) CYCB3;1 forms a complex with CDKA;1. Pull down assay using Strep-CDKA;1 in the presence or absence of HisMBP-CYCB3;1. The input and pull down fractions detected by immunoblotting with anti-Strep (upper panel) and anti-MBD (lower panel) antibodies. (D) Chromosome spread analysis of the *cycb3;1/-* versus *VF cdka;1/- cycb3;1/-* during metaphase I, anaphase I, telophase I, interkinesis, metaphase II and telophase II. Red arrows mark

lagging chromosomes at anaphase I and telophase I. Scale bar 10 μm. Confocal laser scanning micrographs of TagRFP:TUA5 during metaphase I in *cycb3;1/-* (E) and *VF cdka;1/- cycb3;1/-* (F). Microtubule arrays are altered in *VF cdka;1/- cycb3;1/-* as represented by irregular spindles at metaphase I..Scale bar 10 μm.

Chao Yang performed the kinase assay in figure 7C and generated the CYCB3;1 reporter line.

To investigate whether CDKA;1 and CYCB3;1 work together in organizing microtubules, we first performed an *in-vitro* pull down assay using Strep-CDKA;1 and HisMBP-CYCB3;1 (Figure 8C) showing clearly an interaction of both proteins. Second, we combined our *VF cdka;1/-* with a *cycb3;1/-* mutant and performed chromosome spreads. In *cycb3;1/-* meiocytes, similar to wild-type meiosis (Figure 1A), chromosomes condensed into five bivalents at metaphase I, correctly segregated to two opposite poles at anaphase I, shortly decondensed at interkinesis before re-condensing at metaphase II and, after sister chromatid separation, distributed equally to four pools at telophase II (Figure 8D, first row). However, several meiotic defects were observed in *VF cdka;1/- cycb3;1/-* mutants: chromosomes failed to properly align in the metaphase I plane, lagging chromosomes were found in anaphase I and telophase I (Figure 8D, second row, red arrows), the organellar band separating the two pools of chromosomes was not correctly positioned or fully missing in interkinesis, and irregular and unbalanced metaphase II chromosome assemblies, likely as a consequence of unequal chromosome segregation in meiosis I, were observed leading to unbalanced tetrads in 72% of cases (Figure 8D, second row). The defective meiotic progression is supported by a high level of pollen abortion and very short siliques in *VF cdka;1/- cycb3;1/-* plants (Figure S5B-F).

The introgression of the tubulin marker Tag:RFP:TUA5 in *VF cdka;1/- cycb3;1/-* plants showed defective spindle structures in metaphase I (Figure 8F) whereas *cycb3;1/-* single mutants were characterized by a fully assembled and condensed spindle (Figure 8E). Thus, combining *cycb3;1/-* with *VF cdka;1/-* strongly enhanced the *VF cdka;1/-* mutant phenotype, similar to the enhancement found in combinations of *VF cdka;1/-* with *cdkd* mutants. This genetic interaction together with the physical interaction of CYCB3;1 and CDKA;1 indicates that they build a functional complex *in vivo*.

To further investigate the regulation of microtubules by CYCB3;1, we developed an *in vivo* oryzalin treatment assay and monitored meiotic progression using confocal microscopy. Briefly, anthers from the wildtype and *cycb3;1/-* mutant

plants expressing TagRFP:TUA5 were simultaneously transferred to plates containing DMSO or oryzalin prior to time lapse imaging (Figure 9A). On media containing DMSO as control, meiotic progression from mid prophase I (half-moon stage) to the tetrad formation was undistinguishable between *cycb3;1/-* mutants and the wildtype matching the progression in the wildtype without any treatment as described above (Figure 9B,C from Video8). On media containing 200nM oryzalin, wild-type meiocytes also correctly progressed through meiosis (Figure 9D from Video 9), while in *cycb3;1/-* mutants microtubule structures were perturbed at late prophase I and the length of the first meiotic spindle was shorter at metaphase I when compared to the wildtype (Figure 9E from Video 9, H). Strikingly, microtubule structures in *cycb3;1/-* meiocytes completely dissolved on media containing 500nM oryzalin shortly after the start of image acquisition, and the two meiotic spindles were never formed. After two events of NEB, unreduced gametes were produced, whereas wild-type meiocytes were still able to form two spindles with the subsequent appearance of tetrads (Figure 9F,G from Video 10, H,I).

Taken together these data suggest a novel role of CYCB3;1 as a CDKA;1 partner in regulating microtubule organization during meiosis.
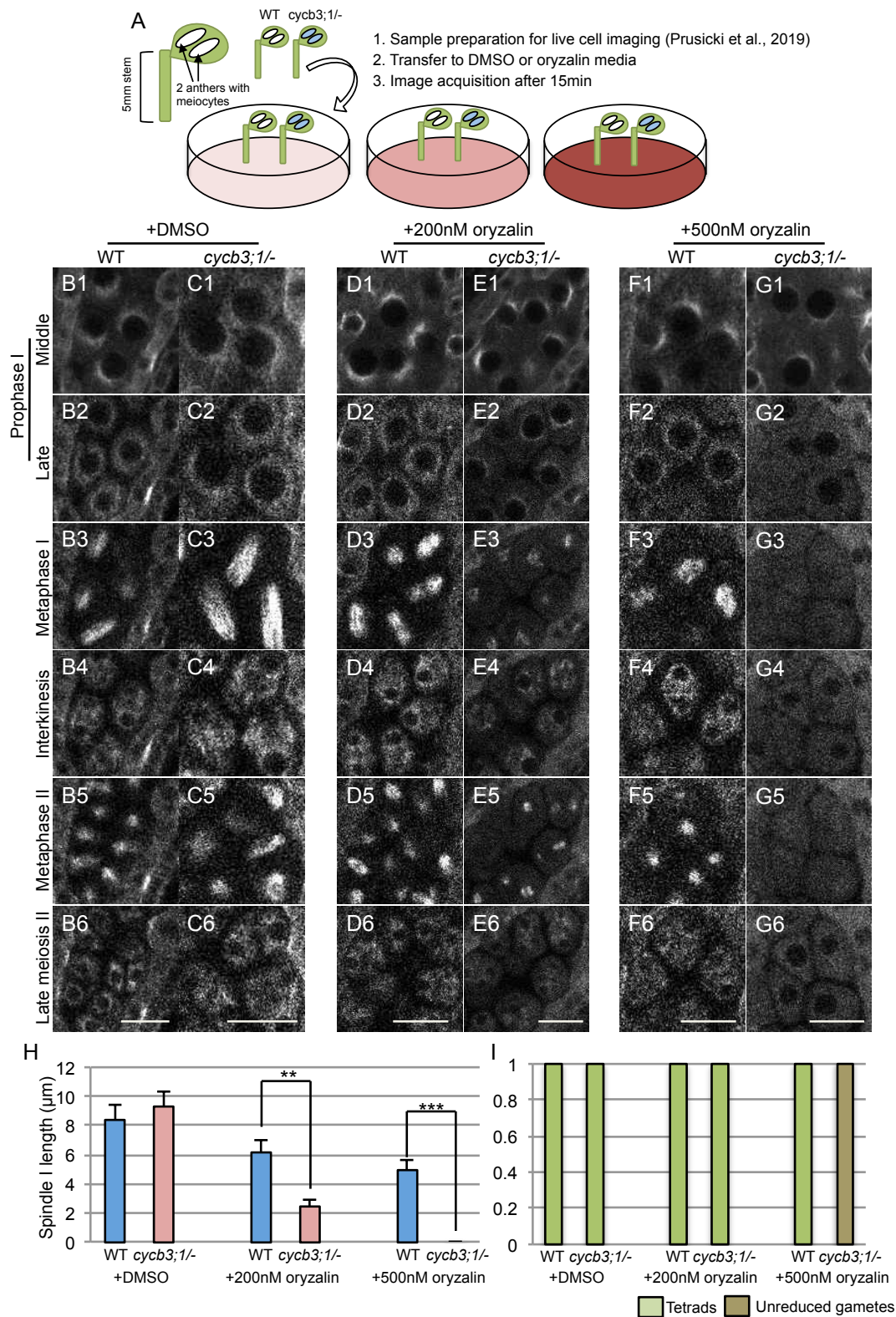
Figure 9. Meiocytes of *cycb3;1/-* mutants are hypersensitive to oryzalin. (A) Scheme of live cell imaging of male meiocytes treated with oryzalin . (B-G) Time points of meiotic progression in meiocytes expressing TagRFP:TUA5 in wildtype (WT) (B1-B6) and *cycb3;1/-* (C1-C6) with DMSO (from Video 8), WT (D1-D6) and *cycb3;1/-* (E1-E6) with 200nM oryzalin (from Video 9), WT (F1-F6) and *cycb3;1/-* (G1-G6) with 500nM oryzalin (from Video 10). Scale bar 10 μm. (H) Spindle length at metaphase I of meiocytes from at least 3 different anthers of the wildtype (n=28) and *cycb3;1/-* (n=23)

treated with DMSO, the wildtype (n=22) and *cycb3;1/-* (n=25) treated with 200nM oryzalin, and the wildtype (n=23) and *cycb3;1/-* (n=20) treated with 500nM oryzalin. Level of significance ($P<0.05$*; $P<0.01$**;$P<0.001$***) is determined by one-way ANOVA followed by Tukey's test. (I) Number of meiotic products (tetrads or unreduced gametes) of meiocytes from at least 3 different anthers of the wildtype (n=28) and *cycb3;1/-* (n=23) treated with DMSO, the wildtype (n=22) and *cycb3;1/-* (n=25) treated with 200nM oryzalin, and the wildtype (n=23) and *cycb3;1/-* (n=20) treated with 500nM oryzalin.

Discussion

Here, we have analyzed the role of CDKDs as CDKA;1-activating kinases in meiosis. Earlier work already indicated that activation of CDKA;1 through T-loop phosphorylation, similar to the regulation of Cdk1-type kinase in other model systems, is crucial for cell division control in mitosis and meiosis in Arabidopsis (Harashima et al., 2007; Dissmeyer et al., 2007; Bulankova et al., 2010; Takatsuka et al., 2015). Our genetic experiments and the co-localization data support previous *in vitro* kinase assays that this activation is catalyzed by D-type CDKs. Combining mutants in any of the three partially redundantly acting *CDKDs* together with a weak loss-of-function mutant in *CDKA;1* gives rise to a very fine grained genetic reduction of CDKA;1 activity and hence, is a powerful tool to dissect the requirement of CDKA;1 action in meiosis.

CDK levels in mitosis versus meiosis

Progression through the mitotic cell cycle is thought to be driven by oscillating levels of CDK activity leading to a quantitative control system of the cell cycle, i.e. low kinase levels are required for the licensing of DNA replication, moderate levels to trigger DNA replication, high levels to execute mitosis followed by again low levels of kinase activity to exit mitosis and execute cytokinesis paving the road for a new S-phase (Stern and Nurse, 1996). These events are intriguingly connected by different circuits, for instance successful attachment of all kinetochores with spindle fibers triggers the decline of CDK activity by activating the anaphase promoting complex/cyclosome (APC/C) that mediates the degradation of the cyclin cofactors (Komaki and Schnittger, 2017).

The concept of quantitative cell cycle control is largely based on experiments in yeast, especially fission yeast, in which a single CDK-cyclin pair has been found to be sufficient to drive progression through the entire mitotic cell cycle (Fisher and

Nurse, 1996; Coudreuse and Nurse, 2010; Gutiérrez-Escribano and Nurse, 2015). In multicellular animals, the situation is less clear since many more CDKs and cyclins are present and appear to be required for a development-specific regulation of the cell cycle (Pagliuca et al., 2011). None-the-less, all CDKs but Cdk1 are dispensable in mice (Santamaría et al., 2007). Moreover, in Arabidopsis even the Cdk1ortholog CDKA;1 is not essential to drive cell division (Nowack et al., 2012), suggesting that a quantitative rather than a qualitative model of cell cycle regulation is, at least in part, at the heart of the cell cycle of multicellular eukaryotes, too.

The control of progression through meiosis is particularly complex since a single DNA replication phase is followed by two chromosome separation events. Largely based on experiments in yeast, it has been proposed that CDK activity after anaphase I drops due to the activation of the APC/C but is not fully eliminated. This residual level of CDK activity is important to prevent the initiation of another S-phase and to trigger the second meiotic division (Pesin and Orr-Weaver, 2008). Consistent with this model, APC/C inhibitors have been identified in different model systems, including Arabidopsis, that prevent the full activation of the APC/C and hence the complete loss of CDK activity (Pesin and Orr-Weaver, 2008). Accordingly, mutants in the APC/C inhibitor *OSD1/GIG1* resulted in the termination of meiosis after the first division in Arabidopsis (d'Erfurth et al., 2009). Likewise, mutants in the meiotic cyclin *TAM* exit meiosis after meiosis I (Magnard et al., 2001; Wang et al., 2004b; d'Erfurth et al., 2010; Bulankova et al., 2010), and, as detailed in this study, strong reduction of CDK activity also results in exit of meiosis after the first meiotic division.

We can currently not exclude that the meiotic defects seen in plants with low kinase activity could be indirectly caused from defects in the neighboring tissue, i.e. tapetum cells. Indeed, defects in the tapetum layer can affect the differentiation of male meiocytes and/or the progression through meiosis, often through the action of small RNAs that are produced outside of meiocytes (Lei and Liu, 2020). Defects in cytokinesis of meiocytes have been reported when the signaling pathway of the plant hormone gibberellic acid (GA) was disturbed by exogenous application of GA or in double mutants for the GA-signaling repressors GAI and RGA, which function as transcriptional repressors (Liu et al., 2017). Interestingly, a RGA reporter construct revealed that this DELLA protein is largely absent in meiocytes but accumulated in the surrounding cells, including tapetum cells. While the expression pattern of GAI in

anthers has not been revealed, this result hints at a possible non-cell-autonomous function of GA signaling controlling cytokinesis in meiocytes (Liu et al., 2017).

However, the cytokinesis defects seen in plants with reduced CDKA;1 activity do not resemble the effects after application of GA as for instance triads are predominantly formed when the GA pathway is perturbed but not in mutants with reduced CDKA;1 activity. We also did not find any obvious hints for defective tapetum cells. In addition, so far none of the mutants with defects in tapetum cells has been found to cause the formation of univalents or affect other aspects of chromosomal dynamics in prophase I as observed here (Lei and Liu, 2020). Consistently, live cell imaging of chromosome dynamics in male meiocytes also suggested that chromosome behavior in meiosis progresses rather independently from the differentiation of tapetal cells (Prusicki et al., 2019). Moreover, the termination of meiosis and the formation of ectopic phragmoplast-like structures in plants with low CDKA;1 activity resemble the defects seen in *tam* mutants (Magnard et al., 2001; Wang et al., 2004b; d'Erfurth et al., 2010; Bulankova et al., 2010; Prusicki et al., 2019). *TAM* encodes for a cyclin, which forms active complexes with CDKA;1 and is not present in tapetal cells (Wang et al., 2004b; Bulankova et al., 2010; Cifuentes et al., 2016). These data, together with the accumulation pattern of CDKA;1 and CDKDs in meiocytes (this study and (Bulankova et al., 2010), suggest a cell-autonomous role of CDKA;1 in meiosis.

Unexpectedly, we found here that a moderate reduction of CDK activity was enough to trigger cytokinesis but did not necessarily lead to termination of meiosis in male meiocytes as previously observed in *tam* and *osd1/gig* mutants (Magnard et al., 2001; Wang et al., 2004b; d'Erfurth et al., 2009, 2010; Bulankova et al., 2010; Prusicki et al., 2019). Instead, a second meiotic division was executed resulting in four spores as in the wildtype. This result is surprising since cell cycle regulators are usually interconnected to generate bistable switches in which both the high and the low activity levels are reinforced by positive feedback loops (Tyson and Novák, 2015). In contrast, we observed here a rather gradual, yet apparently stable response to high, moderate and low levels of CDK activity. This gives rise to the speculation that some of the feedback mechanisms of mitosis are not implemented in meiosis. Interestingly, it has been found that meiosis requires much higher kinase levels than mitosis possibly due to lower affinities of CDKs for meiotic substrates and/or the requirement of high levels of phosphorylation of meiotic substrates (Gutiérrez-

Escribano and Nurse, 2015). Our findings now offer an additional reason, i.e. if reinforcement circuits are not present or less active in meiosis, higher CDK levels might be needed to promote meiosis. In turn, the possible absence of these reinforcement circuits might be necessary to prevent the complete loss of CDK activity after meiosis I.

CDKA;1 - a master regulator of meiosis?

It is well-established that Cdk1 is a master regulator of mitosis that controls many different processes and several hundred possible Cdk1 substrates have been identified from yeast to plants (Ubersax et al., 2003; Holt et al., 2009; Van Leene et al., 2010; Pusch et al., 2012). The role of Cdks in meiosis is less understood, possibly due to the requirement of Cdk1 for somatic/sporophytic development of multicellular organisms that make a functional analysis of Cdk1 action in meiosis challenging. In addition, several other kinases have been found in yeast and animals to be important for meiotic entry and progression, including Cdk2 (Ortega et al., 2003). However, analyzing conditional Cdk1 knock-out mice, it was demonstrated that Cdk1 is essential for meiosis in mammalian oocytes (Adhikari et al., 2012). Moreover, Cdk1 function in meiosis cannot be substituted by Cdk2 (Satyanarayana *et al.*, 2008). In parallel, several meiotic proteins have been found to be phosphorylated by Cdks. These include Mer2/Rec107 (for Meiotic Recombination 2, or Recombination 107), which is important for double strand break (DSB) formation (Henderson *et al.*, 2006), and Sae2/Com1 (for Sporulation in the absence of Spo11, or Completion of meiotic recombination), a nuclease, which is important to process DSBs (Huertas et al., 2008).

In plants, the Cdk1 ortholog CDKA;1 has been found to control meiotic progression, cohesion of sister chromatids, formation of the chromosome axis, and crossover number and placement (Dissmeyer et al., 2007; Yang et al., 2019; Wijnker et al., 2019). Possible substrates are the chromosome axis associated protein ASYNAPTIC 1 (ASY1), the putative APC/C inhibitor THREE DIVISION MUTANT (TDM1), the endonuclease MLH1, and SWITCH1/DYAD, a novel repressor of the cohesin remodeling factor WINGS APART LIKE (WAPL) (Cifuentes et al., 2016; Wijnker et al., 2019; Yang et al., 2019, 2020). The list of putative substrates of CDKA;1 in meiosis is very long and includes further key proteins involved in all aspects of meiosis, e.g. ZYP1, a protein of the central region of the synaptonemal complex, which harbors many CDKA;1 consensus phosphorylation sites.

Here, we have assigned a new role to CDKA;1, i.e. the regulation of microtubule organization in meiosis. Interestingly, CDKA;1 is needed for different aspects of microtubule dynamics which include foremost the organization of the meiotic spindle and the repression of a premature/ectopic phragmoplast-like structure. An antagonist relationship between CDK activity and cytokinesis has been found in mitosis. A mitosis-specific B-type CDK was found to phosphorylate and inhibit the function of NACK1, a kinesin, and NPK1, a MAP3K, in Arabidopsis. By that a mitotic CDK prevents that NACK1 together with NPK1 triggers a MAP kinase phosphorylation cascade that results in the activation of MAP65-3 and subsequent cytokinesis (Sasabe et al., 2011).

Whether CDKA;1 targets the same cytokinesis regulators in meiosis is not clear at the moment and awaits further studies. In addition, CDKA;1 has likely many more targets in regulating the microtubule organization in meiosis. One of them could be MAP65-3 itself, which has three predicted CDK phosphorylation sites. Interestingly, the human MAP65-1 homolog, PRC1, which has a redundant function with MAP65-3, shows decreased MT bundling activity upon phosphorylation by Cdk1 and Cdk2 complexes (Jiang et al., 1998; Mollinari et al., 2002). Consistent with a possible regulation of MAP65-3 by CDKA;1, we found that MAP65-3 localization is more diffuse in mutants with reduced CDKA;1 activity than that in the wildtype. Thus, although we could show the importance for CDKA;1 activity for proper timing and organization of spindle and phragmoplast microtubules in meiosis, additional work is needed to identify and characterize the phospho-targets of CDKA;1 involved in these processes.

Modulation of CDK activity to dissect the regulation of cytokinesis

Most cytokinetic events in multicellular land plants follow an inside-out modus, i.e. a phragmoplast starts to be assembled in the middle of the division plane and then expands laterally (Müller and Jürgens, 2016; De Storme and Geelen, 2013).

The here-observed conversion of a simultaneous into a successive cytokinesis without a concomitant change of the outside-in to an inside-out modus shows that the type of cytokinesis in Arabidopsis is not strictly coupled to the mode of cell wall deposition. This is in accordance with observation in monocotyledonous species where cytokinesis in male meiosis follows the inside-out strategy not only in species that go through successive cytokinesis (De Storme and Geelen, 2013) but also species

that undergo simultaneous cytokinesis (Ressayre et al., 2005). It is interesting to note that, while the timing of division is under control of CDK activity, the type of cell division mode seems to be dependent on the developmental state of the mother cell. The termination of meiosis with the formation of a cell wall after meiosis I in a *tam* mutant has been regarded as a partially successive cytokinesis and staining of the cell wall component callose has suggested that cell wall formation follows and outside-in pattern (Magnard et al., 2001; Albert et al., 2011). The defects in *tam* are consistent with TAM being a cyclin partner for CDKA;1 and are furthermore in accordance with the idea that CDKA;1-TAM complexes control phragmoplast formation as described here and in Prusicki et al. (2019). Interestingly, *tam* does not appear to affect the meiotic spindle (Bulankova et al., 2010; Prusicki et al., 2019) and CDKA;1 together with CYCB3;1, and likely additional cyclins, regulate spindle microtubules as shown here.

Coupled to the question whether a successive versus simultaneous cytokinesis is executed, is the question how the geometry of cell division is controlled. Is the reorientation of the second spindle that leads to a tetrahedral organization of the male meiotic products due to some preset landmarks in the male meiocyte that are read-out at the duration of first division or is it *de novo* established after the first division? The here-presented analysis and previous work on a hypomorphic *tam* mutant, in which a second meiotic division occasionally takes place (Magnard et al., 2001; Albert et al., 2011), indicate that the re-orientation of the second spindle is likely established after the first division and does not use any cues present in the male meiocyte before cytokinesis (Albert et al., 2011). Thus, the first spindle itself likely influences directly or indirectly the orientation of the second spindle. It will now be interesting to explore how such a cross-talk could be molecularly realized.

Material and Methods

Plant material and growth conditions

The *Arabidopsis thaliana* accession Columbia (Col-0) was used as wild-type reference for this study. The T-DNA insertion lines SALK_106809 (*cdka;1*) (Nowack et al., 2006) MPI_8258 (*cdkd;1-1*), SALK_065163 (*cdkd;2-1*), SALK_120536

($cdkd;3-1$) (Shimotohno et al., 2006; Hajheidari et al., 2012) and WiscDsLox461-464I10 ($cycb3;1-1$) (Bulankova et al., 2013) were obtained from the SALK SiGNAL, GABI-Kat and WISC T-DNA mutant collections. All genotypes were determined by polymerase chain reaction (PCR) using the primers shown in Supplementary Table I. The mutants $PRO_{CDKA;1}:CDKA;1^{T14V;Y15F}$ as well as $PRO_{CDKA;1}:CDKA;1^{T161D}$ and the reporter lines KINGBIRD2 ($PRO_{REC8}:REC8:GFPxPRO_{RPS5A}TagRFP:TUA5$), $PRO_{CDKA;1}CDKA;1:mVenus$, $PRO_{RPS5A}TagRFP:TUA5$ and $PRO_{SYP132}GFP:SYP132$ were previously described (Dissmeyer et al., 2007, 2009; Prusicki et al., 2019; Park et al., 2018; Enami et al., 2009; Yang et al., 2020). All seeds were surface-sterilized with chloride gas, sown on 1% agar plates containing ½ Murashige and Skoog (MS) salts and 1% sucrose, pH 5.8. Hygromycin B (25 mg/L, Duchefa Biochemie B.V., Haarlem, The Netherlands) was used for seed selection. Seeds were germinated on plate in long-day conditions (16h day/8h night regime at 22°C/18°C, 7 days) and then transferred to soil. After a two-week period under short-day conditions (12h day/12h night regime) plants were grown at long-day conditions with 60% humidity until seed production.

Plasmid construction and plant transformation

To generate the $PRO_{CDKD}:CDKD:mVenus$ reporters, a genomic fragment of $CDKD;1$, $CDKD;2$ and $CDKD;3$ from 1697, 2011 and 2000 bp upstream of the start codon to 994, 118 and 1000 bp downstream of the stop codon was amplified by PCR, respectively, and cloned into the gateway entry vector $pDONR221$ (Invitrogen). Then, $mVenus$ fragments amplified by PCR were cloned into the vectors by conducting *In-Fusion Cloning* (Clontech). In each case, the $mVenus$ tag was inserted directly before the STOP codon. A Gateway LR reaction (Invitrogen) was used to transfer the genomic $PRO_{CDKD}:CDKD:mVenus$ fusions into the destination vector $pGWB1$ (Nakagawa et al., 2007). For the $PRO_{CDKA;1}:CDKA;1:mVenus$ reporter, a 6210 bp genomic sequence containing the presumptive promoter and 3'UTR regions and for the $PRO_{CDKA;1}:mVenus$, reporter a 2000bp genomic sequence of the presumptive $CDKA;1$ reporter were amplified by PCR and subsequently integrated into the $pENTR2B$ vector by SLiCE reaction. A *Sma*I restriction site was then introduced directly before the stop codon. After linearization by *Sma*I restriction, the constructs were ligated with $mTurquoise2$ or $mVenus$ fragments, followed by a Gateway LR reaction with the destination vector $pGWB501$. To generate $PRO_{MAP65-3}:GFP:MAP65-$

3 reporter, the genomic sequence of *MAP65-3* was amplified by PCR with primers flanking the *attB* recombination sites and subcloned into *pDONR221* vector using the Gateway BP reaction. A *Sma*I restriction site was then introduced directly before the start codon. After linearization by *Sma*I restriction, the construct was ligated with the GFP fragment, followed by a Gateway LR reaction with the destination vector *pGWB601*. To generate the *PRO$_{CYCB3;1}$:CYCB3;1:GFP* reporter, the genomic sequence of *CYCB3;1* was amplified by PCR with primers flanking the *attB* recombination sites and subcloned into *pDONR221* vector using the Gateway BP reaction. The resulting *CYCB3;1* expression cassette was then integrated into the destination vector *pGWB504* harboring a C-terminal GFP tag by the Gateway LR reaction. Transgenic Arabidopsis plants were generated using the *Agrobacterium tumefaciens* strain *GV3101* (*pMP90*). A 100 ml overnight culture of Agrobacterium harboring these constructs was pelleted and resuspended in a solution containing 5% sucrose and 0.02% Silwet L-77 and plants were transformed by floral dip. The *VFD* construct was generated by site-directed mutagenesis using PfuTurbo polymerase (Stratagene) with *CDKA;1 VF* variant (Dissmeyer et al., 2009) as template and the similar primers used to generate *CDKA;1-T161D* (Dissmeyer et al., 2007). The *CDKA;1* sequence was flanked by Gateway *attB1* and *attB2* sites and recombined in *pDONR201* (Invitrogen). After sequencing, the obtained gateway entry clones were recombined with the binary gateway destination vector *pAM-PAT-GW-ProCDKA;1*. Resulting expression vectors conferring phosphinothricin resistance were retransformed into *Agrobacterium tumefaciens GV3101-pMP90RK* and transformed into heterozygous *cdka;1/+* by floral dip.

Phenotypic evaluation

To test for potential meiotic abnormalities the following analyses were performed.

Pollen size and viability was analyzed by Peterson staining as described previously (Peterson et al., 2010). For pollen analysis, three mature flower buds containing dehiscent anthers were dipped in 15 µl of Peterson staining solution (10% ethanol, 0.01% malachite green, 25% glycerol, 0.05% fuchsin, 0.005% orange G and 4% glacial acetic acid) and incubated overnight at room temperature. Similarly, for anther staining, 5 non-dehiscent anthers were dissected and immersed in 50 µl of Peterson staining and incubated overnight. Slides were heated at 80°C for 30min, prior to light microscope observation.

Cytogenetic analyses were performed via cell spreads as described in (Ross et al., 1996). In brief, fresh flower buds were fixed in 3:1 Ethanol:Acetic Acid (fixative solution) for at least 48h at 4°C, washed two times with fresh fixative solution and stored for further use in 70% ethanol at 4°C. Prior to chromosome spreading, the entire flower buds were digested in 10mM citrate buffer containing 1.5% cellulose, 1.5% pectolyase and 1.5% cytohelicase for 3h at 37°C. Single flower buds were transferred onto a glass slide and squashed with a bended needle for 1min in 12 µl of 45% acetic acid. Spreading was performed on a 48°C hot plate for 2min and the slide was washed afterwards with the fixative solution. After overnight incubation at 37°C slides were mounted in Vectashield with DAPI (Vector Laboratories).

Live imaging of meiotic progression

Live cell imaging was performed using the same protocol and sample preparation as described by (Prusicki et al., 2019). Up to 10 samples including the wild-type control next to the mutants were followed in the same petri dish. A W-plan-Apochromat 40X/1.0 DIC water immersion objective on a Zeiss LSM880 confocal microscope with ZEN 2.3 SP1 software (Carl Zeiss AG, Oberkochen, Germany) permitted the time-lapse acquisition. mTurquoise2 was exited at λ 458nm and detected at λ between 460-510nm, GFP was exited at 488nm and detected between 495-560 nm, mVenus was exited at 514nm and detected 520-620nm, TagRFP was exited at 561nm and detected at 570-650 nm. Time lapses were acquired as series of 8 Z-stacks with 4 µm interval (step size) using fluorescence auto-focusing. Acquisitions were carried out at 18°C. Image drift on Z plane was corrected manually using the review multi dimensional data option on Metamorph Version 7.8. Image drift on XY plane was corrected using the Stack Reg plugin (Rigid Body option) of Fiji.

Oryzalin treatment

A stock solution of oryzalin at the concentration of 100mM (Duchefa Biochemie) in dimethyl sulfoxide (DMSO) was prepared and kept at -20°. Plates containing oryzalin for live cell imaging were prepared as described previously (Prusicki et al., 2019). The final concentration of DMSO in the medium was 0.05%. The flower buds together with 5mm stem from 4 wild-type and 4 mutant plants were transferred simultaneous ly into the oryzalin or DMSO control plates. The time-lapse acquisition started 15min after transfer to the plates and only the anthers containing meiocytes

having the microtubule half-moon configuration (middle prophase) were kept for further imaging.

For quantification of root growth, nine-day-old seedlings grown on plates with and without oryzalin were photographed and the primary root length was measured by ImageJ.

Quantification of the duration of the meiotic phases

For quantification of the duration of the meiotic phases from diakinesis to telophase II/tetrad stage, cells were assigned manually by taking a starting point 10 min before the spindle I was visible until tetrad or eventually dyad formation. Data was collected from meiocytes located in at least 4 different anthers from different plants of the same genotype.

Co-localization analyses

For the pixel intensity plot, the pixel brightness through a region of interest was measured using ImageJ and plotted against the X dimension. The co-localized pixel map and scatter plot were calculated using the Coloc2 plugin in ImageJ.

Kinase and pull-down assays

To generate the expression construct for HisMBP-CYCB3;1, the full-length coding sequence of CYCB3;1 was amplified by PCR from a cDNA library for Col-0 wild-type plants with primers flanking *attB* recombination sites, and subsequently subcloned into *pDONR223* vector by gateway BP reaction (Supplementary Table 1). The resulting construct was then integrated into the protein expression vector *pHMGWA* by gateway LR reaction. The Strep-CDKA;1 expression construct was generated previously (Harashima and Schnittger, 2012).

To perform the pull down assay, bacteria of BL21(DE3)pLysS strain harboring either both HisMBP-CYCB3;1 and Strep-CDKA;1 vectors or only the Strep-CDKA;1 vector used as control, were generated by the heat shock transformation. Bacteria lysate from 50 ml IPTG induced bacteria were subjected to the pull down experiment using Ni-NTA agarose (QIAGEN) as the binding matrix. After 1 h incubation, Ni-NTA agarose were washed four times and then boiled quickly in 2X SDS-PAGE sample buffer. The eluted proteins were analyzed by western blot using antibodies against MBP (New England Biolabs, E8032S) and Strep (Sigma, 71590-M).

Kinase assays with precipitated kinases from plant extracts of transgenic lines were performed as previously described (Dissmeyer et al., 2007). Loading of CDKA;1 variants was shown using a rabbit polyclonal epitope antibody directed against the conserved α-PSTAIRE motif of Cdks (Cdc2 p34 (PSTAIRE): sc-53, Santa Cruz Biotechnology, Inc.).

Statistical analysis

To evaluate the significance of the differences between genotypes, Student's t-test was used. The significance of differences between more than two groups was calculated using the ANOVA one-way, followed by Turkey's test. * $P<0.05$ **$P<0.01$ and ***$P<0.001$. The numbers of samples are indicated in the figure legends.

Online supplemental material

Figure S1 shows the functionality of *CDKD;1, CDKD;2, CDKD;3* and *CDKA;1* reporter lines used in this study as they fully complement the *cdkd;1/- cdkd;3/-*, *cdkd;2/- cdkd;3/-* and *cdka;1/-* mutant phenotypes respectively. **Figure S2** shows the expression pattern and co-localization level of CDKA;1 and CDKD;3 throughout meiosis as well as the localization pattern of CDKD;1 and CDKD;2 in Arabidopsis anthers. **Figure S3** shows the chromosome spreads of single and double *cdkd* mutants and *CDKD;1* reporter used in this study. **Figure S4** shows the phenotypic characterization of VF cdka;1/- cdkd;3 mutants i.e. seed abortion, pollen viability, pollen size together with the meiotic stage repartition and chromosome spreads analysis of VF cdka;1/- cdkd;1 mutants. **Figure S5** shows root growth assay of WT, *CYCB3;1* reporter, *cycb3;1/-* and *mad1/-* mutants under oryzalin treatment as well as phenotypical analyses i.e. seed abortion, pollen viability of *VF cdka;1/- cycb3;1/-* mutant compared to WT and single *cycb3;1/-* mutant. **Table S1** shows the list of primers used in this study. **Video 1** shows microtubule dynamics from late prophase to tetrad formation in WT (A) and *VF cdka;1/-*. (B). **Video 2** shows microtubule dynamics during successive cytokinesis in *VF cdka;1/- cdkd;3/+*. **Video 3** highlights microtubule dynamics during meiotic exit in *VF cdka;1/- cdkd;3/-*. **Video 4** shows plasma membrane dynamics during meiotic exit in *VF cdka;1/- cdkd;3/-* compared to the WT. **Video 5** shows MAP65-3 dynamics during meiosis in WT. **Video 6**

highlights the differences of MAP65-3 dynamics between the WT and *VF cdka;1/-cdkd;3/-*. **Video 7** shows the localization of CYCB3;1 from late prophase to telophase II. **Video 8** shows microtubule dynamics from mid prophase to tetrad formation in WT and *cycb3;1/-* in media containing DMSO only. **Video 9** shows microtubule dynamics from mid prophase to tetrad formation in WT and *cycb3;1/-* in media containing 200nM oryzalin. **Video 10** shows microtubule dynamics from mid prophase to gamete formation in WT and *cycb3;1/-* in media containing 500nM oryzalin.

Author Contributions

K.S., M.U., Y.H. and A.S. conceived and designed the experiments. K.S., H.T., C.Y., S.K., L.B. and N.D. performed the experiments. M.U. and A.S. contributed material and reagents. K.S., M.U., and A.S. analyzed the data. K.S., M.U. and A.S. wrote the article.

Conflict of Interest

The authors declare that there is no conflict of interests.

References

Adhikari, D., W. Zheng, Y. Shen, N. Gorre, Y. Ning, G. Halet, P. Kaldis, and K. Liu. 2012. Cdk1, but not Cdk2, is the sole Cdk that is essential and sufficient to drive resumption of meiosis in mouse oocytes. *Hum. Mol. Genet.* 21:2476–2484. doi:10.1093/hmg/dds061.

Albert, B., C. Raquin, M. Prigent, S. Nadot, F. Brisset, M. Yang, and A. Ressayre. 2011. Successive microsporogenesis affects pollen aperture pattern in the tam mutant of Arabidopsis thaliana. *Ann. Bot.* 107:1421–1426. doi:10.1093/aob/mcr074.

Azumi, Y., D. Liu, D. Zhao, W. Li, G. Wang, Y. Hu, and H. Ma. 2002. Homolog interaction during meiotic prophase I in Arabidopsis requires the SOLO DANCERS gene encoding a novel cyclin-like protein. *EMBO J.* 21:3081–3095. doi:10.1093/emboj/cdf285.

Binarová, P., J. Doležel, P. Draber, E. Heberle-Bors, M. Strnad, and L. Bögre. 1998. Treatment of Vicia faba root tip cells with specific inhibitors to cyclin-dependent kinases leads to abnormal spindle formation. *Plant J.* 16:697–707. doi:10.1046/j.1365-313x.1998.00340.x.

Bulankova, P., S. Akimcheva, N. Fellner, and K. Riha. 2013. Identification of Arabidopsis meiotic cyclins reveals functional diversification among plant cyclin genes. *PLoS Genet.* 9:e1003508. doi:10.1371/journal.pgen.1003508.

Bulankova, P., N. Riehs-Kearnan, M.K. Nowack, A. Schnittger, and K. Riha. 2010. Meiotic progression in Arabidopsis is governed by complex regulatory interactions between SMG7, TDM1, and the meiosis I-specific cyclin TAM. *Plant Cell*. 22:3791–3803. doi:10.1105/tpc.110.078378.

Christophorou, N., T. Rubin, I. Bonnet, T. Piolot, M. Arnaud, and J.-R. Huynh. 2015. Microtubule-driven nuclear rotations promote meiotic chromosome dynamics. *Nat. Cell Biol.* 17:1388–1400. doi:10.1038/ncb3249.

Cifuentes, M., S. Jolivet, L. Cromer, H. Harashima, P. Bulankova, C. Renne, W. Crismani, Y. Nomura, H. Nakagami, K. Sugimoto, A. Schnittger, K. Riha, and R. Mercier. 2016. TDM1 Regulation Determines the Number of Meiotic Divisions. *PLoS Genet.* 12:e1005856. doi:10.1371/journal.pgen.1005856.

Colasanti, J., S. Cho, S. Wick, and V. Sundaresan. 1993. Localization of the Functional p34cdc2 Homolog of Maize in Root Tip and Stomatal Complex Cells: Association with Predicted Division Sites. *Plant Cell*. 5:1101–1111.

Coudreuse, D., and P. Nurse. 2010. Driving the cell cycle with a minimal CDK control network. *Nature*. 468:1074–1079. doi:10.1038/nature09543.

Cromer, L., J. Heyman, S. Touati, H. Harashima, E. Araou, C. Girard, C. Horlow, K. Wassmann, A. Schnittger, L. De Veylder, and R. Mercier. 2012. OSD1 promotes meiotic progression via APC/C inhibition and forms a regulatory network with

TDM and CYCA1;2/TAM. *PLoS Genet.* 8:e1002865. doi:10.1371/journal.pgen.1002865.

De Storme, N., and D. Geelen. 2013. Cytokinesis in plant male meiosis. *Plant Signal. Behav.* 8. doi:10.4161/psb.23394.

De Storme, N., M.C. Van Labeke, and D. Geelen. 2007. Formation of unreduced pollen in Arabidopsis thaliana. *Commun. Agric. Appl. Biol. Sci.* 72:159–163.

DeLuca, K.F., A. Meppelink, A.J. Broad, J.E. Mick, O.B. Peersen, S. Pektas, S.M.A. Lens, and J.G. DeLuca. 2018. Aurora A kinase phosphorylates Hec1 to regulate metaphase kinetochore-microtubule dynamics. *J. Cell Biol.* 217:163–177. doi:10.1083/jcb.201707160.

Ding, D.Q., Y. Chikashige, T. Haraguchi, and Y. Hiraoka. 1998. Oscillatory nuclear movement in fission yeast meiotic prophase is driven by astral microtubules, as revealed by continuous observation of chromosomes and microtubules in living cells. *J. Cell Sci.* 111 (Pt 6):701–712.

Dissmeyer, N., M.K. Nowack, S. Pusch, H. Stals, D. Inzé, P.E. Grini, and A. Schnittger. 2007. T-loop phosphorylation of Arabidopsis CDKA;1 is required for its function and can be partially substituted by an aspartate residue. *Plant Cell*. 19:972–985. doi:10.1105/tpc.107.050401.

Dissmeyer, N., and A. Schnittger. 2011. The age of protein kinases. *Methods Mol. Biol. Clifton NJ*. 779:7–52. doi:10.1007/978-1-61779-264-9_2.

Dissmeyer, N., A.K. Weimer, S. Pusch, K. De Schutter, C.L. Alvim Kamei, M.K. Nowack, B. Novak, G.-L. Duan, Y.-G. Zhu, L. De Veylder, and A. Schnittger. 2009. Control of cell proliferation, organ growth, and DNA damage response operate independently of dephosphorylation of the Arabidopsis Cdk1 homolog CDKA;1. *Plant Cell*. 21:3641–3654. doi:10.1105/tpc.109.070417.

Dumitru, A.M.G., S.F. Rusin, A.E.M. Clark, A.N. Kettenbach, and D.A. Compton. 2017. Cyclin A/Cdk1 modulates Plk1 activity in prometaphase to regulate kinetochore-microtubule attachment stability. *eLife*. 6. doi:10.7554/eLife.29303.

Enami, K., M. Ichikawa, T. Uemura, N. Kutsuna, S. Hasezawa, T. Nakagawa, A. Nakano, and M.H. Sato. 2009. Differential Expression Control and Polarized Distribution of Plasma Membrane-Resident SYP1 SNAREs in Arabidopsis thaliana. *Plant Cell Physiol.* 50:280–289. doi:10.1093/pcp/pcn197.

d'Erfurth, I., L. Cromer, S. Jolivet, C. Girard, C. Horlow, Y. Sun, J.P.C. To, L.E. Berchowitz, G.P. Copenhaver, and R. Mercier. 2010. The cyclin-A CYCA1;2/TAM is required for the meiosis I to meiosis II transition and cooperates with OSD1 for the prophase to first meiotic division transition. *PLoS Genet.* 6:e1000989. doi:10.1371/journal.pgen.1000989.

d'Erfurth, I., S. Jolivet, N. Froger, O. Catrice, M. Novatchkova, and R. Mercier. 2009. Turning Meiosis into Mitosis. *PLOS Biol.* 7:e1000124. doi:10.1371/journal.pbio.1000124.

Fisher, D.L., and P. Nurse. 1996. A single fission yeast mitotic cyclin B p34cdc2 kinase promotes both S-phase and mitosis in the absence of G1 cyclins. *EMBO J.* 15:850–860.

Furness, C.A., and P.J. Rudall. 1999. Microsporogenesis in Monocotyledons. *Ann. Bot.* 84:475–499. doi:10.1006/anbo.1999.0942.

Girard, C., L. Chelysheva, S. Choinard, N. Froger, N. Macaisne, A. Lehmemdi, J. Mazel, W. Crismani, and R. Mercier. 2015. AAA-ATPase FIDGETIN-LIKE 1 and Helicase FANCM Antagonize Meiotic Crossovers by Distinct Mechanisms. *PLOS Genet.* 11:e1005369. doi:10.1371/journal.pgen.1005369.

Gutiérrez-Escribano, P., and P. Nurse. 2015. A single cyclin-CDK complex is sufficient for both mitotic and meiotic progression in fission yeast. *Nat. Commun.* 6:6871. doi:10.1038/ncomms7871.

Hajheidari, M., S. Farrona, B. Huettel, Z. Koncz, and C. Koncz. 2012. CDKF;1 and CDKD protein kinases regulate phosphorylation of serine residues in the C-terminal domain of Arabidopsis RNA polymerase II. *Plant Cell*. 24:1626–1642. doi:10.1105/tpc.112.096834.

Harashima, H., and A. Schnittger. 2012. Robust reconstitution of active cell-cycle control complexes from co-expressed proteins in bacteria. *Plant Methods*. 8:23. doi:10.1186/1746-4811-8-23.

Harashima, H., A. Shinmyo, and M. Sekine. 2007. Phosphorylation of threonine 161 in plant cyclin-dependent kinase A is required for cell division by activation of its associated kinase. *Plant J. Cell Mol. Biol.* 52:435–448. doi:10.1111/j.1365-313X.2007.03247.x.

Ho, C.-M.K., Y.-R.J. Lee, L.D. Kiyama, S.P. Dinesh-Kumar, and B. Liu. 2012. Arabidopsis Microtubule-Associated Protein MAP65-3 Cross-Links Antiparallel Microtubules toward Their Plus Ends in the Phragmoplast via Its Distinct C-Terminal Microtubule Binding Domain. *Plant Cell*. 24:2071–2085. doi:10.1105/tpc.111.092569.

Holt, L.J., B.B. Tuch, J. Villén, A.D. Johnson, S.P. Gygi, and D.O. Morgan. 2009. Global analysis of Cdk1 substrate phosphorylation sites provides insights into evolution. *Science*. 325:1682–1686. doi:10.1126/science.1172867.

Huertas, P., F. Cortés-Ledesma, A.A. Sartori, A. Aguilera, and S.P. Jackson. 2008. CDK targets Sae2 to control DNA-end resection and homologous recombination. *Nature*. 455:689–692. doi:10.1038/nature07215.

Jiang, W., G. Jimenez, N.J. Wells, T.J. Hope, G.M. Wahl, T. Hunter, and R. Fukunaga. 1998. PRC1: a human mitotic spindle-associated CDK substrate protein required for cytokinesis. *Mol. Cell*. 2:877–885.

Jürgens, G. 2005. Cytokinesis in higher plants. *Annu. Rev. Plant Biol.* 56:281–299. doi:10.1146/annurev.arplant.55.031903.141636.

Kaldis, P. 1999. The cdk-activating kinase (CAK): from yeast to mammals. *Cell. Mol. Life Sci. CMLS*. 55:284–296.

Komaki, S., and A. Schnittger. 2017. The Spindle Assembly Checkpoint in Arabidopsis Is Rapidly Shut Off during Severe Stress. *Dev. Cell*. 43:172-185.e5. doi:10.1016/j.devcel.2017.09.017.

Lei, X., and B. Liu. 2020. Tapetum-Dependent Male Meiosis Progression in Plants: Increasing Evidence Emerges. *Front. Plant Sci.* 10. doi:10.3389/fpls.2019.01667.

Liu, B., N. De Storme, and D. Geelen. 2017. Gibberellin Induces Diploid Pollen Formation by Interfering with Meiotic Cytokinesis1[OPEN]. *Plant Physiol.* 173:338–353. doi:10.1104/pp.16.00480.

Magnard, J.L., M. Yang, Y.C. Chen, M. Leary, and S. McCormick. 2001. The Arabidopsis gene tardy asynchronous meiosis is required for the normal pace and synchrony of cell division during male meiosis. *Plant Physiol.* 127:1157–1166.

Mogessie, B., K. Scheffler, and M. Schuh. 2018. Assembly and Positioning of the Oocyte Meiotic Spindle. *Annu. Rev. Cell Dev. Biol.* 34:381–403. doi:10.1146/annurev-cellbio-100616-060553.

Mollinari, C., J.-P. Kleman, W. Jiang, G. Schoehn, T. Hunter, and R.L. Margolis. 2002. PRC1 is a microtubule binding and bundling protein essential to maintain the mitotic spindle midzone. *J. Cell Biol.* 157:1175–1186. doi:10.1083/jcb.200111052.

Morgan, D.O. 1997. Cyclin-dependent kinases: engines, clocks, and microprocessors. *Annu. Rev. Cell Dev. Biol.* 13:261–291. doi:10.1146/annurev.cellbio.13.1.261.

Müller, S., and G. Jürgens. 2016. Plant cytokinesis-No ring, no constriction but centrifugal construction of the partitioning membrane. *Semin. Cell Dev. Biol.* 53:10–18. doi:10.1016/j.semcdb.2015.10.037.

Nakagawa, T., T. Suzuki, S. Murata, S. Nakamura, T. Hino, K. Maeo, R. Tabata, T. Kawai, K. Tanaka, Y. Niwa, Y. Watanabe, K. Nakamura, T. Kimura, and S. Ishiguro. 2007. Improved Gateway binary vectors: high-performance vectors for creation of fusion constructs in transgenic analysis of plants. *Biosci. Biotechnol. Biochem.* 71:2095–2100. doi:10.1271/bbb.70216.

Nannas, N.J., D.M. Higgins, and R.K. Dawe. 2016. Anaphase asymmetry and dynamic repositioning of the division plane during maize meiosis. *J. Cell Sci.* 129:4014–4024. doi:10.1242/jcs.194860.

Nowack, M.K., P.E. Grini, M.J. Jakoby, M. Lafos, C. Koncz, and A. Schnittger. 2006. A positive signal from the fertilization of the egg cell sets off endosperm proliferation in angiosperm embryogenesis. *Nat. Genet.* 38:63–67. doi:10.1038/ng1694.

Nowack, M.K., H. Harashima, N. Dissmeyer, X. Zhao, D. Bouyer, A.K. Weimer, F. De Winter, F. Yang, and A. Schnittger. 2012. Genetic framework of cyclin-dependent kinase function in Arabidopsis. *Dev. Cell*. 22:1030–1040. doi:10.1016/j.devcel.2012.02.015.

Ortega, S., I. Prieto, J. Odajima, A. Martín, P. Dubus, R. Sotillo, J.L. Barbero, M. Malumbres, and M. Barbacid. 2003. Cyclin-dependent kinase 2 is essential for meiosis but not for mitotic cell division in mice. *Nat. Genet.* 35:25–31. doi:10.1038/ng1232.

Pagliuca, F.W., M.O. Collins, A. Lichawska, P. Zegerman, J.S. Choudhary, and J. Pines. 2011. Quantitative proteomics reveals the basis for the biochemical specificity of the cell-cycle machinery. *Mol. Cell*. 43:406–417. doi:10.1016/j.molcel.2011.05.031.

Park, M., C. Krause, M. Karnahl, I. Reichardt, F.E. Kasmi, U. Mayer, Y.-D. Stierhof, U. Hiller, G. Strompen, M. Bayer, M. Kientz, M.H. Sato, M.T. Nishimura, J.L. Dangl, A.A. Sanderfoot, and G. Jürgens. 2018. Concerted Action of Evolutionarily Ancient and Novel SNARE Complexes in Flowering-Plant Cytokinesis. *Dev. Cell*. 44:500-511.e4. doi:10.1016/j.devcel.2017.12.027.

Pesin, J.A., and T.L. Orr-Weaver. 2008. Regulation of APC/C Activators in Mitosis and Meiosis. *Annu. Rev. Cell Dev. Biol.* 24:475–499. doi:10.1146/annurev.cellbio.041408.115949.

Peterson, R., J.P. Slovin, and C. Chen. 2010. A simplified method for differential staining of aborted and non-aborted pollen grains. *Int. J. Plant Biol.* 1:e13–e13. doi:10.4081/pb.2010.e13.

Prusicki, M.A., E.M. Keizer, R.P. van Rosmalen, S. Komaki, F. Seifert, K. Müller, E. Wijnker, C. Fleck, and A. Schnittger. 2019. Live cell imaging of meiosis in Arabidopsis thaliana. *eLife*. 8. doi:10.7554/eLife.42834.

Pusch, S., H. Harashima, and A. Schnittger. 2012. Identification of kinase substrates by bimolecular complementation assays. *Plant J. Cell Mol. Biol.* 70:348–356. doi:10.1111/j.1365-313X.2011.04862.x.

Ressayre, A., L. Dreyer, S. Triki-Teurtroy, A. Forchioni, and S. Nadot. 2005. Post-meiotic cytokinesis and pollen aperture pattern ontogeny: comparison of development in four species differing in aperture pattern. *Am. J. Bot.* 92:576–583. doi:10.3732/ajb.92.4.576.

Ross, K.J., P. Fransz, and G.H. Jones. 1996. A light microscopic atlas of meiosis inArabidopsis thaliana. *Chromosome Res.* 4:507–516. doi:10.1007/BF02261778.

Santamaría, D., C. Barrière, A. Cerqueira, S. Hunt, C. Tardy, K. Newton, J.F. Cáceres, P. Dubus, M. Malumbres, and M. Barbacid. 2007. Cdk1 is sufficient to drive the mammalian cell cycle. *Nature*. 448:811–815. doi:10.1038/nature06046.

Sasabe, M., V. Boudolf, L. De Veylder, D. Inzé, P. Genschik, and Y. Machida. 2011. Phosphorylation of a mitotic kinesin-like protein and a MAPKKK by cyclin-dependent kinases (CDKs) is involved in the transition to cytokinesis in plants. *Proc. Natl. Acad. Sci. U. S. A.* 108:17844–17849. doi:10.1073/pnas.1110174108.

Shamina, N.V., E.I. Gordeeva, N.M. Kovaleva, E.G. Seriukova, and N.V. Dorogova. 2007. Formation and function of phragmoplast during successive cytokinesis stages in higher plant meiosis. *Cell Biol. Int.* 31:626–635. doi:10.1016/j.cellbi.2006.12.001.

Shimotohno, A., S. Matsubayashi, M. Yamaguchi, H. Uchimiya, and M. Umeda. 2003. Differential phosphorylation activities of CDK-activating kinases in Arabidopsis thaliana. *FEBS Lett.* 534:69–74.

Shimotohno, A., R. Ohno, K. Bisova, N. Sakaguchi, J. Huang, C. Koncz, H. Uchimiya, and M. Umeda. 2006. Diverse phosphoregulatory mechanisms controlling cyclin-dependent kinase-activating kinases in Arabidopsis. *Plant J. Cell Mol. Biol.* 47:701–710. doi:10.1111/j.1365-313X.2006.02820.x.

Smertenko, A., F. Assaad, F. Baluška, M. Bezanilla, H. Buschmann, G. Drakakaki, M.-T. Hauser, M. Janson, Y. Mineyuki, I. Moore, S. Müller, T. Murata, M.S. Otegui, E. Panteris, C. Rasmussen, A.-C. Schmit, J. Šamaj, L. Samuels, L.A. Staehelin, D. Van Damme, G. Wasteneys, and V. Žárský. 2017. Plant Cytokinesis: Terminology for Structures and Processes. *Trends Cell Biol.* 27:885–894. doi:10.1016/j.tcb.2017.08.008.

Stern, B., and P. Nurse. 1996. A quantitative model for the cdc2 control of S phase and mitosis in fission yeast. *Trends Genet.* 12:345–350. doi:10.1016/S0168-9525(96)80016-3.

Takatsuka, H., C. Umeda-Hara, and M. Umeda. 2015. Cyclin-dependent kinase-activating kinases CDKD;1 and CDKD;3 are essential for preserving mitotic activity in Arabidopsis thaliana. *Plant J. Cell Mol. Biol.* 82:1004–1017. doi:10.1111/tpj.12872.

Tapley, E.C., and D.A. Starr. 2013. Connecting the nucleus to the cytoskeleton by SUN-KASH bridges across the nuclear envelope. *Curr. Opin. Cell Biol.* 25:57–62. doi:10.1016/j.ceb.2012.10.014.

Tyson, J.J., and B. Novák. 2015. Models in biology: lessons from modeling regulation of the eukaryotic cell cycle. *BMC Biol.* 13:46. doi:10.1186/s12915-015-0158-9.

Ubersax, J.A., E.L. Woodbury, P.N. Quang, M. Paraz, J.D. Blethrow, K. Shah, K.M. Shokat, and D.O. Morgan. 2003. Targets of the cyclin-dependent kinase Cdk1. *Nature*. 425:859–864. doi:10.1038/nature02062.

Umeda, M., A. Shimotohno, and M. Yamaguchi. 2005. Control of cell division and transcription by cyclin-dependent kinase-activating kinases in plants. *Plant Cell Physiol.* 46:1437–1442. doi:10.1093/pcp/pci170.

Van Leene, J., J. Hollunder, D. Eeckhout, G. Persiau, E. Van De Slijke, H. Stals, G. Van Isterdael, A. Verkest, S. Neirynck, Y. Buffel, S. De Bodt, S. Maere, K. Laukens, A. Pharazyn, P.C.G. Ferreira, N. Eloy, C. Renne, C. Meyer, J.-D. Faure, J. Steinbrenner, J. Beynon, J.C. Larkin, Y. Van de Peer, P. Hilson, M. Kuiper, L. De Veylder, H. Van Onckelen, D. Inzé, E. Witters, and G. De Jaeger. 2010. Targeted interactomics reveals a complex core cell cycle machinery in Arabidopsis thaliana. *Mol. Syst. Biol.* 6:397. doi:10.1038/msb.2010.53.

Vavrdová, T., J. ˇSamaj, and G. Komis. 2019. Phosphorylation of Plant Microtubule-Associated Proteins During Cell Division. *Front. Plant Sci.* 10. doi:10.3389/fpls.2019.00238.

Wang, G., H. Kong, Y. Sun, X. Zhang, W. Zhang, N. Altman, C.W. dePamphilis, and H. Ma. 2004a. Genome-Wide Analysis of the Cyclin Family in Arabidopsis and Comparative Phylogenetic Analysis of Plant Cyclin-Like Proteins. *Plant Physiol.* 135:1084–1099. doi:10.1104/pp.104.040436.

Wang, Y., J.-L. Magnard, S. McCormick, and M. Yang. 2004b. Progression through meiosis I and meiosis II in Arabidopsis anthers is regulated by an A-type cyclin predominately expressed in prophase I. *Plant Physiol.* 136:4127–4135. doi:10.1104/pp.104.051201.

Weimer, A.K., M.K. Nowack, D. Bouyer, X. Zhao, H. Harashima, S. Naseer, F. De Winter, N. Dissmeyer, N. Geldner, and A. Schnittger. 2012. RETINOBLASTOMA RELATED1 Regulates Asymmetric Cell Divisions in Arabidopsis[C][W][OA]. *Plant Cell*. 24:4083–4095. doi:10.1105/tpc.112.104620.

Weingartner, M., P. Binarova, D. Drykova, A. Schweighofer, J.-P. David, E. Heberle-Bors, J. Doonan, and L. Bögre. 2001. Dynamic Recruitment of Cdc2 to Specific Microtubule Structures during Mitosis. *Plant Cell*. 13:1929–1944. doi:10.1105/TPC.010109.

Weingartner, M., M.-C. Criqui, T. Mészáros, P. Binarova, A.-C. Schmit, A. Helfer, A. Derevier, M. Erhardt, L. Bögre, and P. Genschik. 2004. Expression of a Nondegradable Cyclin B1 Affects Plant Development and Leads to Endomitosis by Inhibiting the Formation of a Phragmoplast. *Plant Cell*. 16:643–657. doi:10.1105/tpc.020057.

Wijnker, E., H. Harashima, K. Müller, P. Parra-Nuñez, C.B. de Snoo, J. van de Belt, N. Dissmeyer, M. Bayer, M. Pradillo, and A. Schnittger. 2019. The Cdk1/Cdk2 homolog CDKA;1 controls the recombination landscape in Arabidopsis. *Proc. Natl. Acad. Sci. U. S. A.* doi:10.1073/pnas.1820753116.

Yang, C., Y. Hamamura, K. Sofroni, F. Böwer, S.C. Stolze, H. Nakagami, and A. Schnittger. 2019. SWITCH 1/DYAD is a WINGS APART-LIKE antagonist that maintains sister chromatid cohesion in meiosis. *Nat. Commun.* 10:1755. doi:10.1038/s41467-019-09759-w.

Yang, C., K. Sofroni, E. Wijnker, Y. Hamamura, L. Carstens, H. Harashima, S.C. Stolze, D. Vezon, L. Chelysheva, Z. Orban-Nemeth, G. Pochon, H. Nakagami, P.

Schlögelhofer, M. Grelon, and A. Schnittger. 2020. The Arabidopsis Cdk1/Cdk2 homolog CDKA;1 controls chromosome axis assembly during plant meiosis. *EMBO J.* 39:e101625. doi:10.15252/embj.2019101625.

Yoshida, M., S. Katsuyama, K. Tateho, H. Nakamura, J. Miyoshi, T. Ohba, H. Matsuhara, F. Miki, K. Okazaki, T. Haraguchi, O. Niwa, Y. Hiraoka, and A. Yamamoto. 2013. Microtubule-organizing center formation at telomeres induces meiotic telomere clustering. *J. Cell Biol.* 200:385–395. doi:10.1083/jcb.201207168.

Zhao, X., H. Harashima, N. Dissmeyer, S. Pusch, A.K. Weimer, J. Bramsiepe, D. Bouyer, S. Rademacher, M.K. Nowack, B. Novak, S. Sprunck, and A. Schnittger. 2012. A General G1/S-Phase Cell-Cycle Control Module in the Flowering Plant Arabidopsis thaliana. *PLoS Genet.* 8. doi:10.1371/journal.pgen.1002847.

Supplementary figures

A   WT   CDKD;2:mVenus *cdkd;2/- cdkd;3/-*   CDKD;3:mVenus *cdkd;2/- cdkd;3/-*   *cdkd;2/- cdkd;3/-*

B   WT   CDKD;2:mVenus *cdkd;2/- cdkd;3/-*   CDKD;3:mVenus *cdkd;2/- cdkd;3/-*   *cdkd;2/- cdkd;3/-*

C   WT   CDKD;2:mVenus in *cdkd;2/- cdkd;3/-*   CDKD;3:mVenus in *cdkd;2/- cdkd;3/-*   CDKD;1:mVenus in *cdkd;1/- cdkd;3/-*   *cdkd;1/- cdkd;3/+*

D   CDKD;1:mVenus *cdkd;1/- cdkd;3/-*   *cdkd;1/- cdkd;3/+*

E   WT   CDKD;1:mVenus *cdkd;1/- cdkd;3/-*   CDKD;2:mVenus *cdkd;2/- cdkd;3/-*   CDKD;3:mVenus *cdkd;2/- cdkd;3/-*

F (CDKA;1:mTurquoise2 *cdka;1/-*): Pachytene | Diplotene | Metaphase I | Anaphase/Telophase I | Interkinesis | Metaphase II | Telophase II/Tetrad

G (*cdka;1/- D*): Pachytene | Diplotene | Metaphase I | Post-meiosis I

Supplementary Figure 1. The *CDKD;1*, *CDKD;2*, *CDKD;3* and *CDKA;1* reporter constructs are fully functional. (A) Phenotypes of *cdkd;2/- cdkd;3/-* double mutants, *cdkd;2/- cdkd;3/-* double mutants containing a *CDKD;2* and *CDKD;3* reporter, respectively, in comparison to the wildtype (WT). Photographs were taken 5 weeks after sawing. Scale bar 3cm. (B) Inflorescences of the *cdkd;2/- cdkd;3/-* double mutants and the CDKD;2 and CDKD;3 reporter lines (in a *cdkd;2/- cdkd;3/-* mutant background) in comparison to wild-type plants of the same age. Photographs were taken 14 weeks after sawing. Scale bar 7cm. (C) Siliques of the wildtype, the *CDKD;2* and *CDKD;3* reporters in a *cdkd;2/- cdkd;3/-* mutant background and the *CDKD;1* reporter in a *cdkd;1/- cdkd;3/-* mutant background versus *cdkd;1/- cdkd;3/+* double mutants, which have a high level of seed abortion indicated by red asterisks. Scale bar 1mm. (D) The main stem and siliques of the *CDKD;1* reporter line in a *cdkd;1/-* cdkd;3/-

background versus *cdkd;1/-* cdkd;3/+ double mutant. Scale bar 3cm. (E) Peterson staining of anthers for the wildtype, *CDKD;1*, *CDKD;2* and *CDKD;3* reporter lines in the indicated *cdkd* mutant background. Scale bar 20 μm. Chromosome spread analysis of CDKA;1:mTurquoise2 in *cdka;1/-* (F) versus *cdka;1/- D* mutant (G). Scale bar 10 μm.
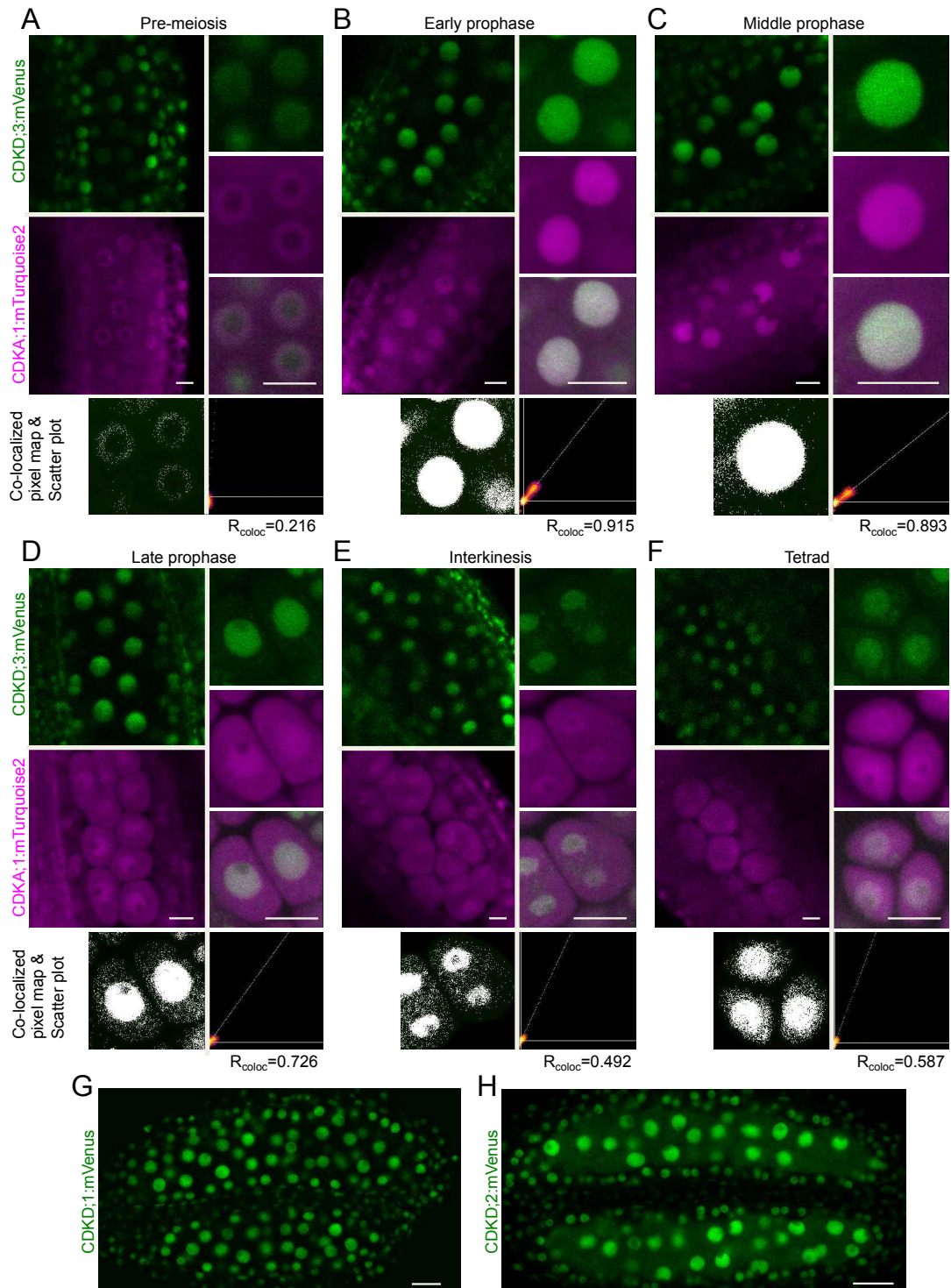
Supplementary Figure 2. CDKD;3 and CDKA;1 are expressed throughout meiosis and co-localize in the nucleus. Confocal laser scanning micrographs showing the localization of the functional CDKD;3:mVenus (green) and CDKA;1:mTurquoise2 (magenta) fusion proteins in male anthers of Arabidopsis. During prophase I (A-D), interkinesis (E) and tetrad stage (F) both proteins

enrich and differentially co-localize in the meiocyte nucleus as shown in every third row by the co-localized pixel map and scatter plot. The diagonal white line in the scatter plot represents the ratio of the intensities of the 2 channels (R_{coloc}). Scale bar 10 μm.

(G) Confocal laser scanning micrographs of anthers showing the accumulation of the CDKD;1:mVenus fusion protein in green. (H) Accumulation pattern of the CDKD;2:mVenus fusion protein in whole anthers. Scale bar 20 μm.

Hirotomo Takatsuka generated the CDKD;1, CDKD;2 and CDKD;3 reporter lines.
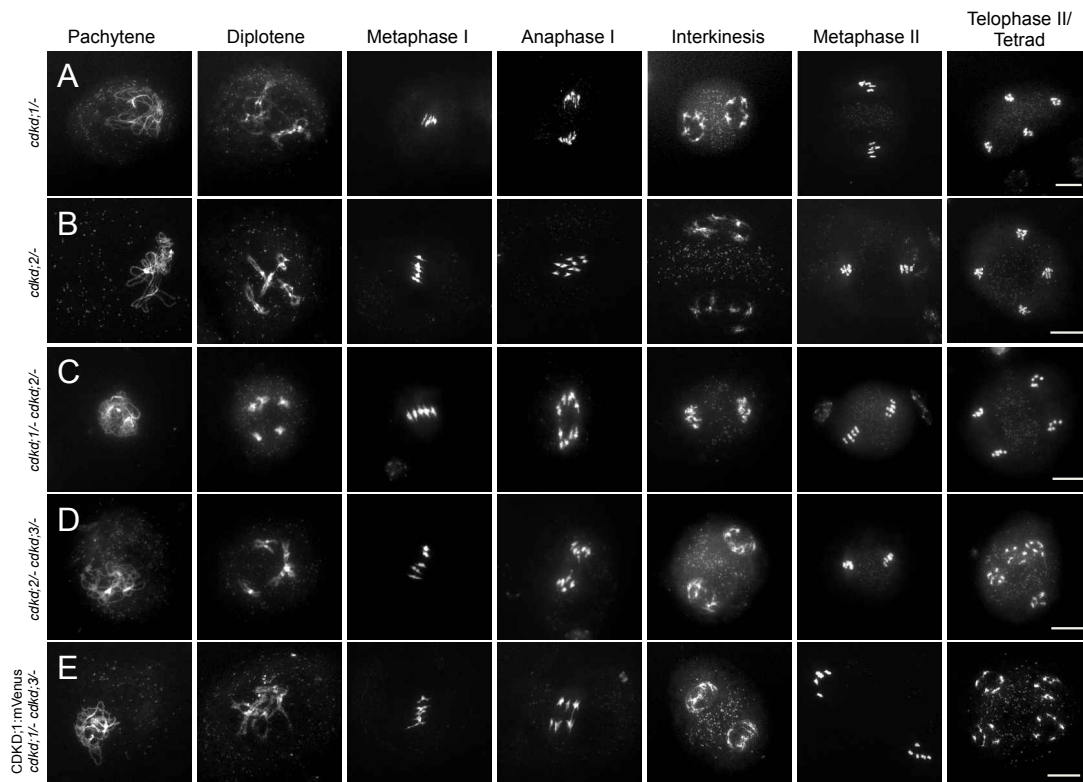
Supplementary Figure 3. Chromosome spreads of single and double *cdkd* mutants and CDKD reporter lines used in this study. Chromosome spreads with wild-type like meiotic progression in *cdkd;1/-* (A), *cdkd;2/-* (B), *cdkd;1/- cdkd;2/-* (C) *cdkd;2/- cdkd;3/-* (D) and *CDKD;1:mVenus* in *cdkd;1/- cdkd;3/-* (E). Scale bar 10 μm.
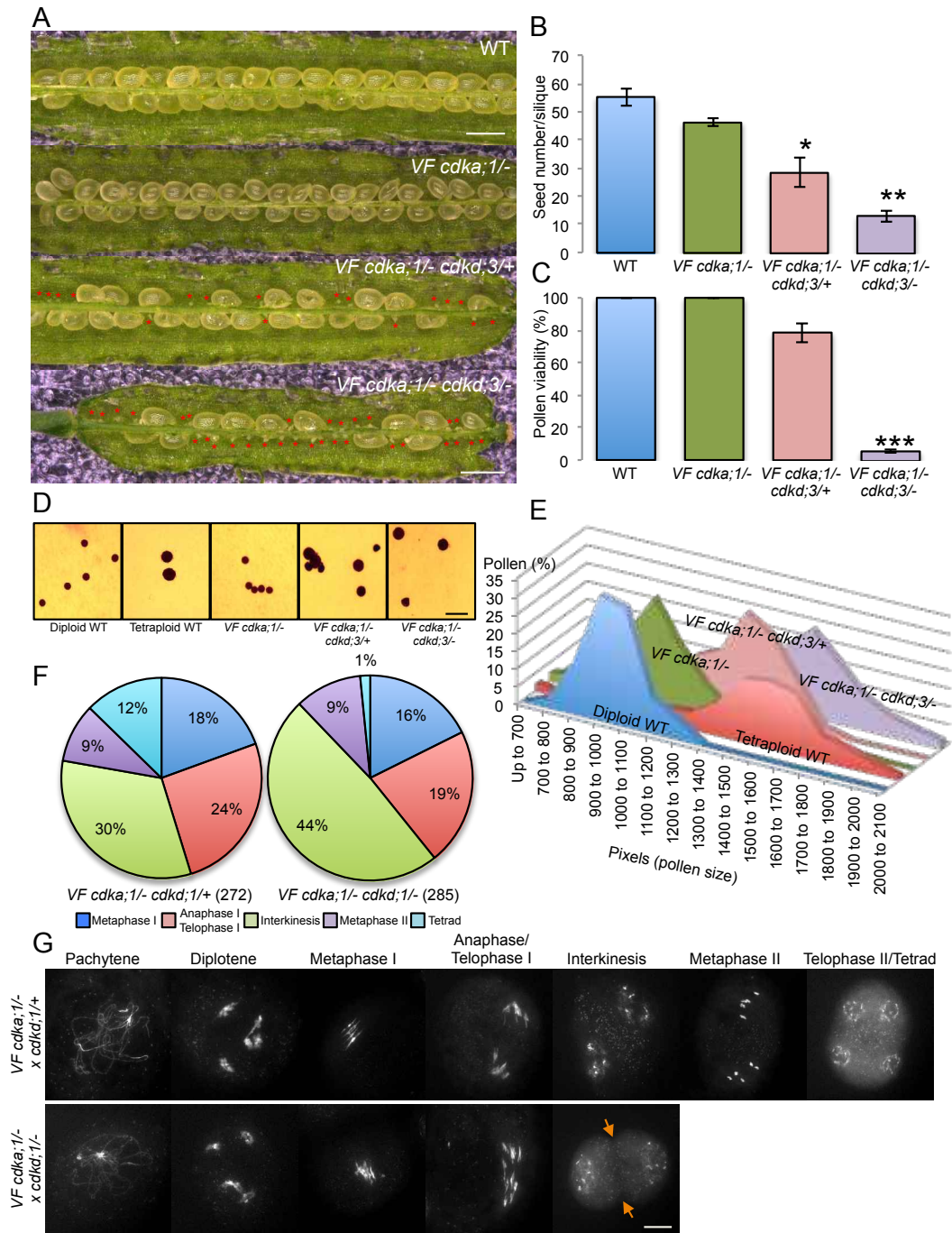
Supplementary Figure 4. Phenotypic characterization of *VF cdka;1 cdkd;3* and *VF cdka;1 cdkd;1* mutant combinations. (A) Siliques of the wildtype (WT) versus *VF cdka;1/-*, *VF cdka;1/- cdkd;3/+* and *VF cdka;1/- cdkd;3/-*. Red asterisks indicate aborted seeds. Scale bar 1mm. (B) Number of aborted seeds in at least 5 siliques and (C) pollen viability using at least 8 flower buds for the genotypes shown in (A). Level of significance (P<0.05*; P<0.01**;P<0.001***) is determined by one-way ANOVA followed by Tukey's test. (D) Pollen sizes (in pixels) after Peterson's staining of diploid and tetraploid wild-type pollen versus pollen from *VF cdka;1/-*, *VF cdka;1/- cdkd;3/+*, and *VF cdka;1/- cdkd;3/-* from at least 500 pollen grains for each genotype. (D) Peterson staining revealing the difference in pollen size for the genotypes quantified in (E). Scale bar 20 μm. (F) Repartition of meiotic stages within one flower bud undergoing meiosis from metaphase I to telophase II/tetrad in *VF cdka;1/- cdkd;1/+*

(n=272) and *VF cdka;1/- cdkd;1/-* (n=285) (G) Chromosome spread analysis of male meiocytes of *VF cdka;1/- cdkd;1/+* and *VF cdka;1/- cdkd;1/-.* Orange arrows highlight the premature exit after meiosis I in 75% of the meiocytes analyzed. Scale bar 10 μm.
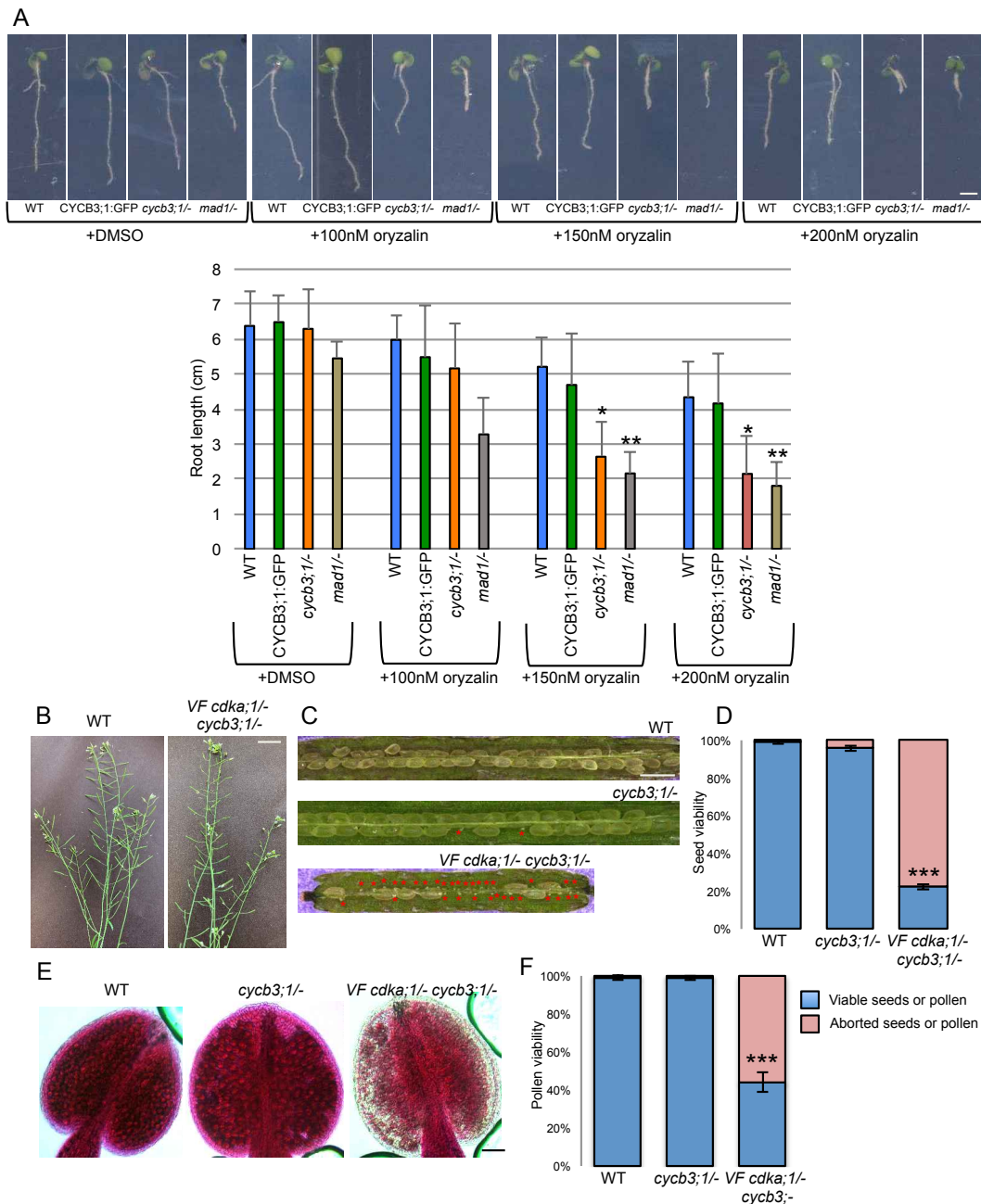
Supplementary Figure 5.Analysis of *VF cdka;1/- cycb3;1/-* mutant and functionality of the CYCB3;1:GFP reporter construct . (A) Nine-day-old seedlings grown on plates with DMSO, 100 nM, 150 nM and 200 nM oryzalin (upper panel). Mutants in the spindle assembly checkpoint component *MAD1* are used as a positive control for hypersensitivity to oryzalin. Scale bar 2cm. Root lenght on plates with and without oryzalin (lower panel). The mean (±SD) of more then 20 seedlings per indicated genotype is shown. Level of significance (P<0.05*; P<0.01**;P<0.001***) is determined by one-way ANOVA followed by Tukey's test. (B) The main stem and siliques of *VF cdka;1/- cycb3;1/-* mutant in comparison to the wildtype. Scale bar 3cm. (C) Siliques of the wildtype, *cycb3;1/-*

and *VF cdka;1/- cycb3;1/-* double mutant, which show seed abortion highlighted by red asterisks. Scale bar 1mm. (D) Quantification of seed abortion in at least 6 siliques for each genotype. The percentage of viable seeds is represented by blue bars and red bars indicate the percentage of aborted seeds from (C). (E) Peterson staining of anthers for the wildtype*, cycb3;1/-* and *VF cdka;1/- cycb3;1/-*. Scale bar 20 µm. (F) Quantification of pollen viability from at least 6 flower buds for each genotype. Blue bars indicate the percentage of viable pollen and red bars give the percentage of aborted pollen from (E). *Lev Böttger performed and analyzed the data presented on Figure S5A.*

Purpose	Primer name	Sequence
CDKA;1:mTurquoise2 reporter	gCDKA;1-F	CCAAGCGCAACAACGAAAGT
	gCDKA;1-R	GGCTACTTGGACCCTCTTGTC
	pENTR2B-CDKA;1-F	GACAAGAGGGTCCAAGTAGCCCGCGGCCGCACTCGAGATA
	pENTR2B-CDKA;1-R	ACTTTCGTTGTTGCGCTTGGGGATCCAGTCGACTGAATTG
	gCDKA;1-SmaISTOP-F	GGGATCTTTCCGTATTTTGGTCATT
	gCDKA;1-SmaISTOP-R	GGGAGGCATGCCTCCAAGATCCTTG
PRO$_{CDKA;1}$:mVenus reporter	gPRO$_{CDKA;1}$-F	CCAAGCGCAACAACGAAAGT
	gPRO$_{CDKA;1}$-R	CAATTCCTGAATAATAAAG
	pENTR2B-gPRO$_{CDKA;1}$-F	CTTTATTATTCAGGAATTGCGCGGCCGCACTCGAGATAT
	pENTR2B-gPRO$_{CDKA;1}$-R	ACTTTCGTTGTTGCGCTTGGGGATCCAGTCGACTGAATTG
CDKD;1:mVenus reporter	pDONR221-CDKD;1-F	AAAAAGCAGGCTTTCTTCCATCGTCAGATCAAGATC
	pDONR221-CDKD;1-R	AGAAAGCTGGGTAGATTTATGGTTGCAGGGGTTGC
CDKD;2:mVenus reporter	pDONR221-CDKD;2-F	AAAAAGCAGGCTTTGCTGATTCTTATGGATTGTTTTC
	pDONR221-CDKD;2-R	AGAAAGCTGGGTACCACTGATTAAGACACTCAC
CDKD;3:mVenus reporter	pDONR221-CDKD;3-F	AAAAAGCAGGCTTTTTTGGCACTCCAACCACTCTTC
	pDONR221-CDKD;3-R	AGAAAGCTGGGTAGGTGTCAGTGCAACTCCAGACATTC
CYCB3;1: GFP reporter	gCYCB3;1-attB1-F	GGGGACAAGTTTGTACAAAAAAGCAGGCTTATTTATTAGTGTGAAGCAGTTGGC
	gCYCB3;1-attB1-R	GGGGACCACTTTGTACAAGAAAGCTGGGTTGAGAGGGAGTTTATCTAAGGGCT
CYCB3;1 pull down assay	gCYCB3;1-attB1-F	GGGGACAAGTTTGTACAAAAAAGCAGGCTTCATGGCGTTCGCGAAGGCACCACG
	gCYCB3;1-attB1-R	GGGGACCACTTTGTACAAGAAAGCTGGGTTAGAGAGGGAGTTTATCTAAGGGC
GFP:MAP65-3 reporter	pDONR221-MAP65-3-F	GGGGACAAGTTTGTACAAAAAAGCAGGCTTGTACTCCTTGCAGAA
	pDONR221-MAP65-3-R	GGGGACCACTTTGTACAAGAAAGCTGGGTTTCGTCCCGTACAAAT
	Nter-SmaI-MAP65-3-F	GGGATGGCAAGTGTTCAAAAAGAT
	Nter-SmaI-MAP65-3-R	GGGTTCGAAATGCTTAAGCCTGTA
Genotyping of *cdka;1*	N048_Intron CDKA;1	CAGATCTCTTCCTGGTTATTCACA
	N049_Intron CDKA;1	TGTACAAGCGAATAAAGACATTTGA
	SALK_106809	GCGTGGACCGCTTGCTGCAACTCTCTCAGG
	Genotype T1 WT allele	TGCAGCTTTCCCTTTTTACGAG
Genotyping of VF construct	N125 revEXPR	GATAGATTTGTAGAGAGAGACTGG
	N265 fetch11	GAGTTTACTTCAGCTTTATTATTCAGG
Genotyping of *cdkd;1*	N643-WT-F	GTTGTGGCAATTTGTAGAATGG
	N435-WT-R	GATGTTGGCCGTACATTGGTCTTTAGAA
	MPI_8258	CTGGGAATGGCGAAATCAAGGCATC
Genotyping of cdkd;2	N602-WT-F	GATGGTTTGTTTTTGGTGTGG
	N603-WT-R	CCTTCAGGACCCATCACTCTCCTC
	SALK_065163	TTATTGGTTTCGGTTGGTG
Genotyping of cdkd;3	N637-WT-F	GAGTCGTCTTCAAAGCCACTG
	N638-WT-R	GCATTTGGAAACAGAGCTCAC
	SALK_120536	GCGTGGACCGCTTGCTGCAACTCTCTCAGG
Genotyping of cycb3;1	B31-13	CGGTCTAATAAGTCCATTGTCAGGTA
	B31-22	TTCTTTTATCGTTTGTGGGCAGCAA
	LB-wisc	AACGTCCGCAATGTGTTATTAAGTTGTC

Supplementary Table 1. List of primers used in this study.

Video legends

Video 1AB. Meiotic progression from late prophase to tetrad formation in two anthers of a wild-type flower (A) and in one anther of a *VF cdka;1/-* mutant plant (B). Tubulin (RFP) in magenta highlights microtubules during meiosis I to meiosis II transition. The interval between image acquisitions is 7 min. Time format (h:min). Scale bar 10 μm.

Video 2. Successive cytokinesis in one anther of a *VF cdka;1/- cdkd;3/+* mutant flower. Tubulin (RFP) in magenta highlights microtubules from late prophase to tetrad formation and the bright field image (cell shape) appears in grey. Cell wall deposition is observed after the first meiotic division (first cytokinesis) followed by the assembly of two spindles and a second cell wall deposition after the second meiotic division (second cytokinesis). See also Figure 5B. The interval between image acquisition is 10 min. Time format (h:min). Scale bar 10 μm.

Video 3. Meiotic exit after the first division in one anther of a *VF cdka;1/- cdkd;3/-* mutant flower. Tubulin (RFP) in magenta highlights microtubules from late prophase to dyad formation and the bright field image (cell shape) appears in grey. Cell wall deposition is observed after the first meiotic division and meiocytes do not progress through a second division. See also Figure 5C. The interval between image acquisition is 10 min. Time format (h:min). Scale bar 10 μm.

Video 4. Plasma membrane dynamics during simultaneous cytokinesis in the wildtype and meiotic exit in *VF cdka;1/- cdkd;3/-*. SYP132 (GFP) in green highlights the plasma membrane during the simultaneous cell wall deposition in the wildtype (white box, left panel) leading to the formation of a tetrad. In contrast, premature cell wall deposition in *VF cdka;1/- cdkd;3/-* (white box, right panel) causes the formation of a dyad. In both cases, cell wall deposition follows the same direction, i.e. from the outside to the inside. See also figure 5D Time format (h:min). Scale bar 10 μm.

Video 5. MAP65-3 is loaded twice at interkinesis and tetrad formation during wild-type meiosis. Progression of meiosis from late prophase to tetrad in one anther of wild-type flowers. MAP65-3 (GFP) is highlighted in green and tubulin (RFP) in magenta. Note the appearance of MAP65-3 at the onset of anaphase I and II and its localization at the mid-zone in interkinesis and telophase II. See also Figure 6D. The interval between image acquisitions is 5 min. Scale bar 10 μm.

Video 6. Dynamics of MAP65-3 in plants with low CDKs levels. Comparison of meiotic progression in one anther of the wildtype (left) and *VF cdka;1/- cdkd;3/-* mutant (right). MAP65-3 (GFP) in green highlights premature phragmoplast-like structures before NEB. Moreover, the pattern of MAP65-3 localization is more diffuse and less regular in comparison to the wildtype. See also Figure 6I. The interval between image acquisitions is 10 min. Scale bar 10 μm.

Video 7. CYCB3;1 localizes to the first meiotic spindle. Progression of meiosis from late prophase to tetrad formation in one anther of wild-type flowers. CYCB3;1 (GFP) is highlighted in green (first panel), tubulin (RFP) in magenta (second panel) and their merge in the last panel. CYCB3;1 is strongly associated with the first but not the second spindle. See also Figure 8B. The interval between image acquisitions is 5 min. Scale bar 10 μm.

Video 8. Meiotic progression from mid prophase (*half-moon* stage) to tetrad formation in one anther of the wildtype treated with DMSO (left) versus *cycb3;1* treated with DMSO (right). Tubulin (RFP) is highlighted in white. Note that microtubules are not affected and the meiocytes progress through meiosis as untreated flowers. See also Figure 9B,C. The interval between image acquisitions is 10 min. Scale bar 10 μm.

Video 9. Meiotic progression from middle prophase (*half-moon* stage) to tetrad formation in two anthers of the wildtype treated with 200nM oryzalin (left) versus *cycb3;1/-* treated with 200nM oryzalin (right). Tubulin (RFP) is highlighted in white. While microtubules are not affected in the wildtype, the spindle length is reduced in treated *cycb3;1/-*. See also Figure 9D,E. The interval between image acquisitions is 10 min. Scale bar 10 μm.

**Video 10. Meiotic progression from middle prophase (*half-moon* stage) in two anthers of the wildtype treated with 500nM oryzalin (left) versus *cycb3;1/- treated with 500nM oryzalin (right).* Tubulin (RFP) is highlighted in white. In treated wild-type flowers (WT), meiotic spindles are shorter in comparison to untreated flowers or flowers treated with lower concentrations of oryzalin (left panel). In contrast, spindles are completely absent in treated *cycb3;1/-* mutants (right panel). In addition, microtubules are very diffuse in *cycb3;1/-* mutants (right panel) and after 2 NEB events the formation of completely unreduced gametes is observed. See also Figure 9F,G. The interval between image acquisitions is 10 min. Scale bar 10 μm.

CHAPTER 2: Cdks regulate chromosome axis and cohesion during meiosis

2.1 The Arabidopsis Cdk1/Cdk2 homolog CDKA;1 controls chromosome axis assembly during plant meiosis

The following paper has been published in EMBO Journal, 2020.

My contribution to this work is summarized below:

- Generation, cytological and phenotypical characterization of the functional reporter line $Pro_{CDKA;1}CDKA;1:mVenus$ (Figure EV1A-C)
- Localization pattern of CDKA;1 together with tubulin during meiosis (Figure 1A) and quantitative analysis of the signal distribution of the nuclear versus cytoplasmic fraction of CDKA;1:mVenus during prophase I, revealed by live cell imaging (Figure 1B and Movie EV1)
- Chromosome spreads of the hypomorphic *cdka;1* mutant $CDKA;1^{T161D}$ in *cdka;1* mutant background (Figure 1D second row)

The *Arabidopsis* Cdk1/Cdk2 homolog CDKA;1 controls chromosome axis assembly during plant meiosis

Chao Yang[1], Kostika Sofroni[1] iD, Erik Wijnker[1,†], Yuki Hamamura[1], Lena Carstens[1,‡],
Hirofumi Harashima[2,§], Sara Christina Stolze[3], Daniel Vezon[4], Liudmila Chelysheva[4] iD,
Zsuzsanna Orban-Nemeth[5,¶], Gaëtan Pochon[1], Hirofumi Nakagami[3] iD, Peter Schlögelhofer[5],
Mathilde Grelon[4] & Arp Schnittger[1,*] iD

Abstract

Meiosis is key to sexual reproduction and genetic diversity. Here, we show that the *Arabidopsis* cyclin-dependent kinase Cdk1/Cdk2 homolog CDKA;1 is an important regulator of meiosis needed for several aspects of meiosis such as chromosome synapsis. We identify the chromosome axis protein ASYNAPTIC 1 (ASY1), the *Arabidopsis* homolog of Hop1 (homolog pairing 1), essential for synaptonemal complex formation, as a target of CDKA;1. The phosphorylation of ASY1 is required for its recruitment to the chromosome axis via ASYNAPTIC 3 (ASY3), the *Arabidopsis* reductional division 1 (Red1) homolog, counteracting the disassembly activity of the AAA⁺ ATPase PACHYTENE CHECKPOINT 2 (PCH2). Furthermore, we have identified the closure motif in ASY1, typical for HORMA domain proteins, and provide evidence that the phosphorylation of ASY1 regulates the putative self-polymerization of ASY1 along the chromosome axis. Hence, the phosphorylation of ASY1 by CDKA;1 appears to be a two-pronged mechanism to initiate chromosome axis formation in meiosis.

Introduction

Cell division relies on a highly orchestrated order of events to allow the faithful distribution of chromosomes to daughter cells. Progression through the cell cycle is controlled by the activity of cyclin-dependent kinases (Cdks; Morgan, 1997; Malumbres *et al*, 2009; Harashima *et al*, 2013). Eukaryotes usually contain several different families of cyclins that are thought to provide substrate specificity to Cdk–cyclin complexes and guide their intracellular localization (Miller & Cross, 2001; Pagliuca *et al*, 2011). However, the absolute levels of kinase activity have been found to be of key importance for cell cycle control, and at least in fission yeast, a single Cdk–cyclin complex is sufficient to drive both mitosis and meiosis (Coudreuse & Nurse, 2010; Gutiérrez-Escribano & Nurse, 2015).

In comparison with mitosis, much less is known about how Cdks control the progression of the two consecutive division events of meiosis. Meiosis II leads to the separation of sister chromatids that, at least formally, resembles a mitotic division and is thought to largely rely on similar control mechanisms as mitosis. In contrast, meiosis I holds many features that are not known from mitosis, foremost recombination between homologous chromosomes. Nonetheless, Cdk–cyclin complexes have been shown to control several aspects of meiosis I such as the formation of DNA double-strand breaks (DSBs) at the beginning of the meiotic recombination process by phosphorylating Mer2/Rec107 (meiotic recombination 2/recombination 107; Rockmill & Roeder, 1990; Henderson *et al*, 2006; Li *et al*, 2006).

Furthermore, the repair of DSBs through meiotic recombination has been found to involve Cdks, namely to phosphorylate the nuclease Sae2/Com1 (sporulation in the absence of spo eleven 2/completion of

1 Department of Developmental Biology, University of Hamburg, Hamburg, Germany
2 RIKEN Center for Sustainable Resource Science, Yokohama, Japan
3 Max-Planck-Institute for Plant Breeding Research, Cologne, Germany
4 Institut Jean-Pierre Bourgin, INRA, AgroParisTech, CNRS, Université Paris-Saclay, Versailles, France
5 Department of Chromosome Biology, Max F. Perutz Laboratories, Vienna Biocenter, University of Vienna, Vienna, Austria
   *Corresponding author. Tel: +49 40 428 16 502; Fax: +49 40 428 16 503; E-mail: arp.schnittger@uni-hamburg.de
   †Present address: Laboratory of Genetics, Wageningen University & Research, Wageningen, The Netherlands
   ‡Present address: Plant Developmental Biology & Plant Physiology, Kiel University, Kiel, Germany
   §Present address: Solution Research Laboratory, AS ONE Corporation, Kawasakiku, Kawasaki, Japan
   ¶Present address: Institute of Molecular Pathology, Vienna Biocenter, Vienna, Austria
   [The copyright line of this article was changed on 16 December 2019 after original online publication.]

meiotic recombination 1) and by that promotes its activity to generate 3′ overhangs at the DSB site (Huertas & Jackson, 2009; Anand *et al*, 2016; Cannavo *et al*, 2018). These DNA ends are further processed by the MRN/MRX complex comprising the subunits Mre11 (meiotic recombination 11), Rad50 (radiation 50), and Nbs1/Xrs2 (Nijmegen breakage syndrome 1/X-ray sensitive 2) (Mimitou and Symington, 2009; Manfrini *et al*, 2010). Subsequently, the single DNA strands are bound by the recombinases Rad51 (radiation 51) and Dmc1 (disrupted meiotic cDNA1) to promote strand invasion and formation of heteroduplex DNA (Shinohara *et al*, 1997; Kurzbauer *et al*, 2012; Da Ines *et al*, 2013). Depending on how the subsequently resulting double Holliday junctions are resolved, meiotic crossovers (COs) can be formed that lead to the reciprocal exchange of DNA segments between homologous chromosomes (Zickler & Kleckner, 2015; Lambing *et al*, 2017). Cdks were found to partially co-localize with Rad51 as well as other components acting downstream of Rad51 involved in CO formation (Baker *et al*, 1996; Zhu *et al*, 2010). This, together with the observation that inhibition of Cdk activity in early meiosis abolished the formation of Rad51 foci, led to the conclusion that the activity of Cdk is essential for DSB formation and/or processing (Henderson *et al*, 2006; Huertas *et al*, 2008; Zhu *et al*, 2010).

In many species, the synaptonemal complex (SC) stabilizes the pairing of homologous chromosomes and plays an important role in promoting the interhomolog bias during recombination and in maturation of recombination intermediates into COs (Zickler & Kleckner, 1999; Mercier *et al*, 2015). The SC is formed by the two proteinaceous axes of homologous chromosomes that will become then the lateral elements of the SC after synapsis. A number of proteins have been identified that are required for the correct formation of the chromosome axis. These include Red1 in yeast and its orthologs such as ASY3 in *Arabidopsis* (Rockmill & Roeder, 1990; Smith & Roeder, 1997; Ferdous *et al*, 2012). Another key protein of the chromosome axis is the HORMA domain protein Hop1 in yeast and its ortholog ASY1 in *Arabidopsis* (Hollingsworth *et al*, 1990; Aravind & Koonin, 1998; Armstrong, 2002). The phosphorylation of Hop1 at an [S/T]Q cluster domain by Tel1 (Telomere maintenance 1) and Mec1 (mitosis entry checkpoint 1), the ATM (ataxia telangiectasia mutated) and ATR (ataxia telangiectasia and Rad3-related) orthologs, is essential for the interhomolog-biased recombination, but not for the chromosomal loading of Hop1 (Carballo *et al*, 2008).

For the correct assembly of the SC, Hop1/ASY1 is recruited to the axis by interaction with Red1/ASY3 (Bailis & Roeder, 1998; de los Santos & Hollingsworth, 1999; Ferdous *et al*, 2012). Furthermore, it was recently proposed that Hop1 might build a homopolymer through its C-terminal closure motif and it was thought that this polymerization is likely crucial for its function and axis association since the point mutation K593A in the closure motif of Hop1 causes an 11-fold reduction in CO number and results in high spore lethality (Niu *et al*, 2005; West *et al*, 2018).

In wild type, the chromosome axes (lateral elements) of homologs become connected in the SC via the central region formed by dimers of the Zip1/ZYP1 family of proteins along with other components (Zickler & Kleckner, 2015). SC assembly goes along with the coordinated release of Hop1/ASY1 from the chromosome axis, catalyzed by the triple AAA$^+$ ATPase PCH2 (Wojtasz *et al*, 2009; Chen *et al*, 2014; Lambing *et al*, 2015). However, it is not clear how the dynamic localization Hop1/ASY1 on chromosomes is regulated.

Cdk complexes have also been implicated in the assembly of the SC since mutations in their catalytic core, i.e., in *Cdk2* in mice and in *CDC28* (*Cdk1* homolog) in budding yeast, resulted in defects in SC formation (Ortega *et al*, 2003; Zhu *et al*, 2010). However, although Zip1 has been shown to be phosphorylated by Cdk complexes *in vitro*, the molecular details of Cdk function for SC formation are still obscure since the SC is assembled normally in *zip1* mutants in which the Cdk phosphorylation sites were exchanged with amino acids that cannot be phosphorylated (Zhu *et al*, 2010).

The model plant *Arabidopsis*, similar to other multicellular eukaryotes, has several Cdks and cyclins with some of them having been assigned a function in meiosis (Wijnker & Schnittger, 2013). Six out of the 10 A- and one out of the nine B-type cyclins are expressed in meiosis including SOLO DANCERS (SDS), an atypical cyclin that has similarities to both A- and B-type cyclins (Azumi *et al*, 2002; Bulankova *et al*, 2013). However, of these eight cyclins potentially involved in meiosis, only the loss of either *CYCA1;2*, also known as *TARDY ASYNCHRONOUS MEIOSIS* (*TAM*), *CYCB3;1*, or *SDS* was found to result in meiotic defects (Magnard *et al*, 2001; Azumi *et al*, 2002; d'Erfurth *et al*, 2010; Bulankova *et al*, 2013; Prusicki *et al*, 2019). TAM is required for the repression of meiotic exit after the first meiotic division and the timely progression through meiosis II. SDS is necessary for crossover (CO) formation after DSBs have been induced, and the meiotic recombinase DMC1 does not localize to chromosomes in *sds* mutants (De Muyt *et al*, 2009). Mutants in *CYCB3;*1 have only a weak mutant phenotype and occasionally show premature and ectopic cell wall formation during meiosis I, a phenotype, however, that can be strongly enhanced in double mutants with *sds* demonstrating a redundant function of at least some of the meiotic cyclins in *Arabidopsis* (Bulankova *et al*, 2013).

SDS and TAM build active kinase complexes with CDKA;1, the *Arabidopsis* Cdk1/Cdk2 homolog, that is the main cell cycle regulator in *Arabidopsis* (Cromer *et al*, 2012; Harashima & Schnittger, 2012; Nowack *et al*, 2012; Cifuentes *et al*, 2016). A function of CDKA;1 in meiosis is supported by the analysis of weak loss-of-function mutants, which are completely sterile (Dissmeyer *et al*, 2007, 2009). Next to CDKA;1, CDKG has been implicated in meiosis by controlling synapsis at ambient but not low temperatures (Zheng *et al*, 2014). However, CDKG, which is related to human Cdk10, is likely involved in transcriptional and posttranscriptional control of gene expression and presumably does not control structural components of chromosomes directly (Doonan & Kitsios, 2009; Tank & Thaker, 2011; Huang *et al*, 2013; Zabicki *et al*, 2013).

Here, we demonstrate by detailed cytological and genetics studies that CDKA;1 is an important regulator of meiosis especially for chromosome synapsis and bivalent formation. We show that ASY1 is a phosphorylation target of CDKA;1 and that the phosphorylation of ASY1 is crucial for chromosomal axis formation in *Arabidopsis* by two, possibly interconnected mechanisms, involving the binding to ASY3 as well as to itself leading to ASY1 polymers assembling along the chromosome axis.

Results

Changes in subcellular distribution of CDKA;1 during meiosis

For a detailed understanding of the role of CDKA;1 in meiosis, we first analyzed its localization pattern in male meiocytes. Previous

90

studies using a functional fusion of CDKA;1 to mVenus have shown that CDKA;1 is present in both female meiosis and male meiosis (Nowack *et al*, 2007; Bulankova *et al*, 2010; Zhao *et al*, 2012). Since the previous reporter was subject to frequent silencing effects, a new *CDKA;1* reporter was generated not relying on the cDNA, as in the previous construct. Instead, a 7 kb genomic fragment into which mVenus was introduced before the stop codon of *CDKA;1* was used. The expression of this construct fully rescued the *cdka;1* mutant phenotype and gave rise to stable CDKA;1:mVenus expression (Fig EV1A–C).

By using this reporter, the subcellular localization pattern of CDKA;1 during male meiosis was revealed (Fig 1A and B, and Movie EV1). In early prophase, CDKA;1:mVenus is localized in both the nucleus (~60–70%) and the cytoplasm (~30–40%). As prophase progresses, CDKA;1 accumulates more strongly in the nucleus (~80%). Then, toward the end of prophase, CDKA;1 becomes more cytoplasmically localized (~50%). After nuclear envelope break-down, CDKA;1 decorates the first meiotic spindle and later accumulates in the two forming nuclei. In metaphase II, CDKA;1 is uniformly present in the entire cell, then is enriched at the spindle, and subsequently accumulates in the nuclei of the four meiotic products, i.e., the microspores (Fig 1A).

Due to the strong accumulation in the nucleoplasm, the presence of CDKA;1 at chromosomes, as reported for its mouse homolog Cdk2 or its yeast homolog Cdc28 (Ashley *et al*, 2001; Zhu *et al*, 2010), was difficult to judge. To address the chromosomal localization pattern of CDKA;1, we used plants that express a *StrepIII-tag-CDKA;1* fusion construct known to completely rescue the *cdka;1* mutant phenotype (Pusch *et al*, 2012), and followed the CDKA;1 localization in meiosis by immunolocalization using ASY1, a key component of the chromosome axis, for staging of meiosis. While Cdk2 and Cdc28 show a distinct punctuate staining in meiosis in mice and yeast (Ashley *et al*, 2001; Zhu *et al*, 2010), our experiments revealed that CDKA;1 co-localizes with ASY1 and forms a continuous signal along chromosomes at leptotene. At zygotene, when homologous chromosomes start to synapse, the fluorescent signals for both reporters, ASY1 and CDKA;1, concomitantly disappeared from the chromosome axes (Fig 1C). Since ASY1 is specifically removed from the synapsed chromosomes, we conclude from the similar patterns of CDKA;1 that CDKA;1 is excluded from the synapsed regions. These data suggest that CDKA;1 physically interacts with the chromosome axis during early meiotic prophase and might be important for chromosome pairing and synapsis.

Meiosis is severely affected in hypomorphic *cdka;1* mutants

To assess the requirement of CDKA;1 for early stages of meiosis, we compared meiotic progression by chromosome spreads between wild-type plants and two previously described weak loss-of-function *cdka;1* mutants (Figs 1D and EV1D). These alleles resulted from the complementation of a *cdka;1* null mutant with *CDKA;1* expression constructs, in which conserved amino acids have been replaced resulting in CDKA;1 variants with strongly reduced kinase activity: *cdka;1 PRO_{CDKA;1}:CDKA;1^{T161D}* (in the following designated *CDKA;1^{T161D}*) and *cdka;1 PRO_{CDKA;1}: CDKA;1^{T14D;Y15E}* (in the following referred to as *CDKA;1^{T14D;Y15E}* (Dissmeyer *et al*, 2007, 2009). Both mutants were found to exhibit

similar meiotic phenotypes during male meiosis, because of which we focus on the description of one allele (*CDKA;1^{T161D}*) in the following (Figs 1D and EV1D).

In wild-type meiosis, chromosomes start to condense during early prophase, and initiate chromosome synapsis during zygotene, leading to full homolog synapsis at pachytene. Chromosome morphology becomes diffuse at diplotene followed by chromosome re-condensation toward diakinesis when bivalents become visible (Fig 1D a–c).

In *CDKA;1^{T161D}*, the first difference from the wild type becomes notable at zygotene-like stage manifested by the presence of clear thread-like chromosomes and the accumulation of mitochondria at the side of the meiocytes in which no homolog synapsis is observed (Fig 1D h) (58%; *n* = 120). The absence of synapsis was confirmed by the failure of ZYP1, a component of the central region of the synaptonemal complex, to localize to chromosomes of male meiocytes of *CDKA;1^{T161D}* mutants as revealed by immunofluorescence analysis (Fig EV1E). Pachytene-like stages of *CDKA;1^{T161D}* meiocytes show the characteristically even distribution of mitochondria as that in wild type through the cell, but have largely unpaired chromosomes (Fig 1D i). Like in the wild type, chromosomes in *CDKA;1^{T161D}* then decondense at diplotene and recondense toward diakinesis with a major difference being the appearance of 10 univalents instead of five bivalents (Fig 1D d and k), which is the result of an achiasmatic meiosis (no bivalents found in nine out of nine meiocytes analyzed). These univalents are rod shaped and often show fuzzy borders that may indicate problems in chromosome condensation.

The absence of synapsis and chiasmata can have several reasons, with one of the potentially earliest causes being the absence of SPO11-induced DSBs. However, the DSB repair recombinase DMC1 was localized correctly onto chromosomes with no significant reduction of foci, i.e., 138.5 ± 9.8 in *CDKA;1^{T161D}* (*n* = 10) versus 169.9 ± 15.7 (*n* = 7) in WT (*P* = 0.09, two-tailed *t*-test). This suggested that DSBs are formed along the chromosome axis and that the achiasmatic meiosis in *CDKA;1^{T161D}* results from defects in later steps of meiosis (Fig EV1F). The formation of DSBs was corroborated by the finding that a double mutant of *CDKA;1^{T161D}* with *rad51*, which is required for DSB repair, showed chromosome fragmentation (44 out of 45 meiocytes analyzed) similar to the *rad51* single mutant (39 out of 39 meiocytes; Fig EV1G). Therefore, we conclude that DSB processing, at least up to the loading of DMC1, is functional in *CDKA;1^{T161D}*. With this, we conclude that the phenotype of the hypomorphic *CDKA;1^{T161D}* mutants manifests after the meiotic DSB formation and initiation of repair but before synapsis.

Meiotic progression in *cdka;1* hypomorphic mutants is highly disturbed during meiotic stages after pachytene indicating additional roles of CDKA;1 in meiosis (Fig 1D j–n). At least a part of the cells give rise to interkinesis-like stages where two or more daughter nuclei are separated by a clear organelle band (Fig 1D l and m; 19%; *n* = 39). In such nuclei, up to 10 partially decondensed chromosomes are visible in two or more loosely organized groups, or as single chromosomes (Fig 1D l–n). A clear second meiotic division has not been observed in any cell (*n* = 206), and a phragmoplast occasionally becomes visible within the organelle band at interkinesis (in eight out of 39 cells), indicating that cytokinesis already begins at this stage (Fig 1D m). Taken together, these data suggest that CDKA;1 is an important regulator
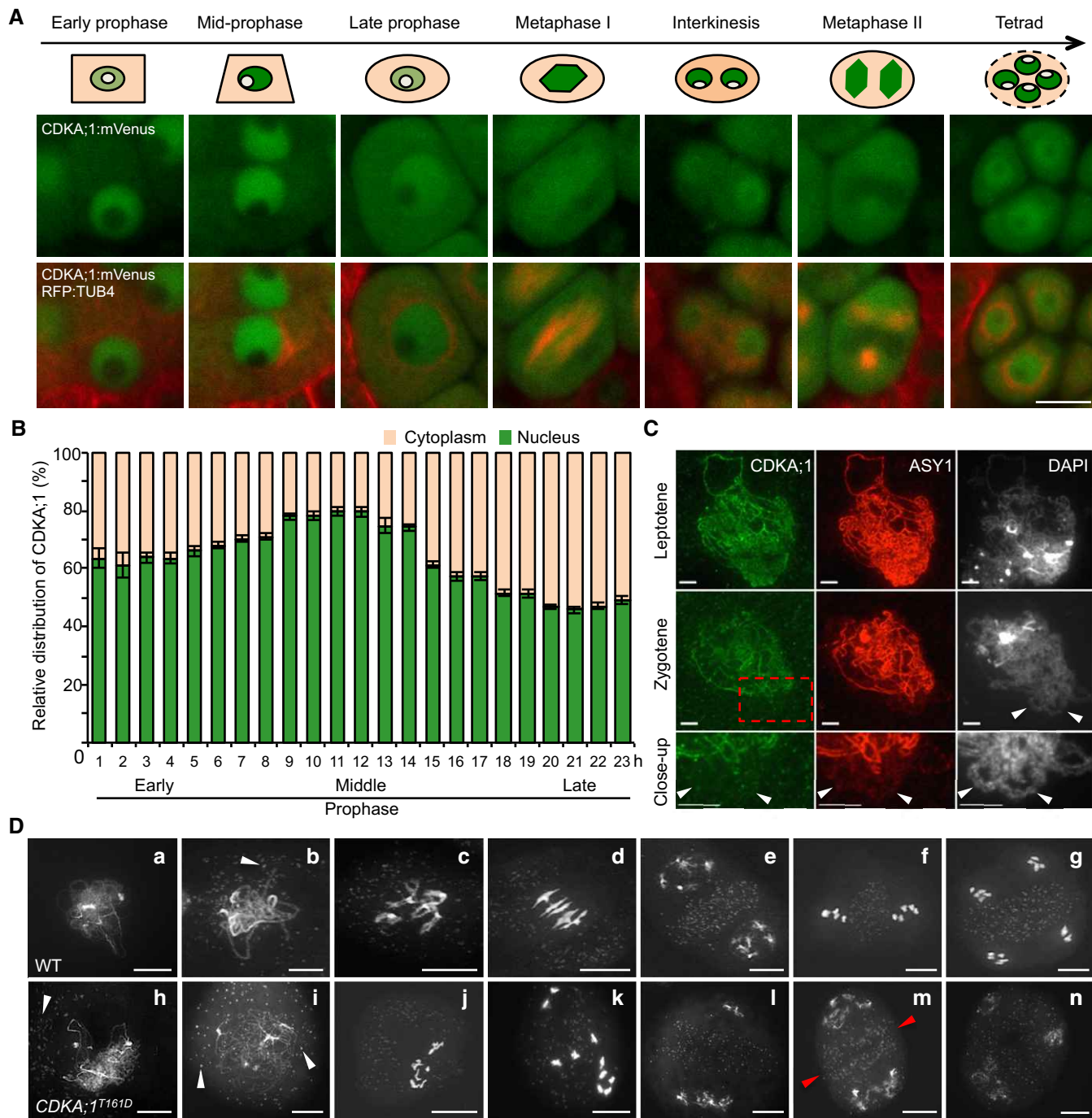
Figure 1. Changes in CDKA;1 distribution and meiotic defects in hypomorphic *cdka;1* mutants in male meiocytes.

A   Confocal laser scanning micrographs showing the localization of a functional CDKA;1:mVenus fusion protein in the wild type (WT) and cartoons on top highlighting the changes in abundance of CDKA;1:mVenus in the nucleus and cytoplasm during the course of meiosis. The region colored in beige represents the cytoplasm, in green the nucleoplasm, and in white the nucleolus. Scale bar: 10 μm.

B   Quantitative analysis of the signal distribution of the nuclear versus cytoplasmic fraction of CDKA;1:mVenus during prophase I of meiosis as revealed by live cell imaging (Movie EV1). Twenty cells at each time point were used for the analysis. Error bars represent mean ± SD, and two biological replicates were performed.

C   Immunolocalization of CDKA;1 (green) and ASY1 (red) on spread chromosomes in leptotene and zygotene of wild-type plants expressing a functional *PRO_CDKA;1:CDKA;1: Strep* construct. The last lane shows a magnification of the region marked by the red rectangle. Arrowheads indicate synapsed regions of homologous chromosomes where CDKA;1 is no longer present. Scale bar: 5 μm.

D   Chromosome spread analysis of the wild type and the hypomorphic *cdka;1* mutant *CDKA;1^T161D*. (a, h) zygotene or zygotene-like stages; (b, i) pachytene or pachytene-like stages; (c, j, k) diakinesis or diakinesis-like stages; (d) metaphase I; (e, i, m, n) end of meiosis I with two (e, m) or three (i) pools of chromosomes; (f) metaphase II; and (g) tetrad. Red arrowheads indicate the initiated formation of a phragmoplast. White arrowheads depict mitochondria. Scale bars: 10 μm.

of meiosis especially for chromosome synapsis and bivalent formation.

Phosphorylation of ASY1 by CDKA;1 promotes its recruitment to the chromosome axis

Since in particular chromosome synapsis was affected in the weak loss-of-function *cdka;1* mutants, we searched for possible phosphorylation targets of CDKA;1 involved in early chromosome engagement. Several meiotic regulators in yeast have been found to contain [S/T]P Cdk consensus phosphorylation sites (Zhu *et al*, 2010). Many of these regulators have homologs in *Arabidopsis* also harboring Cdk consensus sites.

At the top of our list of putative CDKA;1 substrates was the *Arabidopsis* Hop1 homolog ASY1, especially also since *asy1* mutants are known to be asynaptic, hence partially resembling the phenotype of the hypomorphic *cdka;1* mutants (Armstrong, 2002). Moreover, a previous study identified the ASY1 ortholog of Brassica oleracea as a potential *in vivo* ATM/ATR and CDK phosphorylation target (Osman *et al*, 2017). In addition, Hop1 was found to be phosphorylated by Cdc28 in an *in vitro* screen for Cdk substrates in budding yeast (Ubersax *et al*, 2003), but the functional importance of the phosphorylation in both *Brassica* and yeast has remained unknown.

The above-mentioned spatiotemporal co-localization of ASY1 with CDKA;1 on chromosomes revealed by immunolocalization is consistent with the idea that ASY1 could be a phosphorylation target of CDKA;1 (Fig 1C). To further test this, we generated two functional reporters for *ASY1* (PRO_{ASY1}:ASY1:GFP and PRO_{ASY1}:ASY1:RFP), which both restored a wild type-like meiotic program when expressed in homozygous *asy1* mutants (Appendix Fig S1A and C). As expected, and confirming our above-presented and previous immuno-detection studies (Ferdous *et al*, 2012; Lambing *et al*, 2015), ASY1 localizes to the chromosome axis at leptotene and is depleted during zygotene when the synaptonemal complex is formed as revealed by the concomitant analysis of ASY1:RFP together with a PRO_{ZYP1B}:ZYP1B:GFP reporter (Figs 2A and EV2A).

To explore a possible regulation of ASY1 by CDKA;1, we introgressed the ASY1:GFP reporter into the weak *cdka;1* loss-of-function allele $CDKA;1^{T161D}$. In wild-type male meiocytes at late G2, numerous foci and short stretches of ASY1 signal were present ($n = 18$ out of 20 male meiocytes analyzed). The meiotic stage was determined by four morphological criteria: The squared cell shape of meiocytes, the centered position of the nucleolus, the chromosome axis being labeled by a previously generated functional *ASY3* reporter (PRO_{ASY3}:ASY3:RFP), and the finding that tapetum cells were still single-nucleated (Wang *et al*, 2004; Yang *et al*, 2006; Stronghill *et al*, 2014; Prusicki *et al*, 2019). In contrast, only a diffuse ASY1:GFP signal without any foci could be detected in the nuclei of meiocytes of $CDKA;1^{T161D}$ plants (25 out of 25) at a moment when ASY3 forms foci and short stretches (Fig 2A). This diffuse signal of ASY1:GFP in $CDKA;1^{T161D}$ persisted until early leptotene (19 out of 21), as judged by the beginning of the migration of the nucleolus toward one side of the nucleus and the appearance of ASY3 in threads. At this stage, a linear ASY1 signal co-localizes with ASY3 along chromosomes in the wild type (23 out 23; Fig 2A). In late leptotene, as seen by docking of the nucleolus to one side of the nucleus, the ASY1:GFP signal in $CDKA;1^{T161D}$ (30 out of 30) was found to associate with chromosomes indistinguishable from the wild type (28 out

28), indicating a delayed assembly of ASY1 on chromosomes in $CDKA;1^{T161D}$ (Fig 2A).

To test whether ASY1 can be directly phosphorylated by CDKA;1, we performed *in vitro* kinase assays. To this end, we expressed and purified ASY1 from baculovirus-infected insect cells and incubated it with three meiotic CDK–cyclin complexes. This revealed that ASY1 is phosphorylated by CDKA;1-SDS and CDKA;1-TAM but not by CDKA;1-CYCA3;1 *in vitro* (Fig 2B). Since the kinase reaction without added CDK–cyclin complexes showed background phosphorylation, likely due to co-purification of kinases from insect cells, we expressed ASY1 in *Escherichia coli* and subjected the purified protein to CDKA;1-SDS complexes. Subsequent mass spectrometry analyses showed that two sites (T142 and T535) out of the five CDKA;1 consensus phosphorylation sites in ASY1 are targeted by CDKA;1-SDS; in this case, no phosphorylated peptides were found in the reactions without CDKA;1 (Fig 3A and Appendix Fig S2A).

To address the relevance of the phosphorylation sites *in vivo*, we then generated different non-phosphorylatable and phosphorylation-mimicking variants of these five CDKA;1 consensus phosphorylation sites based on the ASY1:GFP construct. These constructs were then introduced into *asy1* mutants harboring the *ASY3:RFP* reporter (PRO_{ASY3}:ASY3:RFP; Table 1 and Fig EV3A). ASY3 is known to be recruited to the chromosome axis prior to ASY1 and present on chromosomes from early leptotene until pachytene (Ferdous *et al*, 2012). Consistent with its chromosomal loading being independent of ASY1, the expression and localization of ASY3 was unaffected in plants harboring different ASY1 variants and hence was used in the following as a marker for staging of meiosis (Fig 3B).

Similar to wild-type ASY1, the triple non-phosphorylatable mutant (ASY1^{3V}), i.e., ASY1 harboring the three amino acid substitutions T365V, S382V, T535V, and even the quadruple non-phosphorylatable mutant ASY1^{4V} (T184V, T365V, S382V, T535V) fully complemented the defects of *asy1*, e.g., pollen abortion, short silique length, and reduced seed set (Table 1 and Fig EV3B–F). Matching their complementing functionality, ASY1^{3V}:GFP and ASY1^{4V}:GFP localized on chromosomes similar to ASY1:GFP that associated with chromosomes at leptotene and progressively dissociated again upon synapsis during zygotene and pachytene, while ASY3 still remained localized to the chromosomes (Fig EV2B).

In contrast, the quintuple non-phosphorylatable mutant ASY1^{5V} (T142V, T184V, T365V, S382V, T535V) did not properly localize to chromosomes (Fig EV2B). Resembling *asy1* null mutants, no clear chromosomal threads were observed in ASY1^{5V} plants, which were also strongly reduced in fertility (Table 1, Figs EV2B and EV3B–F). This result suggested that the *in vitro* identified CDKA;1 phosphorylation site T142 in the HORMA domain is crucial for the chromosome association of ASY1. In support of this hypothesis, we found that the single non-phosphorylatable mutant (ASY1^{T142V} in *asy1*) only partially complemented *asy1*, and in contrast with the wild-type version of ASY1, ASY1^{T142V}:GFP showed compromised chromosome association during leptotene and exhibited a diffuse and nucleoplasmic signal (Fig 3B–D, Table 1, and Fig EV3B–F). We also frequently observed only partially synapsed homologous chromosomes in ASY1^{T142V} plants (Fig 3E and Appendix Fig S3).

An exchange of T142 to serine (ASY1^{T142S}), that maintains the CDKA;1 phosphorylation site, did not result in compromised ASY1 function and expression of this construct fully rescued *asy1* mutants (Figs 3B and EV3B–F). Moreover, the expression of the
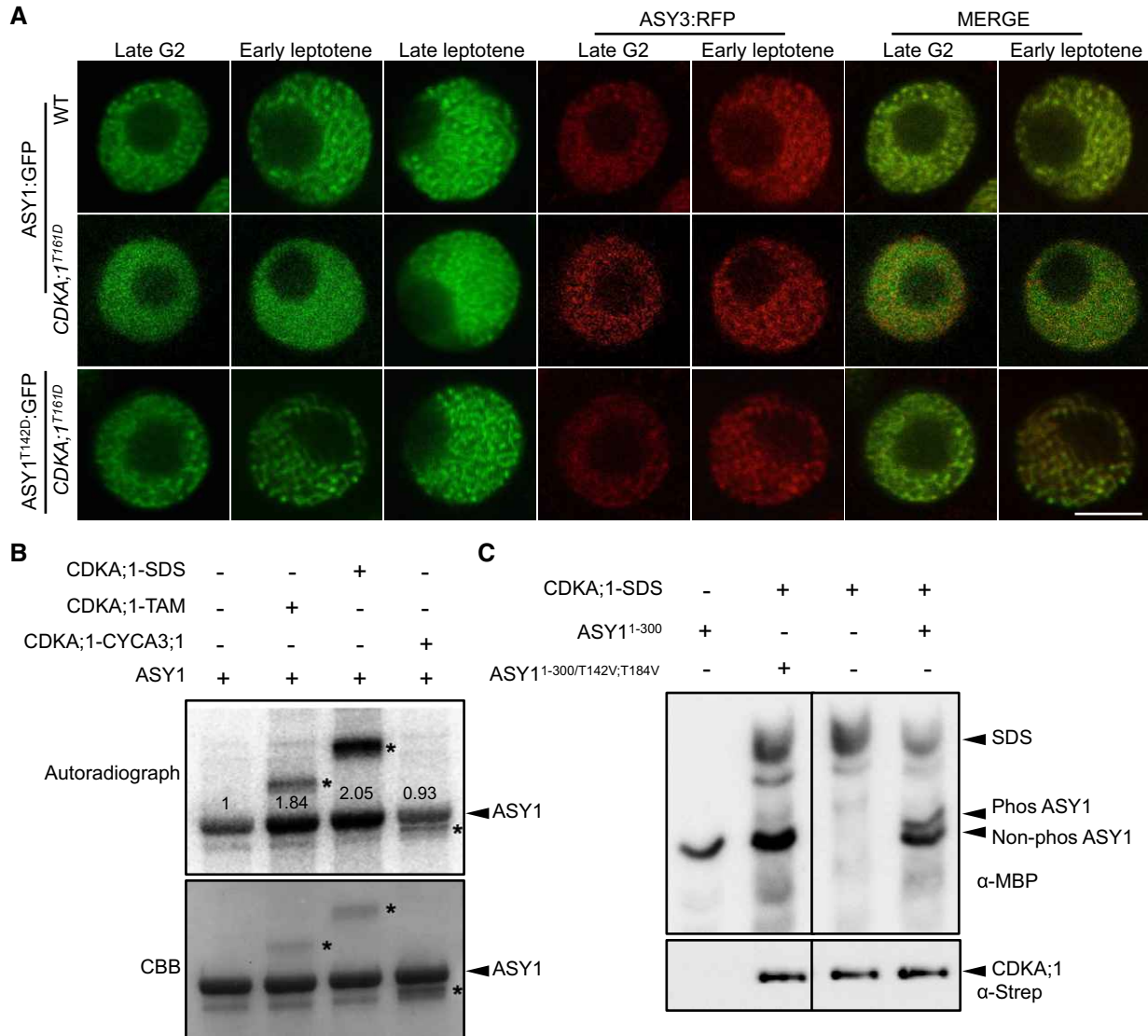
Figure 2. ASY1 is a phosphorylation target of CDKA;1.

A ASY1:GFP and ASY1^{T142D}:GFP localization in late G2 and leptotene of male meiocytes of the wild-type and *CDKA;1^{T161D}* mutants. ASY3:RFP, highlighting chromosomes, was used as a marker for the staging of meiosis. Scale bar: 5 µm.

B Kinase assays of CDKA;1-SDS, CDKA;1-TAM, and CDKA;1-CYCA3;1 complexes using ASY1 purified from baculovirus-infected insect cells as a substrate. The upper panel shows the autoradiograph. The control reaction without CDKA;1–cyclin complex indicates a background activity co-purified from insect cells. The lower panel indicates protein loading by Coomassie Brilliant Blue (CBB) staining. Arrowheads indicate ASY1 proteins, and asterisks depict the relevant cyclin used which also gets phosphorylated in the assay. Numbers indicate the relative intensities of ASY1 bands.

C The upper panel shows a phos-tag gel analysis of ASY1$^{1–300}$ and ASY1$^{1–300/T142V;T184V}$ with and without CDKA;1-SDS kinase complexes using an anti-MBP antibody. The lower panel denotes loading of CDKA;1 using an anti-Strep antibody. Arrowheads represent the proteins as indicated.

Source data are available online for this figure.

phosphorylation-mimicking variant ASY1^{T142D} fully restored meiosis and fertility of *asy1* mutants indicating that most likely the charge and not the structure of the amino acid at position 142 is important for ASY1 function (Figs 3B and EV3B–F). Furthermore, the delayed assembly of ASY1 in *CDKA;1^{T161D}* was reverted to a wild-type pattern when the phosphorylation-mimicking mutation ASY1^{T142D} was expressed in *CDKA;1^{T161D}* (Fig 2A).

Exploring the regulation of ASY1 phosphorylation further, we found that the double non-phosphorylatable mutant T142V, T184V

(ASY1$^{T142V;T184V}$) enhanced the *ASY1^{T142V}* mutant phenotype and was indistinguishable from *asy1* indicating a complete loss of function reminiscent of *ASY1^{5V}* (Figs 3B and EV3B–F, and Appendix Fig S7). Consistently, the N-terminal half of ASY1 in which the phosphorylation sites T142 and T184 were mutated (ASY1$^{1-300/T142V;T184V}$) was no longer phosphorylated by a CDKA;1-SDS complex *in vitro* confirming their specificity as CDKA;1 phosphorylation sites (Fig 2C).

Since no obvious localization defects, especially in leptotene, and no mutant phenotype were found in *asy1* mutants expressing the
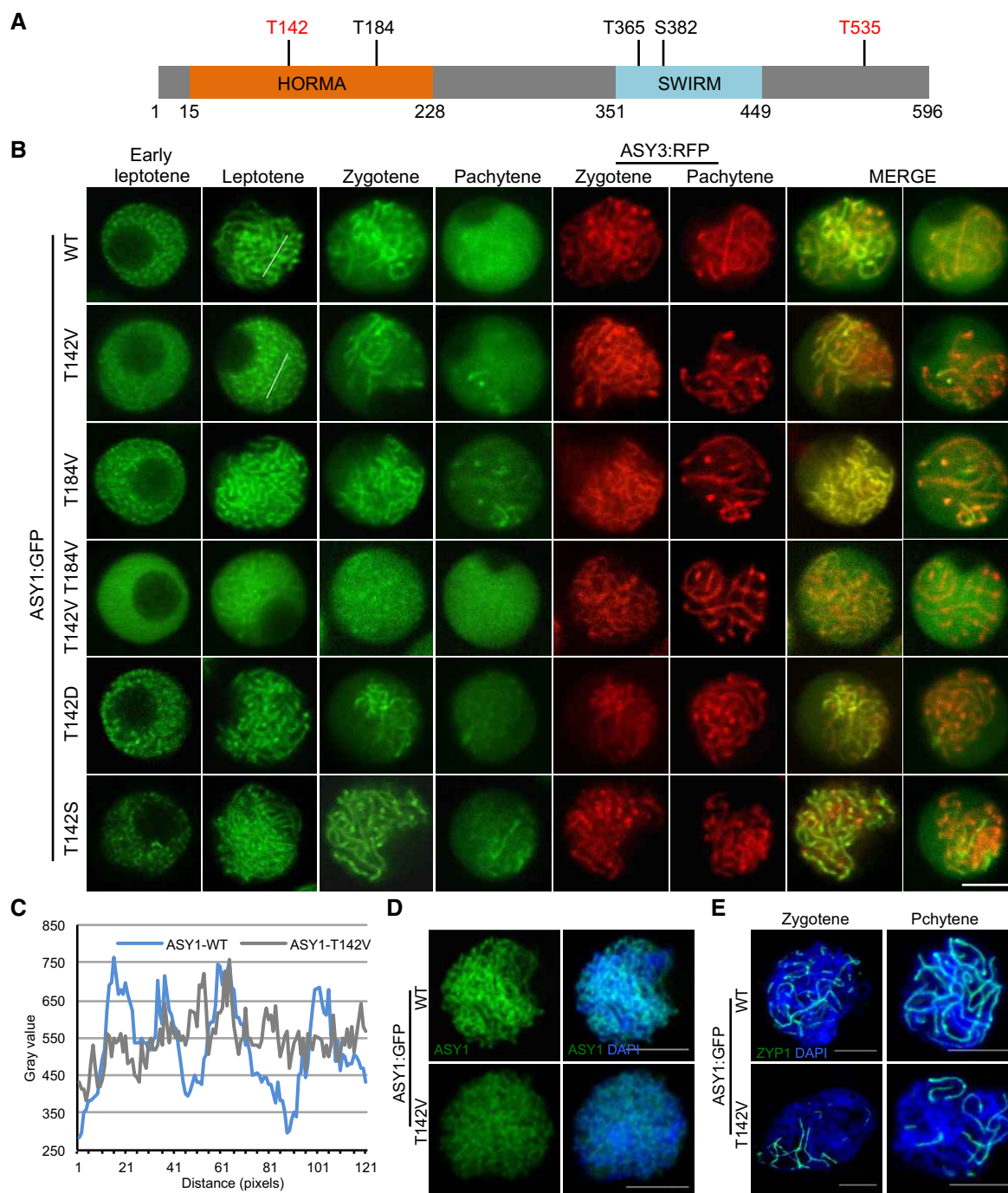
Figure 3. Phosphorylation of ASY1 is essential for its chromosomal localization.

A   Schematic representation of ASY1 with the five predicted consensus Cdk phosphorylation sites. The sites found to be phosphorylated *in vitro* by CDKA;1-SDS complexes are highlighted in red (Appendix Fig S4A).

B   Localization patterns of different ASY1:GFP variants together with ASY3:RFP (for staging of zygotene and pachytene) in a *asy1* mutant background during prophase I. Scale bar: 5 µm.

C   Signal distribution profiles of ASY1:GFP and ASY1^T142V:GFP at leptotene as shown in (B). The regions used for analysis are highlighted by white lines in respective panels in (B). The many small peaks with low amplitude in *ASY1^T142V:GFP* indicate diffused localization as opposed to the clear peaks seen in the wild type.

D, E   Immunolocalization of ASY1 (D) and ZYP1 (E) in *ASY1:GFP* (*asy1*) and *ASY1^T142V:GFP* (*asy1*) plants using anti-GFP and anti-ZYP1 antibodies, respectively. DNA was stained with DAPI (blue). Scale bars: 5 µm.

Table 1. Summary of the phenotypic analysis of ASY1 variants.

Construct	Chromosome association	Background	Seed/silique	Pollen viability (%)
–	–	Wild type	58.35 ± 1.75^a	99.32 ± 0.49^a
–	–	*asy1*	9 ± 1.2^b	55.57 ± 2.55^b
ASY1	Correct	*asy1*	58.75 ± 2.32^a	99.26 ± 0.63^a
ASY1^{T142V}	Compromised	*asy1*	41 ± 2.5^c	81.87 ± 2.35^c
ASY1^{T184V}	Correct	*asy1*	57.78 ± 2.5^a	99.24 ± 0.27^a
ASY1$^{T142V;T184V}$	Largely lost	*asy1*	9.78 ± 1.8^b	59.72 ± 2.27^b
ASY1^{3V}	Correct	*asy1*	57.75 ± 1.83^a	99.38 ± 0.4^a
ASY1^{4V}	Correct	*asy1*	58.15 ± 1.96^a	99.04 ± 0.25^a
ASY1^{5V}	Largely lost	*asy1*	9 ± 1.41^b	55.86 ± 3.57^b
ASY1^{T142D}	Correct	*asy1*	57.95 ± 2.3^a	99.21 ± 0.23^a
ASY1^{T142S}	Correct	*asy1*	56 ± 2.96^a	98.19 ± 0.9^a

The level of significance ($P < 0.05$) is indicated by different letters between the wild-type and ASY1 variants as determined by the one-way ANOVA followed by Turkey's test.

single non-phosphorylatable mutant *ASY1^{T184V}* (Figs 3B and EV3B–F), we conclude that T142 in the HORMA domain is the major site of ASY1 phosphorylation regulation with the site T184 likely having an ancillary role.

Phosphorylation of ASY1 increases its binding affinity with ASY3

The failure of the double non-phosphorylatable mutant protein ASY1$^{T142V;T184V}$ to associate with chromosomes is reminiscent of the localization defects of ASY1 in *asy3* mutants (Figs 3B and EV2C; Ferdous *et al*, 2012). Therefore, we reasoned that the phosphorylation of ASY1 may control its interaction with ASY3. The first 300 amino acids of ASY1 (ASY1$^{1–300}$), which include the HORMA domain, essential for the protein–protein interaction of Hop1 with Red1 (Muniyappa *et al*, 2014; Rosenberg & Corbett, 2015), were found to interact with ASY3 in a yeast two-hybrid assay consistent with earlier results (Ferdous *et al*, 2012). While no obvious effect of ASY1$^{1–300/T184V}$ on the interaction capacities with ASY3 was observed, we found that the binding of ASY1$^{1–300/T142V}$ to ASY3 was strongly decreased, yet not fully abolished, since yeast cells harboring ASY1$^{1–300/T142V}$ and ASY3 cannot grow on the stringent selection media (without histidine and adenine) but do survive on the less stringent media (without histidine; Fig 4A). The interaction with ASY3 was even further reduced in the ASY1$^{1–300/T142V;T184V}$ variant (Fig 4A). Conversely, the phosphorylation site exchange mutant ASY1$^{1–300/T142S}$ and the phosphorylation-mimicking mutant ASY1$^{1–300/T142D}$ interacted with ASY3 to a similar extent as the non-mutated version of ASY1 (Fig 4A). These findings were not due to protein expression levels since we found that non-phosphorylatable mutant versions of ASY1 were even more abundantly present in yeast cells than the non-mutated version (Appendix Fig S2C). These results also suggested that ASY1 was phosphorylated in yeast cells, likely on residue T142. Indeed, the phosphorylation of ASY1 in yeast was confirmed by phos-tag SDS–PAGE (Appendix Fig S2D).

The importance of T142 phosphorylation in ASY1 for the interaction with ASY3 was confirmed by GST pull down assay using recombinant proteins purified from *E. coli*. Similar to the results

from yeast two-hybrid assay, we found that the non-phosphorylated ASY1 (ASY1$^{1–300}$ and ASY1$^{1–300/T142V;T184V}$) had only a residual interaction capacity with ASY3. However, the phosphorylation-mimicking version ASY1$^{1–300/T142D}$ showed enhanced affinity toward ASY3 (Fig 4B and C).

Finally, we addressed whether and if so to what degree the altered interaction of ASY1$^{1–300/T142V}$ with ASY3 in our yeast two-hybrid experiment depends on the exchanged amino acid, i.e., Val, itself. To this end, we tested additional ASY1 variants in which we substituted T142 and T184 with Gly and Ala. Consistent with the Val substitution at T142, we found that the mutations of both ASY1$^{1–300/T142A}$ and ASY1$^{1–300/T142G}$ strongly reduced the interaction with ASY3 (Fig EV4A). The mutation of ASY1$^{1–300/T142A;T184A}$ further reduced the interaction of ASY1$^{1–300/T142A}$ with ASY3 similarly to the ASY1$^{1–300/T142V;T184V}$ mutant (Fig EV4A). These results were not attributed to protein expression levels since we found that all non-phosphorylatable mutant versions of ASY1 were not less abundant in yeast cells than the wild-type version (Appendix Fig S2E). These findings show that a reduced interaction between ASY1 and ASY3 in a yeast two-hybrid system does not depend on a specific amino acid used for substitution and corroborate that the phosphorylation of ASY1 at T142 is important for its binding to ASY3.

Notably, while ASY1$^{1–300/T184V}$ does not show any obvious reduction in binding with ASY3, the substitution of T184 to A (ASY1$^{1–300/T184A}$) largely reduced the interaction, and ASY1$^{1-300/T184G}$ did not interact at all with ASY3 in our assays anymore (Fig EV4A). Since we did not find T184 to be phosphorylated *in vitro*, we cannot judge at the moment whether T184 is structurally a very important position and does not tolerate small amino acids and/or whether T184 is, possibly very transiently, phosphorylated *in vivo*.

Phosphorylation of ASY1 counteracts the action of PCH2 in early but not late prophase

For the synaptonemal complex to be formed, ASY1 has to be depleted from synaptic regions at zygotene mediated by the conserved AAA$^+$ ATPase PCH2 (Ferdous *et al*, 2012; Lambing *et al*,

96
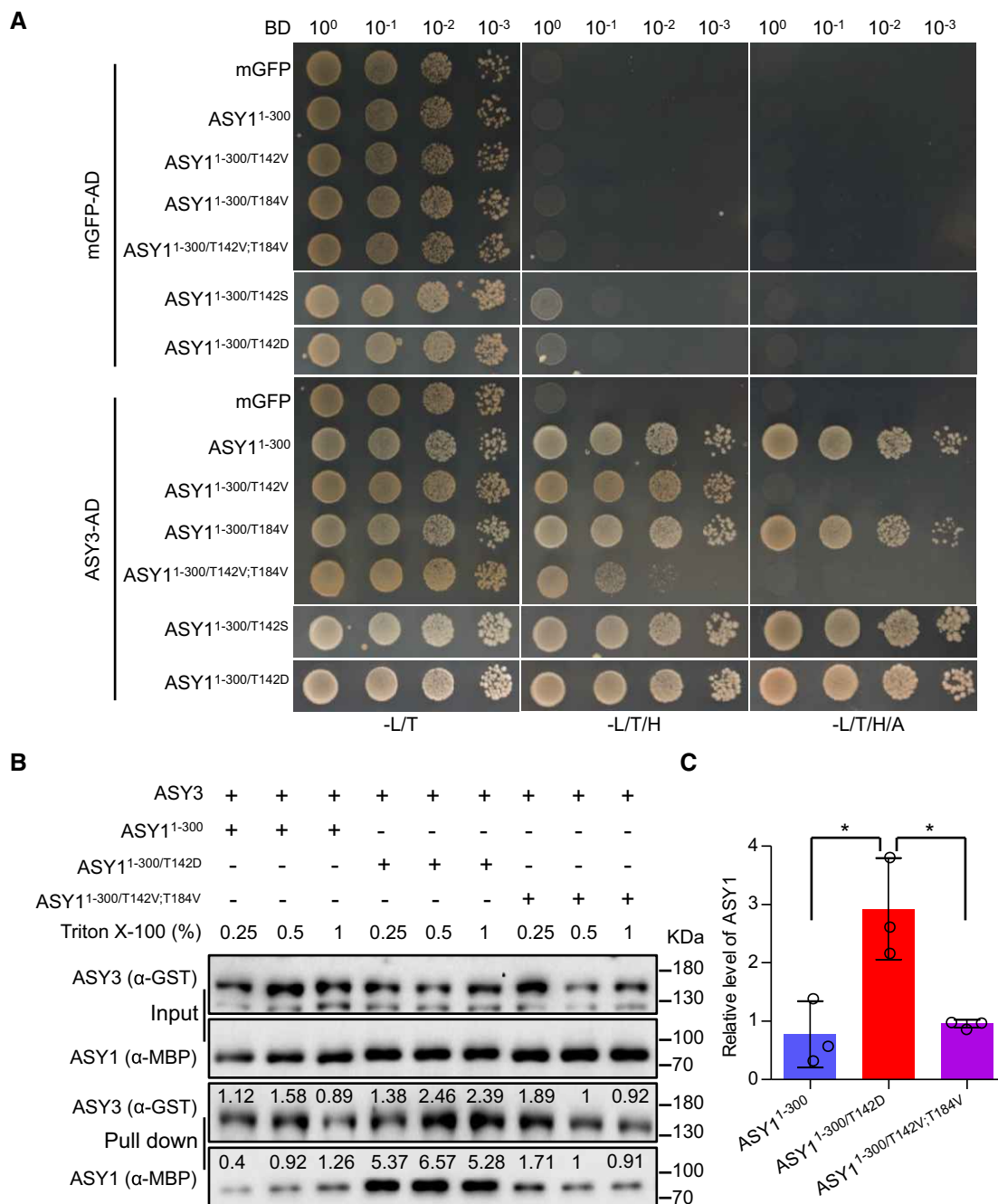
Figure 4. A negative charge at T142 in the HORMA domain of ASY1 promotes its interaction with ASY3.

A Yeast two-hybrid interaction assays of ASY3 with different ASY1 variants. Monomeric GFP (mGFP) fused with AD (activating domain) and BD (binding domain) were used as controls. Yeast cells harboring both the AD and BD plasmids were grown on synthetic medium supplied with glucose in the absence of Leu and Trp (-L/T, left panel), on synthetic dropout (SD) medium in the absence of Leu, Trp, and His (-L/T/H, middle panel), and on SD medium in the absence of Leu, Trp, His and Ade (-L/T/H/A, right panel). Yeast cells were incubated until OD$_{600}$ = 1 and then diluted 10-, 100-, and 1,000-fold for the assays.

B GST pull down of ASY3 with different ASY1 variants. The numbers above the bands show the relative intensity of the bands. The input and pull down fractions were analyzed by immuno-blotting with the anti-GST (ASY3) and anti-MBP (ASY1) antibodies.

C Quantification of the pull down fractions of ASY1 as shown in (B). The band intensity in the pull down of ASY1$^{1–300/T142V;T184V}$ at a Triton X-100 concentration of 0.5% was defined as 1. The relative amount of ASY1 in the pull down fractions was normalized by the band intensity of the pulled down ASY3 fraction. The average band intensity of ASY1 at different concentrations of Triton X-100 used was plotted. Asterisks indicate significant difference (two-tailed *t*-test, *P* < 0.05). Error bars represent mean ± SD, and two biological replicates were performed.

2015). Therefore, we asked whether the phosphorylation status of ASY1 also affects its removal by PCH2. However, the phosphorylation-mimicking version ASY1^{T142D} was equally well depleted from chromosomes as the non-mutated version of ASY1 (Fig 3B). Conversely, we introduced the non-phosphorylatable version ASY1$^{T142V;T184V}$ into *pch2* mutants to ask whether the loss of the chromosomal association of the ASY1$^{T142V;T184V}$ was affected by PCH2.

Strikingly, while ASY1$^{T142V;T184V}$ could not properly localize to chromosomes in both *asy1* mutant and a wild-type background (see above, Figs 3B and 5A), the localization pattern of ASY1$^{T142V;T184V}$:GFP in *pch2* was nearly identical to the pattern of the non-mutated version of ASY1 in leptotene (Fig 5A). This observation suggests a so far not recognized function of PCH2 in counteracting the recruitment of ASY1 to ASY3 in leptotene when ASY1 needs to assemble on the chromosomes (see below). This early function of PCH2 for the regulation of the chromosome assembly of ASY1 at leptotene was further corroborated by the finding that although ASY1$^{T142V;T184V}$:GFP could not rescue the fertility reduction of *asy1* mutants, it largely complemented the fertility of *asy1 pch2* double mutants to the level of *pch2* single mutants (Fig 5B). This result also suggested that ASY1$^{T142V;T184V}$:GFP is largely functional as long as it can be localized on chromosomes. The finding that ASY1$^{T142V;T184V}$ in a *pch2* mutant background stays tightly associated with the chromosomes at both zygotene and pachytene when ASY1 in wild-type plants is already largely removed from the synaptic chromosomes, underlines the key role of PCH2 for the late release, which we conclude is independent of the CDKA;1-dependent phosphorylation status of ASY1 (Figs 3B and 5A).

To further explore the new finding of an early function of PCH2, we generated a functional genomic reporter line for *PCH2* (*PRO$_{PCH2}$: PCH2:GFP*) which revealed that PCH2 is already present in male meiocytes from pre-meiosis throughout prophase I (Fig 5D, Appendix S1B and D). This observation implies the necessity of a mechanism for counteracting the releasing force of PCH2 on ASY1 at early leptotene, which we speculate to be the here-discovered phosphorylation of ASY1.

To elaborate on a possible early function of PCH2, we introduced the non-mutated functional *ASY1:GFP* reporter into *pch2* mutants. While ASY1:GFP is exclusively localized to the nucleus and chromosomes in a wild-type background, we found that the same reporter was not only present in the nucleus but also strongly accumulated in the cytoplasm in *pch2* mutants (Fig 5C). Revisiting the non-phosphorylatable mutant localization ASY1$^{T142V;T184V}$:GFP in *pch2*, we also observed that it accumulates cytoplasmically (Fig 5C). Interestingly, we noted that the signal intensities of both ASY1:GFP and ASY1$^{T142V;T184V}$:GFP in the nucleus of *pch2* mutants appeared to be weaker than that of ASY1:GFP in the wild type (Fig 5C). Thus, we conclude that PCH2 directly or indirectly facilitates the nuclear accumulation of ASY1 in early meiosis, a function that is consistent with the presence of PCH2 in the cytoplasm at that time (Fig 5D).

Taken together, these observations suggest that PCH2 has at least three, possibly interconnected functions. In early leptotene, it promotes the release of the non-phosphorylated ASY1 from chromosomes and ASY1 phosphorylation in the HORMA domain antagonizes this PCH2 activity by increasing the binding affinity of ASY1 with ASY3. At the same time, PCH2 helps ASY1 to accumulate in the nucleus. Later in zygotene and pachytene, PCH2 removes ASY1,

as shown in previous publications, in a fashion that appears to not depend on its phosphorylation (Lambing *et al*, 2015).

Self-assembly of ASY1 through its C-terminal closure motif is affected by the phosphorylation in the HORMA domain

The chromosomal localization of the meiotic HORMA domain proteins (HORMADs) including the budding yeast Hop1, mammalian HORMAD1 and HORMAD2, and *Caenorhabditis elegans* HORMADs (HTP-1, HTP-2, HTP-3, and HIM3) was recently shown to depend on at least two mechanisms, the initial recruitment by its binding partners such as Red1 in yeast, and the putative self-assembly through its N-terminal HORMA domain-C-terminal closure motif interactions (Smith & Roeder, 1997; Wojtasz *et al*, 2009; Kim *et al*, 2014; West *et al*, 2018). Hence, we asked whether the phosphorylation by CDKA;1 would also affect a possible self-assembly mechanism of ASY1.

To explore this possibility, we first tested whether the self-assembly is also conserved in *Arabidopsis* by using yeast two-hybrid assays. We found that ASY1 binds to itself and mapped this interaction to the HORMA domain of ASY1 making contact with the very C-terminus of ASY1 (residues 571–596), strongly suggesting that ASY1 likely possesses a C-terminal closure motif as its orthologs in yeast, *C. elegans*, and mammals (Fig 6A and B). While this work was in progress, West *et al* (2019) also independently identified the closure motif of ASY1 as being located in the same region as here revealed by us. Deletion of the closure motif of ASY1 in the *ASY1: GFP* reporter construct (ASY1$^{1-570}$:GFP) almost abolished its chromosome association, indicating the necessity of the closure motif for its correct localization pattern (Fig 5C). At the same time, we also observed that ASY1$^{1-570}$:GFP accumulated in the cytoplasm demonstrating that the nuclear targeting of ASY1 is also compromised in this version. Next, we asked whether the compromised chromosome association of ASY1$^{1-570}$:GFP depends on PCH2. Remarkably, the chromosome localization of ASY1$^{1-570}$:GFP was largely recovered (Fig 5C), when the *ASY1$^{1-570}$:GFP* reporter was introduced into *pch2* mutant. This suggests that the closure motif is also important for antagonizing the releasing force of PCH2, presumably via the self-oligomerization during chromosome axis formation.

We also noticed in our yeast two-hybrid assays that the full-length ASY1 could not interact with ASY3 (Fig 6B). This is consistent with previous studies that show that full-length Hop1 has a very low affinity toward Red1 *in vitro* (West *et al*, 2018). However, strong interaction with ASY3 was found when the closure motif was depleted (ASY1$^{1-570}$; Fig 6B).

Finally, we tested the interaction of the different mutant variants of the ASY1 HORMA domain with the above-identified closure motif and found that the affinity of ASY1$^{1-300/T142V}$ and ASY1$^{1-300/T142V;T184V}$ to the closure motif was dramatically reduced. Conversely, the phosphorylation-mimicking version ASY1^{T142D} showed higher interaction strength despite a slight decrease compared to that of the non-mutated ASY1 version (Fig 6C). These data suggest that the phosphorylation of the ASY1 HORMA domain regulates its chromosomal assembly not only by enhancing the affinity to ASY3 but also by promoting the potential self-assembly along the chromosomes. Thus, the phosphorylation of ASY1 by CDKA;1 appears to represent a two-pronged mechanism for the faithful loading of ASY1 to the chromosome axis.
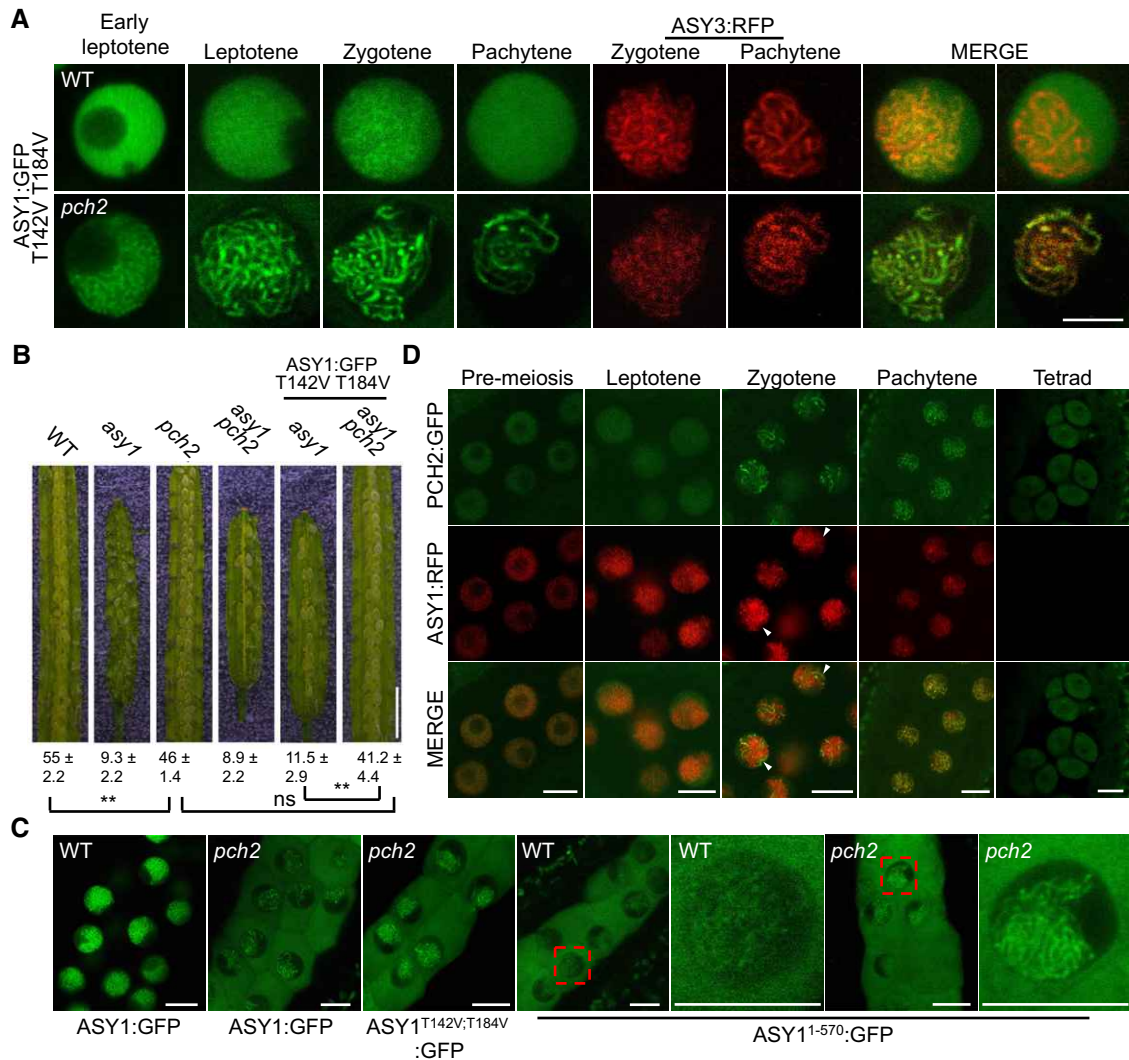
Figure 5. Phosphorylation of ASY1 counteracts the action of PCH2 in early prophase.

A Localization patterns of ASY1$^{T142V;T184V}$:GFP together with ASY3-RFP in the wild-type and *pch2* mutants. Please note that images of ASY1$^{T142V;T184V}$:GFP in *pch2* mutants were taken with increased sensitivity for a better visibility. Scale bar: 5 μm.

B Seed sets (mean ± SD, *n* = 5) of WT, *asy1*, *pch2*, *asy1 pch2*, *ASY1$^{T142V;T184V}$:GFP* (*asy1*), and *ASY1$^{T142V;T184V}$:GFP* (*asy1 pch2*) plants. Asterisks indicate significant differences (two-tailed *t*-test, *P* < 0.01), and ns depicts no significant difference. Scale bar: 2 mm.

C Localization patterns of ASY1:GFP, ASY1$^{T142V;T184V}$:GFP, and ASY1$^{1–570}$:GFP in the wild-type (WT) and/or in *pch2* mutant plants at early prophase I. Scale bars: 5 μm.

D Localization pattern of PCH2:GFP together with ASY1:RFP in the male meiocytes of wild type. Arrowheads indicate the chromosomal regions where the ASY1 removal was concomitant with the localization of PCH2. Scale bar: 10 μm.

Source data are available online for this figure.

Discussion

Cdks are known to be the major driving force of cell divisions (Morgan, 1997). Due to their requirement in mitosis, the study of Cdks in meiosis is challenging in multicellular organisms since meiosis usually takes place late during embryonic or postembryonic development, i.e., after several mitotic divisions. This is exemplified by the early embryonic lethality of Cdk1 mutants that precludes a straightforward functional analysis of Cdk1 in mouse meiocytes (Santamaría *et al*, 2007). By replacing Cdk1 with Cdk2 and by using conditional Cdk1 knock out mice, it was shown that Cdk1 is indeed key for meiosis in mammalian oocytes and cannot be substituted by

Cdk2 (Satyanarayana *et al*, 2008; Adhikari *et al*, 2012). However, it is still largely not clear how Cdk1 controls meiotic progression and what the phenotypic consequences of the loss of Cdk1 activity in meiosis are at the cellular level.

Since weak loss-of-function mutants in the *Arabidopsis* Cdk1/Cdk2 homolog *CDKA;1* are viable and produce flowers containing meiocytes (Dissmeyer *et al*, 2007, 2009), they represent a unique tool to study the requirement of Cdks in meiosis of a multicellular eukaryote. Exploiting these mutants, we find that in particular chromosome synapsis and bivalent formation are affected by reduced Cdk activity. However, the identification of Cdk targets in multicellular organisms is still challenging. Especially for specific tissues
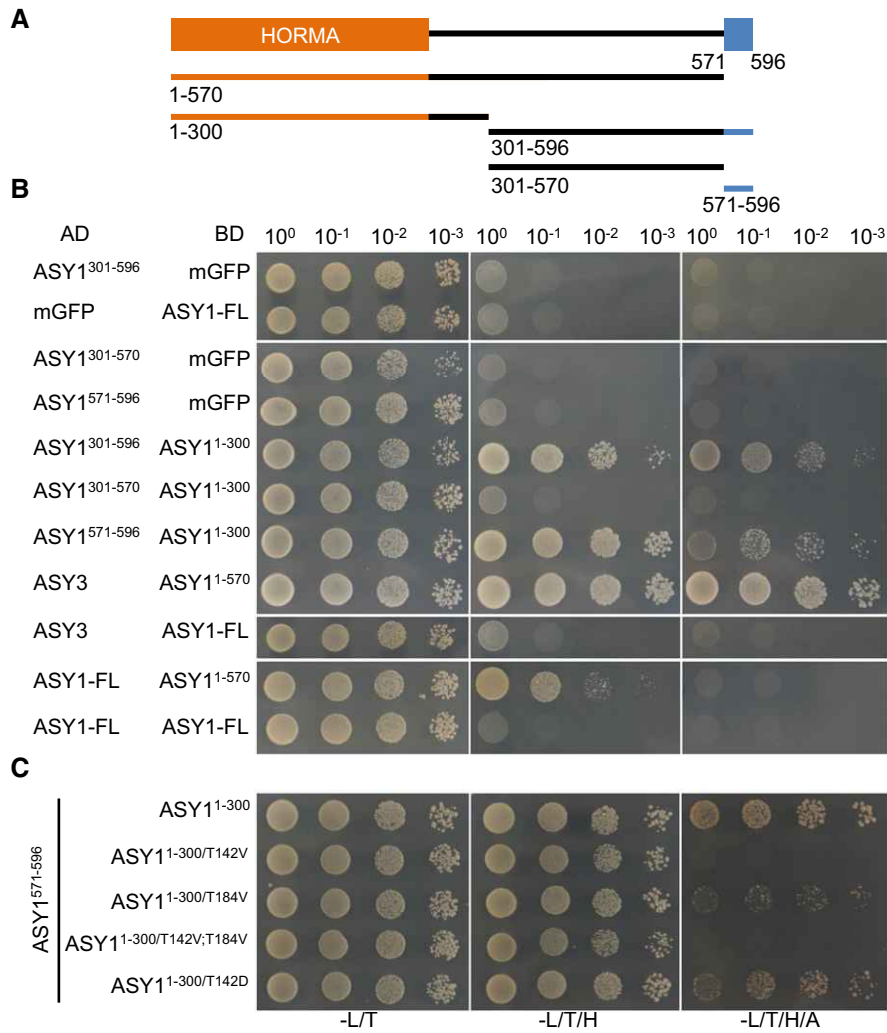
Figure 6. Phosphorylation of ASY1 affects its self-assembly.

A   Schematic graph of ASY1 full-length protein (aa 1–596). The HORMA domain is depicted in orange, and the presumptive closure motif is highlighted in blue. The lines below indicate the constructs used for yeast two-hybrid interaction assays.

B   Interaction assays of different ASY1 fragments (with and without the closure motif).

C   Interaction analysis of the ASY1 closure motif (ASY1$^{571-596}$) with different ASY1 HORMA domain variants.

such as meiocytes, and/or when phosphorylated proteins are only transiently present, the power of phosphoproteomics approaches and the identification of the phosphorylation sites *in vivo* are still limited. Combining genetic, cytological, and biochemical approaches, we have accumulated evidence, suggesting that the phosphorylation of ASY1 by CDKA;1 complexes is needed for the formation of the chromosome axis in meiosis. We show that T142 is very likely the key phosphorylation-dependent regulatory site, with T184 playing an ancillary role.

So far, the ASY1 homolog Hop1 has been found to be phosphorylated by Mec1/ATR and Tel1/ATM in budding yeast, which promotes DMC1-dependent interhomolog recombination without affecting the chromosomal association of Hop1 (Carballo *et al*, 2008). Orthologs of Hop1 in plants, e.g., ASY1 in *Arabidopsis* and PAIR2 in rice, harbor also ATM/ATR consensus phosphorylation sites ([S/T]Q), but whether an ATM/ATR-dependent

phosphorylation is functionally conserved in plants is still unclear. Given the finding that Hop1 can be also phosphorylated by Cdk complexes in budding yeast (Ubersax *et al*, 2003) and the presence of Cdk consensus phosphorylation sites in both HORMAD1 and HORMAD2 proteins of human and mouse, it is tempting to speculate that the here-revealed phosphorylation regulation of ASY1, needed for its chromosome localization, is conserved among eukaryotes.

The role of ASY1 phosphorylation by CDKA;1

Combining our CDKA;1 localization data with the molecular and biochemical analysis of ASY1 phosphorylation, we propose a model of how CDKA;1 regulates ASY1 (Fig 7). At early prophase I, CDKA;1 changes from a distribution of approximately 40% versus 60% in the cytoplasm and nucleus to a prominently nuclear localization (~80%), likely promoted by a meiotic cyclin such as SDS. In the

100

nucleus, CDKA;1 phosphorylates ASY1 and by that enhances its binding affinity with ASY3. It is possible that CDKA;1 acts directly at the chromosome axis based on our immunolocalization data (Fig 1C). The related kinases Cdk2 from mammals and Cdc28 from budding yeast have both been found to localize to chromatin, too (Ashley *et al*, 2001; Zhu *et al*, 2010). However, these two kinases show a punctuate localization pattern, while CDKA;1 has more continuous appearance along chromosome axis resembling the localization of ASY3 and ASY1 itself (Ashley *et al*, 2001; Armstrong, 2002; Ferdous *et al*, 2012).

The phosphorylation of ASY1 has several consequences. First, it enhances the affinity toward ASY3 promoting the recruitment of ASY1 to the chromosome axis. Second, it antagonizes a releasing force executed by PCH2, which is already present very early in meiosis. At the same time, PCH2 promotes the nuclear accumulation of ASY1 (Fig 7).

Moreover, the phosphorylation of ASY1 likely promotes the formation of ASY1 polymers similar to the proposed Hop1/HORMADs polymers in budding yeast *Saccharomyces cerevisiae* and *C. elegans*, that is likely essential for its chromosome localization (Kim *et al*, 2014; Rosenberg & Corbett, 2015; West *et al*, 2018). HORMA domain proteins, such as Hop1, have been shown to bind to closure motifs in partner proteins (West *et al*, 2018). This interaction is stabilized by the folding of the C-terminal safety belt region of the HORMA domain protein around this binding motif from the respective partner resulting in a so-called closed state. Meiotic HORMA domain proteins such as Hop1 contain themselves closure motifs and have been shown to bind to other HORMAD molecules and by that likely leading to HORMAD polymers along the

unsynapsed chromosome axes (Kim *et al*, 2014; West *et al*, 2018). These polymers are presumably anchored by binding to cohesin and/or axis proteins such as Red1/ASY3. However, the full-length *Arabidopsis* ASY1 (ASY1^{FL}) showed a very low affinity toward ASY3 in our yeast two-hybrid assays (Fig 6B). Similar findings were recently reported for Hop1 and Red1 *in vitro* (West *et al*, 2018). The binding capacity of ASY1 to ASY3 was strongly enhanced when the short C-terminal region of ASY1 including the presumptive closure motif was deleted (Fig 6B). These results argue that a full-length ASY1, at least when being expressed in yeast cells, is in a closed conformation being bound by its own closure motif in the C-terminus or by the closure motif from another ASY1. However, we could not detect any interaction of ASY1^{FL} to ASY1^{FL} using the yeast two-hybrid assay, suggesting that ASY1 tends to fold in a closed state through binding to its own closure motif at least when being expressed in yeast (Fig 6B). Assuming that the same holds true *in planta*, one needs to postulate that there is a factor that regulates the close-to-open state switch of ASY1. Our finding that ASY1 accumulates in the cytoplasm in *pch2* mutants suggests that PCH2 could have a function in converting ASY1 from the closed to the open state and at the same time probably avoiding the premature polymerization (in the cytoplasm) and providing a pool of available and reactive ASY1.

Mapping the ASY1 protein sequence onto the structure of *C. elegans* HIM-3 (c4trkA) using Phyre2 protein folding prediction shows that the T142 residue is likely located at the N-terminus of the alpha-C helix, a position just at the terminus of the long loop between beta-5 and alpha-C (Fig EV4B; Kim *et al*, 2014). Since this loop anchors the C-terminal safety belt in place, one idea might be
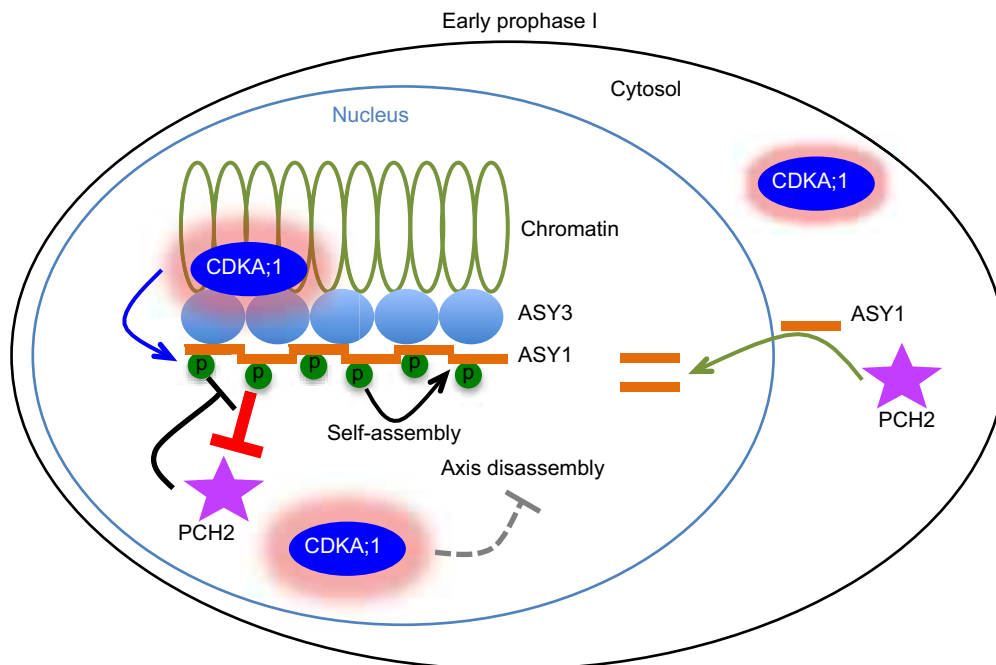
Figure 7. Model for the regulation of the chromosomal assembly of ASY1.

In early prophase I, ASY1 is expressed and imported into nucleus, facilitated by PCH2. Concomitantly, CDKA;1 becomes enriched in the nucleus, localizes on chromosomes, and phosphorylates ASY1. The phosphorylation enhances the binding affinity of ASY1 to ASY3 and the self-assembly and thus, in turn, antagonizes the releasing force of PCH2. At the same time, high CDKA;1 activity in the nucleus may block other axis disassembling factors that will be activated later in synapsed regions where CDKA;1 is not present.

that the phosphorylation of T142 imparts greater flexibility to the loop, and thereby may allow the safety belt to disengage, i.e., to "open" the protein and thus, allow the closure motif binding/dissociation (Kim *et al*, 2014; West *et al*, 2018).

When homologs synapse at zygotene and pachytene, ASY1 is displaced from chromosome axes by PCH2 and this removal is essential for completing chromosome synapsis and recombination (Lambing *et al*, 2015). Concomitantly with the ASY1 removal, the nuclear levels of CDKA;1 drop and CDKA;1 is also evicted from chromatin of synapsed regions (Fig 1A–C). Whether a possible drop in CDKA;1 activity in the nucleus is relevant for the removal of ASY1 is not clear. At least the phosphorylation-mimicking mutant ASY1^{T142D} can be released from chromatin indicating that the removal of ASY1 functions independently from its phosphorylation. This suggests either that an unknown regulator/cofactor of PCH2 exists, which enhances the activity of PCH2, or that PCH2 has a higher activity at synaptic regions. The latter is supported by the observation that while the PCH2 signal shows a diffuse nuclear localization before zygotene when ASY1 is assembled on the chromosome axis, it starts to accumulate specifically at the synaptic regions at zygotene coinciding with ASY1 removal. After that, PCH2 is largely present along the entire chromosomes at pachytene (Fig 5D). It is tempting to speculate that CDKA;1 might phosphorylate and by that inhibit an ASY1 disassembly factor (Fig 7). Hence, a reduction of CDKA;1 in the nucleus as seen here by live cell imaging could also throw the switch for this removal step. Although PCH2 has a Cdk phosphorylation site, it seems unlikely that PCH2 itself could be the target of this potential mechanism since we found here that at a phase of presumed high CDKA;1 activity, PCH2 is able to displace ASY1 from the chromosome axis as seen by the restoration of this interaction in a *pch2* mutant background (Fig 5A and B). On the other hand, the removal of ASY1 at zygotene may be regulated through other post-translational modifications. Consistent with this hypothesis, Osman *et al* (2017) have identified several other phosphorylation sites on ASY1, notably ATM/ATR phosphorylation sites. Thus, further work is required to understand the mechanisms of how ASY1 is removed from the chromosome axis.

Beyond ASY1 phosphorylation

Here, we have shown that CDKA;1 works together with SDS and TAM. However, the *sds* mutant phenotype is not a subset of the phenotype of the weak loss-of-function *cdka;1* mutants as seen by the apparently correct localization of DMC1 in *cdka;1* versus the localization failure in *sds* (De Muyt *et al*, 2009). One possible explanation is that SDS can work with additional Cdks, such as CDKB1;1, which have been recently shown to function in somatic homologous recombination repair (Weimer *et al*, 2016). However, at least *in vitro* neither CDKB1;1 nor the related kinase CDKB2;2 built an active kinase complex with SDS (Harashima & Schnittger, 2012). Thus, it seems more likely that the residual Cdk activity in the hypomorphic mutants is sufficient to operate together with SDS to promote DMC1 loading/stabilization. Notably, the localization of ASY1 to chromatin is also only delayed and not completely absent in weak loss-of-function mutants.

Earlier work has already indicated that TAM, the other meiotic cyclin used in our assays, is needed to promote the timely progression through meiosis I and entry into meiosis II (d'Erfurth *et al*, 2010). At the same time, CDK-dependent phosphorylation of THREE DIVISION MUTANT 1 (TDM1) has been shown to be crucial for the exact timing of meiotic exit. Mutation of the CDK phosphorylation site in TDM1 also results in termination of meiosis after anaphase I (Cifuentes *et al*, 2016). Furthermore, the loss of the APC/C inhibitor OMISSION OF SECOND MEIOTIC DIVISION 1 (OSD1), also known as GIGAS CELL 1 (GIG), and the presumed increase in APC/C activity also caused a premature termination of meiosis after anaphase I (Iwata *et al*, 2011; Cromer *et al*, 2012). Consistently with these studies, we found that weak loss-of-function mutants of *cdka;1* often terminated meiosis shortly after the first meiotic division.

In addition, we observed in the weak loss-of-function *cdka;1* mutants several other defects, e.g., in chromosome condensation. While we cannot exclude that these defects are an indirect consequence of for instance altered ASY1 dynamics, it seems plausible that CDKA;1 has many more roles in meiosis than the here-revealed function in assembling the chromosome axis. Indeed, MLH1 was recently found to be an *in vitro* target of CDKA;1 activity and in *cdka;1* hypomorphic mutants, in which kinase activity is only mildly reduced, an altered recombination pattern with fewer crossovers than in the wild type was observed (Wijnker *et al*, 2019). Interestingly, an alleged increase in CDKA;1 activity also caused an elevation in recombination events hinting at a dosage dependency of CDKA;1 for crossover formation. A key role of Cdks in meiosis is further supported by the large number of meiotic regulators that have Cdk consensus phosphorylation sites and/or a predicted cyclin binding site (Zhu *et al*, 2010). Thus, it seems very likely that we are still at the beginning to understand the phosphorylation control of meiosis by Cdk1-type proteins.

Materials and Methods

Plant materials

The *Arabidopsis thaliana* accession Columbia (*Col-0*) was used as wild-type reference throughout this study. The T-DNA insertion lines SALK_046272 (*asy1-4*) (Crismani and Mercier, 2013), SALK_031449 (*pch2-2*) (Lambing *et al*, 2015) and SAIL_423H01 (*asy3-1*) (Ferdous *et al*, 2012), and SALK_106809 (*cdka;1-1*) (Nowack *et al*, 2006) were obtained from the T-DNA mutant collection at the Salk Institute Genomics Analysis Laboratory (SIGnAL, http://signal.salk.edu/cgi-bin/tdnaexpress) via NASC (http://arabidopsis.info/). The mutants *cdka;1 PRO$_{CDKA;1}$: CDKA;1^{T161D}* and *cdka;1 PRO$_{CDKA;1}$:CDKA;1$^{T14D;Y15E}$*, the *PRO$_{ZYP1B}$:ZYP1B:GFP* reporter, and the *PRO$_{ASY3}$:ASY3:RFP* reporter plants were described previously (Dissmeyer *et al*, 2007, 2009; Yang *et al*, 2019). The *StrepIII-tag-CDKA;1* (*cdka;1*) line was also generated previously. The StrepIII tag is a Twin-strep-tag® developed by the IBA GmbH, which consists of two tandem Strep II tag moieties separated by a short linker and shows better binding characteristics in comparison with Strep II tag (Pusch *et al*, 2012; Schmidt *et al*, 2013). The protein sequence of StrepIII/Twin-strep-tag is <u>WSHPQFEK</u>-GGGSGGGSGGSA-<u>WSHPQFEK</u> (the Strep II tag moieties are underlined). All plants were grown in growth chambers with a 16-h light/21°C and 8-h/18°C dark cycle at 60% humidity.

Plasmid construction and plant transformation

To generate the *ASY1* reporters, a 6,013 bp genomic sequence of *ASY1* was amplified by PCR and subsequently integrated into *pENTR2B* vector by SLICE reaction. A *SmaI* restriction site was then introduced in front of the stop codon by PCR. The constructs obtained were then linearized by *SmaI* restriction and ligated with GFP, RFP or mVenus fragments, followed by gateway LR reaction with the destination vector *pGWB501*. The *CDKA;1:mVenus* reporter was generated by using the same strategy as described above. For the *PCH2:GFP* reporter, a 5,837 bp genomic sequence of *PCH2* was amplified by PCR and subsequently integrated into *pDONR221* vector by gateway BP reaction. Subsequently, an *AscI* restriction site was inserted into *pDONR221-PCH2* between the 35–36aa of PCH2 by PCR. Following the linearization by *AscI*, a GFP fragment was inserted into *pDONR221-PCH2*. The resulting *PCH2:GFP* expression cassette was integrated into the destination vector *pGWB501* by the gateway LR reaction. For creating variants of the *ASY1:GFP* constructs including *ASY1^{1–570}:GFP*, a PCR-based mutagenesis was performed using *pENTR2B-ASY1:GFP* as a template followed by gateway LR reactions for integration into the destination vector. All constructs were transformed into *Arabidopsis thaliana* plants by floral dipping.

To make the constructs for the yeast two-hybrid assays, the coding sequences of the respective genes were amplified by PCR with primers flanked by *attB* recombination sites and subcloned into *pDONR223* vector by gateway BP reactions. The resulting constructs were subsequently integrated into the *pGADT7-GW* or *pGBKT7-GW* vectors by gateway LR reactions. Primers used for generating all constructs mentioned above are shown in Appendix Table S1.

Microscopy and live cell imaging

Light microscopy was performed with an Axiophot microscope (Zeiss). To study protein localization, young anthers harboring the relevant reporters were dissected and imaged immediately using an Leica TCS SP8 inverted confocal microscope. The meiotic stages were determined by combining the criteria of the chromosome morphology, nucleolus position (mainly for pre-meiosis to leptotene), and cell shape. For tracing the dynamics of ASY1:GFP/RFP variants in *asy1* mutants and/or wild-type plants, live cell imaging was performed as described by Prusicki *et al* (2019) under controlled temperature (18–20°C) and humidity (60%) conditions. In brief, one single fresh flower bud was detached from the stem and dissected with two anthers exposed. Subsequently, the isolated bud including the pedicel and a short part of the floral stem was embedded into the *Arabidopsis* apex culture medium (ACM) and then covered by one drop of 2% agarose. The sample was then subjected to constant image capture with 7 min of intervals by using an upright Zeiss LSM880 confocal microscope.

To analyze the distribution of the nucleus versus cytoplasm localized CDKA;1, live cell imaging was performed with two anthers of *cdka;1* mutants harboring a fully functional *CDKA;1:mVenus* reporter for 26 h (Movie EV1). To quantify the subcellular distribution of the CDKA;1:mVenus, the signal intensities in the nucleus and cytoplasm were calculated every hour by segmenting the respective regions using the image processing software Fiji.

Yeast two-hybrid assay

Yeast two-hybrid assays were performed according to the Match-maker Gold Yeast two-hybrid system manual (Clontech). Different combinations of constructs were co-transformed into yeast strain AH109 using the polyethylene glycol/lithium acetate method as described in the manual. Yeast cells harboring the relevant constructs were grown on the SD/-Leu-Trp, SD/-Leu-Trp-His, and SD/-Leu-Trp-His-Ade plates to test protein–protein interactions.

Protein expression and purification

To generate the HisMBP-ASY1, HisMBP-ASY1^{1–300}, HisMBP-ASY1^{1–300/T142V;T184V}, and HisGST-ASY3 constructs, the respective coding sequences were amplified by PCR and subcloned into *pDONR223* vector by gateway BP reactions. The resulting constructs were integrated by gateway LR reactions into *pHMGWA* or *pHGGWA* vectors for the HisMBP- and the HisGST-tagged fusions, respectively. For heterologous expression, the constructs were transformed into the *E. coli* BL21 (DE3) pLysS cells, which were grown at 37°C in the presence of 100 mg/l ampicillin until the OD_{600} of 0.6, followed by protein induction by adding IPTG to a final concentration of 0.3 mM. The cells were further incubated at 37°C for 3 h (HisMBP-ASY1, HisMBP-ASY1^{1–300}, and HisMBP-ASY1^{1–300/T142V;T184V}) or 18°C overnight (HisGST-ASY3). All proteins were purified under native conditions by using Ni-NTA sepharose (QIAGEN) according to the manual.

GST pull down assays

For GST pull down assay, 4 μg of HisMBP-ASY1^{1–300}, HisMBP-ASY1^{1–300/T142V;T184V}, and 2 μg HisGST-ASY3 were added to the pull down buffer system containing 25 mM Tris–HCl, pH 7.5, 100 mM NaCl, 10% glycerol, and 20 μl GST agarose beads (ChromoTek) as indicated in Fig 4B. After incubation for 1 h at 4°C, GST beads were collected by centrifugation and washed three times with the washing buffer (25 mM Tris–HCl, pH 7.5, 200 mM NaCl, 10% glycerol, and 0.25/0.5/1% Triton X-100). Bead-bound proteins were eluted by boiling in an equal volume of 1X SDS protein loading buffer and subjected to immuno-blotting analysis.

Protein blots

For SDS–PAGE, protein samples were subjected to the gel electrophoresis at room temperature (12% acrylamide, 375 mM Tris–HCl, pH 8.8, and 0.1% SDS) followed by transfer blotting onto nitrocellulose membrane. For Phos-tag SDS–PAGE, proteins from kinase assays were subjected to Phos-tag gel electrophoresis [6% acrylamide, 375 mM Tris–HCl, pH 8.8, 50 μM Phos-tag (Wako), and 100 μM $MnCl_2$] at 4°C followed by transfer blotting. After incubation with the primary and secondary antibodies, the immuno-blots were exposed and observed using a Bio-Rad Image Analyzer. Relative protein levels were quantified with the Image Lab software (Bio-Rad).

Chromosome spreads

Chromosome spreads were performed as described previously (Wijnker *et al*, 2012). In brief, fresh flower buds were fixed in 75%

ethanol and 25% acetic acid for 48 h at 4°C, washed two times with 75% ethanol and stored in 75% ethanol at 4°C. For spreading, flower buds were digested in an enzyme solution (10 mM citrate buffer containing 1.5% cellulose, 1.5% pectolyase, and 1.5% cytohelicase) for 3 h at 37°C and then transferred onto a glass slide, followed by mashing with a bended needle. Spreading was performed on a 46°C hotplate by adding 10 μl of 45% acetic acid. The slide was then rinsed with ice-cold ethanol/acetic acid (3:1) solution and mounted in VECTASHIELD with DAPI (Vector Laboratories).

In vitro kinase assays

CDKA;1-SDS, CDKA;1-TAM, and CDKA;1-CYCA3;1 complexes were expressed as described by Harashima and Schnittger (2012). The kinase complexes were purified by Strep-Tactin Agarose (IBA), followed by desalting with PD MiniTrap G-25 (GE Healthcare). The kinase assay in Fig 2B was performed by incubating the kinase complexes with the ASY1 proteins purified from baculovirus-infected insect cells in the kinase buffer containing 50 mM Tris–HCl, pH 7.5, 10 mM $MgCl_2$, and 5% (V/V) [γ-^{32}P]ATP (9.25 MBq, GE Healthcare) for 30 min. The reaction was then inactivated by boiling at 95°C for 5 min after adding 5X SDS protein loading solution, and autoradiography was subsequently performed following the SDS–PAGE. The kinase assay in Fig 2C was performed by incubating the kinase complexes with HisMBP-ASY1 in the reaction buffer containing 50 mM Tris–HCl, pH 7.5, 10 mM $MgCl_2$, 0.5 mM ATP, and 5 mM DTT for 90 min. The phosphorylation of ASY1 was then verified by Phos-tag SDS–PAGE. The CBB stained gel after kinase reaction is shown in Appendix Fig S2A.

Sample preparation and LC-MS/MS data acquisition

The protein mixtures after kinase assays were reduced with dithiothreitol, alkylated with chloroacetamide, and digested with trypsin. Subsequently, the digested samples were desalted using StageTips with C18 Empore disk membranes (3 M; Rappsilber *et al*, 2003), dried in a vacuum evaporator, and dissolved in 2% ACN, 0.1% TFA. Samples were analyzed using an EASY-nLC 1200 (Thermo Fisher) coupled to a Q Exactive Plus mass spectrometer (Thermo Fisher). Peptides were separated on 16 cm frit-less silica emitters (New Objective, 0.75 μm inner diameter), packed in-house with reversed-phase ReproSil-Pur C18 AQ 1.9 μm resin (Dr. Maisch). Peptides were loaded on the column and eluted for 50 min using a segmented linear gradient of 5–95% solvent B (0 min: 5%B; 0–5 min- > 5%; 5–25 min- > 20%; 25–35 min- > 35%; 35–40 min- > 95%; 40–50 min- > 95%; solvent A 0% ACN, 0.1% FA; solvent B 80% ACN, 0.1%FA) at a flow rate of 300 nl/min. Mass spectra were acquired in data-dependent acquisition mode with a TOP15 method. MS spectra were acquired in the Orbitrap analyzer with a mass range of 300–1,500 m/z at a resolution of 70,000 FWHM and a target value of 3×10^6 ions. Precursors were selected with an isolation window of 1.3 m/z. HCD fragmentation was performed at a normalized collision energy of 25. MS/MS spectra were acquired with a target value of 5×10^5 ions at a resolution of 17,500 FWHM, a maximum injection time of 120 ms, and a fixed first mass of m/z 100. Peptides with a charge of 1, greater than 6, or with unassigned charge state were excluded from fragmentation for

MS^2; dynamic exclusion for 20 s prevented repeated selection of precursors.

For targeted analysis, samples were resolved using the segmented linear gradient as mentioned above. The acquisition method consisted of a full scan method combined with a non-scheduled PRM method. The 16 targeted precursor ions were selected based on the results of DDA peptide search in Skyline. MS spectra were acquired in the Orbitrap analyzer with a mass range of 300–2,000 m/z at a resolution of 70,000 FWHM and a target value of 3×10^6 ions, followed by MS/MS acquisition for the 16 targeted precursors. Precursors were selected with an isolation window of 2.0 m/z. HCD fragmentation was performed at the normalized collision energy of 27. MS/MS spectra were acquired with a target value of 2×10^5 ions at a resolution of 17,500 FWHM, a maximum injection time of 120 ms, and a fixed first mass of m/z 100.

MS data analysis and PRM method development

Raw data from DDA acquisition were processed using MaxQuant software (version 1.5.7.4, http://www.maxquant.org/; Cox and Mann, 2008). MS/MS spectra were searched by the Andromeda search engine against a database containing the respective proteins used for the *in vitro* reaction. Trypsin specificity was required and a maximum of two missed cleavages allowed. Minimal peptide length was set to seven amino acids. Carbamidomethylation of cysteine residues was set as fixed, phosphorylation of serine, threonine and tyrosine, oxidation of methionine, and protein N-terminal acetylation as variable modifications. The match between runs option was disabled. Peptide spectrum matches and proteins were retained if they were below a false discovery rate of 1% in both cases.

The DDA approach only enabled the identification of T142. To analyze the putative phosphorylation sites at T184 and T535, a targeted approach was employed. Raw data from the DDA acquisition were analyzed on MS1 level using Skyline (version 4.1.0.18169, https://skyline.ms; MacLean *et al*, 2010) and a database containing the respective proteins used for the *in vitro* reaction. Trypsin specificity was required and a maximum of two missed cleavages allowed. Minimal peptide length was set to seven maximum length to 25 amino acids. Carbamidomethylation of cysteine, phosphorylation of serine, threonine and tyrosine, oxidation of methionine, and protein N-terminal acetylation were set as modifications. Results were filtered for precursor charges of 2, 3, and 4. For each phosphorylated precursor ion, a respective non-phosphorylated precursor ion was targeted as a control, and several precursor ions from the backbone of ASY1 recombinant protein were chosen as controls between the different samples. In total, 16 precursors were chosen to be targeted with a PRM approach. After acquisition of PRM data, the raw data were again processed using MaxQuant software, with above-mentioned parameters. Peptide search results were analyzed using Skyline using above-mentioned parameters; additionally, data were filtered for b- and y-ions and ion charges +1 and +2.

Quantification and statistical analysis

Student's *t*-test (two-tailed) was used to evaluate the significance of the difference between the two groups. * denotes $P < 0.05$, and ** denotes $P < 0.01$. The significance of the differences in more than two groups was determined by one-way ANOVA followed by

Turkey's test. Level of significance is indicated by different letters. The numbers of samples are indicated in the figure legends.

Data availability

Expanded View for this article is available online.

Acknowledgements

Author contributions

Conflict of interest
The authors declare that they have no conflict of interest.

References

Adhikari D, Zheng W, Shen Y, Gorre N, Ning Y, Halet G, Kaldis P, Liu K (2012) Cdk1, but not Cdk2, is the sole Cdk that is essential and sufficient to drive resumption of meiosis in mouse oocytes. *Hum Mol Genet* 21: 2476−2484

Anand R, Ranjha L, Cannavo E, Cejka P (2016) Phosphorylated CtIP functions as a co-factor of the MRE11-RAD50-NBS1 endonuclease in DNA End resection. *Mol Cell* 64: 940−950

Aravind L, Koonin EV (1998) The HORMA domain: a common structural denominator in mitotic checkpoints, chromosome synapsis and DNA repair. *Trends Biochem Sci* 23: 284−286

Armstrong SJ (2002) Asy1, a protein required for meiotic chromosome synapsis, localizes to axis-associated chromatin in *Arabidopsis* and *Brassica*. *J Cell Sci* 115: 3645−3655

Ashley T, Walpita D, de Rooij DG (2001) Localization of two mammalian cyclin dependent kinases during mammalian meiosis. *J Cell Sci* 114: 685−693

Azumi Y, Liu D, Zhao D, Li W, Wang G, Hu Y, Ma H (2002) Homolog interaction during meiotic prophase I in *Arabidopsis* requires the *SOLO DANCERS* gene encoding a novel cyclin-like protein. *EMBO J* 21: 3081−3095

Bailis JM, Roeder GS (1998) Synaptonemal complex morphogenesis and sister-chromatid cohesion require Mek1-dependent phosphorylation of a meiotic chromosomal protein. *Genes Dev* 12: 3551−3563

Baker SM, Plug AW, Prolla TA, Bronner CE, Harris AC, Yao X, Christie DM, Monell C, Arnheim N, Bradley A *et al* (1996) Involvement of mouse Mlh1 in DNA mismatch repair and meiotic crossing over. *Nat Genet* 13: 336−342

Bulankova P, Riehs-Kearnan N, Nowack MK, Schnittger A, Riha K (2010) Meiotic progression in *Arabidopsis* is governed by complex regulatory interactions between SMG7, TDM1, and the meiosis I-specific cyclin TAM. *Plant Cell* 22: 3791−3803

Bulankova P, Akimcheva S, Fellner N, Riha K (2013) Identification of *Arabidopsis* meiotic cyclins reveals functional diversification among plant cyclin genes. *PLoS Genet* 9: e1003508

Cannavo E, Johnson D, Andres SN, Kissling VM, Reinert JK, Garcia V, Erie DA, Hess D, Thomä NH, Enchev RI *et al* (2018) Regulatory control of DNA end resection by Sae2 phosphorylation. *Nat Commun* 9: 4016

Carballo JA, Johnson AL, Sedgwick SG, Cha RS (2008) Phosphorylation of the axial element protein Hop1 by Mec1/Tel1 ensures meiotic interhomolog recombination. *Cell* 132: 758−770

Chen C, Jomaa A, Ortega J, Alani EE (2014) Pch2 is a hexameric ring ATPase that remodels the chromosome axis protein Hop1. *Proc Natl Acad Sci USA* 111: E44−E53

Cifuentes M, Jolivet S, Cromer L, Harashima H, Bulankova P, Renne C, Crismani W, Nomura Y, Nakagami H, Sugimoto K *et al* (2016) TDM1 regulation determines the number of meiotic divisions. *PLoS Genet* 12: e1005856

Coudreuse D, Nurse P (2010) Driving the cell cycle with a minimal CDK control network. *Nature* 468: 1074−1079

Cox J, Mann M (2008) MaxQuant enables high peptide identification rates, individualized p.p.b.-range mass accuracies and proteome-wide protein quantification. *Nat Biotechnol* 26: 1367−1372

Crismani W, Mercier R (2013) Identifying meiotic mutants in *Arabidopsis thaliana*. *Methods Mol Biol* 990: 227−234

Cromer L, Heyman J, Touati S, Harashima H, Araou E, Girard C, Horlow C, Wassmann K, Schnittger A, De Veylder L *et al* (2012) OSD1 promotes meiotic progression via APC/C inhibition and forms a regulatory network with TDM and CYCA1;2/TAM. *PLoS Genet* 8: e1002865

Da Ines O, Degroote F, Goubely C, Amiard S, Gallego ME, White CI (2013) Meiotic recombination in *Arabidopsis* is catalysed by DMC1, with RAD51 playing a supporting role. *PLoS Genet* 9: e1003787

De Muyt A, Pereira L, Vezon D, Chelysheva L, Gendrot G, Chambon A, Lainé-Choinard S, Pelletier G, Mercier R, Nogué F *et al* (2009) A high throughput genetic screen identifies new early meiotic recombination functions in *Arabidopsis thaliana*. *PLoS Genet* 5: e1000654

Dissmeyer N, Nowack MK, Pusch S, Stals H, Inzé D, Grini PE, Schnittger A (2007) T-loop phosphorylation of *Arabidopsis* CDKA;1 is required for its function and can be partially substituted by an aspartate residue. *Plant Cell* 19: 972−985

Dissmeyer N, Weimer AK, Pusch S, De Schutter K, Alvim Kamei CL, Nowack MK, Novak B, Duan G-L, Zhu Y-G, De Veylder L *et al* (2009) Control of cell proliferation, organ growth, and DNA damage response operate independently of dephosphorylation of the *Arabidopsis* Cdk1 homolog CDKA;1. *Plant Cell* 21: 3641−3654

Doonan JH, Kitsios G (2009) Functional evolution of cyclin-dependent kinases. *Mol Biotechnol* 42: 14−29

d'Erfurth I, Cromer L, Jolivet S, Girard C, Horlow C, Sun Y, To JPC, Berchowitz LE, Copenhaver GP, Mercier R (2010) The cyclin-A CYCA1;2/TAM is required for the meiosis I to meiosis II transition and cooperates with OSD1 for the prophase to first meiotic division transition. *PLoS Genet* 6: e1000989

Ferdous M, Higgins JD, Osman K, Lambing C, Roitinger E, Mechtler K, Armstrong SJ, Perry R, Pradillo M, Cuñado N *et al* (2012) Inter-homolog

crossing-over and synapsis in *Arabidopsis* meiosis are dependent on the chromosome axis protein AtASY3. *PLoS Genet* 8: e1002507

Gutiérrez-Escribano P, Nurse P (2015) A single cyclin-CDK complex is sufficient for both mitotic and meiotic progression in fission yeast. *Nat Commun* 6: 6871

Harashima H, Schnittger A (2012) Robust reconstitution of active cell-cycle control complexes from co-expressed proteins in bacteria. *Plant Methods* 8: 23

Harashima H, Dissmeyer N, Schnittger A (2013) Cell cycle control across the eukaryotic kingdom. *Trends Cell Biol* 23: 345–356

Henderson KA, Kee K, Maleki S, Santini PA, Keeney S (2006) Cyclin-dependent kinase directly regulates initiation of meiotic recombination. *Cell* 125: 1321–1332

Hollingsworth NM, Goetsch L, Byers B (1990) The *HOP1* gene encodes a meiosis-specific component of yeast chromosomes. *Cell* 61: 73–84

Huang X-Y, Niu J, Sun M-X, Zhu J, Gao J-F, Yang J, Zhou Q, Yang Z-N (2013) CYCLIN-DEPENDENT KINASE G1 is associated with the spliceosome to regulate CALLOSE SYNTHASE 5 splicing and pollen wall formation in *Arabidopsis*. *Plant Cell* 25: 637–648

Huertas P, Cortés-Ledesma F, Sartori AA, Aguilera A, Jackson SP (2008) CDK targets Sae2 to control DNA-end resection and homologous recombination. *Nature* 455: 689–692

Huertas P, Jackson SP (2009) Human CtIP mediates cell cycle control of DNA end resection and double strand break repair. *J Biol Chem* 284: 9558–9565

Iwata E, Ikeda S, Matsunaga S, Kurata M, Yoshioka Y, Criqui M-C, Genschik P, Ito M (2011) GIGAS CELL1, a novel negative regulator of the anaphase-promoting complex/cyclosome, is required for proper mitotic progression and cell fate determination in *Arabidopsis*. *Plant Cell* 23: 4382–4393

Kim Y, Rosenberg SC, Kugel CL, Kostow N, Rog O, Davydov V, Su TY, Dernburg AF, Corbett KD (2014) The chromosome axis controls meiotic events through a hierarchical assembly of HORMA domain proteins. *Dev Cell* 31: 487–502

Kurzbauer MT, Uanschou C, Chen D, Schlogelhofer P (2012) The recombinases DMC1 and RAD51 are functionally and spatially separated during meiosis in *Arabidopsis*. *Plant Cell* 24: 2058–2070

Lambing C, Osman K, Nuntasoontorn K, West A, Higgins JD, Copenhaver GP, Yang J, Armstrong SJ, Mechtler K, Roitinger E *et al* (2015) *Arabidopsis* PCH2 mediates meiotic chromosome remodeling and maturation of crossovers. *PLoS Genet* 11: e1005372

Lambing C, Franklin FCH, Wang C-JR (2017) Understanding and manipulating meiotic recombination in plants. *Plant Physiol* 173: 1530–1542

Li J, Hooker GW, Roeder GS (2006) *Saccharomyces cerevisiae* Mer2, Mei4 and Rec114 form a complex required for meiotic double-strand break formation. *Genetics* 173: 1969–1981

MacLean B, Tomazela DM, Shulman N, Chambers M, Finney GL, Frewen B, Kern R, Tabb DL, Liebler DC, MacCoss MJ (2010) Skyline: an open source document editor for creating and analyzing targeted proteomics experiments. *Bioinformatics* 26: 966–968

Magnard JL, Yang M, Chen YC, Leary M, McCormick S (2001) The *Arabidopsis* gene *Tardy Asynchronous Meiosis* is required for the normal pace and synchrony of cell division during male meiosis. *Plant Physiol* 127: 1157–1166

Malumbres M, Harlow E, Hunt T, Hunter T, Lahti JM, Manning G, Morgan DO, Tsai L-H, Wolgemuth DJ (2009) Cyclin-dependent kinases: a family portrait. *Nat Cell Biol* 11: 1275–1276

Manfrini N, Guerini I, Citterio A, Lucchini G, Longhese MP (2010) Processing of meiotic DNA double strand breaks requires cyclin-dependent kinase and multiple nucleases. *J Biol Chem* 285: 11628–11637

Mercier R, Mézard C, Jenczewski E, Macaisne N, Grelon M (2015) The molecular biology of meiosis in plants. *Annu Rev Plant Biol* 66: 297–327

Miller ME, Cross FR (2001) Cyclin specificity: how many wheels do you need on a unicycle? *J Cell Sci* 114: 1811–1820

Mimitou EP, Symington LS (2009) DNA end resection: many nucleases make light work. *DNA Repair (Amst)* 8: 983–995

Morgan DO (1997) Cyclin-dependent kinases: engines, clocks, and microprocessors. *Annu Rev Cell Dev Biol* 13: 261–291

Muniyappa K, Kshirsagar R, Ghodke I (2014) The HORMA domain: an evolutionarily conserved domain discovered in chromatin-associated proteins, has unanticipated diverse functions. *Gene* 545: 194–197

Niu H, Wan L, Baumgartner B, Schaefer D, Loidl J, Hollingsworth NM (2005) Partner choice during meiosis is regulated by Hop1-promoted dimerization of Mek1. *Mol Biol Cell* 16: 5804–5818

Nowack MK, Grini PE, Jakoby MJ, Lafos M, Koncz C, Schnittger A (2006) A positive signal from the fertilization of the egg cell sets off endosperm proliferation in angiosperm embryogenesis. *Nat Genet* 38: 63–67

Nowack MK, Shirzadi R, Dissmeyer N, Dolf A, Endl E, Grini PE, Schnittger A (2007) Bypassing genomic imprinting allows seed development. *Nature* 447: 312–315

Nowack MK, Harashima H, Dissmeyer N, Zhao X, Bouyer D, Weimer AK, De Winter F, Yang F, Schnittger A (2012) Genetic framework of cyclin-dependent kinase function in *Arabidopsis*. *Dev Cell* 22: 1030–1040

Ortega S, Prieto I, Odajima J, Martín A, Dubus P, Sotillo R, Barbero JL, Malumbres M, Barbacid M (2003) Cyclin-dependent kinase 2 is essential for meiosis but not for mitotic cell division in mice. *Nat Genet* 35: 25–31

Osman K, Yang J, Roitinger E, Lambing C, Heckmann S, Howell E, Cuacos M, Imre R, Dürnberger G, Mechtler K *et al* (2017) Affinity proteomics reveals extensive phosphorylation of the *Brassica* chromosome axis protein ASY1 and a network of associated proteins at prophase I of meiosis. *Plant J* 93: 17–33

Pagliuca FW, Collins MO, Lichawska A, Zegerman P, Choudhary JS, Pines J (2011) Quantitative proteomics reveals the basis for the biochemical specificity of the cell-cycle machinery. *Mol Cell* 43: 406–417

Prusicki MA, Keizer EM, van Rosmalen RP, Komaki S, Seifert F, Müller K, Wijnker E, Fleck C, Schnittger A (2019) Live cell imaging of meiosis in *Arabidopsis thaliana*. *Elife* 8: 141

Pusch S, Harashima H, Schnittger A (2012) Identification of kinase substrates by bimolecular complementation assays. *Plant J* 70: 348–356

Rappsilber J, Ishihama Y, Mann M (2003) Stop and go extraction tips for matrix-assisted laser desorption/ionization, nanoelectrospray, and LC/MS sample pretreatment in proteomics. *Anal Chem* 75: 663–670

Rockmill B, Roeder GS (1990) Meiosis in asynaptic yeast. *Genetics* 126: 563–574

Rosenberg SC, Corbett KD (2015) The multifaceted roles of the HORMA domain in cellular signaling. *J Cell Biol* 211: 745–755

Santamaría D, Barrière C, Cerqueira A, Hunt S, Tardy C, Newton K, Cáceres JF, Dubus P, Malumbres M, Barbacid M (2007) Cdk1 is sufficient to drive the mammalian cell cycle. *Nature* 448: 811–815

de los Santos T, Hollingsworth NM (1999) Red1p, a *MEK1*-dependent phosphoprotein that physically interacts with Hop1p during meiosis in yeast. *J Biol Chem* 274: 1783–1790

Satyanarayana A, Berthet C, Lopez-Molina J, Coppola V, Tessarollo L, Kaldis P (2008) Genetic substitution of Cdk1 by Cdk2 leads to embryonic lethality and loss of meiotic function of Cdk2. *Development* 135: 3389–3400

Schmidt TGM, Batz L, Bonet L, Carl U, Holzapfel G, Kiem K, Matulewicz K, Niermeier D, Schuchardt I, Stanar K (2013) Development of the Twin-

Strep-tag® and its application for purification of recombinant proteins from cell culture supernatants. *Protein Expr Purif* 92: 54–61

Shinohara A, Gasior S, Ogawa T, Kleckner N, Bishop DK (1997) *Saccharomyces cerevisiae* recA homologues RAD51 and DMC1 have both distinct and overlapping roles in meiotic recombination. *Genes Cells* 2: 615–629

Smith AV, Roeder GS (1997) The yeast Red1 protein localizes to the cores of meiotic chromosomes. *J Cell Biol* 136: 957–967

Stronghill PE, Azimi W, Hasenkampf CA (2014) A novel method to follow meiotic progression in *Arabidopsis* using confocal microscopy and 5-ethynyl-2′-deoxyuridine labeling. *Plant Methods* 10: 33

Tank JG, Thaker VS (2011) Cyclin dependent kinases and their role in regulation of plant cell cycle. *Biol Plant* 55: 201–212

Ubersax JA, Woodbury EL, Quang PN, Paraz M, Blethrow JD, Shah K, Shokat KM, Morgan DO (2003) Targets of the cyclin-dependent kinase Cdk1. *Nature* 425: 859–864

Wang Y, Wu H, Liang G, Yang M (2004) Defects in nucleolar migration and synapsis in male prophase I in the ask1-1 mutant of *Arabidopsis*. *Sex Plant Reprod* 16: 273–282

Weimer AK, Biedermann S, Harashima H, Roodbarkelari F, Takahashi N, Foreman J, Guan Y, Pochon G, Heese M, Van Damme D *et al* (2016) The plant-specific CDKB1-CYCB1 complex mediates homologous recombination repair in *Arabidopsis*. *EMBO J* 35: 2068–2086

West AMV, Komives EA, Corbett KD (2018) Conformational dynamics of the Hop1 HORMA domain reveal a common mechanism with the spindle checkpoint protein Mad2. *Nucleic Acids Res* 46: 279–292

West AM, Rosenberg SC, Ur SN, Lehmer MK, Ye Q, Hagemann G, Caballero I, Usón I, MacQueen AJ, Herzog F *et al* (2019) A conserved filamentous assembly underlies the structure of the meiotic chromosome axis. *Elife* 8: 213

Wijnker E, van Dun K, de Snoo CB, Lelivelt CL, Keurentjes JJ, Naharudin NS, Ravi M, Chan SW, de Jong H, Dirks R (2012) Reverse breeding in *Arabidopsis thaliana* generates homozygous parental lines from a heterozygous plant. *Nat Genet* 44: 467–470

Wijnker E, Schnittger A (2013) Control of the meiotic cell division program in plants. *Plant Reprod* 26: 143–158

Wijnker E, Harashima H, Müller K, Parra-Nuñez P, de Snoo CB, van de Belt J, Dissmeyer N, Bayer M, Pradillo M, Schnittger A (2019) The Cdk1/Cdk2

homolog CDKA;1 controls the recombination landscape in *Arabidopsis*. *Proc Natl Acad Sci USA* 116: 12534–12539

Wojtasz L, Daniel K, Roig I, Bolcun-Filas E, Xu H, Boonsanay V, Eckmann CR, Cooke HJ, Jasin M, Keeney S *et al* (2009) Mouse HORMAD1 and HORMAD2, two conserved meiotic chromosomal proteins, are depleted from synapsed chromosome axes with the help of TRIP13 AAA-ATPase. *PLoS Genet* 5: e1000702

Yang X, Timofejeva L, Ma H, Makaroff CA (2006) The *Arabidopsis SKP1* homolog *ASK1* controls meiotic chromosome remodeling and release of chromatin from the nuclear membrane and nucleolus. *J Cell Sci* 119: 3754–3763

Yang C, Hamamura Y, Sofroni K, Böwer F, Stolze SC, Nakagami H, Schnittger A (2019) SWITCH 1/DYAD is a WINGS APART-LIKE antagonist that maintains sister chromatid cohesion in meiosis. *Nat Commun* 10: 1755

Zabicki P, Kuta E, Tuleja M, Rataj K, Malec P (2013) *Arabidopsis* cyclin-dependent kinase gene *CDKG;2* is involved in organogenic responses induced *in vitro*. *Acta Biol Crac Ser Bot* 55: 37–48

Zhao X, Harashima H, Dissmeyer N, Pusch S, Weimer AK, Bramsiepe J, Bouyer D, Rademacher S, Nowack MK, Novak B *et al* (2012) A general G1/S-phase cell-cycle control module in the flowering plant *Arabidopsis thaliana*. *PLoS Genet* 8: e1002847

Zheng T, Nibau C, Phillips DW, Jenkins G, Armstrong SJ, Doonan JH (2014) CDKG1 protein kinase is essential for synapsis and male meiosis at high ambient temperature in *Arabidopsis thaliana*. *Proc Natl Acad Sci USA* 111: 2182–2187

Zhu Z, Mori S, Oshiumi H, Matsuzaki K, Shinohara M, Shinohara A (2010) Cyclin-dependent kinase promotes formation of the synaptonemal complex in yeast meiosis. *Genes Cells* 15: 1036–1050

Zickler D, Kleckner N (1999) Meiotic chromosomes: integrating structure and function. *Annu Rev Genet* 33: 603–754

Zickler D, Kleckner N (2015) Recombination, pairing, and synapsis of homologs during Meiosis. *Cold Spring Harb Perspect Biol* 7: a016626

Expanded View Figures

A

CDKA;1^{T161D}   CDKA;1:mVenus (cdka;1)

B

CDKA;1^{T161D}

WT

CDKA;1:mVenus (cdka;1)

C

Zygotene | Pachytene | Diplotene | Diakinesis | Metaphase I

Anaphase I | Interkinesis | Metaphase II | Telophase II | Tetrad

D

CDKA;1^{T14D;Y15E}

a | b | c

d | e | f

E

ZYP1 | ZYP1 DAPI

WT

CDKA;1^{T161D}

F

DMC1/ASY1

WT   CDKA;1^{T162D}

G

rad51

a | b | c

CDKA;1^{T161D} rad51

d | e | f

Figure EV1.

108
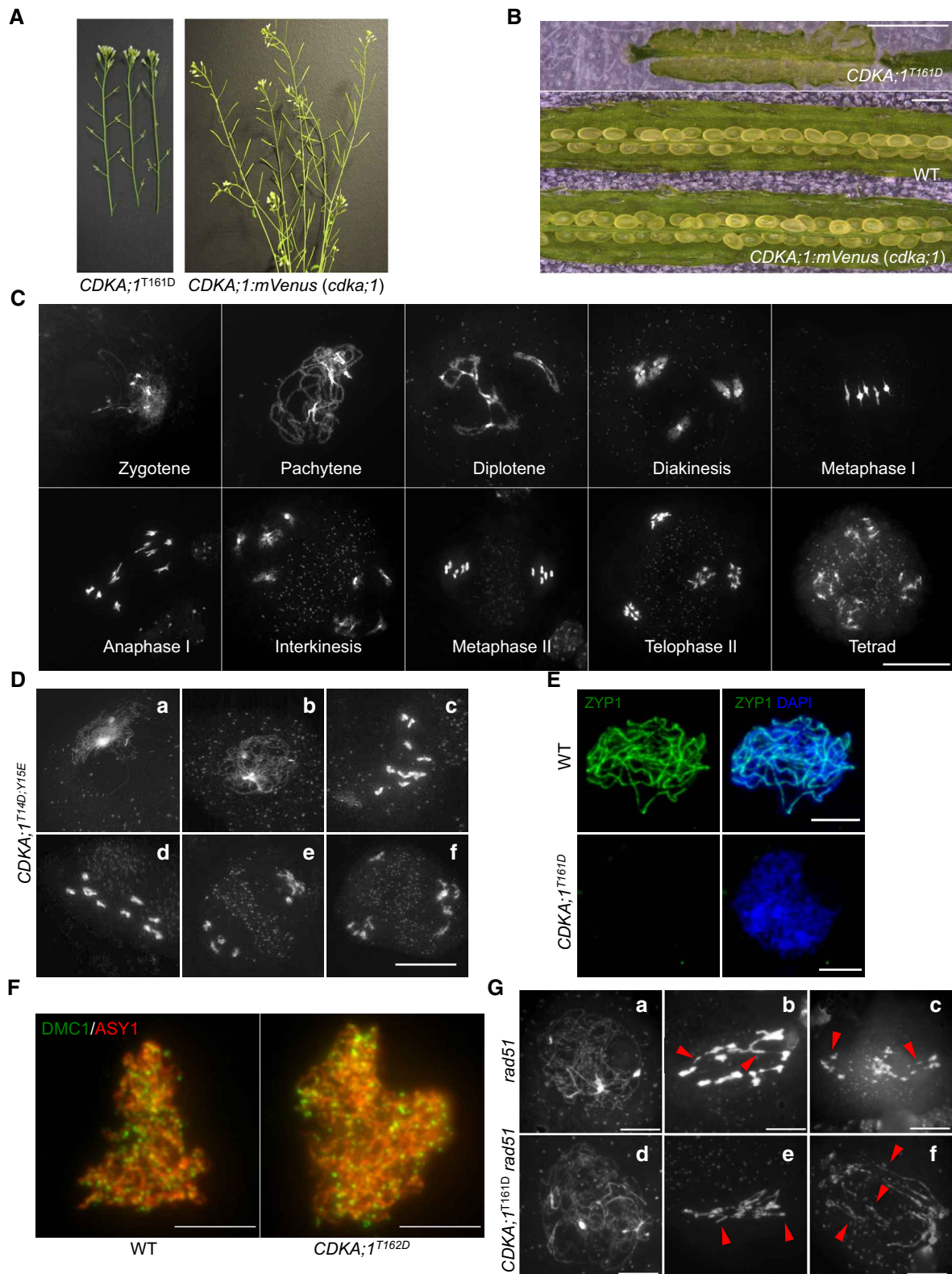
Figure EV1. CDKA;1-mVenus fully complements the *cdka;1* mutant phenotype.

A   The stems of a hypomorphic *cdka;1* mutant CDKA;1^{T161D} are completely sterile as indicated by short siliques in contrast to homozygous *cdka;1* mutant expressing the *CDKA;1:mVenus* reporter construct that form long siliques and are full fertile.

B   The siliques of hypomorphic CDKA;1^{T161D} do not harbor viable seeds in contrast to homozygous *cdka;1* mutant expressing CDKA;1:mVenus that develop healthy and plump seeds. Scale bars: 1 mm.

C   Chromosome spread analysis of male meiocytes of a homozygous *cdka;1* mutant expressing a functional *CDKA;1:mVenus* reporter reveals a wild type-like meiotic program. Scale bar: 20 µm.

D   Chromosome spread analysis of the hypomorphic *cdka;1* mutant CDKA;$1^{T14D;Y15E}$. (a) zygotene-like stage; (b) pachytene-like stage; (c, d) diakinesis-like stages; and (e, f) end of meiosis I with two or three pools of chromosomes. Scale bar: 20 µm.

E   Immunolocalization of ZYP1 (green) in wild-type (WT) and CDKA;1^{T161D} mutants. Chromosomes are stained with DAPI (blue). Scale bars: 5 µm.

F   Immunolocalization analysis of DMC1 (green) together with ASY1 (red) in late leptotene of male meiocytes of wild-type (WT) and CDKA;1^{T161D} mutants. Scale bars: 5 µm.

G   Chromosome spread analysis of *rad51* and *rad51 CDKA;1^{T161D}* mutants. (a, d) pachytene-like stage; (b, c, e, and f) anaphase I-like stage. Red arrowheads indicate the chromosomal fragments. Scale bars: 10 µm.
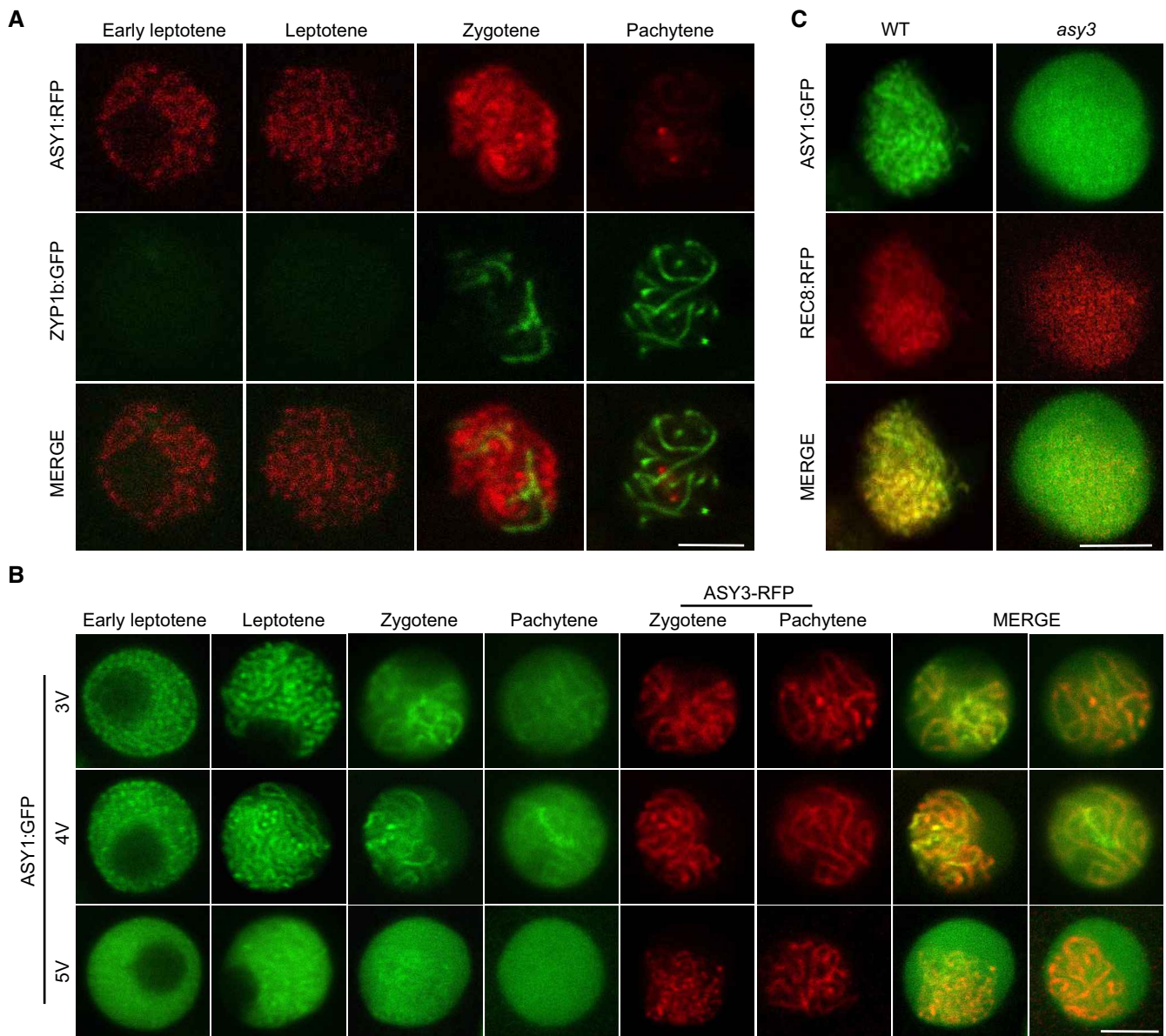
Figure EV2.

Figure EV2. Localization of ASY1 variants in the wild-type and *asy3* mutants.

A   Co-localization analysis of ASY1-RFP with ZYP1b-GFP at different meiotic stages in male meiocytes of the wild type. Scale bars: 5 μm.

B   Localization of ASY1^{3V}:GFP (T365V S382V T535V), ASY1^{4V}:GFP (T184V T365V S382V T535V), and ASY1^{5V}:GFP (T142V T184V T365V S382V T535V) together with ASY3:RFP (for staging of zygotene and pachytene) at different meiotic stages in male meiocytes of *asy1* mutants. Scale bars: 5 μm.

C   Localization of ASY1:GFP in the male meiocytes of the wild-type and *asy3* mutants at leptotene. REC8-RFP was used for staging and to highlight chromosomes. Scale bars: 5 μm.

Figure EV3. Phenotypic characterization of different ASY1:GFP variants.

A   Schematic graph showing different ASY1 non-phosphorylatable mutants.

B, C   Siliques (B) and seed set (C) of the wild type (WT), *asy1*, *ASY1^{T142V}*, *ASY1^{T184V}*, *ASY1^{2V}*, *ASY1^{3V}*, *ASY1^{4V}*, *ASY1^{5V}*, *ASY1^{T142S}*, and *ASY1^{T142D}*. Red arrowheads indicate aborted seeds.

D   Quantification of the seed set shown in (C) from at least five siliques.

E   Peterson staining of anthers for the wild type (WT), *asy1*, *ASY1^{T142V}*, *ASY1^{T184V}*, *ASY1^{2V}*, *ASY1^{3V}*, *ASY1^{4V}*, *ASY1^{5V}*, *ASY1^{T142S}*, and *ASY1^{T142D}*. Red indicates viable pollen grains, and blue denotes aborted pollen grains.

F   Quantification of the pollen viability assay shown in (E) using at least nine flower buds.

Data information: (D, F) Level of significance ($P < 0.05$) is indicated by different letters as determined by the one-way ANOVA followed by Tukey's test. Error bars represent mean ± SD.
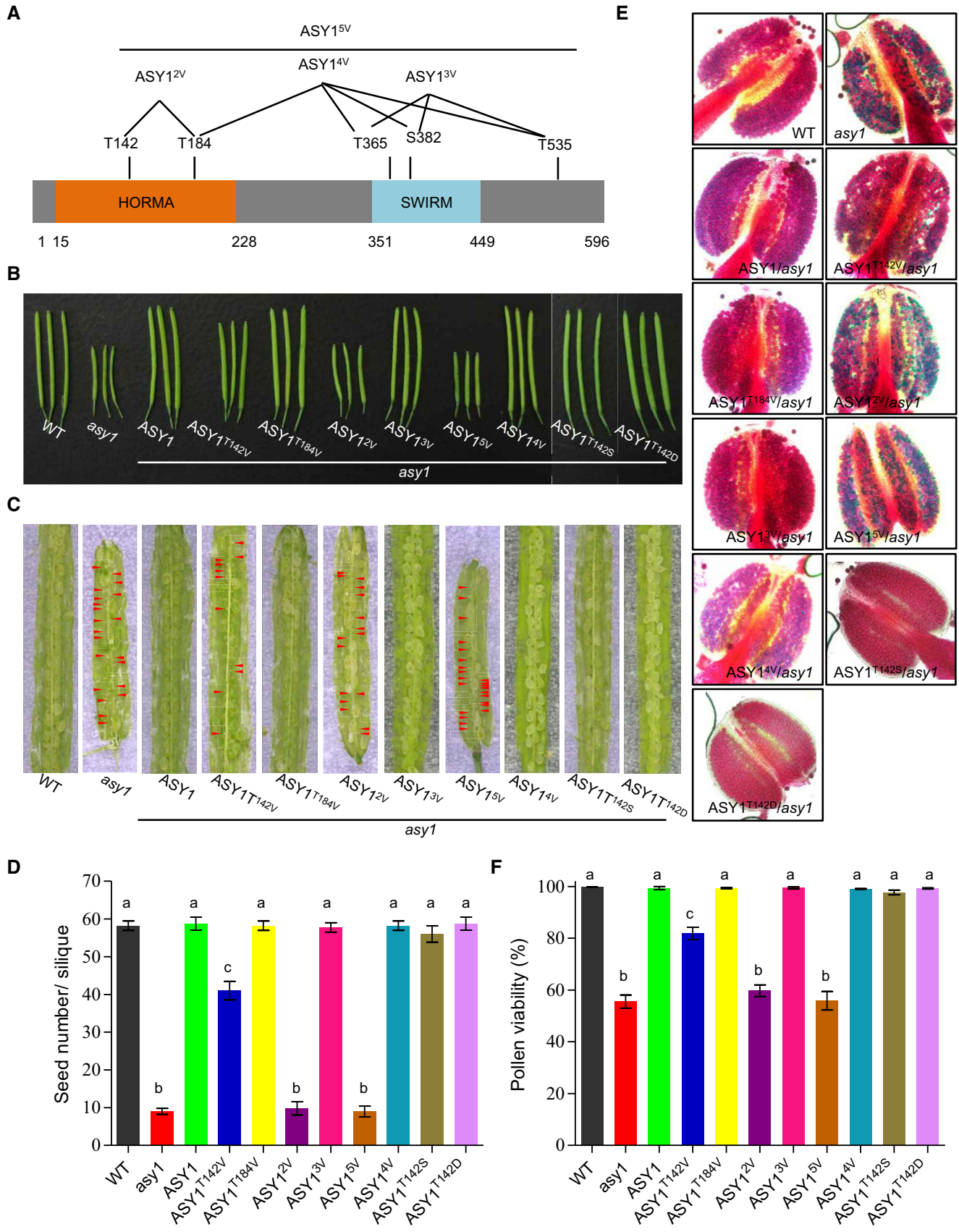
Figure EV3.
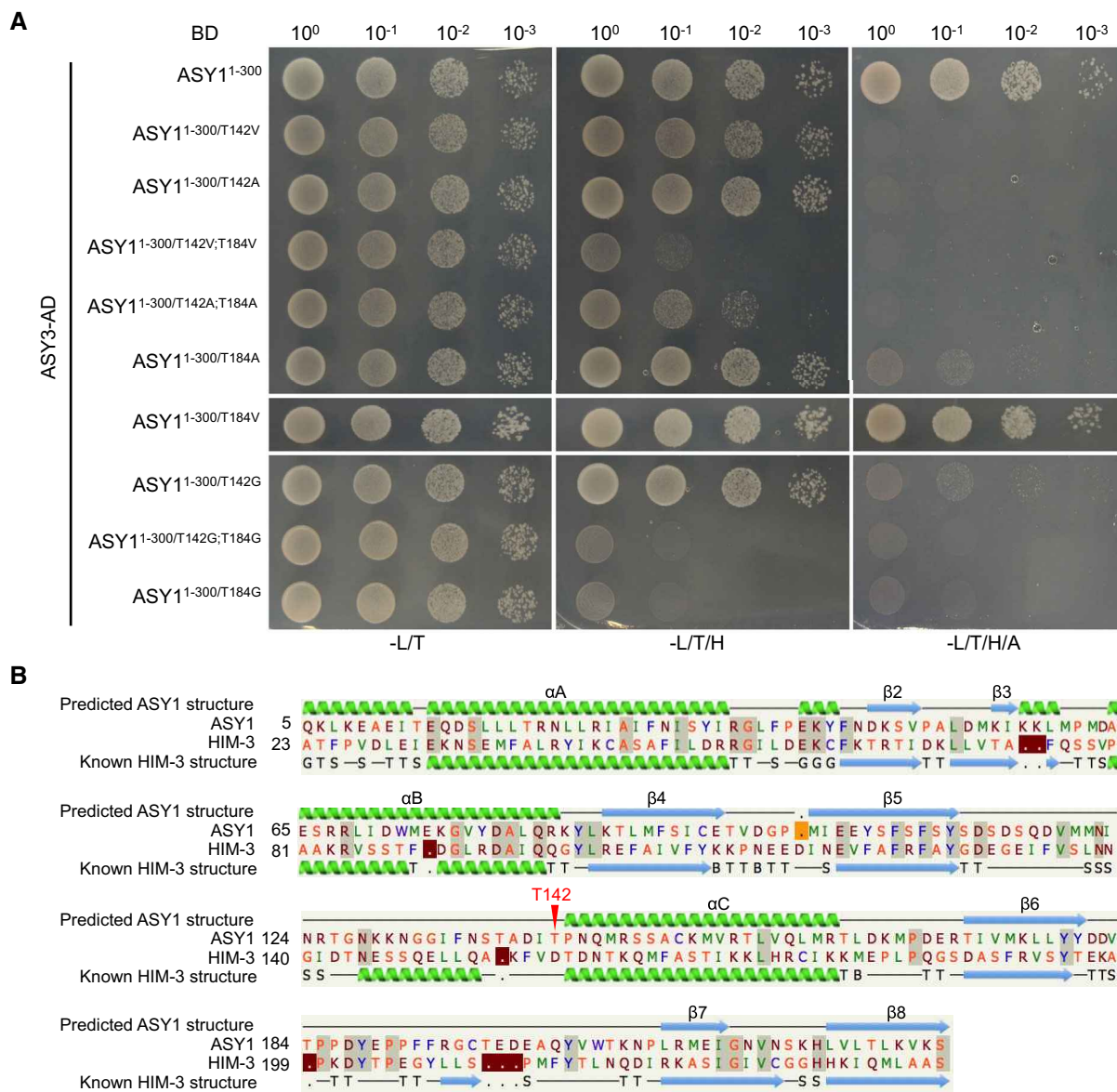
Figure EV4. Non-phosphorylatable substitutions of T142 in ASY1 reduce its interaction strength with ASY3.

A Yeast two-hybrid interaction assays of ASY3 with different ASY1 variants. Yeast cells harboring both the AD and BD plasmids were grown on synthetic medium supplied with glucose in the absence of Leu and Trp (-L/T, left panel), on SD medium in the absence of Leu, Trp, and His (-L/T/H, middle panel), and on SD medium in the absence of Leu, Trp, His, and Ade (-L/T/H/A, right panel). Yeast cells were incubated until OD_{600} = 1 and then diluted 10-, 100-, and 1,000-fold for the assays.

B The predicted structure of ASY1 HORMA domain based on the known structure of *C. elegans* HIM-3 (c4trkA) using Phyre2 protein structure prediction. Red arrowhead indicates the T142 site of ASY1.

2.2 SWITCH 1/DYAD is a WINGS APART-LIKE antagonist that maintains sister chromatid cohesion in meiosis

The following paper has been published in Nature Communications, 2019.
My contribution to this work is summarized below:

- Cytological characterization of the de-phosphomimetic $SWI1^{13A}$ mutant, in which the Cdk-mediated phosphorylated amino acid 13 was exchanged with a hydrophobic amino acid. I performed the chromosome spreads analysis of SWI^{13A}:GFP compared to wildtype and double *wapl1 wapl2* mutants (Figure 8A) and immunolocalization of $SWI1^{13A}$:GFP in wild-type plants (Figure S8b).
- Contribution to the immunolocalization analysis of REC8:GFP during prophase I in wildtype, *swi1-2* and *swi1-4* mutants (Figure S7)
- Chromosome spreads analysis of SWI1:GFP line #2 in *swi1-2* (Figure S2f), ASY3:RFP line #1 in *asy3* (Figure S3d), SWI1:RFP line #1 in *swi1-2* (Figure 5d) and $SWI1^{13A}$:GFP/WT plants (Figure S12)

ARTICLE

SWITCH 1/DYAD is a WINGS APART-LIKE antagonist that maintains sister chromatid cohesion in meiosis

Chao Yang [1], Yuki Hamamura[1], Kostika Sofroni [1], Franziska Böwer[1], Sara Christina Stolze [2], Hirofumi Nakagami [2] & Arp Schnittger [1]

Mitosis and meiosis both rely on cohesin, which embraces the sister chromatids and plays a crucial role for the faithful distribution of chromosomes to daughter cells. Prior to the cleavage by Separase at anaphase onset, cohesin is largely removed from chromosomes by the non-proteolytic action of WINGS APART-LIKE (WAPL), a mechanism referred to as the prophase pathway. To prevent the premature loss of sister chromatid cohesion, WAPL is inhibited in early mitosis by Sororin. However, Sororin homologs have only been found to function as WAPL inhibitors during mitosis in vertebrates and *Drosophila*. Here we show that SWITCH 1/DYAD defines a WAPL antagonist that acts in meiosis of *Arabidopsis*. Crucially, SWI1 becomes dispensable for sister chromatid cohesion in the absence of *WAPL*. Despite the lack of any sequence similarities, we found that SWI1 is regulated and functions in a similar manner as Sororin hence likely representing a case of convergent molecular evolution across the eukaryotic kingdom.

---

[1] Department of Developmental Biology, University of Hamburg, Hamburg 22609, Germany. [2] Max-Planck-Institute for Plant Breeding Research, Cologne 50829, Germany. Correspondence and requests for materials should be addressed to A.S. (email: arp.schnittger@uni-hamburg.de)

The tight regulation of sister chromatid cohesion is essential for accurate chromosome segregation during mitosis and meiosis. During S-phase, the genomic DNA is duplicated resulting in the formation of two sister chromatids per chromosomes. The newly formed sister chromatids are held together by the cohesin complex, which builds a ring-like structure embracing the chromatids. Besides sister chromatid cohesion, the cohesin complex is crucial for genome stability, DNA repair, chromatin structure organization, and gene expression[1–4].

The cohesin complex is highly conserved in the eukaryotic kingdom with homologs present from animals to plants comprising four core subunits: SMC1 and SMC3, two ATPases that belong to the family of structural maintenance of chromosomes (SMC) proteins, the heat-repeat domain protein SCC3/SA and one α-kleisin component RAD21/SCC1, which is replaced in meiosis by REC8/SYN1.

The presence of cohesin on chromosomes is very dynamic. Cohesin is already loaded onto chromosomes by the SCC2-SCC4 loader complex during the G1 phase of the cell cycle. Sister chromatid cohesion is established in the subsequent S-phase and regulated by several cohesin accessory proteins, including the PRECOCIOUS DISSOCIATION OF SISTER 5 (PDS5) and WINGS APART-LIKE (WAPL)[5–7]. PDS5 assists the acetylation of the SMC3 subunit by Establishment of cohesion 1 (Eco1)/Chromosome Transmission Fidelity 7 (CTF7), needed to close the cohesin ring[8–10]. Cohesin is then maintained on chromosomes until late G2 in the mitotic cell cycle and early prophase I in meiosis, respectively. As cell division is approaching metaphase, cohesin, especially on chromosome arms, undergoes tremendous removal mediated by the cohesin dissociation factor WAPL, a process known as prophase pathway of cohesin removal[11–14]. At the centromeric regions, cohesin is largely protected by the Shugoshin-PP2A complex[15,16]. This centromeric cohesin is released by a Separase-dependent proteolytic cleavage of the kleisin subunit RAD21/REC8, thereby allowing the separation of sister chromatids at anaphase onset (anaphase II in meiosis).

To prevent a premature release of sister chromatid cohesion in mitosis, especially on chromosome arms, Sororin counteracts the releasing force of WAPL by binding to PDS5 and displacing WAPL from PDS5[11,17–19]. However, Sororin has so far only been identified in vertebrates. More recently, an ortholog of Sororin, named Dalmatian, was found in *Drosophila*, which exert both Sororin's cohesin stabilizing and Shugoshin's cohesin protecting functions in mitosis[20].

In late prophase, Sororin is recognized by the APC/C^Cdh1 (Anaphase-promoting complex/cyclosome) and degraded by the ubiquitin–proteasome pathway, thereby releasing its repression of WAPL and activating the prophase removal of cohesin[18,21]. Phosphorylation through Cdk1 (cyclin-dependent kinase 1) and Aurora B kinase serves thereby as a signal for the degradation of Sororin[22,23].

In contrast to mitosis, it is not clear how sister chromatid cohesion is protected during early meiotic prophase I. Notably, Sororin does not seem to play a role for the regulation of meiotic cohesion. Although Sororin is present in male meiosis in mouse, it is exclusively localized on the central regions of the synaptonemal complex (SC) and not on the axial/lateral elements of SC where the cohesin complex is found[24]. This localization pattern makes Sororin unlikely, at least in mouse, be the protector of cohesion. This conclusion is substantiated by the finding that the localization of Sororin in the central region of the SC is not dependent on the meiosis-specific subunits REC8 and SMC1β[24].

In contrast, WAPL has been found to remove meiotic cohesin at late prophase in most if not all organisms studied including *Arabidopsis* and other plants[11,14,25–27]. Thus, it remains a puzzle how the activity of WAPL is inhibited in early meiotic prophase I especially since no obvious sequence homolog of Sororin or

Dalmatian has been identified in the plant lineage and other major branches of the eukaryotic kingdom[28].

Here, we report that the previously identified *SWI1* gene in *Arabidopsis* encodes a WAPL inhibitor. Despite any sequence similarities between SWI1 and Sororin, we further reveal that SWI1 antagonizes WAPL in prophase I of meiosis through a similar strategy as Sororin in mitosis. Moreover, SWI1 turned out to be amazingly similarly regulated in *Arabidopsis* as Sororin in vertebrates.

Results

Meiotic cohesin removal is mediated to large extent by WAPL. To get an understanding of cohesin dynamics during meiosis, we followed the expression and localization of a previously generated functional REC8-GFP reporter in male meiocytes by live cell imaging[29]. We observed that the majority of cohesin (~90%) in the wildtype, but not in the previously described *wapl1 wapl2* double mutant[11], is already largely released from chromatin prior to anaphase I indicating that the impact of the WAPL-dependent prophase pathway on cohesin removal is very strong in male meiosis of *Arabidopsis* (Fig. 1a–c; Supplementary Movies 1 and 2).

To follow WAPL1, we generated a WAPL1-GFP reporter, which fully complemented the *wapl1 wapl2* defects (Supplementary Fig. 1) and accumulated in somatic cells of the anther and in male meiocytes. In meiocytes, the WAPL1-GFP signal showed a homogeneous distribution in the nucleoplasm from pre-meiosis until leptotene, suggesting no or only a very weak interaction of WAPL1 with chromatin (Fig. 1di, ii). Subsequently, foci and/or short stretches of WAPL1-GFP appeared in the nucleus at late leptotene/early zygotene, coinciding with the eviction of cohesin from chromatin (Fig. 1diii). The accumulation of WAPL1-GFP signal on chromatin became more prominent in zygotene and pachytene, which is consistent with the progressive release of cohesin (Fig. 1c, d iv,v). In metaphase I, WAPL1-GFP was found at condensed chromosomes (Fig. 1dvi). While WAPL1-GFP signal is still present in the nucleus after the first meiotic division until tetrad stage, it was not localized to chromatin any longer (Fig. 1dvii, viii). This localization pattern was confirmed by immuno-localization of WAPL1-GFP using an antibody against GFP (Supplementary Fig. 1c).

SWI1 is expressed in early meiosis. The observation that WAPL1 is already present in early prophase at a time point when REC8 removal from chromatin has not started, suggested the existence of a WAPL repressor that might prevent WAPL from localizing to chromatin and unloading cohesin prematurely. However, no obvious sequence homolog of Sororin, the only known WAPL repressor in mitosis, exists in *Arabidopsis*[28]. We reasoned that a potential repressor of WAPL during meiosis should have all or at least some of the following characteristics: first, mutants of this repressor should experience premature loss of sister chromatid cohesion and hence probably have a strong mutant phenotype in meiosis. In turn, this makes it likely that such a mutant has already been identified due to the extensive search for meiotic mutants in *Arabidopsis*. Second, this repressor would probably be a protein of unknown molecular function. Third, as a regulator of sister chromatid cohesion, this factor should interact with the cohesin complex and hence, its correct localization to chromatin may also depend on a functional cohesin complex.

The gene *SWITCH1* (*SWI1*), also known as *DYAD*, was previously identified based on its requirement for sister chromatid cohesion in meiosis[30–32]. SWI1 encodes for a protein of unknown biochemical function and its mechanism of action
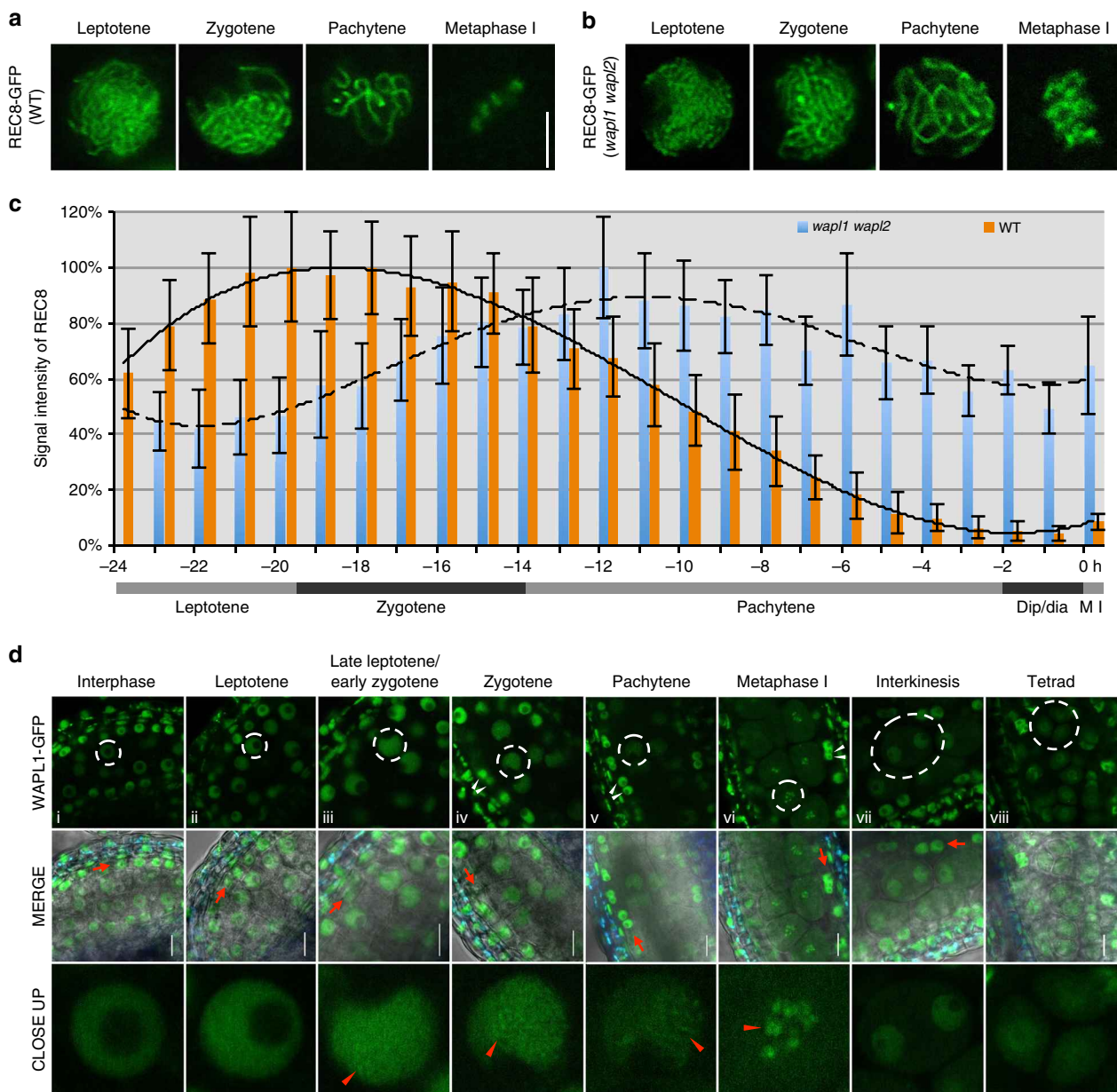
Fig. 1 Dynamics of REC8 and WAPL in male meiocytes. **a**, **b** Confocal laser scanning micrographs of REC8-GFP localization in male meiocytes in the wildtype (WT) (**a**) and in *wapl1 wapl2* double mutants (**b**). Bar: 5 μm. **c** Quantification of cohesin during meiosis I in male meiocytes of the wildtype (WT) and *wapl1 wapl2* mutants based on a REC8-GFP reporter. The graph represents the relative fluorescence intensity of the REC8-GFP signal; error bar represents standard deviation of at least 10 meiocytes analyzed. Dip/dia diplotene/diakinesis, M I metaphase I. Polynomial trendlines are shown (correlation coefficient $R^2 = 0.997$ and 0.898 for the wildtype (solid line) and *wapl1 wapl2* (dashed line), respectively. The source data of this graph are provided in the Source Data file. **d** Confocal laser scanning micrographs of WAPL1-GFP in anthers of *wapl1 wpal2* double mutants. Dashed white cycles indicate the meiocytes magnified in the close-up panel in the bottom row. Red arrowheads denote the accumulated WAPL1-GFP signal at chromatin. Red arrows indicate the layer of tapetal cells that are used as one of the criteria for staging. White arrowheads depict bi-nuclear tapetal cells. Bar: 10 μm

has been unresolved up to now. However, SWI1 was previously reported to be exclusively expressed in interphase prior to meiosis and could neither be detected in leptotene nor in any subsequent meiotic stage[30,31]. This expression pattern is difficult to reconcile with the *swi1* mutant phenotype, e.g., a failure to assemble the chromosome axis and to establish sister chromatid cohesion. Therefore, we revisited the expression pattern of *SWI1* in both male and female meiocytes by generating a genomic reporter in which the coding region of *GFP* was inserted directly before the STOP codon of *SWI1*. Expression of this reporter in *swi1* mutants could fully restore a wild-type meiotic program (Supplementary

Fig. 2). To stage the expression of SWI1, we also generated a functional reporter line for the chromosome axis protein ASYNAPTIC 3 (ASY3), where RFP was used as a fluorescent protein (Supplementary Fig. 3).

Consistent with previous reports, SWI1 was first detected as numerous foci/short stretches in interphase nuclei of both male and female meiocytes (Fig. 2a; Supplementary Fig. 4). In addition, the SWI1-GFP signal was present in leptotene and became even stronger as cells progressed through leptotene as staged by the migration of the nucleolus to one side of the nucleus[33–35] and the appearance of an ASY3 signal on condensing chromosomes
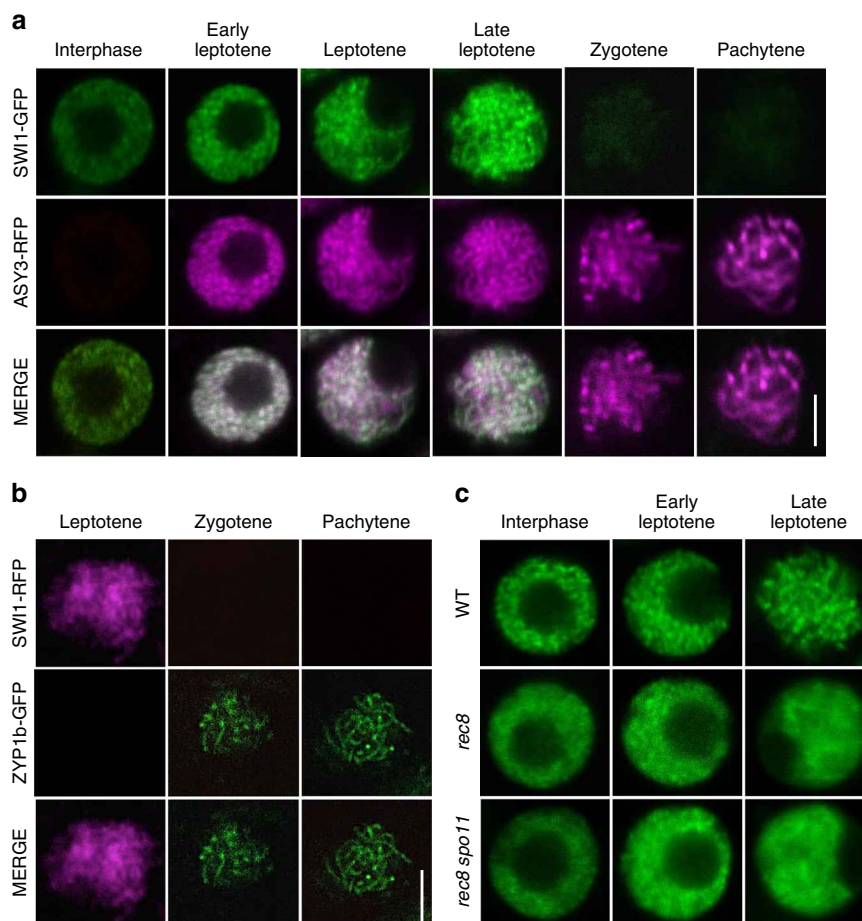
Fig. 2 Localization pattern of SWI1. Co-localization analysis of SWI1-GFP with ASY3-RFP (**a**) and SWI1-RFP with ZYP1b-GFP (**b**) during interphase and prophase I of wild-type male meiocytes using confocal scanning laser microscopy. **c** SWI1-GFP in the male meiocytes of the wildtype (WT), rec8 and rec8 spo11 mutants during interphase and prophase I. Bar: 5 μm

(Fig. 2a; Supplementary Fig. 4). This analysis also showed that SWI1 is chromatin associated. In zygotene, when chromosomes further condensed, highlighted by ASY3-RFP, the SWI1 signal strongly declined until it was not detectable any longer in late pachytene (Fig. 2a; Supplementary Fig. 4).

To confirm that SWI1 reaches its expression peak in late leptotene and decreases by zygotene, we constructed a reporter line for ZYP1b, a component of the central element of the synaptonemal complex. Since a fusion of ZYP1b to RFP resulted in only a very weak fluorescent signal, we generated a ZYP1b-GFP fusion along with a fusion of SWI1 to RFP, which could also restore full fertility and meiotic progression of swi1 mutants (Supplementary Figs. 5 and 6). In late leptotene, the SWI1-RFP signal is strongly present on chromosomes while no signal for ZYP1b was detected (Fig. 2b). From zygotene onwards, when short stretches of ZYP1b indicate partially synapsed chromosomes, the SWI1 signal was hardly detectable, corroborating that SWI1 is largely absent from chromosomes after zygotene corresponding to the removal of REC8 (Fig. 1a).

Chromatin association of SWI1 and REC8 is mutually dependent. Establishment of sister chromatid cohesion has been shown to be compromised during meiosis in swi1 and cohesin components, e.g., REC8 and SMC3, were found to be not properly bound to chromosomes in this mutant[30]. Using live cell imaging and immuno detection assays, we confirmed these cohesion defects by studying REC8-GFP in three different mutant

alleles, swi1-2, swi1-3, and swi1-4, that showed identical REC-GFP localization defects (Fig. 5a; Supplementary Fig. 7).

To address whether SWI1 localization also depends on cohesin, we introgressed the SWI1-GFP reporter into rec8 mutants. Although no obvious differences were found in interphase in comparison to swi1 mutants complemented by the expression of SWI1-GFP, we found that SWI1 did not properly localize to chromatin in rec8 mutants in prophase (Fig. 2c). This failure was not due to chromatin fragmentation present in rec8 since we observed the same pattern when the SWI1 reporter was introgressed into rec8 spo11 double mutants in which the endonuclease SPORULATION DEFECTIVE 11 (SPO11) is not functional and hence no double strand breaks are formed.

However, immuno-localization experiments using an antibody against GFP corroborated that residual levels of SWI1 remain on chromatin in rec8 mutants that expressed the SWI1-GFP reporter construct. This suggested that chromatin association of SWI1 also relies on other factors in addition to the REC8-containing cohesin (Supplementary Fig. 8a).

SWI1 interacts with PDS5 family proteins. A direct interaction of SWI1 with one of the cohesin components is a likely explanation for the observation that proper SWI1 localization is dependent on cohesin. To explore this possibility, we tested the interaction of SWI1 with all core cohesin subunits including SMC1, SMC3, REC8, and SCC3 by yeast two-hybrid assays. However, SWI1 did not interact with any of these proteins
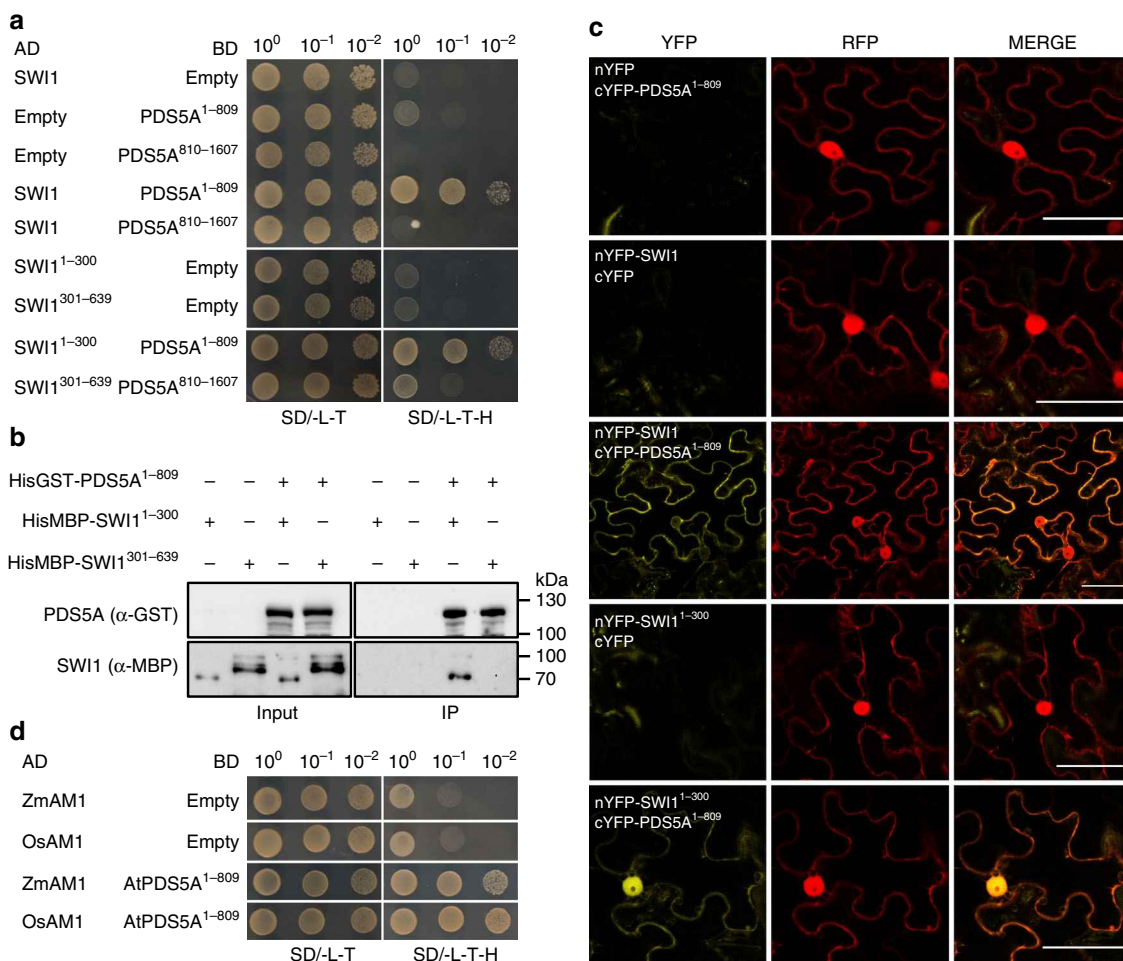
Fig. 3 SWI1 interaction with cohesin components. **a** Yeast two-hybrid interaction assay of SWI1 with PDS5A. SWI1 and PDS5A were divided into an N-terminal part (SWI$^{1-300}$, PDS5A$^{1-809}$) and a C-terminal part (SWI$^{301-639}$, PDS5A$^{810-1607}$). Yeast cells harboring both the AD (activating domain) and BD (binding domain) were grown on synthetic medium supplied with dextrose (SD) in the absence of Leu and Trp (SD/ -L -T, left panel) and on SD medium in the absence of Leu, Trp, and His (SD/ -L -T -H, right panel). Yeast cells were incubated until OD$_{600}$ = 1 and then diluted 10- and 100-fold for assays. **b** Co-immunoprecipitation assay of SWI1 with PDS5A. HisGST-PDS5A$^{1-809}$-bound or unoccupied agarose beads were incubated in the presence of HisMBP-SWI1$^{1-300}$ and HisMBP-SWI1$^{301-639}$. The pull-down fractions were analyzed by immunoblotting with anti-GST (upper panel) and anti-MBP (lower panel) antibodies. The source data of the uncropped immunoblots are provided in the Source Data file. **c** Interaction of SWI1 with PDS5A using bimolecular fluorescence complementation (BiFC) assays. YFP fluorescence indicates a successful complementation and hence interaction of the proteins tested. RFP is used as an indicator for the successful *Agrobacterium* infiltration. **d** Yeast two-hybrid interaction assay of SWI1 homologs in maize (ZmAM1) and rice (OsAM1) with *Arabidopsis* PDS5A (PDS5A)

(Supplementary Fig. 9a). We further investigated the interaction of SWI1 with the cohesin accessory proteins PDS5A, one of the five *PDS5* genes in *Arabidopsis*, and WAPL1, one of the two WAPL homologs. While we did not find an interaction of SWI1 with WAPL1, SWI1 strongly interacted with the N-terminus but not the C-terminus of PDS5A (Fig. 3a; Supplementary Fig. 9b). The interaction domain of SWI1 was then determined to reside in the N-terminal 300 amino acids as the C-terminal domain from amino acid 301-639 failed to bind to N-terminus of PDS5A (Fig. 3a). This interaction was confirmed by GST pull down assay with recombinant proteins purified from *E. coli*, and by bimolecular fluorescence complementation (BiFC) assay in tobacco leaves (Fig. 3b, c). Whether SWI1 also interacts with the other four PDS5 paralogs present in *Arabidopsis*, was next addressed in BiFC assay. While PDS5B and PDS5D only weakly bound to SWI1, an even stronger interaction of SWI1 with PDS5C and PD55E than with PDS5A was found, indicating that SWI1 has the potential to regulate all PDS5 proteins in *Arabidopsis*.

SWI1 antagonizes WAPL. PDS5 has been shown to form a complex with WAPL in several vertebrates and yeast[12,13,36,37]. Correspondingly, we found that *Arabidopsis* WAPL1 bound to the N- but not the C-terminus of PDS5A by yeast two-hybrid and BiFC assays (Supplementary Fig. 9b, c). Thus, WAPL1 and SWI1 interact, at least broadly, with the same region of PDS5. Sororin is known to bind to PDS5 and displace WAPL from the cohesin complex[18]. To assess whether SWI1 may act similarly as Sororin by dislodging WAPL from PDS5, we first compared the binding affinity of PDS5A with SWI1 and WAPL1 by using a ratiometric BiFC (rBiFC) system[38] that allows quantification of the interaction strength. The rBiFC assay revealed that the interaction between SWI1 and PDS5A is stronger than the interaction of WAPL1 with PDS5A (Fig. 4a, b). To further explore the relationship of these three proteins, we perform an in vitro competition experiment. To this end, we loaded recombinant WAPL1-PDS5A heterodimers co-purified from *E. coli* onto PDS5A-bound beads and incubated them with increasing concentrations of SWI1. With increasing concentrations of SWI1, more WAPL1
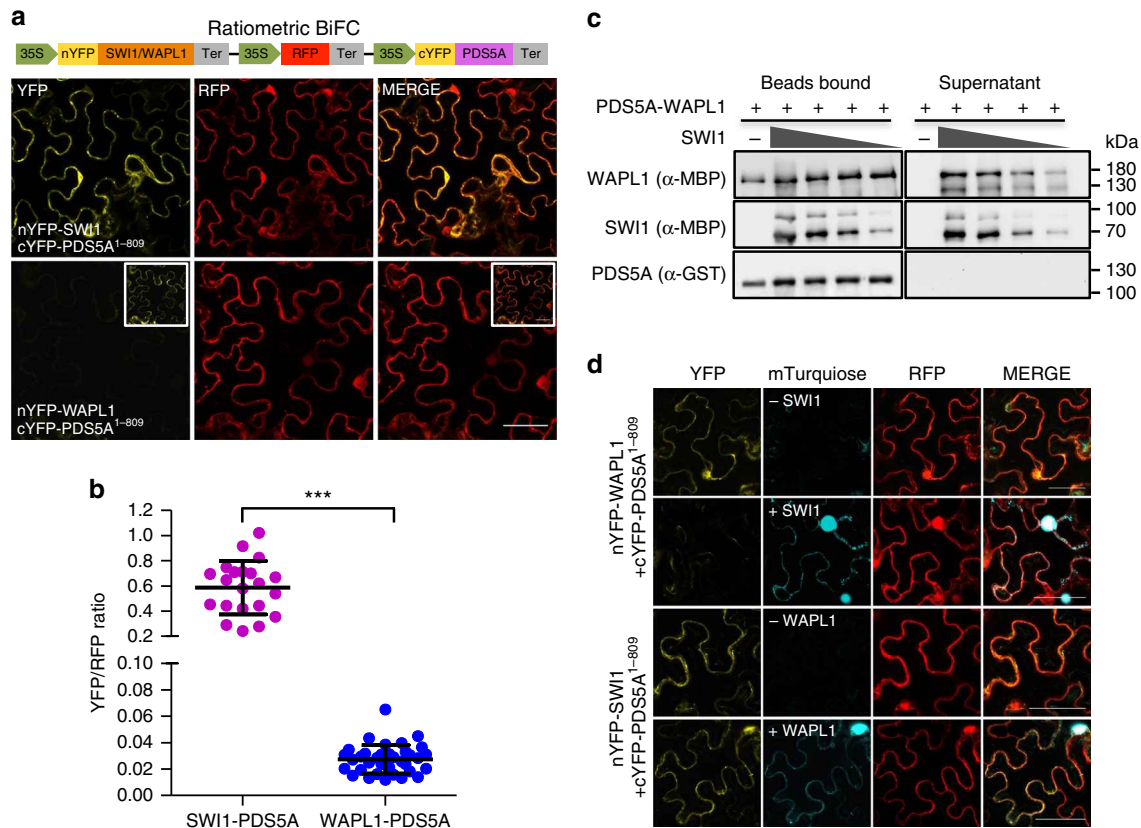
Fig. 4 SWI1 dissociates WAPL1 from PDS5A. **a** Ratiometric BiFC (rBiFC) assays of PDS5A with SWI1 and WAPL1. The upper panel depicts the ratiometric gene expression cassette, and the below panels show representative images of the assay that were captured with the same settings at a confocal laser scanning microscope. The level of YFP fluorescence indicates the interaction strength with the RFP fluorescence used as a reference. The images in the white box represent the same pictures as the ones shown in the respective panel but taken with increased sensitivity revealing an interaction between WAPl1 and PDS5A. Bar: 50 µm. **b** Quantification of the rBiFC assay by calculating the ratio between YFP and RFP signal intensity shown in **a**. Asterisks indicate significant difference (Student's t-test, $P < 0.001$). Error bars represent standard deviations. **c** SWI1 causes the dissociation of WAPL from PDS5. Anti-GST beads were incubated with or without SWI1[1-300] in the presence or absence of PDS5A[1-809]-WAPL1 heterodimers. PDS5A[1-809] is His-GST tagged. WAPL1 and SWI1[1-300] are His-MBP tagged. Beads bound proteins were separated from the supernatant and analyzed by immunoblotting. Different amounts of SWI1[1-300] were used for the experiment. The empty beads control was shown in Supplementary Fig. 9e. The source data of the uncropped immunoblots are provided in the Source Data file. **d** Co-expression of SWI1-mTurquoise inhibits the interaction of WAPL1 with PDS5A in tobacco leaf cells while the presence of WAPL1-mTurquoise has no obvious impact on the interaction of SWI1 with PDS5A. Bar: 50 µm

protein could be released from PDS5A into the supernatant (Fig. 4c). Conversely, more SWI1 was bound to PDS5 with increasing concentrations of SWI1.

The displacement of WAPL from PDS5 by SWI1 was further confirmed by a competitive binding assay in tobacco leaf cells (Fig. 4d). While the simultaneous presence of WAPL1 tagged with mTuquoise did not affect the interaction of SWI1 with PDS5A, the co-expression of SWI1-mTurquoise resulted in a strong reduction of the BiFC signal from WAPL1-PDS5A interaction (Fig. 4d). Thus, despite any sequence similarities, SWI1 appears to act in a similar fashion as Sororin in animals.

Therefore, we speculated that the absence of WAPL should restore the presence of REC8 on chromatin in *swi1* mutants. To this end, we generated the triple mutant *swi1 wapl1 wapl2* containing in addition the *REC8-GFP* reporter. REC8 localization was then analyzed in male meiocytes at different meiotic stages of this triple mutant in comparison to the wildtype, *swi1* and *wapl1 wapl2* double mutants. In contrast to *swi1* mutants (Fig. 5a, b; Supplementary Fig. 7; Supplementary Movie 3), REC8 localization in *swi1 wapl1 wapl2* mutants was nearly identical to the pattern found in *wapl1 wapl2* double mutants, i.e., residing on chromosomes till metaphase I (Figs. 1a, b and 5c, d; Supplementary Movie 4). Note that due to the failure of chromosome axis

formation and of the aberrant migration of nucleolus in *swi1* mutants, the meiotic stages in *swi1* mutants were determined by the morphology of meiocytes in combination with the number of nuclei in tapetal cells[29,34]. The restoration of cohesion in the *swi1 wapl1 wapl2* and the resemblance to the *wapl1 wapl2* mutant phenotype was further confirmed by chromosome spread analysis (Fig. 5c). Since *swi1* mutants do not have an obvious growth defect and since we also could not detect SWI1 outside of meiocytes, we conclude that SWI1 specifically maintains cohesion in meiosis by antagonizing WAPL. We also found that the putative SWI1 homologs from maize and rice, *AMEIOTIC 1* (*AM1*), which likewise are required for meiotic progression and cohesion establishment[39,40], both interacted with *Arabidopsis* PDS5A in a yeast two-hybrid interaction assay (Fig. 3d). Thus, it is likely that the SWI1 function as a WAPL antagonist in meiosis is conserved in flowering plants and, given the presence of SWI1 homologs in moss, possibly in all land plants.

SWI1 presence is controlled by Cdk-cyclin activity. A crucial question is how WAPL is liberated from the inhibition by SWI1 in late prophase to mediate the release of cohesin (Fig. 1a–c). In vertebrate mitosis, this problem is solved by the phosphorylation
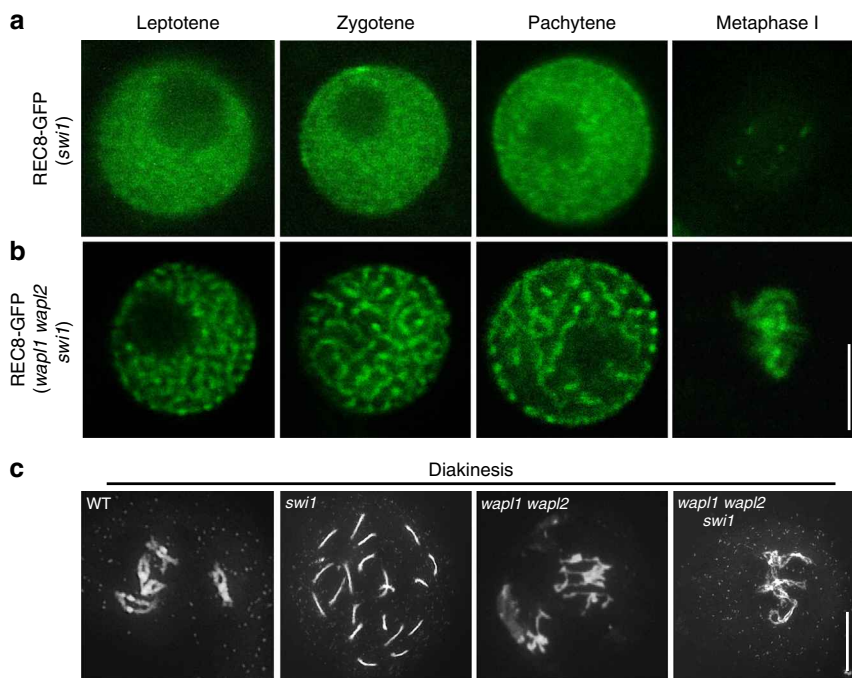
Fig. 5 SWI1 is dispensable for the sister chromatid cohesion in the absence of WAPL. **a**, **b** Confocal laser scanning micrographs of REC8-GFP localization in male meiocytes in *swi1* (**a**) and in *swi1 wapl1 wapl2* (**b**). Bar: 5 μm. **c** Chromosome spreads of the wildtype (WT), *swi1*, *wapl1 wapl2* and *swi1 wapl1 wapl2* mutants in diakinesis. Bar: 10 μm

dependent release of Sororin from chromatin. Two kinases have been observed to participate in this regulation, Cyclin-dependent kinase 1 (Cdk1) and Aurora B[22,23]. We observed that SWI1 contains 13 consensus Cdk phosphorylation sites, 12 [S/T]P and 1 [S/T]Px[R/K] sites. We found that at least 7 of these sites can be phosphorylated in an in vitro kinase assay by CDKA;1, the *Arabidopsis* Cdk1/Cdk2 homolog, together with the meiotic cyclin SOLO DANCERS (SDS) (Fig. 6a; Supplementary Table 1).

To address whether the analogies between SWI1 and Sororin would extend to phospho-regulation, we introgressed the *SWI1-GFP* reporter, together with the *ASY3-RFP* reporter for staging, into weak loss-of-function alleles of *cdka;1* (*CDKA;1^T161D*)[41]. Similar to the wildtype, SWI1 is present on chromatin in *CDKA;1^T161D* plants until leptotene (Fig. 6b). However, the SWI1 signal does not decline as strongly in *CDKA;1^T161D* plants as in the complemented *swi1* mutants. Remarkably, SWI1 stayed associated with chromosomes even until pachytene (Fig. 6b). Similarly, SWI1-GFP was also prolonged present in meiocytes of *sds* mutants (Fig. 6c).

To test whether the phosphorylation of SWI1 is essential for its release from chromosomes at late prophase I, we generated de-phospho mutant constructs. The localization pattern of SWI1 with four mutated CDK phosphorylation sites in the N-terminus of SWI1 (SWI1^4A-GFP), was indistinguishable from wildtype SWI1 protein (Fig. 6c). However, mutating all 13 or only the C-terminal nine phosphorylation sites in SWI1 (SWI1^13A-GFP and SWI1^9A-GFP), resulted in extended occupancy of SWI1 on chromosomes, reminiscent of the pattern found in *CDKA;1^T161D* and *sds* mutants (Fig. 6c; Supplementary Fig. 8b). Note that SWI1^13A-GFP and SWI1^9A-GFP seems to be functional since the cohesion defects in early prophase I were completely rescued in *swi1* mutants harboring either version (Supplementary Fig. 10d, e; for effects in later stages of meiosis, see below).

To complement this analysis, we also generated a phospho-mimic version of SWI1 in which the Serine or Threonine of all 13 CDK phosphorylation sites were mutated to the negatively charged amino acid Aspartate (SWI1^13D-GFP) and introduced

this construct into wild-type plants. SWI1^13D-GFP showed the same localization pattern as the wild-type version, indicating that the phosphomimic SWI1 version is recognized by its releasing factors (Fig. 7). Moreover, we did not find any reduction in fertility of these plants (Supplementary Fig. 11).

Taken together, these findings corroborated that mitosis in vertebrates and meiosis in plants (*Arabidopsis*) utilize a similar mechanism to control the presence of the WAPL inhibitors on chromatin through phosphorylation by CDK-cyclin complexes. However, the observation that SWI1 was not prematurely removed from chromatin by mimicking its phosphorylation indicates that phosphorylation is necessary but not sufficient for SWI1 removal hinting at a higher order coordination of SWI1 phosphorylation and the machinery involved in controlling its stability.

Chromatin release of SWI1 is important for WAPL action. Our above presented cytological and biochemical data suggested that the timely release of SWI1 is needed for WAPL to remove cohesin. To test this in vivo, we made use of the dephospho-mutant version of SWI1^13A-GFP that complemented the early defects of *swi1* mutants (Supplementary Fig. 10d, see above). Notably, *swi1* mutant harboring SWI1^13A-GFP were to a large degree infertile as seen by their short siliques and strongly reduced pollen viability (Supplementary Fig. 10a–c,i). Since these defects precluded discerning between a dominant effect as expected from interfering with WAPL versus a partial functionality of SWI1^13A-GFP, we switched to wild-type plants harboring the SWI1^13A-GFP construct (SWI1^13A-*GFP*/WT) for the following analysis. While the vegetative growth of these plants was not affected, they also suffered from a drastic fertility reduction in 51 out of 55 T1 transformants similar to *swi1* mutants expressing the SWI1^13A-*GFP* mutant version (Supplementary Fig. 10a–c, i), indicating that it is not the lack of a functional version that causes this phenotype.

Chromosome spread analysis showed that chromosome pairing and synapsis was not altered in SWI1^13A-*GFP*/WT
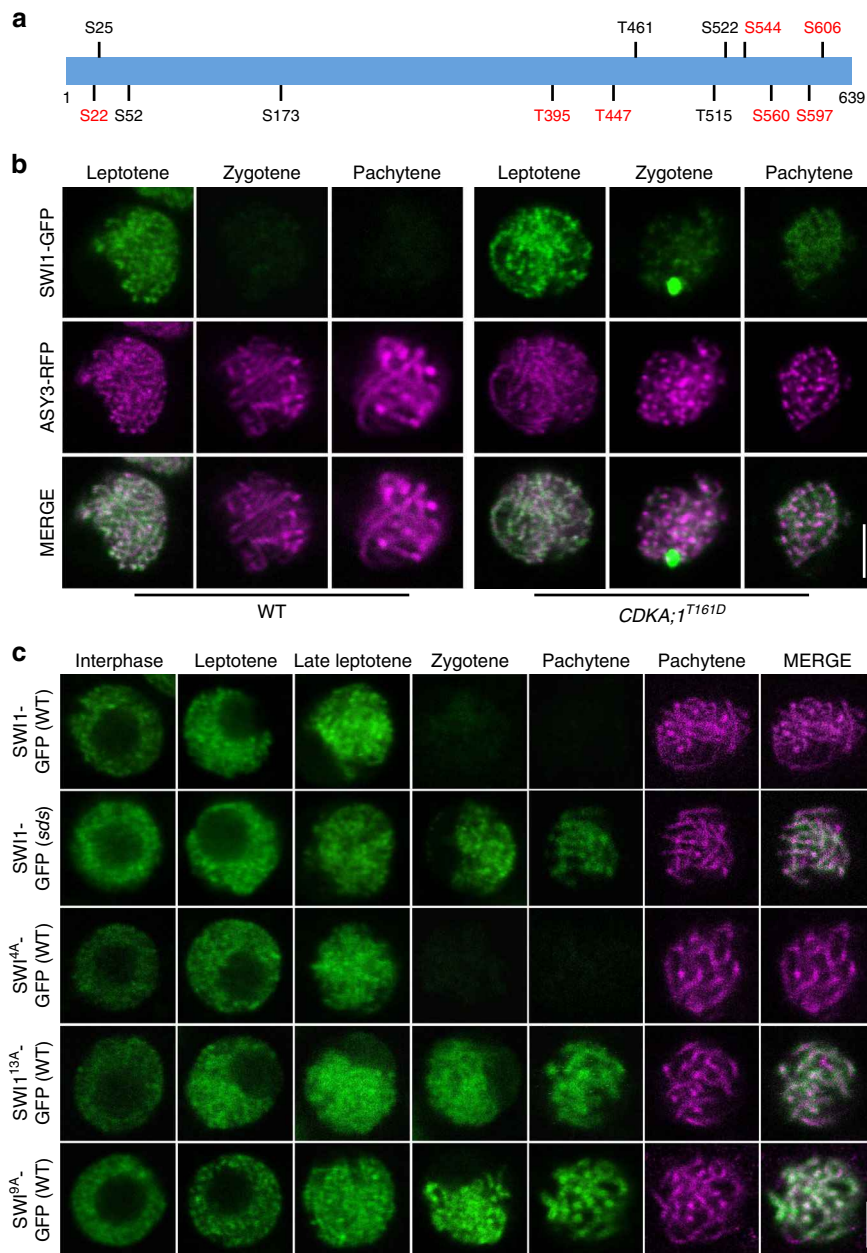
Fig. 6 Phospho-control of SWI1 localization. **a** Schematic representation of SWI1 with the position of the 13 [S/T]P motifs. Phosphorylated sites identified by mass spectrometry are labeled in red. S serine, T threonine. **b** Confocal laser scanning micrographs of SWI1-GFP in comparison with ASY3-RFP as a meiosis staging marker in the wildtype (WT) and $CDKA;1^{T161D}$ male meiocytes. **c** The expression of SWI1-GFP and the de-phospho mutants SWI1^{4A}-GFP, SWI1^{9A}-GFP and SWI1^{13A}-GFP were analyzed in interphase and prophase I of male meiocytes of sds mutants and wild-type plants (WT), respectively. ASY3-RFP localization is only shown for pachytene. Bar: 5 μm

($n = 88$) consistent with the restoration of these defects in $swi1$ mutants by the same construct (Fig. 8ai). The first obvious defects were found at diakinesis. Whereas 5 clearly discernable bivalents are then present in the wildtype, chromosomes were entangled and clustered in $SWI1^{13A}$-GFP/WT (51 out of 101 meiocytes analyzed) (Fig. 8aii, xvi). Intertwined chromosomes of $SWI1^{13A}$-GFP/WT persisted until metaphase I (87 out of 190 meiocytes analyzed) (Fig. 8a iii, ix, x, xvii). After metaphase I, chromosome fragmentation was observed (Fig. 8a iv, xi, xviii). Entangled chromosomes were even found at metaphase II (30 out of 71 meiocytes analyzed) (Fig. 8a vi, xiii, xx). Finally, tetrads with an unequal amount of DNA and triads were frequently observed in $SWI1^{13A}$-GFP/WT (84 out of 156 meiocytes analyzed) (Fig. 8a vii, xiv, xxi; Supplementary Fig. 12). Taken together, $SWI1^{13A}$-GFP/

WT plants have an over cohesive phenotype which closely resembled the defects of the $wapl1$ $wapl2$ mutants.

We therefore speculated that the prolonged retention of SWI1 might result in an extended abundance of cohesin on chromatin. To address this question, plants expressing a SWI1^{13A} version without a fluorescent tag were generated and combined with plants harboring the $REC8$-GFP reporter. Based on the time-resolved quantification of REC8-GFP signal in male meiocytes, we found that in comparison to wildtype, REC8-GFP signal showed a decreased speed of removal in $SWI1^{13A}$ plants (1/2 removal time, 14.66 ± 0.58 h, $n = 3$ in $SWI1^{13A}$ versus 11.33 ± 1.15 h, $n = 3$ in wildtype) (Fig. 8b; Supplementary Movies 5 and 6). At metaphase I, instead of ~10% ($n = 3$) REC8-GFP signal retained in the wildtype, twice the signal, i.e., ~20% ($n = 3$) was
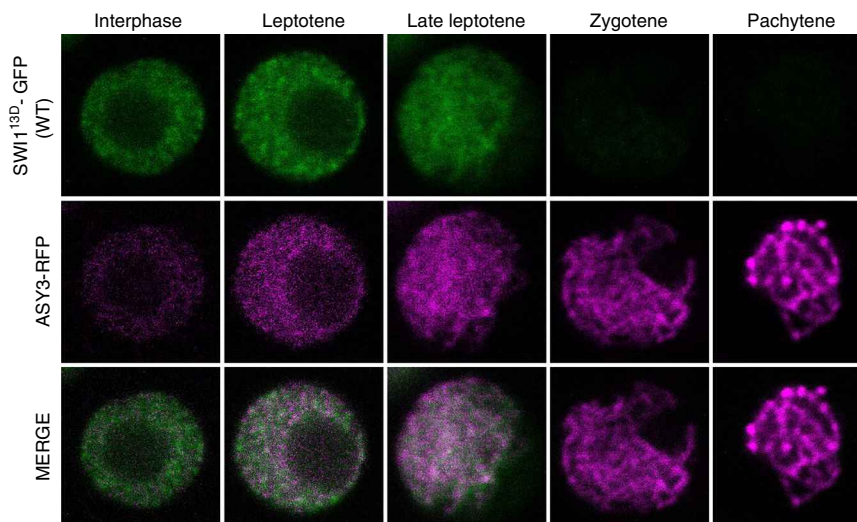
Fig. 7 Localization of the phosphomimic version of SWI1. The localization of the phosphomimic version SWI1^{13D}-GFP is indistinguishable from the wild-type SWI1-GFP version (compare with Fig. 2a). ASY3-RFP is used for staging. Bar: 5 μm

observed in $SWI1^{13A}$ plants (Student's t-test $P < 0.0001$) partially resembling the retention of REC8-GFP in *wapl1 wapl2* mutants. However, it has to be noted that the level of REC8-GFP withholding in *wapl1 wapl2* is higher than in $SWI1^{13A}$ plants (~55% versus ~20%) (Figs. 1a and 8b; Supplementary Movies 2, 5, and 6). The reason for this is not clear and we cannot exclude a slightly altered biochemical property of $SWI1^{13A}$ due to the substitution of 13 amino acids possibly resulting in a less efficient inhibition of WAPL. Consistent with such a scenario is the observation that the eviction of REC8 starts apparently earlier in $SWI1^{13A}$ versus the wildtype (Fig. 8b). In any case, our data strongly suggest that a vast (more than 90%) removal of REC8 is crucial for meiosis and even an increase from 10 to 20% is sufficient to cause an over cohesive effect underlining the importance of the WAPL-PDS5-SWI1 regulatory triangle.

SWI1 abundance is controlled by the APC/C. Our results show that the release of SWI1 from chromosomes is regulated by CDKA;1-mediated phosphorylation. However, the degradation pathway for SWI1 is still obscure. An analysis of SWI1 by the GPS-ARM algorithm[42] revealed five putative destruction boxes (D-box) in the C-terminus of SWI1, including 2 canonical and 3 less conserved D-boxes, hinting at a potential regulation of SWI1 by the APC/C (Supplementary Fig. 13a).

To address the functional relevance of the predicated D-boxes, we first mutated the two conserved D-boxes at position 306-309 and 559-562 (RXXL to AXXA) and generated plants expressing this SWI1 mutant version (*SWI1-Δ2D-box-GFP*). Since plants harboring *SWI1-Δ2D-box-GFP* had no any obviously altered SWI1 protein expression and localization pattern (Supplementary Fig. 13b), we mutated all 5 D-boxes (*SWI1-Δ5D-box-GFP*). Plant expressing *SWI1-Δ5D-box-GFP* showed an extremely prolonged abundance of SWI1 that only disappeared in tetrads, suggesting that SWI1 is targeted by the APC/C for degradation from zygotene onwards (Fig. 9a; Supplementary Fig. 10f–i). We also observed reduced fertility of *SWI1-Δ5D-box-GFP* expressing plants consistent with the prolonged presence of SWI1 on chromatin. However, the reduction in fertility was less severe in plants expressing *SWI1-Δ5D-box-GFP* than in *wapl1 wapl2* mutants or in $SWI1^{13A}$-*GFP* expressing plants (Supplementary Fig. 10f–i). Again, we cannot exclude a compromised function of SWI1-Δ5D-box-GFP due to the many point mutations introduced and, consistent with an affected functionality, we also

observed that SWI1-Δ5D-box-GFP had a slightly less pronounced chromosome association than the non-mutated SWI1-GFP version (compare Fig. 9a with Fig. 2a).

To hence seek further evidence for a possible proteolytic control of SWI1, we performed a cell free degradation assay by incubating protein extracts from flower buds with the purified C-terminal half of the SWI1 protein (HisGST-SWI1$^{301-639}$). We found that SWI1$^{301-639}$ degradation started in mock-treated samples after 15 min of incubation time and the majority of the protein (80%) was not detectable any longer by 90 min. In contrast, SWI1$^{301-639}$ disappeared at a much slower rate in samples treated with the proteasome inhibitor MG132 and after 90 min, more than 50% of the protein was still present (Fig. 9b i, ii, c).

Since we found that phosphorylation is required for the release of SWI1 from chromatin, we next compared the degradation kinetics of wild-type SWI1$^{301-639}$ with the mutated SWI1$^{301-639/9A}$ version. Indeed, the non-phosphorylatable version SWI1$^{301-639/9A}$ was stabilized in comparison to the phosphorylatable version and showed similar turnover kinetics as MG132-treated extracts (Fig. 9b iii, c). To further assess whether the degradation of SWI1 is mediated through the phosphorylation of SWI1 by CDKs, we treated the protein extracts with Roscovitine, a potent CDK inhibitor[43]. In comparison to the mock-treated sample, SWI1$^{301-639}$ was also stabilized under Roscovitine treatment, substantiating that CDK-dependent phosphorylation marks SWI1 for 26S proteasome-dependent degradation which relies on D-boxes and thus, is likely mediated by the APC/C.

Discussion

The precise establishment, maintenance, and removal of sister chromatid cohesion is essential for faithful chromosome segregation in both mitosis and meiosis. In contrast to the well-described mechanisms of cohesion regulation in mitosis[17,18,20], much less is known about the control of cohesion in meiosis. Our study in *Arabidopsis* provides evidence that the prophase pathway of cohesion regulation exists in meiosis including the inhibition of the cohesin remodeler WAPL by a new type of inhibitor represented by the previously identified protein SWI1 that functions and is regulated in an amazingly similar fashion as Sororin in animals. Given that both animals and plants have WAPL homologs and that the lineage that led to plants and to animals were very early separated in eukaryotic evolution, much earlier than the separation of the predecessors of animals and yeast, it is
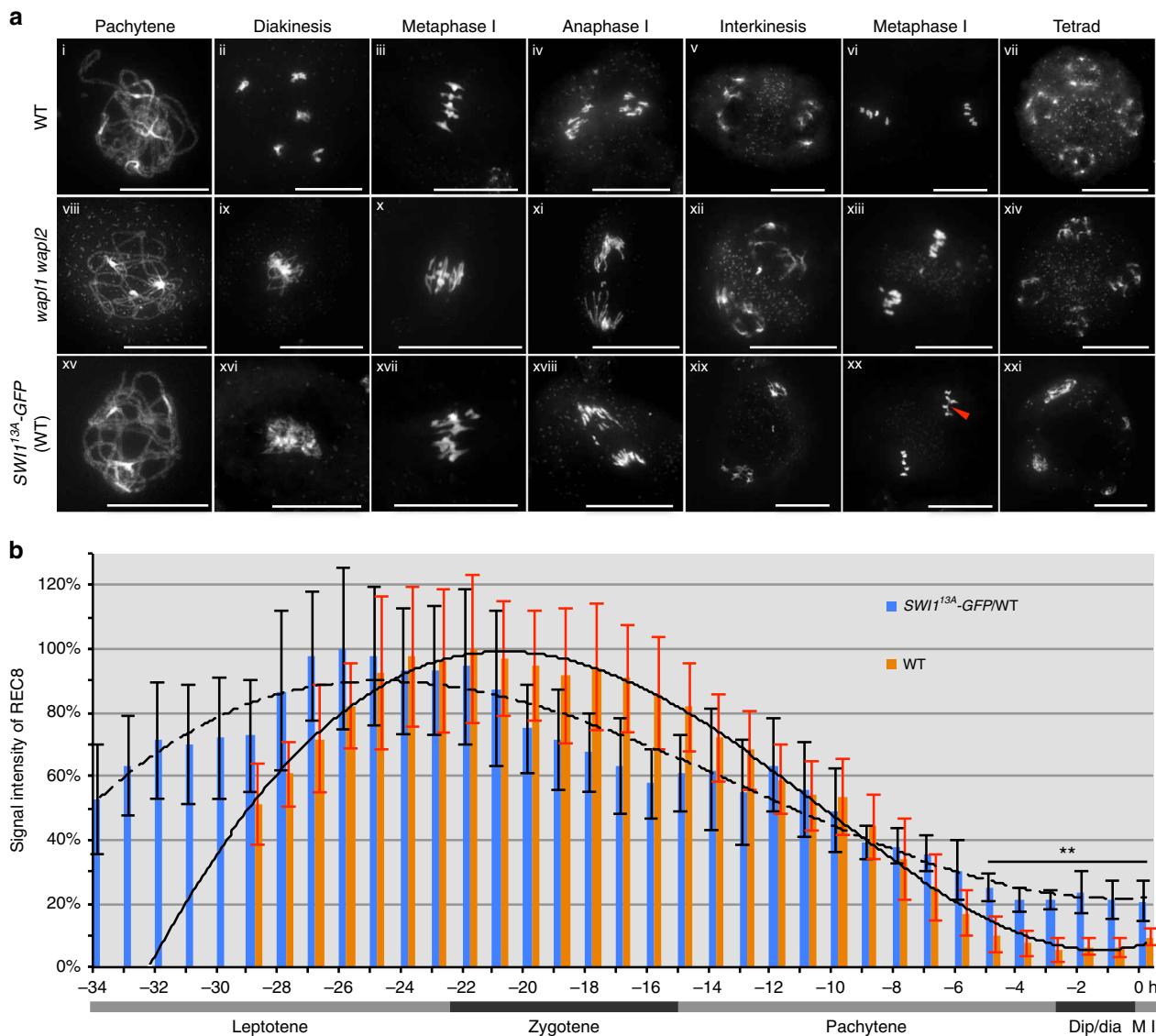
Fig. 8 De-phosphomimic SWI1 13A-GFP interferes with the cohesin removal. **a** Chromosome spreads of male meiocytes of the wildtype (WT), *wapl1 wapl2* mutants, and *SWI1 13A-GFP* in wild-type plants (*SWI1 13A-GFP*/WT). Bar: 20 μm. Red arrowhead in xx highlights intertwined chromosomes. **b** Quantification of cohesin during meiosis I in male meiocytes of the wildtype (WT) and *SWI1 13A-GFP*/WT based on the analysis of a REC8-GFP reporter. The graph represents the relative intensity of the REC8-GFP signal; error bar represents standard deviation of at least 10 meiocytes analyzed. Asterisks represent significant difference (Student's *t*-test, $P < 0.01$). Dip/dia diplotene/diakinesis, M I metaphase I. A solid polynomial trendline is shown for the wildtype and a dashed line for *SWI1 13A-GFP*/WT (correlation coefficient $R^2 = 0.993$ for the wildtype and 0.942 for *SWI1 13A-GFP*/WT). The source data of this graph are provided in the Source Data file

likely that a basic prophase pathway of cohesin removal is very ancient and was probably present in the last common ancestor of animals and plants.

However, the repression of WAPL appears to have evolved independently in animals and plants and hence is likely younger in evolutionary terms. Remarkably, the two independent WAPL regulators, Sororin and SWI1, target the same cohesin subunit, i.e., PDS5, and are themselves controlled by a similar mechanisms, i.e., Cdk phosphorylation. Our finding that SWI1 from *Arabidopsis* can also bind to PDS5 from maize and rice indicates that the function of SWI1 as a WAPL antagonist is conserved in flowering plants. Moreover, the presence of *SWI1* homologs in moss gives rise to the hypothesis that *SWI1* appeared very early in the plant lineage.

Based on our results, we propose the following model of how SWI1 prevents the premature removal of sister chromatid cohesion in *Arabidopsis* (Fig. 10): SWI1 starts to be expressed and is

recruited onto chromosomes by interacting with PDS5 proteins during very early meiosis, likely already during the premeiotic S phase. The recruitment of SWI1 is dependent, at least partially, on the formation of the cohesin complex (Fig. 2c). After entry into meiosis, cohesin needs to be maintained until late prophase to facilitate multiple processes of meiosis, e.g., double-strand break (DSB) repair, chromosome pairing, and homologous recombination[44,45]. The maintenance of cohesin is achieved by SWI1 that has a higher affinity towards PDS5 than WAPL, thereby displacing WAPL from PDS5, consistent with the dispersed localization of WAPL at early stages in prophase I (Fig. 1d). Given the stronger interaction strength between SWI1 and PDS5 versus WAPL and PDS5, it seems likely that both complexes do not co-exist or that at least the SWI1-PDS5 complex is much more prominent than a WAPL-PDS5 complex if all three proteins are equally present.
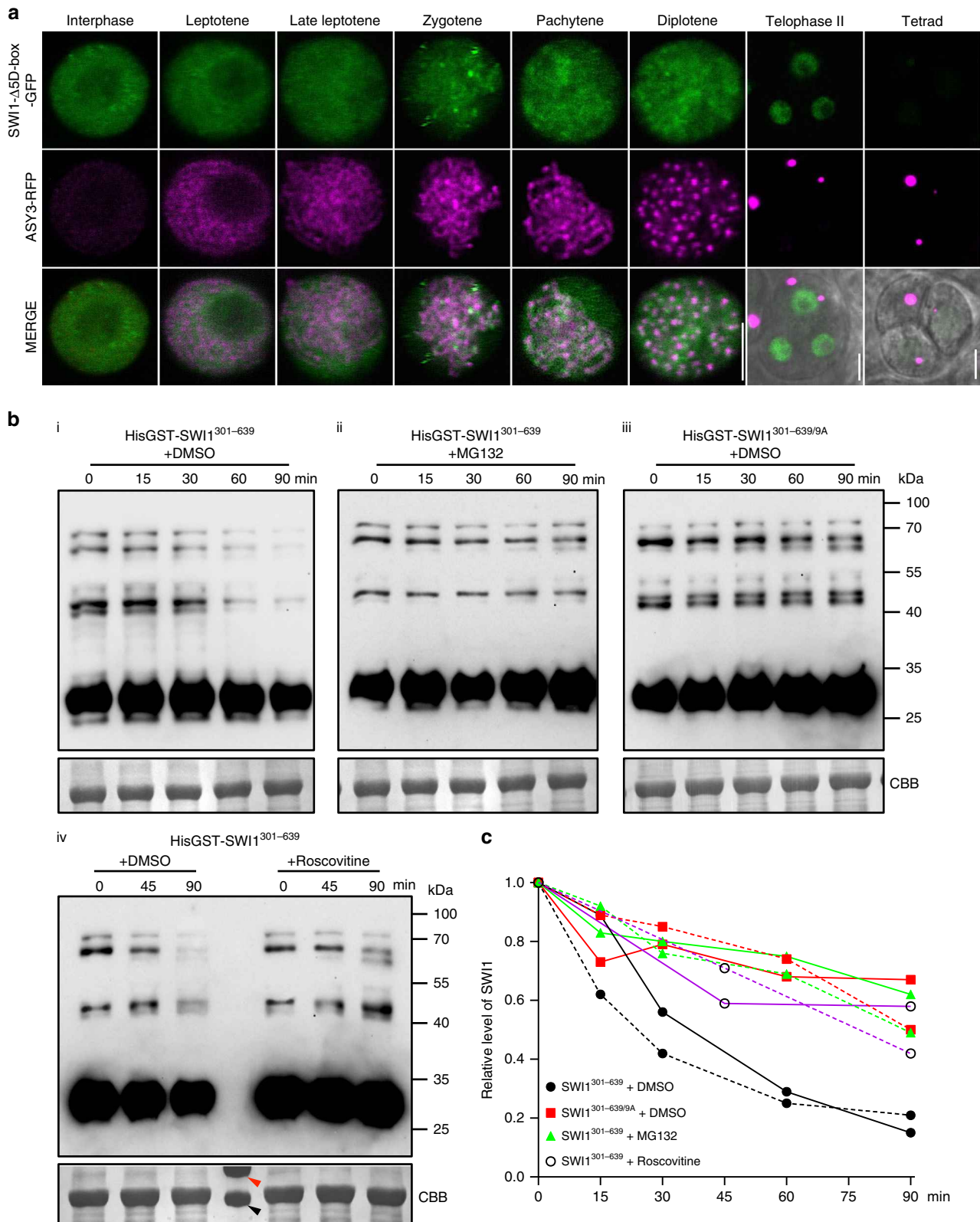
Fig. 9 APC/C-mediated degradation of SWI1. **a** Deletion of the five predicted destruction boxes (D-box) in SWI1 (SWI1-Δ5D-box-GFP) results in prolonged occupancy along chromatin in comparison with SWI1-GFP (Fig. 2a). ASY3-RFP is shown for staging. Bar: 5 μm. **b** Cell free degradation assay of HisGST-SWI$^{301-639}$ and HisGST-SWI$^{310-639}$ in the presence of DMSO (solvent control), 50 μm MG132, or 5 μm Roscovitine. The source data of the uncropped immunoblots are provided in the Source Data file. **c** Relative protein level of SWI1 according to **b**. The intensity of all bands between 100 and 40 kDa was measured and plotted on the graph. The solid lines represent the relative protein level of SWI1 shown in **b** and the dashed lines depict the results of the second biological replicate. The large subunit of Rubisco stained by CBB verifies the equal loading of the samples. The red and black arrowheads indicate the protein marker at 70 and 55 kDa, respectively
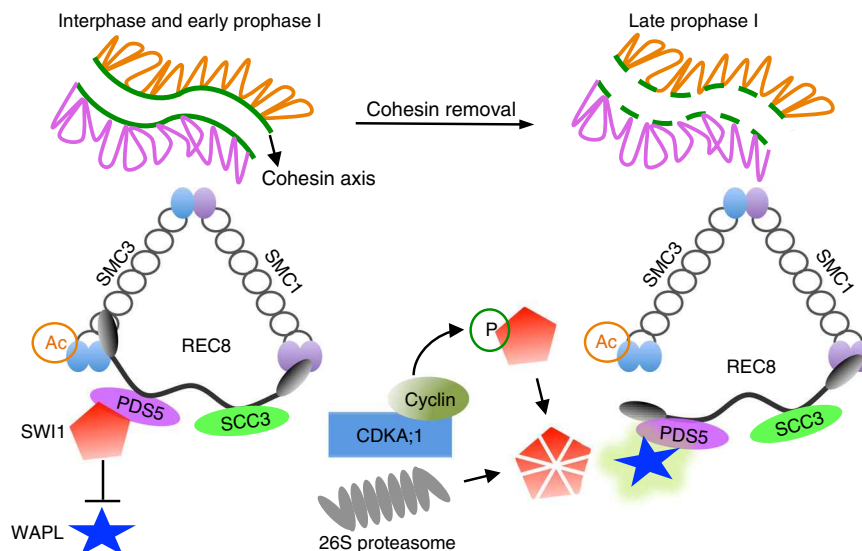
Fig. 10 Model for the role of SWI1 in the regulation of cohesin. During interphase and early prophase I, SWI1 is highly expressed and is recruited to chromatin through interacting with PDS5 family proteins, which in turn inhibits the action of WAPL by dislodging WAPL from PDS5. In late prophase I, SWI1 is phosphorylated by CDKA;1. This phosphorylation of SWI1 then promotes its release from chromatin by facilitating the ubiquitination by APC/C, and subsequent degradation by the 26S proteasome. The release of SWI1 allows the binding of WAPL to PDS5 resulting in the release of cohesin from chromatin

While a protein sequence-based alignment of the first 300 amino acids of the *Arabidopsis* SWI1 with its othologs in other plant species including Brachypodium, bean, maize, sorghum, rapeseed, and rice revealed three conserved domains, no clear motif is emerging and further work will be required to address whether one of these domains or a specific combination mediates the interaction with PDS5. Including Sororin in this alignment did also not pinpoint to a PDS5 binding domain making it likely that the interaction between WAPL inhibitors and PDS5 is complex.

SWI1 is released from chromatin by CDKA;1-dependent phosphorylation and subjected to degradation, likely in an APC/C-mediated manner (Fig. 10). However, CDKA;1 phosphorylation of SWI1 does not appears to be sufficient for degradation and possibly, the degradation machinery needs to be activated as well, perhaps depending on CDKA;1 phosphorylation as well. The removal of SWI1 allows the interaction of WAPL with PDS5 as indicated by the tight chromosome association of WAPL at late prophase (Fig. 1d; Supplementary Fig. 1c), thereby activating the prophase pathway of cohesin removal.

The retained signal of SWI1-GFP in *rec8* mutants suggests that SWI1 might also localize to other cohesin complexes that do not contain REC8. Unlike most other organisms that have only one mitotic *RAD21* gene, three paralogs of the kleisin subunit, *RAD21.1/SYN2*, *RAD21.2/SYN3*, and *RAD21.3/SYN4*, have been identified in *Arabidopsis* next to the meiotic paralog REC8/SYN1. Similarly rice and other plants also have several *SCC1/RAD21* genes[1]. Among the *Arabidopsis* RAD21 genes, especially RAD21.2 has been found to play an important role in reproduction, i.e., meiosis and subsequent gametogenesis, next to a function in vegetative growth since knockdown of RAD21.2 in meiocytes impaired chromosome synapsis and SC formation[46,47]. This together with the observation that sister chromatids are still bound at centromeres in the absence of *REC8* until metaphase I indicates that at least two different kleisins contribute to sister chromatid cohesion. However, RAD21.2 was unexpectedly detected to be predominantly present in the nucleolus of meiocytes and not along chromatin[46]. Thus, the function of this putative kleisin is still obscure and it is also not clear whether SWI1 can regulate different types cohesin complexes in meiosis. Conversely, *wapl* and *swi1* mutants do not show any mitotic

defects raising the question whether there is a prophase pathway in mitosis in *Arabidopsis*.

Although the premature removal of REC8 and with that the REC8-dependent cohesion loss are suppressed by the absence of *WAPL1* and *WAPL2*, *swi1 wapl1 wapl2* plants are still completely sterile similarly to the *swi1* single mutants and much more affected than *wapl1 wapl2* double mutants (Supplementary Fig. 14). This implies that SWI1 might have further roles in meiosis and/or might be involved in other biological processes after meiosis. Indeed, in addition to the cohesion defects, *swi1* mutants are also compromised in the specification of meiocytes resulting in the formation of multiple rather than a single female meiocytes[48,49]. These defects are specific to *swi1* in *Arabidopsis* and have not been reported for *am1* mutants in maize and rice[39,40]. However, AM1 also appears to regulate the entry into meiosis and very early meiotic events.

Interestingly, we found that the number of ovules with a single female meiocyte is significantly higher in the *swi1 wapl1 wapl2* mutants (14.3%, $n = 126$) than in *swi1* mutants (3.9%, $n = 128$) (Chi-squared test, $P = 0.00395$, Supplementary Fig. 15). Whether the loss of cohesin contributes to the formation of multiple meiocytes is not clear as yet. The germline in plants has to be established post-embryonically and there is accumulating evidence that the specification of meiocytes also involves a substantial reprogramming of chromatin possibly contributing to the repression of mitotic regulators and stem cell genes[50–52]. In this context it is interesting to note that the pattern of histone modifications is altered in *swi1* mutants[53]. Our finding that SWI1 binds to PDS5 opens a new perspective here given that PDS5 plays a broad role in regulating plant growth and development[54]. Thus, it is tempting to speculate that PDS5 is also involved in meiocyte specification in *Arabidopsis*. Further work is required to explore the role of SWI1 as a regulator of PDS5 containing complexes.

Methods

was obtained from GABI-Kat T-DNA mutant collection (http://www.GABI-Kat.de) via NASC (http://arabidopsis.info/). The mutant *swi1-2* has a premature stop codon induced by EMS (ethyl methanesulfonate) and was kindly provided by Raphaël Mercier from INRA Centre de Versailles-Grignon. If not mentioned otherwise, *swi1* denotes *swi1-3*. All plants were grown in growth chambers with a 16 h light/21 °C and 8 h/18 °C dark photoperiod and 60% humidity.

Plasmid construction and plant transformation. To create the *SWI1* reporters, the genomic sequence of *SWI1* was amplified by PCR and inserted into *pDONR221* vector by gateway BP reactions (Supplemental Table 2). The *SmaI* restriction site was then introduced in front of the stop codon by PCR. All constructs were then linearized by *SmaI* restriction and ligated to GFP or RFP fragments, followed by gateway LR reactions with the destination vector *pGWB501*[59]. WAPL1-GFP and ASY3-RFP reporters were created by using same strategy as described above. For the ZYP1b-GFP reporter, the *AscI* restriction site was inserted into *pDONR221-ZYP1b* between the 464-465aa of ZYP1b by PCR. Following the linearization by *AscI*, the mEGFP fragment was inserted into *pDONR221-ZYP1b*. The resulting ZYP1b-GFP expressing cassette was integrated into the destination vector *pGWB501* by a gateway LR reaction. Primers used for the creation of these constructs are shown in Supplementary Table 2. All constructs were transformed into *Arabidopsis thaliana* plants by floral dipping.

Yeast two-hybrid assay. The coding sequences of the respective genes were amplified by PCR from cDNA with primers flanking the *attB* recombination sites and subcloned into *pDONR223* vector by gateway BP reactions (Supplementary Table 2). The resulting constructs were integrated into the *pGADT7-GW* or *pGBKT7-GW* vectors by gateway LR reactions. Yeast two-hybrid assays were performed according to the Matchmaker Gold Yeast two-hybrid system manual (Clontech). Different combinations of constructs were co-transformed into yeast strain AH109 using the polyethylene glycol/lithium acetate method as described in the manual of Clontech. Yeast cells harboring the relevant constructs were grown on the SD/-Leu -Trp and SD/-Leu -Trp -His plates to test for protein-protein interactions.

Protein expression and purification. To generate HisMBP-SWI1[1-300], HisMBP-SWI1[301-639], HisGST-PDS5A[1-809] and HisMBP-WAPL1 constructs, the respective coding sequences were amplified by PCR and subcloned into *pDONR223* vector by gateway BP reactions (Table S2). The resulting constructs were integrated by gateway LR reactions into *pHMGWA* or *pHGGWA* vectors for the His MBP- or HisGST- tagged fusions, respectively. The constructs were transformed into the *E. coli* BL21 (DE3)pLysS cells and grown at 37 °C in the presence of 100 mg/l ampicillin until the OD$_{600}$ of 0.6. Protein expression was induced by adding IPTG to a final concentration of 0.3 mM, and the cells were incubated at 37 °C for 3 h (HisMBP-SWI1[301-639]) or 18 °C overnight (HisMBP-SWI1[1-300], HisGST-PDS5A[1-809] and HisMBP-WAPL1). All proteins were purified under native conditions by using Ni-NTA sepharose (QIAGEN) according to the manual.

For the purification of PDS5A[1-809]-WAPL1 heterodimers, the ampicillin resistance gene of WAPL1-*pHMGWA* was first replaced by the kanamycin resistance gene and co-transformed into BL21 (DE3)pLysS cells containing the vector PDS5A[1-809]-*pHGGWA*. The cells harboring both constructs were grown at 37 °C in the presence of 100 mg/l ampicillin and 50 mg/l kanamycin until the OD$_{600}$ to 0.6 and induced with 0.3 mM IPTG at 18 °C for overnight. Cells were harvested and PDS5A[1-809] and WAPL1 heterodimers were purified using GST agarose beads (Novogene). Coomassie Brilliant Blue (CBB) stained gels of all purified proteins used in this study are shown in Supplementary Fig. 15. The protease inhibitor cocktail (Roche) was always used in the purification procedures.

In vitro protein binding affinity assay. For the GST pull-down assay, 1 μg of HisGST-PDS5A[1-809], HisMBP-SWI1[1-300] and HisMBP-SWI1[301-639] protein, purified as described above, were added to the pull-down buffer system containing 25 mM Tris-HCl, pH 7.5, 100 mM NaCl, 10% glycerol, and 20 μl GST agarose beads (Chromotek) as indicated in Fig. 3c. After incubation for 1 h at 4 °C, the GST beads were rinsed 5 times by the washing buffer containing 25 mM Tris-HCl, pH 7.5, 200 mM NaCl, 10% glycerol and 0.1% Triton X-100. The beads-bound proteins were eluted by boiling in an equal volume of 1X SDS protein loading buffer and subjected to immunoblotting.

For the WAPL removal assay, 50 ng/μl HisGST-PDS5A[1-809]-HisMBP-WAPL1 heterodimers were bound to anti-GST agarose beads and incubated with different amounts of HisMBP-SWI1[1-300] (40, 80, 120 or 200 ng/μl) in a buffer containing 25 mM Tris-HCl, pH 7.5, 100 mM NaCl, 10 mM MgCl$_2$, 2 mM DTT, 10% glycerol and 0.1% Triton X-100 for 1 h at 4 °C. After incubation, the proteins in supernatant and from the beads-bound fraction were separated and subjected to immunoblot analysis. The GST (sc-138, 1:1000 dilution), MBP (E8032S, 1:10,000 dilution), and anti-mouse IgG secondary (A9044, 1:10,000 dilution) antibodies used were purchased from Santa Cruz Biotechnology, New England Biolabs, and Sigma, respectively.

Chromosome spread analysis. Chromosome spreads were performed as described previously[60]. In brief, fresh flower buds were fixed in 75% ethanol and 25% acetic acid for 48 h at 4 °C, followed by two washing steps with 75% ethanol and stored in 75% ethanol at 4 °C. For chromosome spreading, flower buds were digested in an enzyme solution (10 mM citrate buffer containing 1.5% cellulose, 1.5% pectolyase, and 1.5% cytohelicase) for 3 h at 37 °C and then transferred onto a glass slide, followed by dispersing with a bended needle. Spreading was performed on a 46 °C hotplate by adding an ~10 μl drop of 45% acetic acid. The slide was then rinsed by ice-cold ethanol/acetic acid (3:1) and mounted in Vectashield with DAPI (Vector Laboratories) to observe the DNA.

In vitro kinase assay. CDKA;1-SDS complexes were expressed and purified as described in Harashima and Schnittger[61] with slight modification using Strep-Tactin agarose (iba) instead of Ni-NTA agarose for the purification. Briefly, the CDKA;1-SDS complexes were first purified by Strep-Tactin agarose (iba), followed by desalting with PD MiniTrap G-25 (GE Healthcare). The quality of purified kinase complexes was checked by CBB staining and immunoblotting (Supplementary Fig. 15). Kinase assays were performed by incubating the kinase complexes with HisMBP-SWI1[1-300] or HisMBP-SWI1[301-639] in the reaction buffer containing 50 mM Tris-HCl, pH 7.5, 10 mM MgCl$_2$, 0.5 mM ATP and 5 mM DTT for 90 min. The CBB stained gel after kinase reaction is shown in Fig. S9.

Cell-free degradation assay. Wild-type *Arabidopsis* flower buds were freshly harvested and immediately grounded into powder in liquid nitrogen. Subsequently, total soluble proteins were extracted in the degradation buffer containing containing 25 mM Tris-HCl (pH 7.5), 10 mM NaCl, 10 mM MgCl$_2$, 4 mM PMSF, 5 mM DTT, and 10 mM ATP as previously described[62]. The supernatant was harvested after two 10-min centrifugations at $16,000 \times g$ at 4 °C and protein concentration was measured using the Bio-Rad protein assay. Two hundred nanograms of recombinant proteins (HisGST-SWI1[301-639] or HisGST-SWI1[301-639/9A]) were mixed with 150 μl protein extracts (600 μg in total) containing either DMSO, 50 μm MG132, or 5 μm Roscovitine. The reactions were incubated at 22 °C and protein samples were collected at the indicated intervals followed by western blot analysis.

Bimolecular fluorescence complementation assay. The coding sequences of *SWI1*, *PDS5* paralogs and *WAPl1* were amplified from cDNA and subcloned into *pDONR221-P3P2* or *pDONR221-P1P4*. The resulting constructs were subsequently integrated into the *pBiFC-2in1-NN* destination vector using a gateway LR reaction[38]. All genes were under the control of the *35S* promoter. The relevant proteins were transiently expressed in tobacco leaves by *Agrobacterium* infiltration at a concentration of OD600. The fluorescence of YFP was imaged 2 days after infiltration using a Leica SP8 laser-scanning confocal microscope. For the competitive interaction BiFC assay in tobacco, *SWI1-mTurquoise2* and *WAPL1-mTurquoise2*, both driven by *35S* promoter, were generated by integrated their coding sequences into *pGWB502* vector. The resulting constructs were then brought into *Agrobacterium*. Co-infiltration was performed by mixing the *Agrobacterium* of *SWI1-mTurquoise2* and *WAPL1-mTurquoise2* with the *pBiFC-2in1-NN* harboring relevant combinations. YFP fluorescence was imaged 2 days after infiltration using a Leica SP8 laser-scanning confocal microscope with the same setup.

Immunolocalization. For immunolocalization analyses, freshly harvested young flower buds were sorted by different size and the intact anthers were macerated in 10 μl enzyme mix (0.4% cytohelicase with 1% polyvinylpyrrolidone) for 5 min in a moisture chamber at 37 °C followed by a squashing. Subsequently, 10 μl enzyme mix was added onto the Poly-Prep slides (Sigma) that were incubated for further 7 min in a moisture chamber. Afterwards, a fine smashing of the anthers was performed in 20 μl 1% Lipsol for 2 min. Cell fixation was then performed by incubating 35 μl 4% (w/v) paraformaldehyde for 2–3 h until dry. After three times washing with PBST buffer (PBS with 1% Triton X-100), slides were then blocked in PBS buffer with 1% BSA (PBSA) for 30 min at 37 °C in a moisture chamber followed by an incubation with anti-GFP (1:100 in PBSA) antibody at 4 °C for 72 h (Takara 632381/JL-8)). After three times of washing (10 min each) in PBST, fluorescein-conjugated horse anti-mouse antibody (FI-2000, Vector Laboratories) were added onto the slides (1:500 dilution) followed by 2 h incubation at 37 °C in a moisture chamber. After three times washing in PBST, the chromosomes were counterstained with anti-fade DAPI solution (Vector Laboratories). The images were captured using the Leica SP8 laser scanning microscopy.

Sample preparation and LC-MS/MS data acquisition. The protein mixtures were reduced with dithiothreitol, alkylated with chloroacetamide, and digested with trypsin. These digested samples were desalted using StageTips with C18 Empore disk membranes (3 M)[63], dried in a vacuum evaporator, and dissolved in 2% ACN, 0.1% TFA. Samples were analyzed using an EASY-nLC 1200 (Thermo Fisher) coupled to a Q Exactive Plus mass spectrometer (Thermo Fisher). Peptides were separated on 16 cm frit-less silica emitters (New Objective, 0.75 μm inner diameter), packed in-house with reversed-phase ReproSil-Pur C18 AQ 1.9 μm resin (Dr. Maisch GmbH). Peptides were loaded on the column and eluted for 50 min using a segmented linear gradient of

5% to 95% solvent B at a flow rate of 300 nl/min (0 min: 5%B; 0–5 min ->5%B; 5–25 min ->20%B; 25–35 min ->35%B; 35–40 min ->95%B; 40–50 min ->95%B; solvent A 0% ACN, 0.1% FA; solvent B 80% ACN, 0.1%FA). Mass spectra were acquired in data-dependent acquisition mode with a TOP15 method. MS spectra were acquired in the Orbitrap analyzer with a mass range of 300–1500 m/z at a resolution of 70,000 FWHM and a target value of 3×10^6 ions. Precursors were selected with an isolation window of 1.3 m/z. HCD fragmentation was performed at a normalized collision energy of 25. MS/MS spectra were acquired with a target value of 5×10^5 ions at a resolution of 17,500 FWHM, a maximum injection time of 120 ms and a fixed first mass of m/z 100. Peptides with a charge of 1, >6, or with unassigned charge state were excluded from fragmentation for MS^2; dynamic exclusion for 20 s prevented repeated selection of precursors.

MS data analysis. Raw data were processed individually using MaxQuant software (version 1.5.7.4, http://www.maxquant.org/)[64]. MS/MS spectra were searched by the Andromeda search engine against a database containing the respective proteins used for the in vitro reaction and a background *E. coli* database (*E. coli* (K12) database, UniProt). Sequences of 244 common contaminant proteins and decoy sequences were added during the search. Trypsin specificity was required and a maximum of two missed cleavages allowed. Minimal peptide length was set to seven amino acids. Carbamidomethylation of cysteine residues was set as fixed, phosphorylation of serine, threonine and tyrosine, oxidation of methionine and protein N-terminal acetylation as variable modifications. Peptide-spectrum-matches and proteins were retained if they were below a false discovery rate of 1%.

Confocal microscopy and sample preparation. For protein localization analyses, young anthers or ovules were dissected and imaged using an Leica TCS SP8 inverted confocal microscope. For tracing the dynamics of cohesin in *swi1 wapl1 wapl2* mutants, live cell imaging was performed as described by Prusicki et al.[29]. Briefly, one single fresh flower bud was detached from the flower and dissected with two anthers exposed. Subsequently, the isolated bud including the pedicel and a short part of the floral stem was embedded into the Arabidopsis Apex Culture Medium (ACM) and then covered by one drop of 2% agarose. The sample was then subjected to constant image capture with 15 min intervals by using an upright Zeiss LSM880 confocal microscope with Airyscan.

For analyzing the dynamics of cohesin during meiosis, live cell imaging was performed with the anthers of the wildtype and *wapl1 wapl2* mutant plants harboring a functional REC8-GFP reporter. To quantify the dynamics of the REC8-GFP signal, the metaphase I was denoted as 0 h and the REC8-GFP signal from at least 20 meiocytes was calculated for every one hour prior to metaphase I by using the image processing software Fiji[65]. Representative movies for the wildtype and *wapl1 wapl2* mutants are shown in the Supplementary Movie 1 and S2, respectively.

Pollen viability assay. The Peterson staining method was used to analyze the pollen viability[66]. For counting of pollen, three mature flower buds containing dehiscent anthers were collected and dipped in 13 μl Perterson staining solution (10% ethanol, 0.01% malachite green, 25% glycerol, 0.05% acid fuchsin, 0.005% orange G, 4% glacial acetic acid) for 10 s on a microscope slide, which was then covered by a cover-slip; for the staining of entire anthers, 8 non-dehiscent anthers from mature flower buds were dissected under a binocular, immersed in 30 μl Perterson staining solution on a microscope slide, and stained for overnight. Subsequently, slides were heated on a hotplate at 80 °C for 10 min (for pollen counting) or 60 min (for entire anther staining) to distinguish aborted and non-aborted pollen grains. Slides were analyzed and imaged using a light microscope.

Reporting summary. Further information on research design is available in the Nature Research Reporting Summary linked to this article.

Data availability

The mass spectrometry proteomics data have been deposited to the ProteomeXchange Consortium via the PRIDE[67] partner repository with the dataset identifier PXD009959 (http://proteomecentral.proteomexchange.org/cgi/GetDataset?ID=PXD009959). The *Arabidopsis* mutants and transgenic lines, as well as plasmids generated in this study are freely available from the corresponding author upon request. The source data of the immunoblots of Figs. 2b, 4c, 9b and the data underlying Figs. 1c and 8b are provided in the Source Data file.

References

1. Bolaños-Villegas, P., De, K., Pradillo, M., Liu, D. & Makaroff, C. A. In favor of establishment: regulation of chromatid cohesion in plants. *Front. Plant Sci.* **8**, 846 (2017).

2. Litwin, I., Pilarczyk, E. & Wysocki, R. The emerging role of cohesin in the DNA damage response. *Genes* **9**, 581 (2018).

3. Makrantoni, V. & Marston, A. L. Cohesin and chromosome segregation. *Curr. Biol.* **28**, R688–R693 (2018).

4. Suja, J. A. & Barbero, J. L. Cohesin complexes and sister chromatid cohesion in mammalian meiosis. *Genome Dyn.* **5**, 94–116 (2009).

5. Ciosk, R. et al. Cohesin's binding to chromosomes depends on a separate complex consisting of Scc2 and Scc4 proteins. *Mol. Cell* **5**, 243–254 (2000).

6. Watrin, E. et al. Human Scc4 is required for cohesin binding to chromatin, sister-chromatid cohesion, and mitotic progression. *Curr. Biol.* **16**, 863–874 (2006).

7. Petela, N. J. et al. Scc2 is a potent activator of cohesin's ATPase that promotes loading by binding Scc1 without Pds5. *Mol. Cell* **70**, 1134–1148.e7 (2018).

8. Lengronne, A. et al. Establishment of sister chromatid cohesion at the *S. cerevisiae* replication fork. *Mol. Cell* **23**, 787–799 (2006).

9. Ben-Shahar, T. R. et al. Eco1-dependent cohesin acetylation during establishment of sister chromatid cohesion. *Science* **321**, 563–566 (2008).

10. Vaur, S., Feytout, A. E. L., Vazquez, S. E. P. & Javerzat, J.-P. Pds5 promotes cohesin acetylation and stable cohesin–chromosome interaction. *EMBO Rep.* **13**, 645–652 (2018).

11. De, K., Sterle, L., Krueger, L., Yang, X. & Makaroff, C. A. Arabidopsis thaliana WAPL is essential for the prophase removal of cohesin during meiosis. *PLoS Genet* **10**, e1004497 (2014).

12. Gandhi, R., Gillespie, P. J. & Hirano, T. Human Wapl is a cohesin-binding protein that promotes sister-chromatid resolution in mitotic prophase. *Curr. Biol.* **16**, 2406–2417 (2006).

13. Sutani, T., Kawaguchi, T., Kanno, R., Itoh, T. & Shirahige, K. Budding yeast Wpl1(Rad61)-Pds5 complex counteracts sister chromatid cohesion-establishing reaction. *Curr. Biol.* **19**, 492–497 (2009).

14. Challa, K. et al. Meiosis-specific prophase-like pathway controls cleavage-independent release of cohesin by Wapl phosphorylation. *PLoS Genet.* **15**, e1007851 (2019).

15. Liu, H., Rankin, S. & Yu, H. Phosphorylation-enabled binding of SGO1-PP2A to cohesin protects sororin and centromeric cohesion during mitosis. *Nat. Cell Biol.* **15**, 40–49 (2013).

16. Hara, K. et al. Structure of cohesin subcomplex pinpoints direct shugoshin-Wapl antagonism in centromeric cohesion. *Nat. Publ. Group* **21**, 864–870 (2014).

17. Ladurner, R. et al. Sororin actively maintains sister chromatid cohesion. *EMBO J.* **35**, 635–653 (2016).

18. Nishiyama, T. et al. Sororin mediates sister chromatid cohesion by antagonizing Wapl. *Cell* **143**, 737–749 (2010).

19. Kueng, S. et al. Wapl controls the dynamic association of cohesin with chromatin. *Cell* **127**, 955–967 (2006).

20. Yamada, T., Tahara, E., Kanke, M., Kuwata, K. & Nishiyama, T. Drosophila Dalmatian combines sororin and shugoshin roles in establishment and protection of cohesion. *EMBO J.* **36**, 1513–1527 (2017).

21. Rankin, S., Ayad, N. G. & Kirschner, M. W. Sororin, a substrate of the anaphase-promoting complex, is required for sister chromatid cohesion in vertebrates. *Mol. Cell* **18**, 185–200 (2005).

22. Dreier, M. R., Bekier, M. E. 2nd & Taylor, W. R. Regulation of sororin by Cdk1-mediated phosphorylation. *J. Cell Sci.* **124**, 2976–2987 (2011).

23. Nishiyama, T., Sykora, M. M., Huis in 't Veld, P. J., Mechtler, K. & Peters, J.-M. Aurora B and Cdk1 mediate Wapl activation and release of acetylated cohesin from chromosomes by phosphorylating Sororin. *Proc. Natl Acad. Sci. USA* **110**, 13404–13409 (2013).

24. Gómez, R. et al. Sororin loads to the synaptonemal complex central region independently of meiotic cohesin complexes. *EMBO Rep.* **17**, 695–707 (2016).

25. Brieño-Enríquez, M. A. et al. Cohesin removal along the chromosome arms during the first meiotic division depends on a NEK1-PP1γ-WAPL axis in the mouse. *Cell Rep.* **17**, 977–986 (2016).

26. Challa, K., Lee, M.-S., Shinohara, M., Kim, K. P. & Shinohara, A. Rad61/Wpl1 (Wapl), a cohesin regulator, controls chromosome compaction during meiosis. *Nucleic Acids Res.* **44**, 3190–3203 (2016).

27. Crawley, O. et al. Cohesin-interacting protein WAPL-1 regulates meiotic chromosome structure and cohesion by antagonizing specific cohesin complexes. *Elife* **5**, e10851 (2016).

28. Rankin, S. Sororin, the cell cycle and sister chromatid cohesion. *Cell Cycle* **4**, 1039–1042 (2005).

29. Prusicki, M. A. et al. Live cell imaging of meiosis in *Arabidopsis thaliana* - a landmark system. Preprint at https://www.biorxiv.org/content/10.1101/446922v1 (2018).

30. Mercier, R. et al. SWITCH1 (SWI1): a novel protein required for the establishment of sister chromatid cohesion and for bivalent formation at meiosis. *Genes Dev.* **15**, 1859–1871 (2001).

31. Mercier, R. The meiotic protein SWI1 is required for axial element formation and recombination initiation in Arabidopsis. *Development* **130**, 3309–3318 (2003).

32. Ravi, M., Marimuthu, M. P. A. & Siddiqi, I. Gamete formation without meiosis in Arabidopsis. *Nature* **451**, 1121–1124 (2008).

33. Wang, Y., Wu, H., Liang, G. & Yang, M. Defects in nucleolar migration and synapsis in male prophase I in the ask1-1 mutant of Arabidopsis. *Sex. Plant Reprod.* **16**, 273–282 (2004).

34. Stronghill, P. E., Azimi, W. & Hasenkampf, C. A. A novel method to follow meiotic progression in Arabidopsis using confocal microscopy and 5-ethynyl-2'-deoxyuridine labeling. *Plant Methods* **10**, 33 (2014).

35. Yang, X., Timofejeva, L., Ma, H. & Makaroff, C. A. The Arabidopsis SKP1 homolog ASK1 controls meiotic chromosome remodeling and release of chromatin from the nuclear membrane and nucleolus. *J. Cell Sci.* **119**, 3754–3763 (2006).

36. Kanke, M., Tahara, E., Huis In't Veld, P. J. & Nishiyama, T. Cohesin acetylation and Wapl-Pds5 oppositely regulate translocation of cohesin along DNA. *EMBO J.* **35**, 2686–2698 (2016).

37. Goto, Y. et al. Pds5 regulates sister-chromatid cohesion and chromosome bi-orientation through a conserved protein interaction module. *Curr. Biol.* **27**, 1005–1012 (2017).

38. Grefen, C. & Blatt, M. R. A 2in1 cloning system enables ratiometric bimolecular fluorescence complementation (rBiFC). *BioTechniques* **53**, 311–314 (2012).

39. Che, L. et al. OsAM1 is required for leptotene-zygotene transition in rice. *Nat. Publ. Group* **21**, 654–665 (2011).

40. Pawlowski, W. P. et al. Maize AMEIOTIC1 is essential for multiple early meiotic processes and likely required for the initiation of meiosis. *Proc. Natl Acad. Sci. USA* **106**, 3603–3608 (2009).

41. Dissmeyer, N. et al. T-loop phosphorylation of Arabidopsis CDKA;1 is required for its function and can be partially substituted by an aspartate residue. *Plant Cell* **19**, 972–985 (2007).

42. Liu, Z. et al. GPS-ARM: computational analysis of the APC/C recognition motif by predicting D-boxes and KEN-boxes. *PLoS ONE* **7**, e34370 (2012).

43. Taylor, S. L., Kinchington, P. R., Brooks, A. & Moffat, J. F. Roscovitine, a cyclin-dependent kinase inhibitor, prevents replication of varicella-zoster virus. *J. Virol.* **78**, 2853–2862 (2004).

44. Cai, X., Dong, F., Edelmann, R. E. & Makaroff, C. A. The Arabidopsis SYN1 cohesin protein is required for sister chromatid arm cohesion and homologous chromosome pairing. *J. Cell Sci.* **116**, 2999–3007 (2003).

45. Bhatt, A. M. et al. The DIF1 gene of Arabidopsis is required for meiotic chromosome segregation and belongs to the REC8/RAD21 cohesin gene family. *Plant J.* **19**, 463–472 (1999).

46. Jiang, L., Xia, M., Strittmatter, L. I. & Makaroff, C. A. The Arabidopsis cohesin protein SYN3 localizes to the nucleolus and is essential for gametogenesis. *Plant J.* **50**, 1020–1034 (2007).

47. Yuan, L., Yang, X., Ellis, J. L., Fisher, N. M. & Makaroff, C. A. The Arabidopsis SYN3 cohesin protein is important for early meiotic events. *Plant J.* **71**, 147–160 (2012).

48. Agashe, B., Prasad, C. K. & Siddiqi, I. Identification and analysis of DYAD: a gene required for meiotic chromosome organisation and female meiotic progression in Arabidopsis. *Development* **129**, 3935–3943 (2002).

49. Siddiqi, I., Ganesh, G., Grossniklaus, U. & Subbiah, V. The dyad gene is required for progression through female meiosis in Arabidopsis. *Development* **127**, 197–207 (2000).

50. Zhao, X. et al. RETINOBLASTOMA RELATED1 mediates germline entry in Arabidopsis. *Science* **356**, eaaf6532 (2017).

51. Schmidt, A., Schmid, M. W. & Grossniklaus, U. Plant germline formation: common concepts and developmental flexibility in sexual and asexual reproduction. *Development* **142**, 229–241 (2015).

52. Olmedo-Monfil, V. et al. Control of female gamete formation by a small RNA pathway in Arabidopsis. *Nature* **464**, 628–632 (2010).

53. Boateng, K. A., Yang, X., Dong, F., Owen, H. A. & Makaroff, C. A. SWI1 is required for meiotic chromosome remodeling events. *Mol. Plant* **1**, 620–633 (2008).

54. Pradillo, M. et al. Involvement of the cohesin cofactor PDS5 (SPO76) during meiosis and DNA repair in *Arabidopsis thaliana. Front. Plant Sci.* **6**, 3020 (2015).

55. Ferdous, M. et al. Inter-homolog crossing-over and synapsis in *Arabidopsis meiosis* are dependent on the chromosome axis protein AtASY3. *PLoS Genet* **8**, e1002507 (2012).

56. Stacey, N. J. et al. Arabidopsis SPO11-2 functions with SPO11-1 in meiotic recombination. *Plant J.* **48**, 206–216 (2006).

57. Crismani, W. et al. MCM8 is required for a pathway of meiotic double-strand break repair independent of DMC1 in *Arabidopsis thaliana. PLoS Genet* **9**, e1003165 (2013).

58. Schubert, V. et al. Cohesin gene defects may imprair sister chromatid alignment and genome stability in *Arabidopsis thaliana. Chromosoma* **118**, 591–605 (2009).

59. Nakagawa, T. et al. Improved Gateway binary vectors: high-performance vectors for creation of fusion constructs in transgenic analysis of plants. *Biosci. Biotechnol. Biochem.* **71**, 2095–2100 (2007).

60. Wijnker, E. et al. Reverse breeding in *Arabidopsis thaliana* generates homozygous parental lines from a heterozygous plant. *Nat. Genet.* **44**, 467–470 (2012).

61. Harashima, H. & Schnittger, A. Robust reconstitution of active cell-cycle control complexes from co-expressed proteins in bacteria. *Plant Methods* **8**, 23 (2012).

62. Yang, C. et al. LIGHT-INDUCED RICE1 regulates light-dependent attachment of LEAF-TYPE FERREDOXIN-NADP + OXIDOREDUCTASE to the Thylakoid membrane in rice and Arabidopsis. *Plant Cell* **28**, 712–728 (2016).

63. Rappsilber, J., Ishihama, Y. & Mann, M. Stop and go extraction tips for matrix-assisted laser desorption/ionization, nanoelectrospray, and LC/MS sample pretreatment in proteomics. *Anal. Chem.* **75**, 663–670 (2003).

64. Cox, J. & Mann, M. MaxQuant enables high peptide identification rates, individualized p.p.b.-range mass accuracies and proteome-wide protein quantification. *Nat. Biotechnol.* **26**, 1367–1372 (2008).

65. Schindelin, J. et al. Fiji: an open-source platform for biological-image analysis. *Nat. Methods* **9**, 676–682 (2012).

66. Peterson, R., Slovin, J. P. & Chen, C. A simplified method for differential staining of aborted and non-aborted pollen grains. *Int J. Plant Biol.* **1**, 13–e13 (2010).

67. Vizcaíno, J. A. et al. 2016 update of the PRIDE database and its related tools. *Nucleic Acids Res.* **44**, 11033–11033 (2016).

Acknowledgements

Author contributions

C.Y. and A.S. conceived the experiments. C.Y., Y.H., K.S., and F.B. performed the experiments and statistical analyses; S.C.S. and H.N. performed the mass spectrometry experiment and data analysis. C.Y. and A.S. analyzed the data. C.Y. and A.S. wrote the manuscript.

Additional information

Supplementary Figure 1

WAPL1-GFP is functional and accumulates on chromatin from late leptotene/early zygotene till metaphase I. (a) Main branches (upper panel) and siliques (lower panel) of the wildtype (WT), *wapl1 wapl2*, and two lines expressing WAPL1-GFP in a *wapl1 wapl2* mutant background. (b) Peterson staining of anthers in the wildtype (WT), *wapl1 wapl2* mutants, and two WAPL1-GFP lines. Blue staining indicates dead pollen. (c)

Immunolocalization of WAPL1-GFP during meiosis I of male meiocytes. Anti-

GFP antibody was used for detecting WAPL1-GFP. Bar: 5 µm.
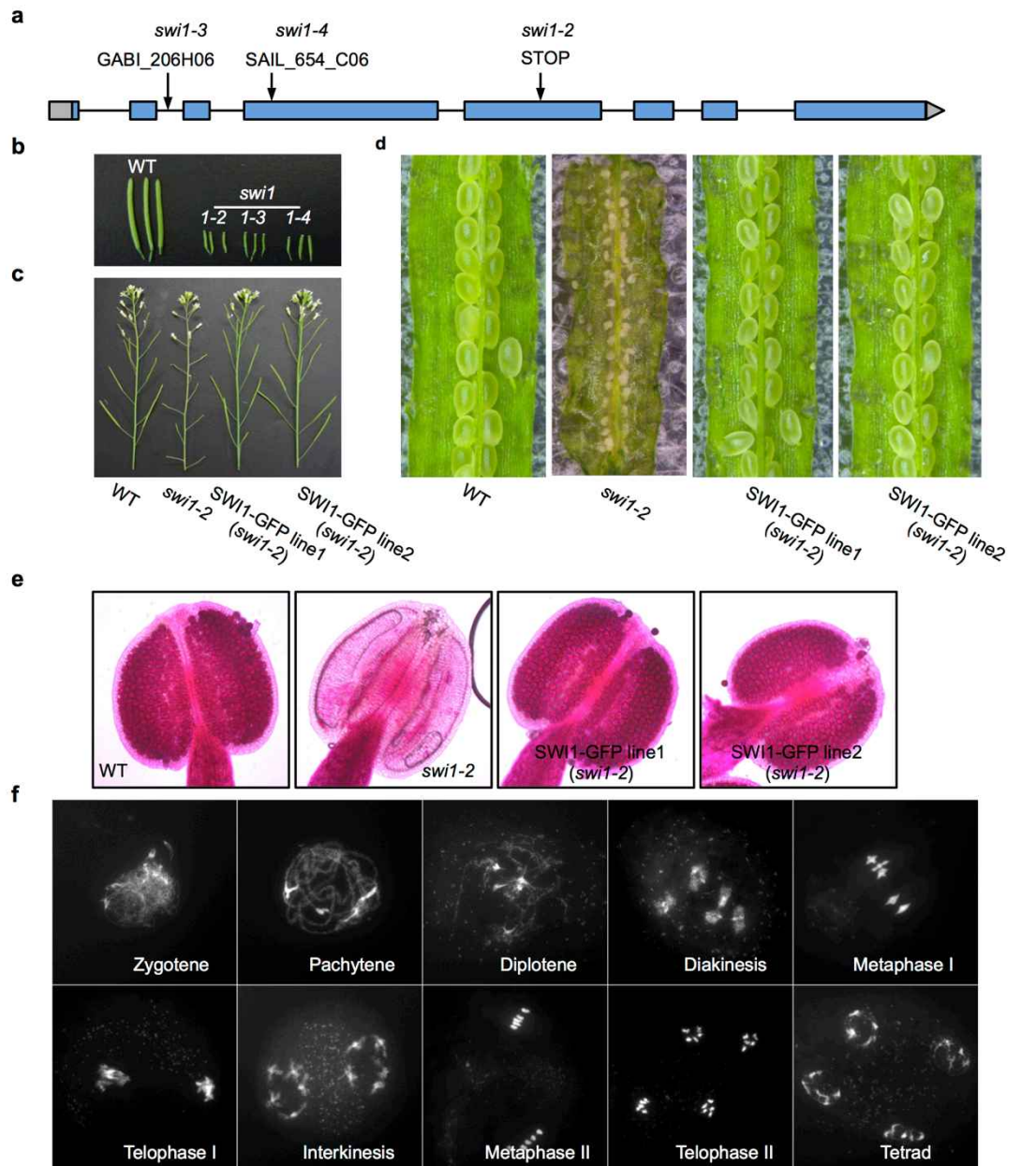
Supplementary Figure 2

SWI1-GFP fully complements the meiotic defects in *swi1* mutants. (a)

Scheme of the genomic region of SWI1. Arrows denote the position of T-DNA

insertions (*swi1-3*, *swi1-4*) and of a premature stop codon (*swi1-2*). (b)

Siliques of the wildtype (WT) and different *swi1* mutant alleles, which are

completely sterile. (c) The main branches of the wildtype, *swi1-2* and two

SWI1-GFP lines. (d) Seed sets in siliques of the wildtype, two *SWI1-GFP* lines

and the *swi1-2* mutant. (e) Peterson staining of pollen for the wildtype, *swi1-2*

and *SWI1-GFP* lines. No pollen was found in the *swi1-2* mutants. Blue

staining indicates dead pollen. (f) Chromosome spread analysis of male

meiocytes in *SWI1-GFP* line #2 (*swi1-2*) shows a wild-type meiotic program.
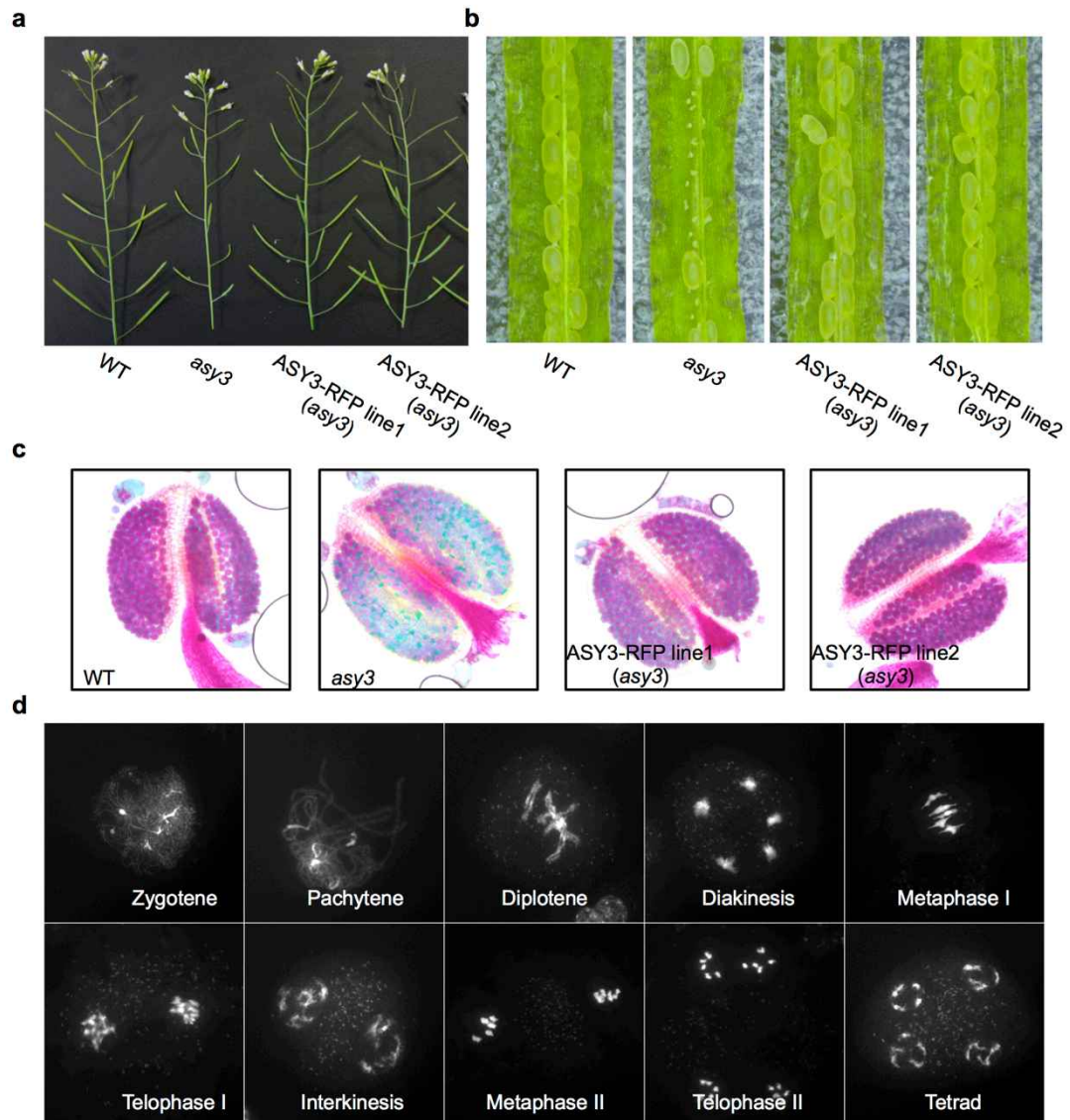
Supplementary Figure 3

ASY3-RFP fully complements the meiotic defects in *asy3* mutants. (a)

The main branches of the wildtype (WT) and two *ASY3-RFP* lines. (b) Seed

sets in siliques of the wildtype (WT) and two *ASY3-RFP* complementary lines.

(c) Peterson staining of pollens for the wildtype (WT), *asy3* and *ASY3-RFP*

lines. (d) Chromosome spread analysis of male meiocytes in *ASY3-RFP* line

#1 (*asy3*) reveals a normal meiotic program.
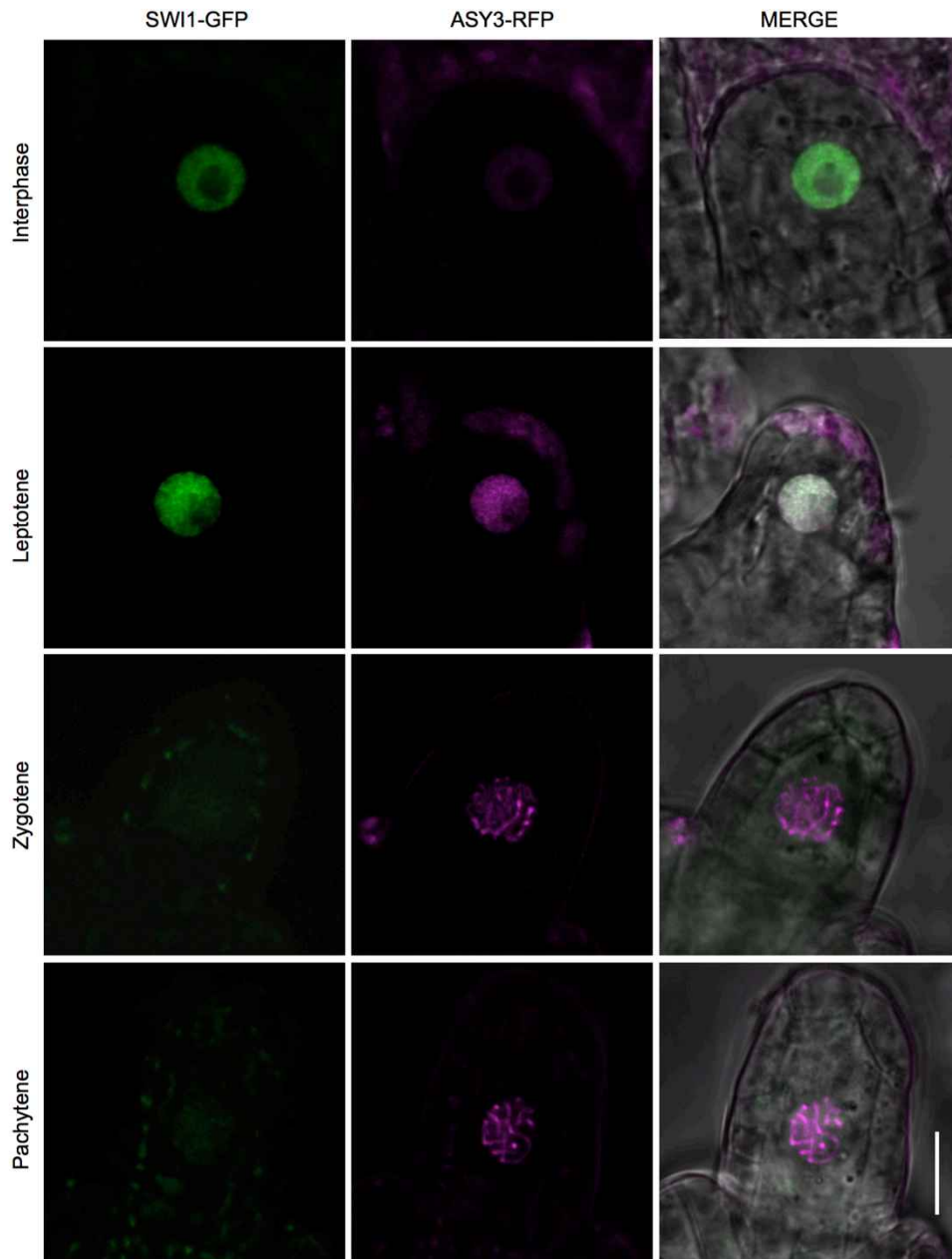
Supplementary Figure 4

Co-localization of SWI1 with ASY3 in female meiocytes. Co-localization analysis of SWI1-GFP (green) with ASY3-RFP (red) during interphase and prophase I in female meiocytes by using confocal laser scanning microscopy. Bar: 10 μm.
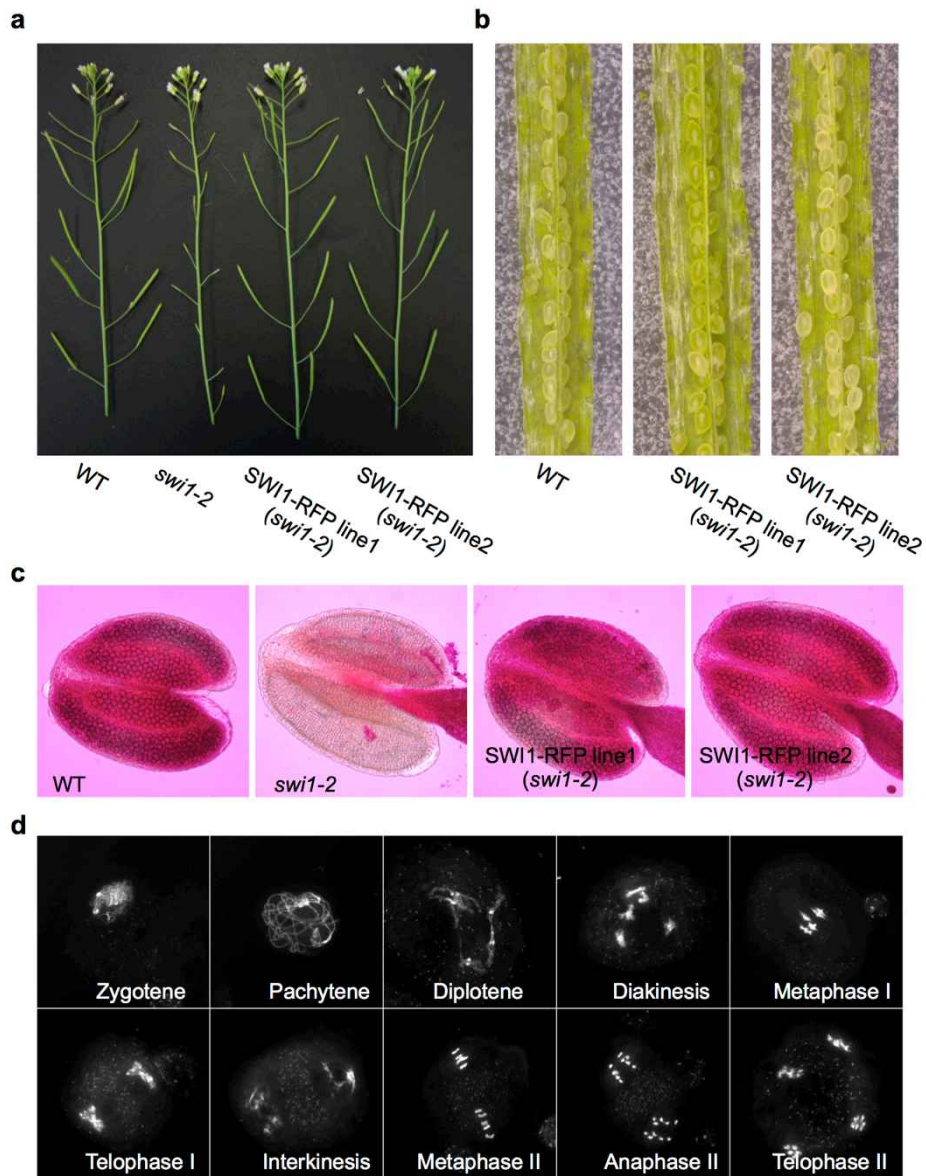
Supplementary Figure 5

SWI1-RFP fully complements the meiotic defects in *swi1* mutants. (a)

Main branches of the wildtype (WT), *swi1-2* and two *SWI1-RFP* lines. (b)

Seed sets in siliques of the wildtype (WT) and two *SWI1-RFP* lines. (c)

Peterson staining of anthers for the wildtype (WT), *swi1-2* and *SWI1-GFP*

lines. (d) Chromosome spread analysis of male meiocytes in *SWI1-RFP* line

#1 (*swi1-2*) reveals a wild-type meiotic program.
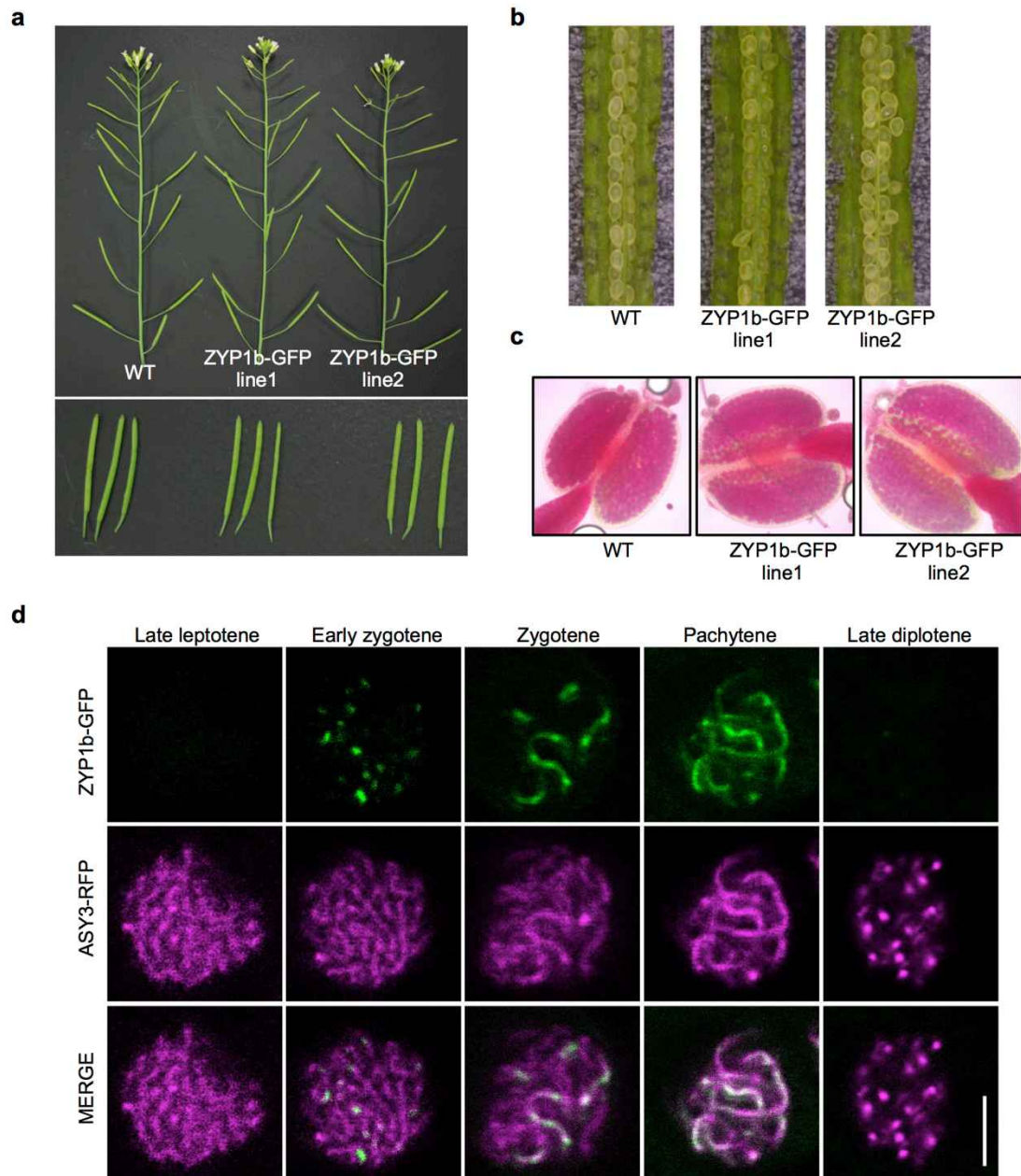
Supplementary Figure 6

ZYP1b-GFP is a good reporter for staging and has no dominant effect on plants. (a) Main branches of the wildtype (WT) and two *ZYP1b-GFP* lines in wildtype bacground. (b) Seed sets in siliques of the WT and two *ZYP1b-GFP* lines. (c) Peterson staining of anthers for the WT and and two *ZYP1b-GFP* lines. (d) Co-localization of ZYP1b-GFP with ASY3-RFP in the male

meiocytes of wildtype shows that ZYP1b-GFP specifically localizes to synaptic regions during prophase I. Bar: 5 µm.
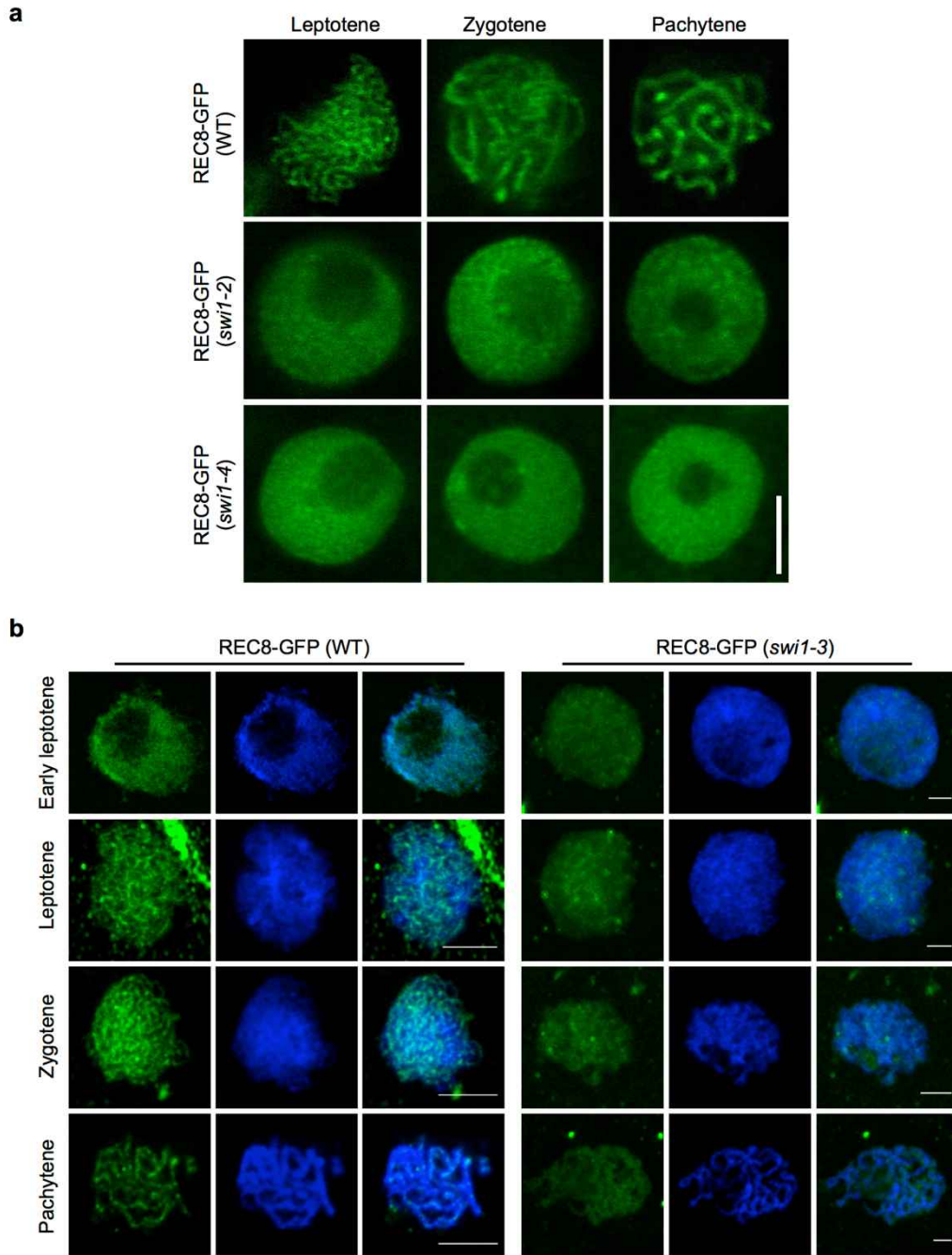
Supplementary Figure 7

Cohesion establishment is compromised in different *swi1* alleles. (a)

Localization of REC8-GFP was analyzed by using laser confocal microscopy

during prophase I of male meiocytes in the wildtype (WT), *swi1-2 and swi1-4*.

Bar: 5 µm. (b) Immunolocalization of REC8-GFP in the male meiocytes of the

wildtype and *swi1-3* mutants during prophase I. Anti-GFP antibody was used

for detecting REC8-GFP. Bar: 5 μm.
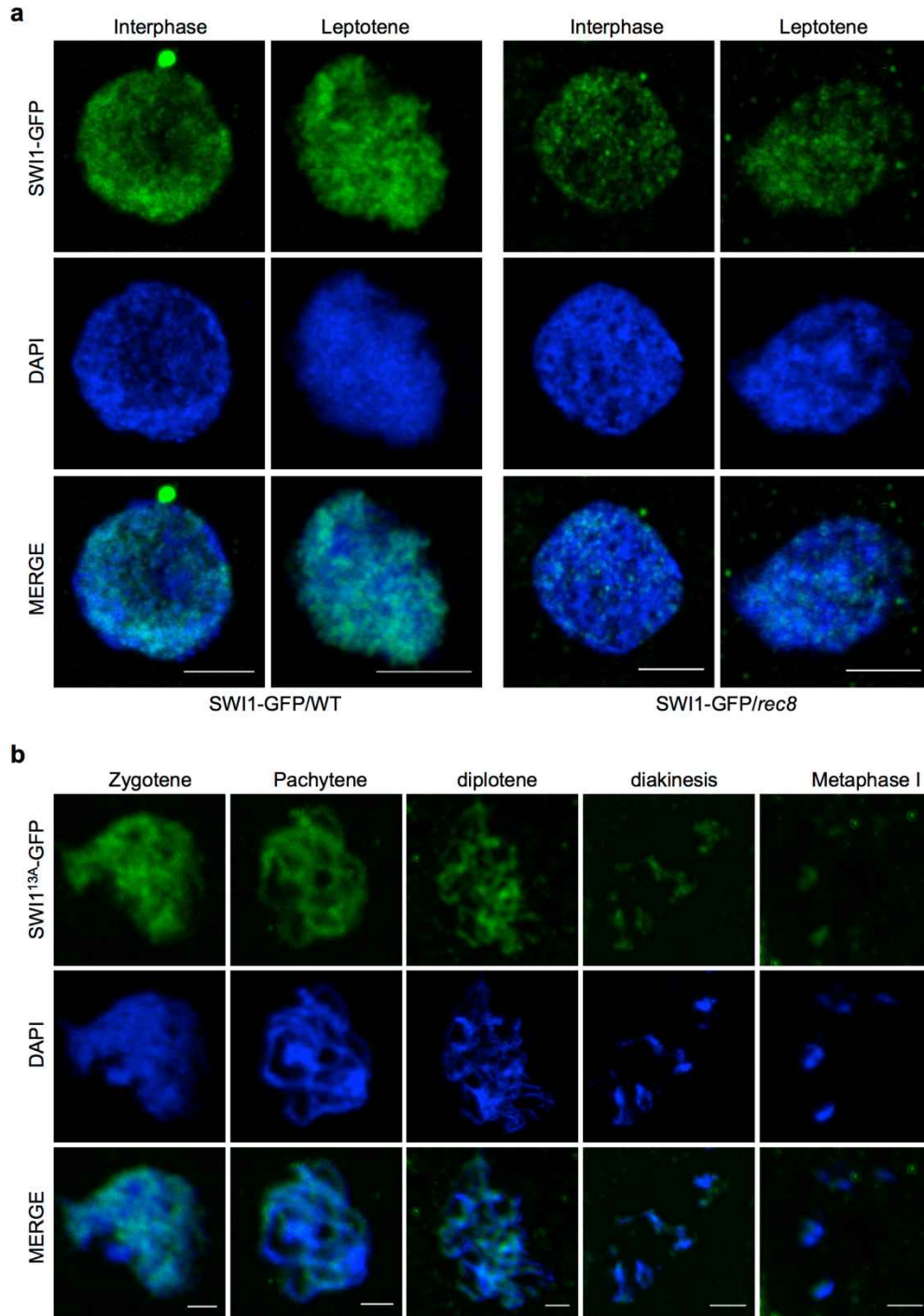
Supplementary Figure 8

Immunolocalization of SWI1-GFP and SWI1^{13A}-GFP. (a)

Immunolocalization of SWI1-GFP in the wildtype (WT) and *rec8* mutants. Bar:

5 µm. (b) Immunolocalization of SWI1^{13A}-GFP in the wildtype. Bar: 5 µm. Anti-

GFP antibody was used for detecting SWI1.

a

AD	BD	10^0	10^{-1}	10^{-2}	10^0	10^{-1}	10^{-2}
SWI1	Empty						
Empty	SCC3						
Empty	SMC1						
Empty	REC8						
SWI1	SCC3						
SWI1	SMC1						
SWI1	REC8						
SWI1	SMC3						

SD/-L-T   SD/-L-T-H

b

AD	BD	10^0	10^{-1}	10^{-2}	10^0	10^{-1}	10^{-2}
PDS5A$^{810-1607}$	Empty						
PDS5A$^{1-809}$	Empty						
Empty	WAPL1						
PDS5A$^{1-809}$	WAPL1						
PDS5A$^{810-1607}$	WAPL1						
SWI1	WAPL1						

SD/-L-T   SD/-L-T-H

c

YFP   RFP   MERGE

nYFP
cYFP-PDS5A$^{1-809}$

nYFP-WAPL1
cYFP

nYFP-WAPL1
cYFP-PDS5A$^{1-809}$

d

YFP   RFP   MERGE

nYFP +
cYFP-PDS5B$^{1-667}$

nYFP-SWI1 +
cYFP-PDS5B$^{1-667}$

nYFP +
cYFP-PDS5C

nYFP-SWI1 +
cYFP-PDS5C

nYFP +
cYFP-PDS5D

nYFP-SWI1 +
cYFP-PDS5D

nYFP +
cYFP-PDS5E

nYFP-SWI1 +
cYFP-PDS5E

e

bound unbound

HisMBP-SWI1$^{1-300}$

α-MBP

Supplementary Figure 9

Interaction analyses of SWI1, PDS5, and WAPL. (a) Yeast two-hybrid

interaction assay of SWI1 with the core cohesin subunits SMC1, SMC3,

REC8 and SCC3. (b) Yeast two-hybrid analysis of the interactions of WAPL1

with PDS5 and SWI1. (c) BiFC interaction assay of WAPL1 with PDS5A. Bar: 50 μm. (d) BiFC interaction assay of SWI1 with PDS5B, PDS5C, PDS5D, and PDS5E. (e) Immunoprecipitation for HisMBP-SWI1$^{1-300}$ only using GST binding beads showing no unspecific binding.
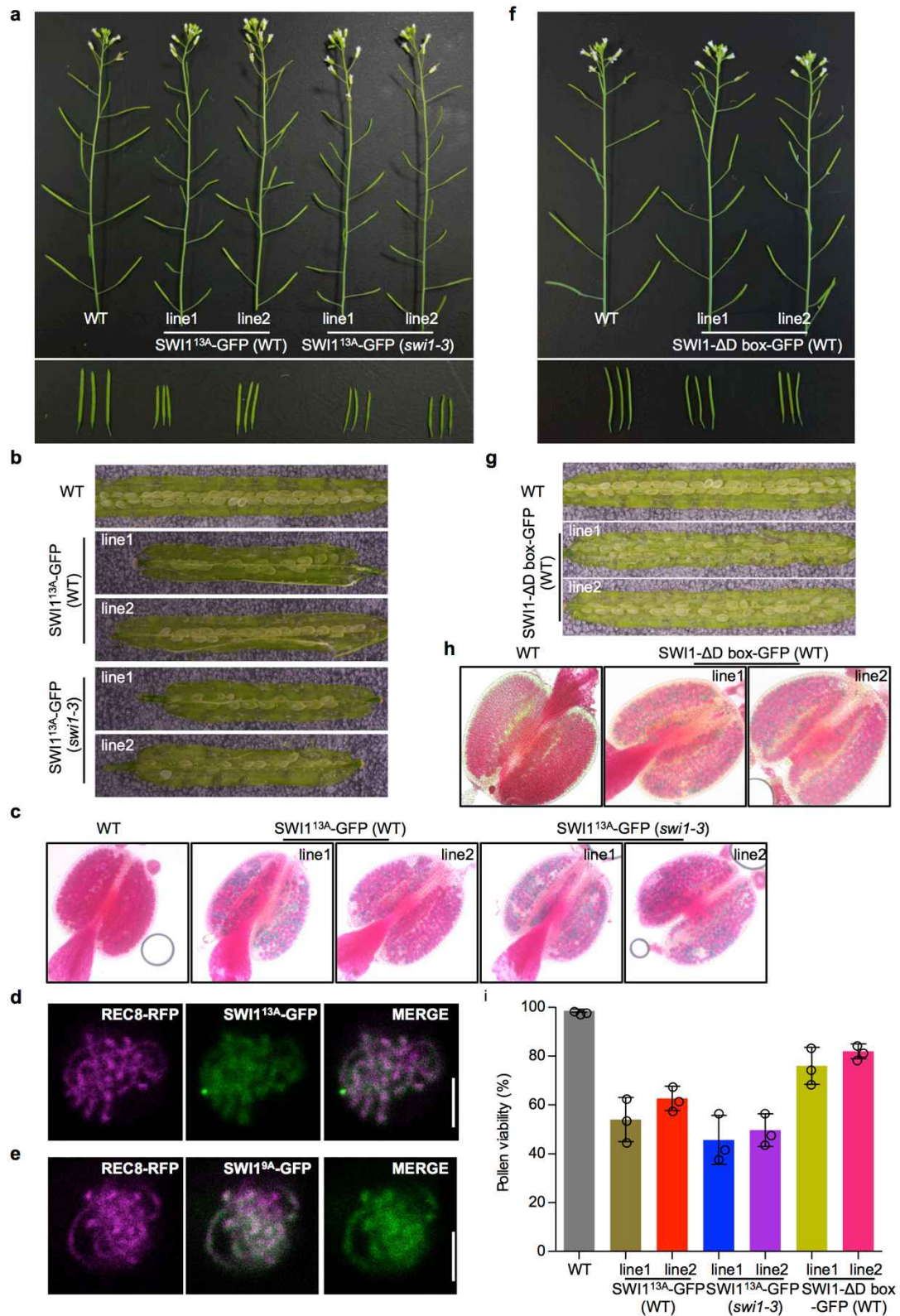
Supplementary Figure 10

Fertility of plants harboring the SWI1^{13A}-GFP and SWI1-ΔD box-GFP constructs. (a) Main branches (upper panel) and siliques (lower panel) of

the wildtype (WT) and two *SWI1*[13A]*-GFP* lines in both WT and *swi1-3* muatnt

background. (b) Seed sets in siliques of the WT and two *SWI1*[13A]*-GFP* lines in

both WT and *swi1-3* muatnt background. (c) Peterson staining of anthers for

the WT and and two *SWI1*[13A]*-GFP* lines in both WT and *swi1-3* muatnt

background. (d, e) Co-localization of REC8-RFP and SWI1[13A]-GFP (d) and

SWI1[9A]-GFP (e) in the male meiocytes of *swi1-3* mutant at pachytene. Bar: 5

µm. (f) Main branches (upper panel) and siliques (lower panel) of the

wildtype (WT) and two *SWI1-ΔD box-GFP* lines in WT background. (g) Seed

sets in siliques of the WT and two *SWI1-ΔD box-GFP* lines in WT

background. (h) Peterson staining of anthers for the WT and and two *SWI1-*

ΔD box-GFP lines in WT background. (i) Quantification of the pollen viability

for the plants shown in (a) and (f). Error bars represent standard deviations.
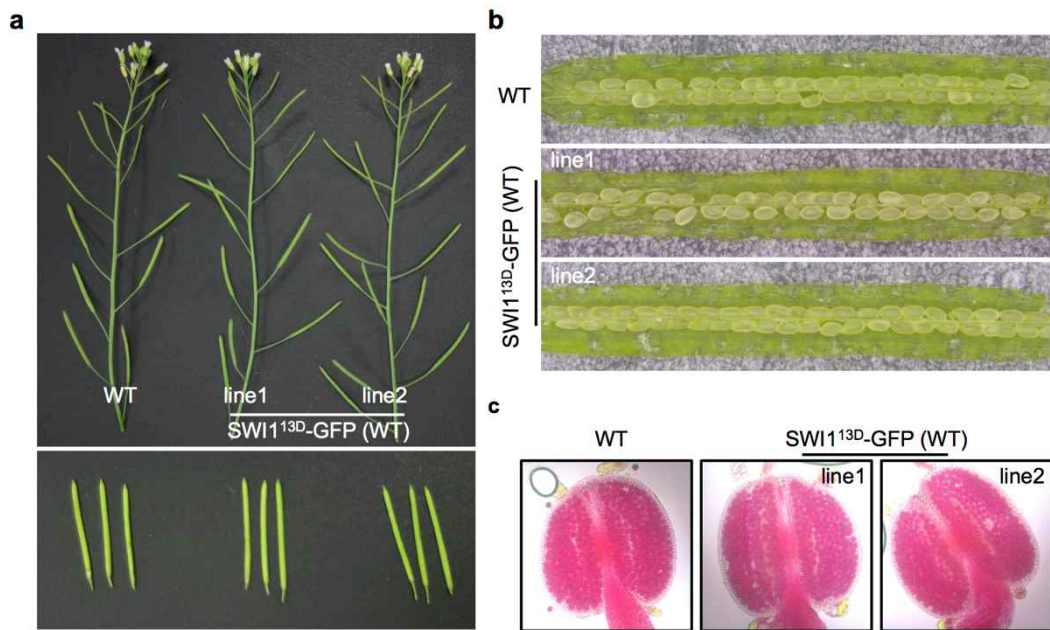
Supplementary Figure 11

Fertility of plants harboring the SWI1^13D^-GFP construct. (a) Main branches (upper panel) and siliques (lower panel) of the wildtype (WT) and two *SWI1^13D^-GFP* lines in wildtype (WT) background. (b) Seed sets in siliques of the WT and two *SWI1^13D^-GFP* lines. (c) Peterson staining of anthers for the WT and and two *SWI1^13D^-GFP* lines.
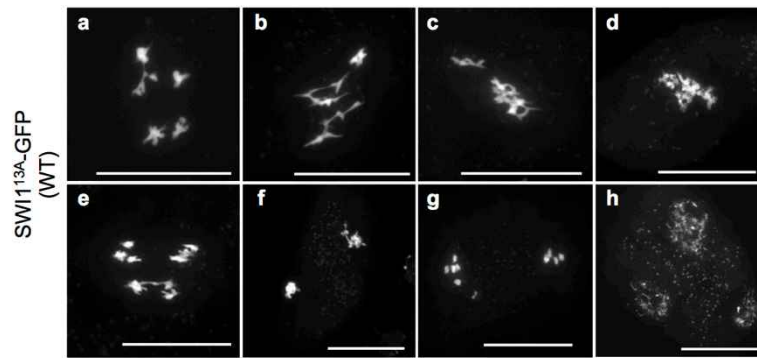
Supplementary Figure 12

Chromosome spread analysis of male meiocytes in *SWI1^{13A}-GFP*/WT plants. (a, b) diakinesis-like stage; (c, d) metaphase I-like stage; (e) anaphase I; (f, g) late telophase I or interkinesis; (h) Tetrad-like stage. Bar: 20 μm.

Supplementary Figure 13

Mutation of two conserved destruction box (D-box) has no impact on the localization pattern of SWI1. (a) Scheme of SWI1 coding region. Arrowheads indicate the positions of five putative D-boxes. (b) Localization analysis of SWI1-Δ2D-box-GFP (306-309 and 559-562) in the male meiocytes during prophase I. Bar: 5 μm.
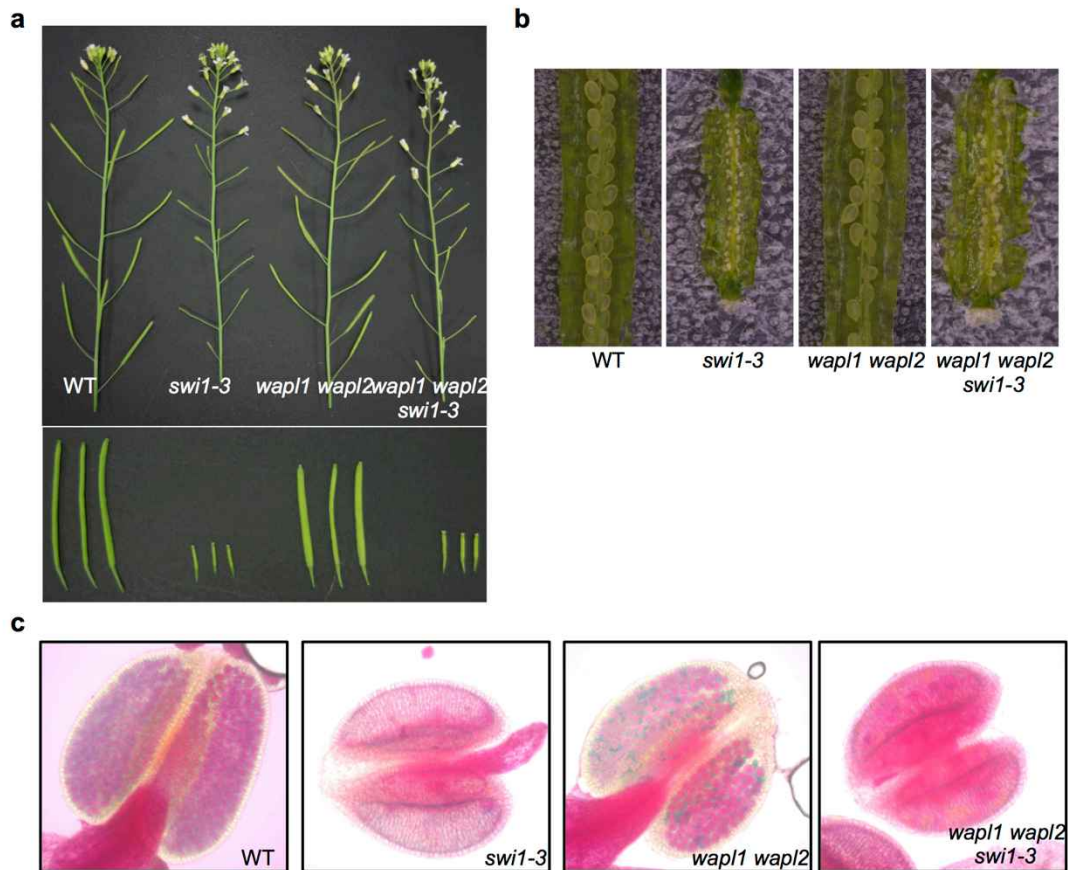
Supplementary Figure 14

The absence of *WAPL1 WAPL2* does not restore the fertility of *swi1-3*

mutants. (a) Main branches (upper panel) and siliques (lower panel) of the

wildtype (WT), *swi1-3*, *wapl1 wapl2* and *wapl1 wapl2 swi1-3* mutants. (b)

Seed sets in siliques of the wildtype (WT), *swi1-3*, *wapl1 wapl2* and *wapl1*

wapl2 swi1-3 mutants. (c) Peterson staining of anthers for the wildtype (WT),

swi1-3, *wapl1 wapl2* and *wapl1 wapl2 swi1-3* mutants.
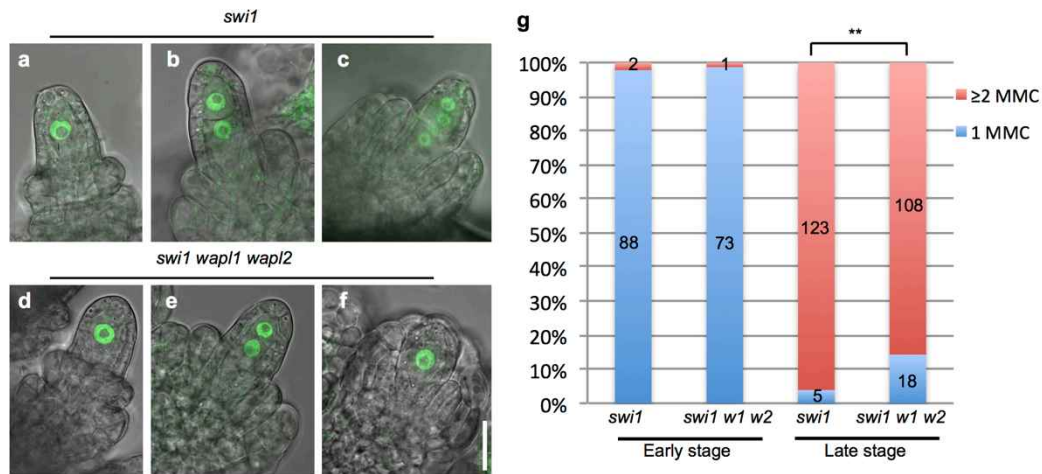
Supplementary Figure 15

The formation of single megaspore mother cell (MMC) in *swi1* mutants is partially rescued by depletion of WAPL. REC8-GFP was used as a maker for the counting of MMC. (a, d) Early premeiotic ovule with short integument primordia harboring one MMC. (b, e) Further developed ovules with elongated integuments containing two MMCs. (c) Older ovules than shown in (b) encompassing four MMCs. (f) Ovule at the similar stages as shown in (b, e) with only one MMC. Bar: 20 μm. (g) Statistical analysis of the number of MMCs at early (as in a, d) and late stages (as in b, c, e, f) in *swi1* and *swi1 wapl1 wapl2* (*swi1 w1 w2*) mutants. The numbers on the columns denote the amount of ovules counted. Asterisks indicate the significant difference (Chi-squared test, P< 0.01).
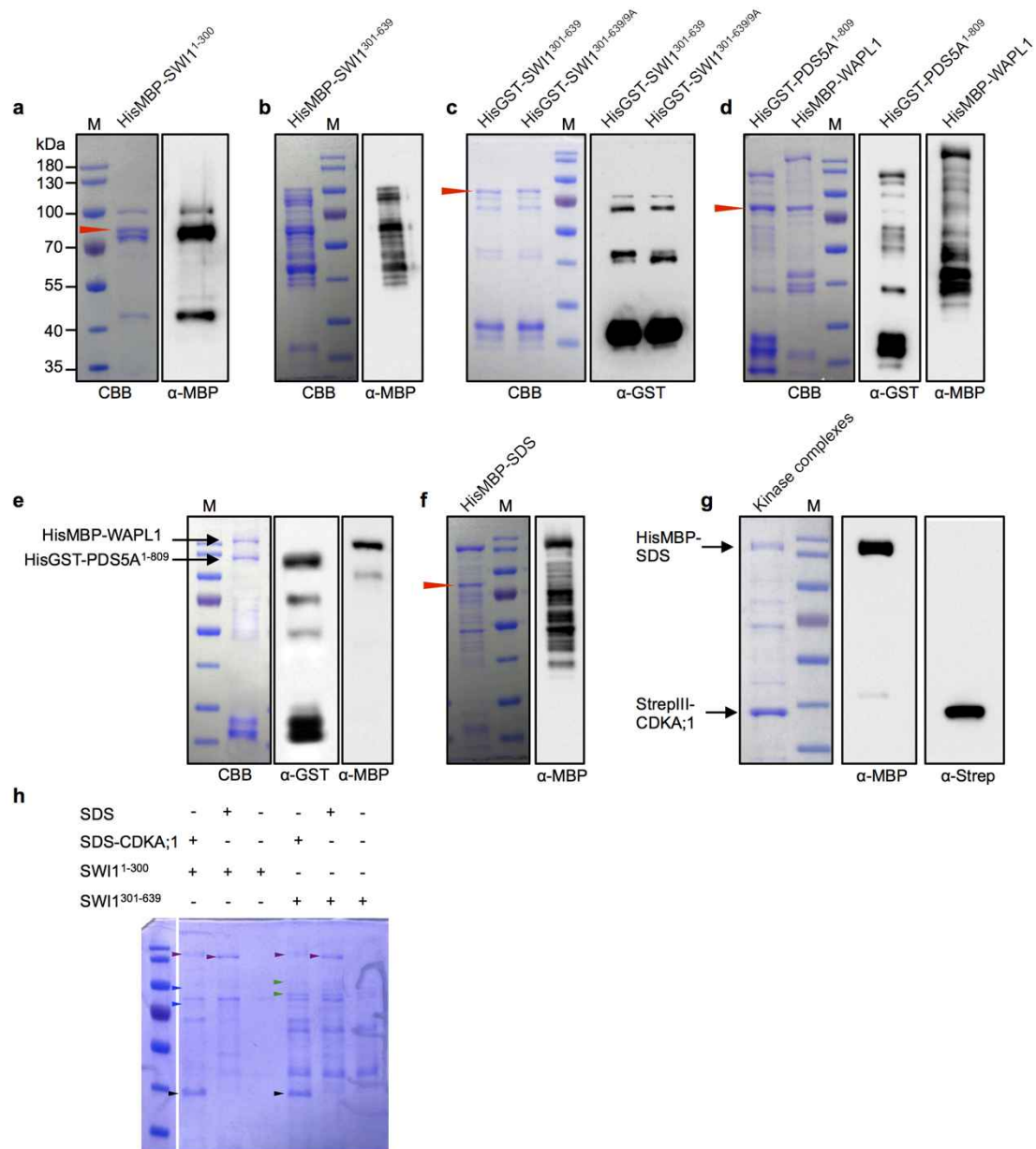
Supplementary Figure 16

CBB stained gels of all purified proteins from *Escherichia Coli* used in this research. (a-c) CBB staining and western blot confirmation of purified HisMBP-SWI1$^{1-300}$ (a), HisMBP-SWI1$^{301-639}$ (b), HisGST-SWI1$^{301-639}$ and HisMBP-SWI1$^{301-639/9A}$ (c), HisMBP-PDS5A$^{1-809}$ and HisMBP-WAPL1 (d), HisMBP-PDS5A$^{1-809}$-HisMBP-WAPL1 heterodimers (e), HisMBP-SDS (f) and CDKA;1-SDS complexes (g) from *E.coli*. The arrowheads indicate the bands

of unspecific protein binding generally to Ni-NTA beads. (h) CBB staining of the proteins after kinase reaction of SWI1 with CDKA;1-SDS complexes. The purple, blue, green or black arrowheads denote the main bands of SDS, SWI1$^{1-300}$, SWI1$^{301-639}$ or CDKA;1 proteins, respectively.

Supplementary table 1. Phosphorylated sites in SWI1.

Experiments	Proteins	Positions	Amino acid	Localization probabilities	peptides and Phospho Probabilities
replicate 1	SWI1 1-300; AT5G51330.1	22	S	0,99989	ISS(1)PSSPTLNVAVAHIR
	SWI1 1-300; AT5G51330.1	166	T	0,998469	REVVSQPAY(0.002)NT(0.998)R
	SWI1 301-639; AT5G51330.1	395	T	1,00000	EAGVKDPYWT(1)PPPGWK
	SWI1 301-639; AT5G51330.1	447	T	0,89016	KEEEELVIMT(0.11)T(0.89)PNSCVTSQNDNLMTPAK
	SWI1 301-639; AT5G51330.1	544	S	0,99992	VVNKGNQITES(1)PQNR
	SWI1 301-639; AT5G51330.1	560	S	1,00000	KHDQQERS(1)PLSLISNTGFR
	SWI1 301-639; AT5G51330.1	597	S	0.34000	ICRPVGMFAWPQLPALAAATDT(0.037)NAS(0.478)S(0.34)PS(0.117)HR
	SWI1 301-639; AT5G51330.1	606	S	1,00000	QAYPS(1)PFPVKPLAAK
replicate 2	SWI1 1-300; AT5G51330.1	22	S	0,99998	ISS(1)PSSPTLNVAVAHIR
	SWI1 1-300; AT5G51330.1	166	T	0,893899	REVVS(0.001)QPAY(0.106)NT(0.894)R
	SWI1 301-639; AT5G51330.1	395	T	1,00000	EAGVKDPYWT(1)PPPGWK
	SWI1 301-639; AT5G51330.1	447	T	0,60282	KEEEELVIMT(0.354)T(0.603)PNS(0.035)CVTSQNDNLMTPAK
	SWI1 301-639; AT5G51330.1	544	S	0,99997	VVNKGNQITES(1)PQNR
	SWI1 301-639; AT5G51330.1	560	S	0,98042	KHDQQERS(0.98)PLS(0.02)LISNTGFR
	SWI1 301-639; AT5G51330.1	597	S	0,70145	ICRPVGMFAWPQLPALAAATDTNAS(0.073)S(0.701)PS(0.225)HR
	SWI1 301-639; AT5G51330.1	606	S	0,99999	QAYPS(1)PFPVKPLAAK

Phosphorylated peptides of SWI1 were identified by mass spectrometry analysis after subjecting SWI1 to *in vitro* kinase assays with CDKA;1-SDS complexes, as shown in Fig. S9d. No phosphorylated peptides were found in reactions without CDKA;1. Results from two independent biological replicates are shown. Data are available via ProteomeXchange Consortium with the identifier PXD009959.

Supplementary Table 2. Primers used in this research.

Purpose	Prmer name	sequence
SWI1 reporter	gSWI1-F	TTGACATTGTGAGAGTAACG
	gSWI1-R	AACTAGTCTAGAGAACGGGT
	gSWI1-attB1-F	GGGGACAAGTTTGTACAAAAAAGCAGGCTTAGCACTTTATGGTTTTTCCG
	gSWI1-attB2SmaI-R	GGGGACCACTTTGTACAAGAAAGCTGGGTTTCACCCGGGAACGTTGAAGAGAT TCTTGG
ASY3 reporter	gASY3-F	TTTGAGAACTCCACTTTACTGCGT
	gASY3-R	CTGCTACTATCTTGTCGTCTTCTC
	gASY3-attB1-F	GGGGACAAGTTTGTACAAAAAAGCAGGCTTAAAAACATTACTTCCCCTACCAAA
	gASY3-attB2-SmaI-R	GGGGACCACTTTGTACAAGAAAGCTGGGTTTCACCCGGGATCATCCCTCAAAC ATTCTGCGA
ZYP1b reporter	gZYP1b-F	GAAATCAGATGAGCCCTTCCTTAA
	gZYP1b-R	GGGAACTGACTTTGTGTGGTAGAC
	gZYP1b-attB1-F	GGGGACAAGTTTGTACAAAAAAGCAGGCTTAGAAATCAGATGAGCCCTTCC
	gZYP1b-attB2-R+T	GGGGACCACTTTGTACAAGAAAGCTGGGTTTTATCAATCAAATGCATAGGGATC
	gZYP1b-AscI-F	AAGCATGGCGCGCCGGTAATAAGAGAAGCGAGCA
	gZYP1b-AscI-R	AAGCATGGCGCGCCACCAAGACGAGATTCTTTCA
	GFP-AscI-F	AAGCATGGCGCGCCAGGTGGCGGTGGATCAGGCGG
	GFP-AscI-R	AAGCATGGCGCGCCCAGACCCTCCACCTCCCTTGT
Y2H	SMC1-EcoRI-F	CCGGAATTCATGCCTGCGATACAATCCCCATCG
	SMC1-SalI-R	ACGCGTCGACTCACGATTCTTGGTAGTTCCTAAGG
Y2H	SMC3-NcoI-F	CATGCCATGGGAATGTTTATCAAGCAGGTTATAATCG
	SMC3-BamHI-R	CGCGGATCCTCAGGTATCGTGGGACTGATCTTTC
Y2H	REC8-EcoRI-F	CCGGAATTCATGTTGAGACTGGAGAGTTTGATAG
	REC8-SalI-R	ACGCGTCGACTTACATGTTGGGTCCTCTTGCAATG
Y2H	SCC3-EcoRI-F	CCGGAATTCATGGAAGACAGTCCTCAAGGCCTTA
	SCC3-SalI-R	ACGCGTCGACTCAGTGTCCCTTGGACCGTTCACCC
Y2H	SWI1-EcoRI-F	CCGGAATTCATGAGTAGTACGATGTTCGTGAAAC
	SWI1-XhoI-R	CCGCTCGAGTCAAACGTTGAAGAGATTCTTGG
Y2H and protein expression	SWI1-attB1-F	GGGGACAAGTTTGTACAAAAAAGCAGGCTTCATGAGTAGTACGATGTTCGTGAA A
	SWI1-300aa-attB2-R	GGGGACCACTTTGTACAAGAAAGCTGGGTTTCACCTCTCAACAGACCATCTATC A
	SWI1-301aa-attB1-F	GGGGACAAGTTTGTACAAAAAAGCAGGCTTCTACAAACTAGCTGAGAGGAACAT G
	SWI1-639aa-attB2-R	GGGGACCACTTTGTACAAGAAAGCTGGGTTTCAAACGTTGAAGAGATTCTTGGG
Y2H and protein expression	AtPDS5A 1-809aa-F	ATGGCTCAGAAGCCGGAGGAACAGTTGAAAG
	AtPDS5A 1-809aa-R	CTACTTAACCAACGTCTTGATCCCATATATCTTC
	AtPDS5A 810-1607aa-F	CTGAAGATATATGGGATCAAGACGTTGGTT
	AtPDS5A 810-1607aa-R	CTATATTGCTGTCCTCGAGATTGACTTACCCAC
	AtPDS5A 1-809-attB1 F	GGGGACAAGTTTGTACAAAAAAGCAGGCTTCATGGCTCAGAAGCCGGAGGAAC AG
	AtPDS5A 1-809-attB2 R	GGGGACCACTTTGTACAAGAAAGCTGGGTTCTACTTAACCAACGTCTTGATCCC A
	AtPDS5A 810-1607-attB1 F	GGGGACAAGTTTGTACAAAAAAGCAGGCTTCCTGAAGATATATGGGATCAAGAC
	AtPDS5A 810-1607-attB2 R	GGGGACCACTTTGTACAAGAAAGCTGGGTTCTATATTGCTGTCCTCGAGATTGA C
Y2H and protein expression	WAPL1-CDS-F	ATGATAATTGTAAAACTAACGGCCAATCGC
	WAPL1-CDS-R	CTACGGTGATTTGCAGGATTCAATCACTCCC
	WAPL1-CDS-attB1-F	GGGGACAAGTTTGTACAAAAAAGCAGGCTTCATGATAATTGTAAAACTAACGGC C

	WAPL1-CDS-attB2-R	GGGGACCACTTTGTACAAGAAAGCTGGGTTCTACGGTGATTTGCAGGATTCAATC
Y2H	OsAM1-CDS F	ATGGACGCGGAGATGGCGGCTCCTGCGCTTG
	OsAM1-CDS R	TCAGCAGTAGGACGGAGTGGCCAGTGCCAGCTC
	OsAM1-attB1-F	GGGGACAAGTTTGTACAAAAAAGCAGGCTTCATGGACGCGGAGATGGCGGCTCC
	OsAM1-attB2-R	GGGGACCACTTTGTACAAGAAAGCTGGGTTTCAGCAGTAGGACGGAGTGGCCAG
	ZmAM1-CDS F	ATGGACGTAGAGACGGTGCAGGCGGGTCCTG
	ZmAM1-CDS R	TCAGCAGTAGGATGGAGTAGCCAGGGCCAGCTC
	ZmAM1-attB1-F	GGGGACAAGTTTGTACAAAAAAGCAGGCTTCATGGACGTAGAGACGGTGCAGGC
	ZmAM1-attB2-R	GGGGACCACTTTGTACAAGAAAGCTGGGTTTCAGCAGTAGGATGGAGTAGCCAG
Dephospho mutagenesis	SWI1 S22/25A-F	GCTCCGTCGGCTCCGACTTTGAATGgtaaactactga
	SWI1 S22/25-R	AGAGATTTTCCCGGCGGTGGTTTCT
	SWI1 S52A-F	GCTCCGGAAAATCTTAAATCGATTAGAG
	SWI1 S52-R	TCTCTGAGGAAGAATCGAAGCATCG
	SWI1 S173A-F	GCTCCGGAGGGAAAGTGCTCGTCTGAG
	SWI1 S173-R	AGCAGCGCGACAGAGACGAGTATTG
	SWI1 T242A-F	GCTAAACAAGAGGCAAAGGAGATAACTA
	SWI1 T242-R	GCCTCCTATTTCATTCCCATCATCA
	SWI1 S261A-F	GCTAGTACTGAGAGACTCGCTCAGAAAG
	SWI1 S261-R	TTCAATCAGCTTTCTCTTACGATT
	SWI1 T395A-F	GCTCCTCCACCTGGTTGGAAGCTTGGTG
	SWI1 T395-R	CCAGTAAGGATCTTTAACTCCTGCT
	SWI1 T447A-F	GCTCCTAATTCTTGTGTTACTAGTCAG
	SWI1 T447-R	AGTCATGATAACAAGCTCCTCCTCT
	SWI1 T461A-F	GCTCCAGCAAAGgtaagagctcgaaaca
	SWI1 T461-R	CATCAGATTATCATTCTGACTAGTA
	SWI1 T515A-F	GCTCCTTTGCTACTAGAGGATTCACCAC
	SWI1 T515-R	CTCTGTTGAGTCTGGCTTTTTAGGA
	SWI1 S522A-F	GCTCCACCAATACAGACACTAGAAGGAG
	SWI1 S522-R	ATCCTCTAGTAGCAAAGGTGTCTCT
	SWI1 S544A-F	GCTCCTCAAAACAGAGAAAAAGGAAGGA
	SWI1 S544-R	CTCTGTGATTTGGTTACCCTTGTTC
	SWI1 S560A-F	GCTCCACTTTCACTAATAAGCAACACTG
	SWI1 S560-R	TCTTTCTTGTTGATCATGCTTCCTT
	SWI1 S597A-F	GCTCCAAGTCACAGACAAGCCTACCCAT
	SWI1 S597-R	AGAAGCATTAGTATCAGTAGCAGCA
	SWI1 S606A-F	GCTCCTTTTCCAGTCAAGCCACTTGCAG
	SWI1 S606-R	TGGGTAGGCTTGTCTGTGACTTGGC
genotyping for *swi1-2*	SWI1-CAPS-F	AACAAGAGGCAAAGGAGATAAC
	SWI1-CAPS-R	TTTTCAGCAGATCAGCCGTAGA
genotyping for *swi1-3*	SAIL_654_C06 LP	ACTCATCACCGCTTGATTCTG
	SAIL_654_C06 RP	TGATACTGCACACGCAATCTC
genotyping for *swi1-4*	GABI_206H06 LP	CTCCCAGATTCATTAAATGCG
	GABI_206H06 RP	CTAGAAACCCAGAAACCCCAG
Phosphomimic mutagenesis	SWI1 S22/25D-F	GACCCGTCGGACCCGACTTTGAATGgtaaactactga
	SWI1 S22/25-R	AGAGATTTTCCCGGCGGTGGTTTCT
	SWI1 S52D-F	GACCCGGAAAATCTTAAATCGATTAGAG

	SWI1 S52-R	TCTCTGAGGAAGAATCGAAGCATCG
	SWI1 S173D-F	GACCCGGAGGGAAAGTGCTCGTCTGAG
	SWI1 S173-R	AGCAGCGCGACAGAGACGAGTATTGTAC
	SWI1 T395D-F	GACCCTCCACCTGGTTGGAAGCTTGGTG
	SWI1 T395-R	CCAGTAAGGATCTTTAACTCCTGCT
	SWI1 T447D-F	GACCCTAATTCTTGTGTTACTAGTCAG
	SWI1 T447-R	AGTCATGATAACAAGCTCCTCCTCT
	SWI1 T461D-F	GACCCAGCAAAGgtaagagctcgaaaca
	SWI1 T461-R	CATCAGATTATCATTCTGACTAGTA
Phosphomimic mutagenesis	SWI1 T515D-F	GACCCTTTGCTACTAGAGGATTCACCAC
	SWI1 T515-R	CTCTGTTGAGTCTGGCTTTTTAGGA
	SWI1 S544D-F	GACCCTCAAAACAGAGAAAAAGGAAGGA
	SWI1 S544-R	CTCTGTGATTTGGTTACCCTTGTTC
	SWI1 S560D-F	GACCCACTTTCACTAATAAGCAACACTG
	SWI1 S560-R	TCTTTCTTGTTGATCATGCTTCCTT
	SWI1 S597D-F	GACCCAAGTCACAGACAAGCCTACCCAT
	SWI1 S597-R	AGAAGCATTAGTATCAGTAGCAGCA
	SWI1 S522D-F	GACCCACCAATACAGACACTAGAAGGAG
	SWI1 S522-R	ATCCTCTAGTAGCAAAGGTGTCTCT
	SWI1 S606D-F	GACCCTTTTCCAGTCAAGCCACTTGCAG
	SWI1 S606-R	TGGGTAGGCTTGTCTGTGACTTGGC
	AtPDS5A-attB1 F1	GGGGACAAGTTTGTACAAAAAAGCAGGCTTCATGGCTCAGAAGCCGGAGGAACAG
	AtPDS5A-attB4 R1-T 809aa	GGGGACAACTTTGTATAGAAAAGTTGGGTGCTTAACCAACGTCTTGATCCCA
	AtPDS5B-CDSattB1-F1	GGGGACAAGTTTGTACAAAAAAGCAGGCTTCATGGAGAAAACTCCGACGCAG
	AtPDS5B-CDSattB4-R1_T	GGGGACAACTTTGTATAGAAAAGTTGGGTGGCCACAAAGCTGATTCAAAAG
	AtPDS5C-CDSattB1-F	GGGGACAAGTTTGTACAAAAAAGCAGGCTTCATGTCGGATTCTGATAAAGAG
	AtPDS5C-CDSattB4-R_T	GGGGACAACTTTGTATAGAAAAGTTGGGTGTCGCTTCCTCTTCTTACCGG
BiFC constructs	AtPDS5D-CDSattB1-F	GGGGACAAGTTTGTACAAAAAAGCAGGCTTCATGCAAAGTGCCCTAATTCCATC
	AtPDS5D-CDSattB4-R_T	GGGGACAACTTTGTATAGAAAAGTTGGGTGTGACTTTCTCTTCTCTTCATC
	AtPDS5E-CDSattB1-F	GGGGACAAGTTTGTACAAAAAAGCAGGCTTCATGGGTCCTCTTGTCGAAGCG
	AtPDS5E-CDSattB4-R_T	GGGGACAACTTTGTATAGAAAAGTTGGGTGTGGATCAACCTCAAGCACC
	AtSWI1-CDS-attB3-F	GGGGACAACTTTGTATAATAAAGTTGTAATGAGTAGTACGATGTTCGTGAAA
	AtSWI1-639-attB2-R-T	GGGGACCACTTTGTACAAGAAAGCTGGGTTAACGTTGAAGAGATTCTTGGG
	AtSWI1-300-attB2-R-T	GGGGACCACTTTGTACAAGAAAGCTGGGTTCCTCTCAACAGACCATCTATCA
	WAPL1-attB3-F	GGGGACAACTTTGTATAATAAAGTTGTAATGATAATTGTAAAACTAACGGCC
	WAPL1-attB2-R-T	GGGGACCACTTTGTACAAGAAAGCTGGGTTCGGTGATTTGCAGGATTCAATC

CHAPTER 3: Cdks/cyclins beyond meiosis

3.1 Protein and metabolite composition of *Arabidopsis* stress granules

The following paper has been published in New Phytologist, 2018.

My contribution to this work is summarized below:

- Generation of the CDKA;1:mVenus reporter line to investigate stress response in Arabidopsis leafs and roots

Protein and metabolite composition of Arabidopsis stress granules

Monika Kosmacz[1] (iD), Michał Gorka[1], Stephan Schmidt[1], Marcin Luzarowski[1], Juan C. Moreno[1] (iD), Jagoda Szlachetko[1], Ewa Leniak[1], Ewelina M. Sokolowska[1], Kostika Sofroni[2] (iD), Arp Schnittger[2] (iD) and Aleksandra Skirycz[1] (iD)

[1]Max Planck Institute of Molecular Plant Physiology, 14476 Potsdam, Germany; [2]Department of Developmental Biology, University of Hamburg, 22069 Hamburg, Germany

Author for correspondence:
Aleksandra Skirycz
Tel: +49 03315678216
Email: skirycz@mpimp-golm.mpg.de

Summary

- Stress granules (SGs) are evolutionary conserved aggregates of proteins and untranslated mRNAs formed in response to stress. Despite their importance for stress adaptation, no complete proteome composition has been reported for plant SGs. In this study, we addressed the existing gap. Importantly, we also provide evidence for metabolite sequestration within the SGs.
- To isolate SGs we used Arabidopsis seedlings expressing green fluorescent protein (GFP) fusion of the SGs marker protein, Rbp47b, and an experimental protocol combining differential centrifugation with affinity purification (AP). SGs isolates were analysed using mass spectrometry-based proteomics and metabolomics.
- A quarter of the identified proteins constituted known or predicted SG components. Intriguingly, the remaining proteins were enriched in key enzymes and regulators, such as cyclin-dependent kinase A (CDKA), that mediate plant responses to stress. In addition to proteins, nucleotides, amino acids and phospholipids also accumulated in SGs.
- Taken together, our results indicated the presence of a preexisting SG protein interaction network; an evolutionary conservation of the proteins involved in SG assembly and dynamics; an important role for SGs in moderation of stress responses by selective storage of proteins and metabolites.

Introduction

Stress granules (SGs) are large aggregates of proteins and mRNAs formed in response to stress as a consequence of translational repression (Protter & Parker, 2016). Stress granules are evolutionarily conserved and have been reported in animal (Collier *et al.*, 1988), plant (Nover *et al.*, 1983), and yeast cells (Hoyle *et al.*, 2007). The main role of SGs is to establish and subsequently moderate the stress translatome and proteome by selective storage and protection of mRNAs (Merret *et al.*, 2013) and proteins (Takahara & Maeda, 2012), respectively. Sequestration into SGs provides an elegant way to inhibit mRNA translation and protein activity, while SG disassembly allows rapid reactivation upon stress recovery.

The important role of SGs in stress responses has led to intensive study of SG composition. In HeLa cell lines, the SG proteome was demarcated using transgenic lines expressing GFP–G3BP protein, a Ras-GTPase-activating protein SH3 domain-binding protein (Matsuki *et al.*, 2013) involved in initiation of SG assembly. Treatment of the cells with sodium arsenite, a stress condition known to promote SG formation (Jain *et al.*, 2016), followed by a series of differential centrifugations and affinity purification (AP) using anti–GFP

antibody, revealed more than 300 proteins that were at least twice as abundant in the stressed cells than in unstressed cells, thereby identifying these proteins as putative SG components. A similar approach using a different SG marker protein as bait defined the yeast SG proteome and yielded over 200 proteins (Jain *et al.*, 2016). More recent studies have determined the protein composition of human SGs using proximity-labeling approaches (Markmiller *et al.*, 2018; Youn *et al.*, 2018).

The available yeast and mammalian SGs proteome data can be summarised as follows: (1) Mammalian and yeast SGs share a subset of conserved proteins that participate in SG assembly and dynamics (Jain *et al.*, 2016; Markmiller *et al.*, 2018; Youn *et al.*, 2018). (2) Stress granules sequester organism, cell-type, and stress-specific proteins, which in turn contribute to specific stress responses (Jain *et al.*, 2016; Markmiller *et al.*, 2018; Youn *et al.*, 2018). (3) Proximity-labeling experiments reveal the operation of a preexisting interaction network between core SG proteins even in unstressed cells (Markmiller *et al.*, 2018; Youn *et al.*, 2018).

Unlike the case for animal and yeast cells, no complete proteome composition has been reported for plant SGs. The current list of known Arabidopsis SG components is no longer than 25 proteins, and these were identified (mostly) based on their

homology with animal and yeast SGs (Chantarachot & Bailey-Serres, 2018). We have addressed this gap in our understanding of plant SGs by adapting a protocol used for SG isolation from yeast and HeLa cells (Jain *et al.*, 2016) that takes advantage of SG marker lines that overexpress the RNA-binding protein Rbp47b (AT3G19130) fused to GFP (Gutiérrez-Beltrán *et al.*, 2015). Our proteomic analyses revealed the presence of 118 proteins in Arabidopsis SGs. As expected, we found both previously reported as well as novel proteins. Whereas the first group is important for SG assembly and dynamics, the second group comprised key enzymes (e.g. enzymes responsible for ethylene, glucosinolate, and rhamnose metabolism), regulators of plant growth (e.g. cyclin-dependent kinase 1 [CDKA;1] and translationally controlled tumor protein 1 [TCPT1]), and proteins involved in response to stress (e.g. mitogen activated kinases and glutathione *S*-transferases).

Our previous work demonstrating that metabolites are retained in the protein complexes during biochemical separation (Luzarowski *et al.*, 2017; Veyel *et al.*, 2017) led us to the present investigation of the small molecule composition of isolated SGs. To our knowledge, this has not been reported for any organism so far. Excitingly, our metabolic analysis revealed an accumulation of nucleotides, amino acids and phospholipids in Arabidopsis SGs that can be linked to the SG protein composition, and points to a novel and important role for SGs in metabolite sequestration. Our results provide innovative insights into the function of SGs and suggest that the selective storage/protection of proteins and metabolites in SGs might play a role in moderating plant responses to stress.

Materials and Methods

Plant growth conditions and heat treatment

Arabidopsis thaliana wild-type Col-0, *35S:GFP–Rbp47b* (Gutiérrez-Beltrán *et al.*, 2015) and *35S:GFP* (Merkulova *et al.*, 2014) transgenic seedlings (1.5 mg seeds *c.* 100 plants) were grown in sterile liquid cultures (100 ml Erlenmeyer glass flasks) on orbital shakers with constant, uniform fluorescent lighting (*c.* 80 μmol m^{-2} s^{-1}) and temperature (22°C), in 35 ml of half-strength Murashige and Skoog (½MS) liquid medium (Murashige & Skoog, 1962) supplied with 1% sucrose. The shaker speed was 130 rpm. After 7 d, the medium was changed in all flasks, and after 10 d, the temperature was increased to 42°C and the plants held for 30 min in darkness to induce SG formation. Control seedlings were kept at room temperature (RT) and in the light. SG formation was checked by confocal microscopy. For microscopy studies, *A. thaliana* CDKA1;−mVenus seedlings were grown on ½MS agar horizontal plates supplied with 1% of sucrose for 5 d.

Stress granule isolation

The protocol was adapted from Jain *et al.*, 2016. A 6 g sample of ground material (per condition: control and heat treatment) was pulverised with a precooled mortar and pestle in 6 ml of lysis buffer (50 mM Tris-HCl pH 7.4, 100 mM potassium acetate, 2 mM magnesium acetate, 0.5% NP-40, 0.5 mM DTT, 1 mM NaF, 1 mM Na$_3$VO$_4$, protease inhibitor cocktail (Sigma P9599), and 1 U μl^{-1} RNasin). The resulting slurry was centrifuged at 4000 g for 10 min at 4°C, the supernatant was removed, and the pellet was resuspended in 4 ml of lysis buffer. This suspension was then divided into three or four technical replicate samples and the samples were centrifuged at 18 000 g for 10 min at 4°C. The pellets were resuspended in 0.5 ml lysis buffer, vortexed, and centrifuged at 18 000 g at 4°C for 10 min. As in the previous step, the supernatant was discarded and the pellets were resuspended in 0.5 ml of lysis buffer. After a final centrifugation at 850 g for 10 min at 4°C, the supernatant was checked for the presence of SG by confocal microscopy, and used in the further purification steps. A 50 μl volume of this SG fraction was used for protein extraction using an acetone precipitation protocol. Briefly, 4 volumes of −20°C acetone were added to the SG-enriched sample, followed by 2 h precipitation at −20°C and 10 min centrifugation at 20 000 g. The resulting protein pellets were dried in a Speed-vac rotary evaporator and stored at −80°C.

A 1 ml volume (100 μl per sample) of Dynabeads protein A (Thermo Fisher 10002D, Hennigsdorf, Germany) was equilibrated for 1 h at RT with 1 ml of DEPC-treated phosphate-buffered saline (PBS) buffer (on a rotating wheel). The beads were separated with a magnet and washed once with DEPC-treated PBS buffer supplemented with 0.05% NP-40 for 5 min at 4°C and then three times with the lysis buffer for 5 min at 4°C. A 370 μl volume of the SG fraction supplemented with RNasin (1:100 final dilution) was incubated (on a rotating wheel) with 30 μl of equilibrated Dynabeads for 15 min at room temperature (RT). The beads were then separated and the supernatant was incubated (on a rotating wheel) in a new tube with 12.5 μl anti–GFP rabbit IgG antibody (Life Technologies A11122, Hennigsdorf, Germany) for 60 min at RT. The excess anti–GFP antibody was separated by centrifugation at 14 000 g for 15 min at 4°C. The supernatant was removed and the pellet was resuspended in 500 μl of lysis buffer supplemented with an additional 5 μl of RNasin. This resuspension was mixed (on a rotating wheel) with 60 μl of equilibrated Dynabeads for 15 min at RT, followed by several washing steps: three times for 5 min with lysis buffer at 4°C, followed by 5 min with washing buffer 1 (lysis buffer with 2 M urea), 2 min with washing buffer 2 (lysis buffer with 300 mM potassium acetate), and 5 min with lysis buffer. In the final step, the supernatant was removed and the SGs remained attached to the beads. Note that NP-40 was removed from the solutions when SGs were isolated for the small molecule analysis.

Affinity purification for control 35S:GFP and wild-type

Affinity purification was performed as in the previous SGs extraction procedure with the exclusion of first differential centrifugation step. A 5 g sample of ground material (*35S:GFP* and wild-type (WT) seedlings treated for 30 min at 42°C) was used as starting material. The experiment was performed in four technical replicates.

160

Tandem affinity purification

Cloning of the *35S:Rbp47b-TAP* construct was performed using Gateway technology, as previously described (Van Leene *et al.*, 2007). The sequences of the primers for the Rbp47b amplification were as follows: Fwd: GGGGACAAGTTTGTACAAAA AAGCAGGCGCCACCATGCAGACAACCAACGGCTC Rev: GGGGACCACTTTGTACAAGAAAGCTGGGTGATTCTC CCCATGATAGTTGTTG The empty vector control was as previously described (Luzarowski *et al.*, 2017). Transformations of *Escherichia coli*, *A. tumefaciens*, and Arabidopsis PSB cell cultures were performed as previously described (Van Leene *et al.*, 2007). PSB-L Arabidopsis cells cultures were maintained as previously described (Van Leene *et al.*, 2007). Cells were collected during logarithmic growth using a nylon mesh (wire diameter 34 μm, thickness 55 μm, open area 14%, Prosepa) and vacuum filtration. Dried cells were immediately frozen in liquid nitrogen, and the frozen material was pulverised to homogeneity in liquid nitrogen with a mortar and pestle. The TAP experiment was performed as published previously (Luzarowski *et al.*, 2017). Briefly, IgG Sepharose 6 Fast Flow beads (GE Healthcare, Solingen, Germany) were equilibrated with lysis buffer composed of 25 mM Tris-HCl pH 7.5, 500 mM NaCl, 15 mM MgCl$_2$, 0.5 mM DTT, 1 mM Na$_3$VO$_4$, 1 mM NaF, and protease inhibitor cocktail (Sigma P9599). A 1 ml aliquot of lysis buffer was added per 1 g of pulverised material. The homogenised samples were centrifuged at 20 000 *g* for 10 min at 4°C. On average, 3 g of plant material (corresponding to *c.* 90 mg of total protein) and 100 μl of IgG beads were used per pull-down. tandem affinity purification (TAP)-tag AP (including the empty vector as a control) was performed on three technical replicates. Binding to the beads was performed by 1 h incubation on a rotating wheel at 4°C and the beads were transferred to a Mobicol 'Classic' filter (35 μM pore size; MoBiTec, Gottingen, Germany) and washed with 10 ml of wash buffer (25 mM Tris-HCl pH 7.5 and 500 mM NaCl). The lower cap of the 'Mobicol Classic' was closed and 400 μl of elution buffer (10 mM Tris-HCl pH 7.5, 150 mM NaCl, 0.5 mM EDTA, E64, and 1 mM phenylmethylsulphonyl fluoride containing) 50 U of an improved version of the tobacco etch virus (AcTEV) protease was added. Samples were incubated for 1 h at 16°C on a table shaker at 1000 rpm. After 30 min, an additional 50 U of protease were added. The eluate was collected in a 2 ml Eppendorf tube. An additional 200 μl of elution buffer was passed over the beads and pooled with the previous eluate.

A 600 μl volume of the eluate was used for protein extraction by acetone precipitation. Briefly, 4 volumes of −20°C acetone were added to the eluate, followed by 2 h precipitation at −20°C and 10 min centrifugation at 20 000 *g*. The resulting protein pellets were dried in a Speed-vac evaporator and stored at −80°C.

Protein preparation for LC–MS/MS

For the SG isolation and control affinity purification experiment: Dynabeads were solubilised in 100 μl of urea buffer (6 M urea and 2 M thiourea in 40 mM ammonium bicarbonate). For the

TAP protocol and the SG-enriched fraction: protein pellets were resuspended in urea buffer, as above. Less than 100 μg of total protein was used for protein digestion. Cysteine residues were reduced by the addition of 5 μl of 100 μM DTT for 30 min at RT, followed by alkylation with 5 μl of 300 mM iodoacetamide for 20 min in dark. The proteins were enzymatically digested using LysC/Trypsin Mix (Promega) according to the manufacturer's instructions. For the SG isolation: Peptides were desalted on C18 SepPack columns, dried to *c.* 4 μl using a centrifugal evaporator, and stored at −80°C until measurement. For the TAP protocol: peptides were desalted using C18 Empore® extraction disc (3M, Maplewood, MN) STAGE tips (Rappsilber *et al.*, 2003). Dried peptides were solubilised in loading buffer (2% ACN, 0.2% TFA) and an amount equivalent to 0.8–1.0 μg of peptides was separated on a reversed-phase column and analysed with a Q-Exactive Plus or Q-Exactive HF spectrometer (Thermo Fisher Scientific, Hennigsdorf, Germany).

Liquid chromatography and mass spectrometry analysis

Peptides were resuspended in 40 μl of resuspension buffer (3% v/v acetonitrile, 0.1% v/v formic acid). Measurements were executed on a Q-Exactive HF coupled to an Easy nLC1000 HPLC (Thermo Scientific, Hennigsdorf, Germany). A 6 μl volume of sample was loaded onto an Acclaim PepMap RSLC reversed-phase column (75 μm inner diameter, 15 cm length, 2 μm bead size (Thermo Scientific) at a flow rate of 0.6 μl min^{-1}. The column was previously equilibrated with buffer A (0.1% formic acid in water). Peptides were eluted by increasing the percentage of buffer B (100% acetonitrile, 0.1% formic acid) in a gradient from 0% to 30% (v/v) over 63 min, from 30% to 50% for the next 18 min, from 50% to 80% for the last 10 min at a flow rate of 0.25 μl min^{-1}. The column was then washed with 80% (v/v) acetonitrile for 5 min and the column was re-equilibrated with buffer A for 4 min. Peptide ions were detected in a full scan from mass-to-charge ratio 150–1600 at resolution of 120 000 (AGC target of 3e6). MS/MS scans were performed for the 15 peptides with the highest MS signal (ddMS2 resolution of 30 000, AGC target 2e5, isolation width mass-to-charge ratio 3 *m/z*, relative collision energy 30). Peptides for which MS/MS spectra had been recorded were excluded from further MS/MS scans for 20 s. Dynamic exclusion of 20 s was used and apex trigger (to 9 s) was enabled.

Protein identification – MaxQuant

Raw files were analysed using MAXQUANT software v.1.6.0.16 for protein identification and quantification (Cox & Mann, 2008). The protein annotation was obtained using *A. thaliana* TAIR10 protein sequences (35 386 entries) by Andromeda. The common contaminant database was also included in the search. The settings used for the search were: 10 ppm peptide mass tolerance; 0.8 Da MS/MS tolerance; maximum of two missed cleavages allowed; threshold for validation of peptides set to 0.01 using a decoy database; carbamidomethylation of cysteine set as a fixed modification and oxidation of methionine set as a variable modification.

The 'label-free quantification' and 'match between runs' options were selected. The minimum peptide length of six amino acids was used. Contaminants and decoy hits were removed from each dataset. Furthermore, at least two unique peptides were required per protein group. Label-free quantification (LFQ) intensities were used in all analysis performed in this manuscript.

Metabolite extraction

A 20 mg sample of the freeze-dried plant material, 100 µl of the SG-enriched fraction, AP beads were extracted as described previously (Giavalisco et al., 2011). In short, proteins, lipids, and polar compounds were separated by a methyl-tert-butyl ether (MTBE)/methanol/water solvent system that separates molecules into a pellet, an organic phase, and an aqueous phase, respectively.

Metabolomics

After MTBE extraction, the aqueous phase containing semi-polar and polar compounds and the organic phase containing lipid compounds were dried in a centrifugal evaporator and then stored at −80°C until LC-MS analysis. Small molecules were separated by ultraperformance liquid chromatography and analysed on an Exactive Orbitrap MS (Thermo Fisher Scientific) in positive and negative ionisation modes, as described previously (Giavalisco et al., 2011). Data processing, including peak detection and integration and removal of isotopic peaks and chemical noise, were performed using REFINER MS 7.5 (GeneData). An in-house database of chemical compounds was used to annotate obtained metabolic features (m/z at a given retention time) allowing 10 ppm and 0.15 min deviations from the reference compound mass and retention time, respectively. This approach led to annotation of eluted metabolites to a single match.

Domain analysis

Protein sequences were downloaded from The Arabidopsis Information Resource (TAIR). Protein sequences were submitted to the Batch CD-Search Tool on the NCBI portal for domain analysis. Proteins with predicted prion-like domains were identified using PLAAC (Lancaster et al., 2014) based on a positive CORE score.

Orthologue search

The orthologue search was conducted using the DIOPT–DRSC Integrative Ortholog Prediction Tool (http://www.flyrnai.org/diopt) with selection of all prediction tools for pairwise search A. thaliana – Homo sapiens and A. thaliana – Saccharomyces cerevisiae excluding low scores (score > 1, unless only match score is 1). The obtained results were revised for agreement with the literature.

Construction of the CDKA;1−mVenus reporter lines

The genomic sequence of *CDKA;1*, together with its 3 kb 5′ upstream region (including the presumptive promoter) and 1 kb downstream region with the 3′UTR, were amplified by polymerase chain reaction (PCR) using the Phusion Ppolymerase and subcloned into *pENTR2B* vector by SLICE. A *Sma*I restriction site was introduced by PCR before the stop codon of *CDKA;1*. The constructs were then linearised by *Sma*I restriction and ligated with the mVenus open reading frame (ORF), followed by Gateway LR reactions into the destination vector *pGWB501* (Nakagawa et al., 2007).

The transgenic Arabidopsis plants were generated by transforming the construct into the *A. tumefaciens* strain GV3101 (pM90). A 100 ml overnight culture of *Agrobacterium* harboring these constructs was pelleted and resuspended in an equal volume of transformation solution containing 5% sucrose and 0.02% Silwet L-77, followed by floral dipping. Heterozygous *cdka;1* mutants transformed with this genomic CDKA;1 reporter line segregated from homozygous *cdka;1* mutants that showed a wild-type growth behavior. List of primers: for CDKA;1 amplification *Fwd*: ACCAAGACACCAAGCGCAA and *Rev*: CAGAA TGGAAGCGTCTTTGCTT, for pENTR2B amplification before SLICE reaction *Fwd*: AAGCAAAGACGCTTCCATT CTGCGCGGCCGCACTCGAGATA and *Rev*: TTGCGCTT GGTGTCTTGGTGGATCCAGTCGACTGAATTG, *Sma*I insertion site *Fwd*: GGGATCTTTCCGTATTTTGGTCATT and *Rev*: GGGAGGCATGCCTCCAAGATCCTTG.

Transient infiltration

Transient leaf transformation using 3-wk-old plants expressing CDKA;1−mVenus with *A. tumefaciens* harboring construct overexpressing RFP–Rbp47b (Gutiérrez-Beltrán et al., 2015) was performed as described previously (Lee & Yang, 2006). All transient expression essays were repeated at least three times using independently grown plants. Each time transformation of three leaves from three independent plants was performed; 30 min of 42°C dark treatment was used to induce stress granule localisation.

Microscopy

The 35S:GFP–Rbp47b transgenic lines used as SG markers were published by Gutiérrez-Beltrán et al. (2015). RHM1:RHM1–GFP lines were published by Kuhn et al. (2011). The Pro: CDKA;1: CDKA;1−mVenus transgenic lines were provided by Prof. Dr Arp Schnittger. For CDKA;1, 5-d-old seedlings growing on vertical plates (½MS medium (Murashige & Skoog, 1962) supplemented with 1% sucrose and 0.8% agar) in continuous light conditions were transferred to water (as a control) or water supplemented with 200 ng µl^{-1} cycloheximide. After 30 min of cycloheximide treatment, 30 min of heat stress (42°C) was applied. For GFP–Rbp47b, RHM1–GFP and CDKA;-1−mVenus, images were acquired using a Leica DM6000B/SP5 confocal laser scanning microscope (Leica Microsystems, Wetzlar, Germany). For disassembly experiment of CDKA;1–Venus seedlings growing on vertical plates, after 30 min at 42°C, were moved to normal light conditions. Localisation was followed starting at the time 0 (corresponding to heat/darkness stress) and

was followed up to 120 min of the recovery phase. Excitation with a 488 nm laser and emission of 520–550 nm was used to visualise Venus protein. The GFP–Rbp47b signal was observed using excitation of a 488 nm laser and emission between 500 and 520 nm. For transient infiltration experiment, co-localisation images of CDKA;1−mVenus and RFP–Rbp47b were taken using sequential scan mode between lines allowing separation for the excitation of two fluorophores at once. RFP–Rbp47b signal was excited with 561 nm laser and emission was detected between 595 and 620 nm.

Dot-blot analysis of GFP–Rbp47b signal

10 μl of control and heat-stressed sample from 35:GFP–Rbp47b seedlings used as starting material for SGs extraction protocol, corresponding to 20 μg of protein were spotted on nitrocellulose membrane in three replicates. GFP signal was visualised using Typhoon Scanner using laser excitation corresponding to 488 nm. Quantification of the signal was performed by measuring intensity of each sample in a Fiji program using the ROI function.

Data availability

The mass spectrometry proteomics data were deposited to the ProteomeXchange Consortium via the PRIDE (Vizcaino *et al.*, 2016) partner repository with the dataset identifier PXD011716.

Results

SG cores can be isolated from plant material

Stress granules are defined as non-membranous organelles containing complexes of mRNA and proteins that form under stress conditions. SGs are composed of stable cores and a more dynamic and fluid shell. Excitingly, the SG cores have recently been isolated from mammalian and yeast cells using a combination of a differential centrifugation steps and AP (Jain *et al.*, 2016; Wheeler *et al.*, 2017). We decided to adapt this existing protocol to plant cells to investigate the composition of SGs in plants (Fig. 1a). We demonstrated that, in addition to mRNAs and proteins, small molecules were also retained in the isolated SGs, and these can be analysed by mass spectrometry-based metabolomics.

We demarcated the proteome and metabolome of plant SGs using transgenic seedlings that overexpress GFP–tagged Rbp47b. Rbp47b is a polyadenylate-binding protein involved in protein aggregation and RNA recruitment, and is important in SG formation (Lorkovic *et al.*, 2000; Weber *et al.*, 2008). The homologs of Rbp47b, TIA-1 (Kedersha *et al.*, 1999) and Pab1 (Hoyle *et al.*, 2007), play an analogous key role in SG assembly in human and yeast cells, respectively. We subjected *35S:GFP–Rbp47b* seedlings grown in liquid medium to either control conditions or a combination of heat and dark treatment (30 min 42°C and darkness), a stress known to promote SG formation (Weber *et al.*, 2008). As

expected, the GFP–Rbp47b was localised predominantly in SGs in the stressed seedlings, whereas it was localised in the cytosol and nucleus in unstressed control seedlings (Fig. 1b, Supporting Information Fig. S1). Plant material was then harvested, snap frozen in the liquid nitrogen and ground to a fine powder before lysis with a native buffer containing protease and RNase inhibitors. The SGs were enriched using a series of differential centrifugations. As expected, SGs were present in the SG-enriched fraction prepared from the heat/dark-treated seedlings but not from the control seedlings (Fig. 1b). Stress granule enriched fractions prepared from control and stress-treated seedlings were then subjected to AP using anti–GFP antibodies and magnetic Sepharose beads (Fig. 1a). The SG-enriched fraction and the AP beads (purified SGs; also referred to as the SG isolate) were then analysed by mass spectrometry (MS)-based proteomics and metabolomics.

The big advantage of the above described protocol is its specificity. Combination of two consecutive purification steps ensures SGs purity. First, centrifugation step enriched for protein aggregates such as SGs. Second, AP step served to separate SGs from the remaining aggregates. Unstressed seedlings were used to exclude false positives, for example, resulting from the unspecific interactions with the antibodies and/or the beads. To further correct for proteins and metabolites that can bind to the GFP tag alone, an additional AP experiment using seedlings that overexpressed GFP protein (*35S:GFP*) was performed. As GFP protein did not accumulate in SGs under heat/dark treatment (Fig. S2) the centrifugation step was omitted. Moreover, to exclude false positives resulting from the unspecific interactions, e.g. with the antibodies and/or the beads, we used WT seedlings. Proteins and metabolites that were at least twice as abundant in the AP from *35S:GFP* in comparison with the WT seedlings comprised the so-called GFP negative list.

Proteome composition of Arabidopsis SGs

Multiple criteria were used to define SG-associated proteins. The SGs were only present in the heat/dark treated cells, so we first looked for proteins that were at least twice as abundant in the SGs isolate from the stress-treated vs the control seedlings. We then excluded plastid and mitochondrial proteins, as these are unlikely to localise into cytoplasmic SGs and can therefore be viewed as false positives. Finally, the obtained list comprising 118 proteins was compared with the GFP–negative list revealing an overlap of 15 proteins. Notably, six of these 15 proteins have been previously associated with SGs, e.g. PAB2, PAB4 and TUDOR2, and therefore we decided against using the GFP–negative list as an exclusion list, but rather as a caution list. Importantly, 97 of the 118 proteins were enriched two-fold after the SG fractionation stage, further validating our selection.

Analysis of the SG proteome revealed the presence of the known Arabidopsis SG proteins. In addition to the Rbp47b used as bait in our experiment, the list contained both TUDOR-SN proteins (TSN1 and TSN2) (Gutiérrez-Beltrán *et al.*, 2015), poly (A)-binding proteins 2 and 8 (PAB2 and PAB8) (Weber *et al.*,
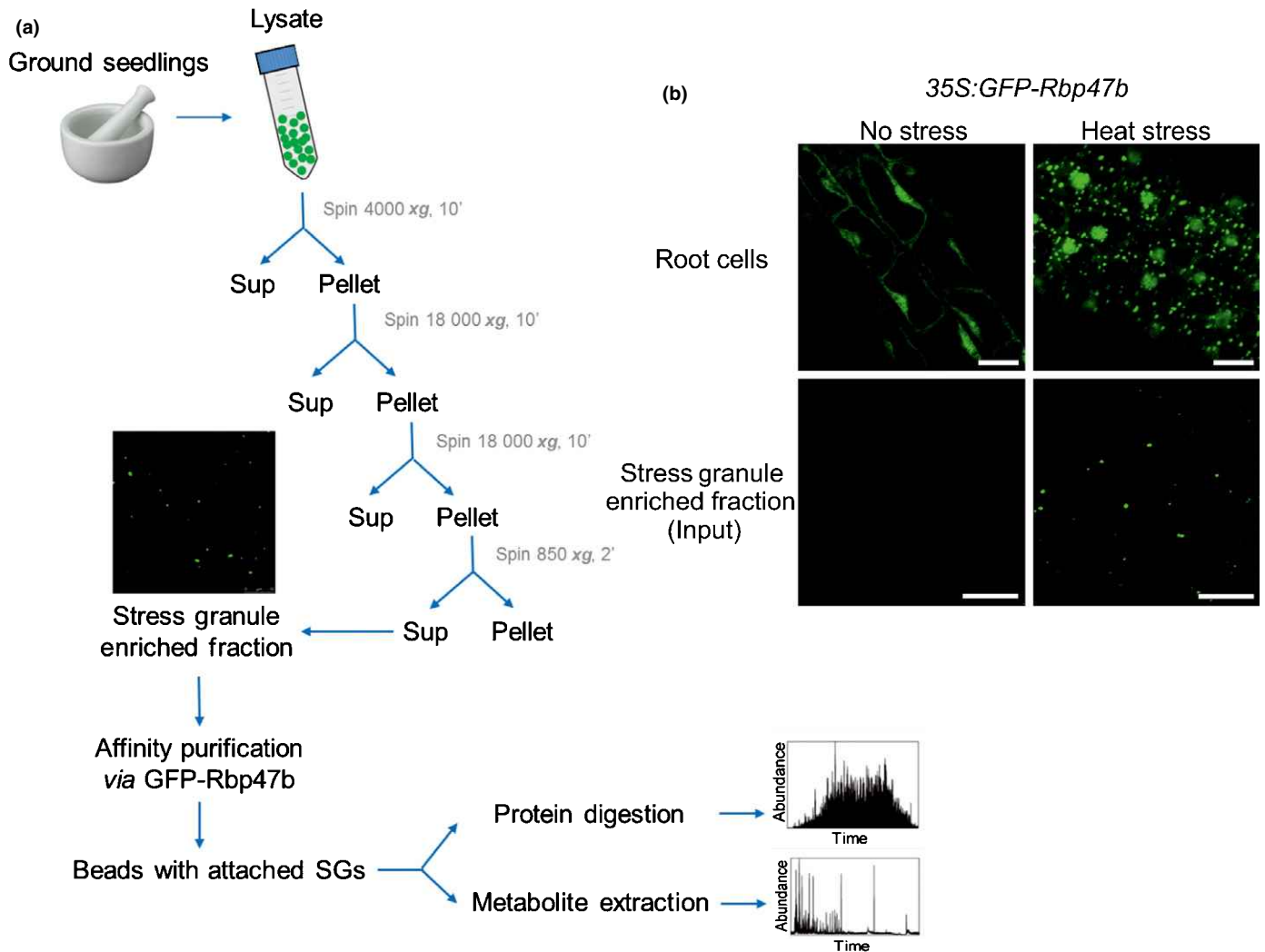
Fig. 1 Stress granule (SG) cores can be isolated from plant material. (a) Schematic representation of the SG isolation protocol. (b) GFP–Rbp47b localisation in Arabidopsis seedlings subjected to control and heat/dark stress (30 min at 42°C, darkness) conditions. Upper panel, intact seedlings. Lower panel, SG-enriched fraction obtained after a series of differential centrifugations, used as input for affinity purification. Bars, 10 μm.

2008; Sorenson & Bailey-Serres, 2014) and evolutionarily conserved C-terminal region 2 (ECT2) protein (Scutenaire *et al.*, 2018) (Fig. 2a). The presence of TSN2 in the SGs was further validated using marker GFP–TSN2 lines (Fig. 2b). These six proteins have SG-localised homologs in either human or yeast (Jain *et al.*, 2016; Markmiller *et al.*, 2018; Youn *et al.*, 2018)' cells, and this was also confirmed for 27 additional proteins identified in our study (Table S1). This total number of 33 conserved SG proteins was designated as the conserved SG proteome. Functional analysis of this conserved proteome revealed the presence of additional RNA-binding proteins, translation initiation factors, chaperones, and, interestingly, two signaling proteins involved in plant growth. Translationally controlled tumor protein 1 (TCPT1), an upstream regulator of the TOR kinase, has important roles in both plant development and abiotic stress responses (Berkowitz *et al.*, 2008). Cyclin-dependent kinase A (CDKA;1), a central cell-cycle regulator, is especially important in the G1/S-phase transition (Dissmeyer *et al.*, 2007; Nowack *et al.*, 2012; Zhao *et al.*, 2012). A subsequent domain analysis of the 33

conserved proteins demonstrated enrichment of prion-like (PrLD), ATPase, and RRM mRNA-binding motifs (Fig. 2c; Table S1), which are all known requirements for either assembly or dynamics of SGs in human and yeast cells (Jain *et al.*, 2016; Protter & Parker, 2016).

The remaining 85 of the 118 SG proteins included many important stress-related proteins (Fig. 2d). For example, glutathione-*S*-transferases, glutathione peroxidase, and ascorbate peroxidases are involved in the mitigation of oxidative stress (Apel & Hirt, 2004). Similarly, mitogen-activated MKK5 and MPK3 kinases are part of the same signaling cascade at the heart of the abiotic and biotic stress response (Asai *et al.*, 2002). SNRK2-1 belongs to the family of abiotic stress-induced SNRK kinases. We also identified enzymes involved in ethylene, glucosinolate, azalaic acid and rhamnose metabolism; these pathways are all associated with plant stress responses (Halkier & Gershenzon, 2006; Jung *et al.*, 2009; Skirycz *et al.*, 2011). Rhamnose, a major monosaccharide component of pectin, for example, is important for cell wall remodeling in response to stress. Our analysis

164
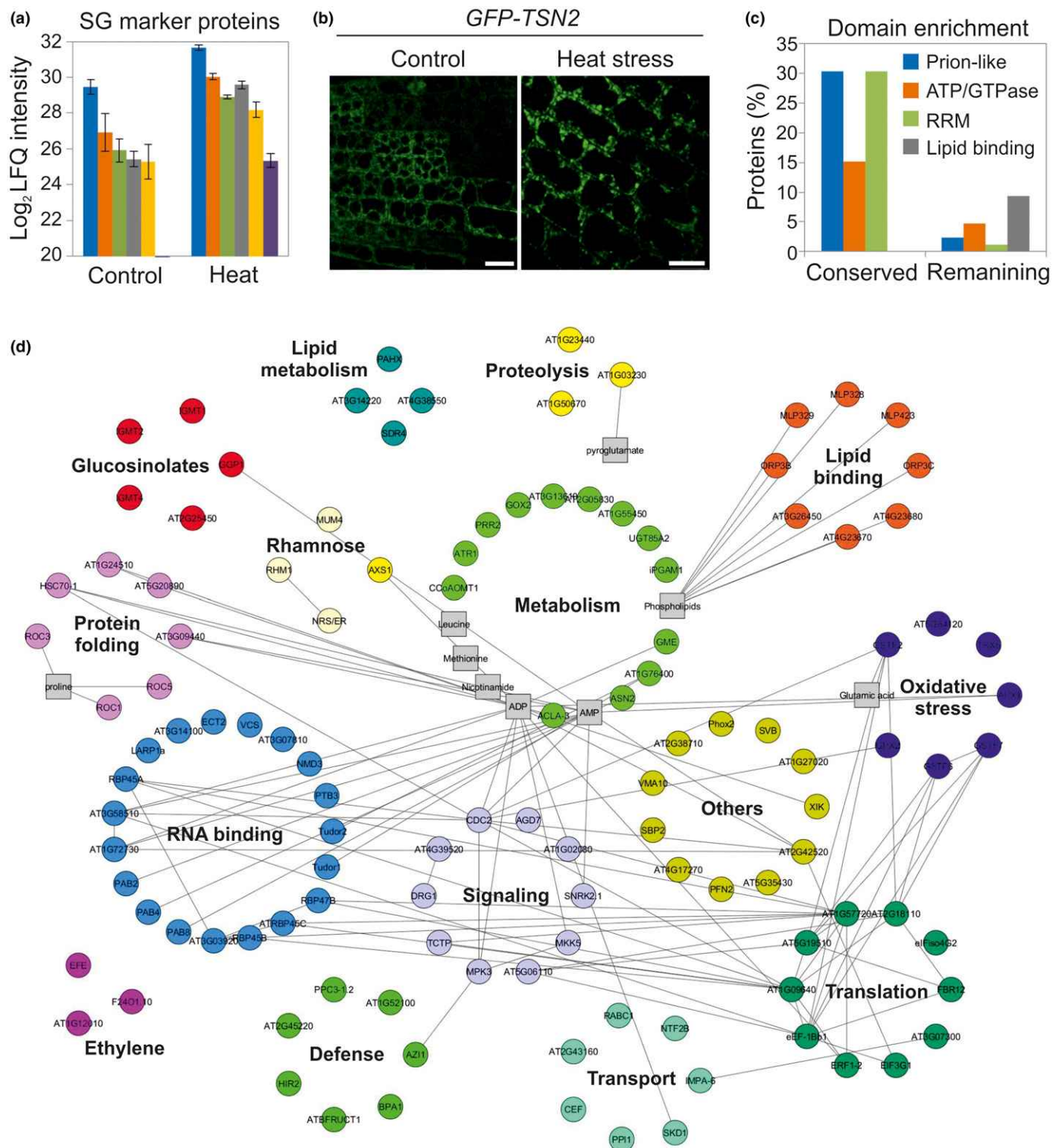
Fig. 2 Proteome composition of Arabidopsis stress granules (SGs). (a) Abundance of the SG marker proteins in the SGs isolated from control and heat/dark-treated plants. Data are mean ± SD, n = 3. Replicas represent independent SG isolations. (b) Localisation of the GFP−TSN2 protein in roots of the control and heat/dark-treated plants. Bars, 10 μm. (c) Domain enrichment analysis using the conserved and remaining SG proteome. Data are expressed as percentages of proteins containing a given domain. (d) Cytoscape (Shannon et al., 2003) visualisation of the SG proteome and metabolome. Nodes represent SG proteins and metabolites, edges were imported from the STITCH database (Szklarczyk et al., 2016) using experimental, database, and literature evidence (score set at 0.4). Functionality was assigned based on UniProt (Apweiler et al., 2004). Note, edges between phospholipids and lipid-binding domain containing proteins were introduced manually and are not present in the STITCH database. Raw data can be found in Supporting Information (Tables S1–S3).

identified RHM1, RHM2 and UER1 enzymes, which catalyse consecutive steps in the biosynthesis of rhamnose, to sequester in the SGs. In agreement and using RHM1:RHM1−GFP lines (Kuhn *et al.*, 2011) we could confirm that RHM1 protein aggregates in leaves and roots of seedlings subjected to 30 min : 1 h heat : dark treatment (Fig. S3).

The presence of the multiple proteins with predicted lipid-binding domains was particularly intriguing. Specifically, these included six members of the Bet v 1 protein superfamily. The Bet v 1 domain is characterised by a deep hydrophobic ligand-binding pocket that, at least *in vitro*, binds diverse ligands, including lipids, flavonols and cytokinins (Radauer *et al.*, 2008). Two oxysterol-binding proteins were annotated as putative sterol transporters based on the presence of a conserved sterol-binding domain (Umate, 2011).

CDKA;1 localises to the Arabidopsis SGs under stress conditions

Our analysis of the SG proteome revealed the presence of the core cell-cycle kinase, CDKA;1. We validated the SG localisation of CDKA;1 in 5-d-old Arabidopsis seedlings expressing a functional fusion of CDKA;1 to mVenus that can fully complement the *cdka;1* mutant phenotype. We subjected these seedlings to a combination of heat and dark stress (30 min, 42°C, darkness). CDKA;1 activity is high in dividing tissues and is required for meristem function (Nowack *et al.*, 2012; Weimer *et al.*, 2012), so we focused our microscopy analysis on root meristem and leaf primordia.

Investigation of the young and actively proliferating leaves revealed a cytosolic and nuclear localisation of CDKA;1−Venus protein under control conditions, in agreement with previous studies (Nowack *et al.*, 2007). However, within 30 min of 42°C treatment, CDKA;1−Venus showed extensive aggregation to the cytosolic foci, reminiscent of SG localisation (Fig. 3a). We determined whether the observed aggregation corresponded to SGs, firstly by, incubating seedlings with cycloheximide (CHX) (an inhibitor of translation-stabilizing polysomes) (Kedersha *et al.*, 2002; Sorenson & Bailey-Serres, 2014) before the heat/dark stress. Administration of CHX abolished the formation of the CDKA;1−Venus cytosolic foci, confirming SG localisation. Secondly, we could demonstrate co-localisation of CDKA;1−Venus with RFP−Rbp47b protein under heat/dark stress by transient infiltration of CDKA;1−Venus plants with RFP−Rbp47b construct (Fig. 3b). Finally, while 30 min of heat/dark stress is sufficient to observe SGs localisation of the CDKA;1−Venus protein, it takes up to 90 min for the CDKA;1−Venus protein to be released from the SGs after stress is relieved (Fig. 3c). Together these results demonstrated that CDKA;1 is sequestered to SGs during heat/dark stress.

Metabolome composition of the Arabidopsis SGs

SGs have been previously analysed with respect to their protein and mRNA content but not in terms of their small molecule composition. We filled this gap using a LC−MS metabolomics approach for comprehensive analysis of polar and lipid compounds (Tables S2, S3).

We defined the SG-associated metabolome by looking for metabolites that were at least twice as abundant in the SGs isolate from the heat/dark-treated sample when compared with the control seedlings. Three groups of compounds showed a significantly greater abundance in the SGs: phospholipids (Fig. 4a) and polar metabolites, which include amino acids and nucleotides (Fig. 4b). As phospholipids were also enriched in the 35S:GFP AP experiment they need to be treated with caution.

Importantly, the presence of the metabolites in the SGs isolate can be well explained by the proteomics results (Fig. 2d; Table S1). For example, the presence of putative lipid-binding proteins (Fig. 2d) might be an explanation of the accumulation of phospholipids in the SGs. Similarly, ADP, as a product of ATP turnover, is necessary for maintenance of SG dynamics and could be associated with proteins having ATPase activity, such as chaperones and RNA helicases (Fig. 2d). STITCH analysis of the SG-associated proteins and metabolites also revealed the presence of the predicted glutamate, pyroglutamate, and proline-binding proteins, further supporting presence of metabolites in SGs (Fig. 2d).

Our previous finding that 2′,3′-cAMP, a small molecule (product of a RNA degradation), binds to Rbp47b to facilitate SG formation (Kosmacz *et al.*, 2018) led us to focus on 2′,3′-cyclic nucleotides in the SGs. Contrary to our expectations, we did not find 2′,3′-cyclic nucleotides in the SGs. Intrigued by this finding, we measured metabolite levels in the *35S:GFP–Rbp47b* plant material. For comparative reasons, we also analysed WT seedlings grown in the same experiment (Table S4). We found no major effect of *Rbp47b* overexpression on metabolite levels measured under control conditions, but we observed pronounced differences under the heat/dark stress treatment. Of particular interest with respect to SG function was the differential response of protein and mRNA degradation products, including 2′,3′-cyclic nucleotides (Fig. 5a,b). Both groups of compounds were up-regulated by heat/dark stress in WT seedlings, but no or only minor accumulation was detected in the *35S:GFP–Rbp47* material. Obtained results demonstrate that increase in the 2′,3′-cAMP level is not obligatory for SGs formation. Rather, as speculated previously, 2′,3′-cAMP facilitates SGs formation under conditions associated with an excessive RNA degradation (Kosmacz *et al.*, 2018).

Phospholipids also showed differential responses, which resulted in a coordinated decrease in phospholipids levels in the WT but not in the *35S:GFP–Rbp47* seedlings (Fig. 5c−e) in response to heat/ bndark stress.

Rbp47b protein interactors identified by tandem affinity purification

Proximity-labeling experiments have previously revealed a preexisting interaction network between core SG proteins present in unstressed human cells (Markmiller *et al.*, 2018; Youn *et al.*, 2018). We investigated whether the same might be true in
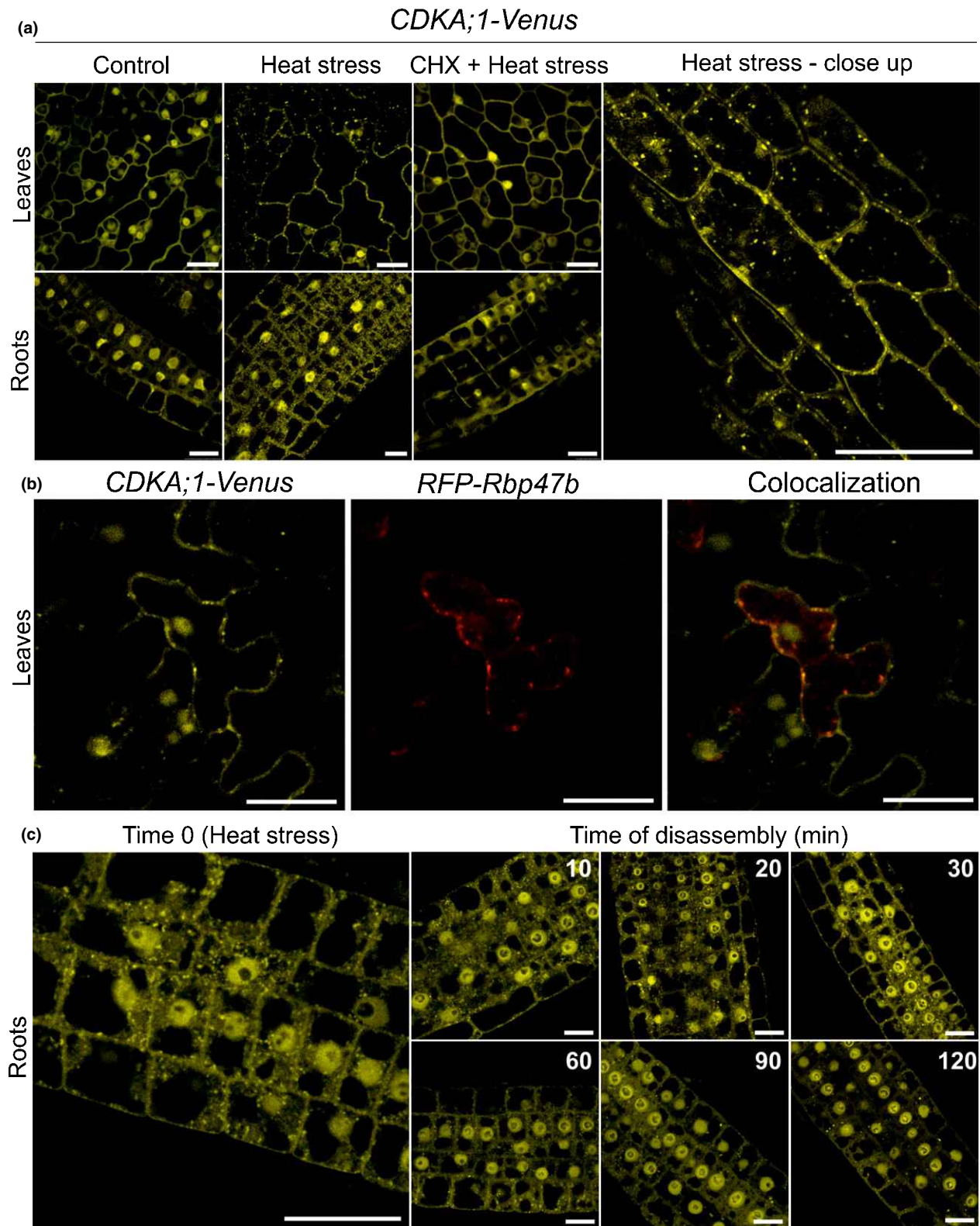
(a) *CDKA;1-Venus*

Fig. 3 Localisation of CDKA;1–Venus in leaves and roots of Arabidopsis seedlings in control and stress conditions. (a) Localisation of CDKA;1−mVenus. Upper panel, CDKA;1−mVenus localisation in leaves; lower panel, localisation in roots. Heat stress corresponds to 30 min at 42°C in darkness. Seedlings were subjected to 30 min of CHX treatment before the 30 min heat/dark stress as a control for stress granule (SG) formation. Higher magnification image shows a heat-treated leaf. (b) Co-localisation of CDKA;1−mVenus (yellow) with SGs marker – RFP−Rbp47b (red) in heat/dark-treated 3-wk-old Arabidopsis leaves. (c) Localisation of CDKA;1−mVenus in the recovery phase. Disassembly of SGs was followed starting from time 0 (30 min of heat/dark stress) up to 120 min at RT. Bars, 10 μm.
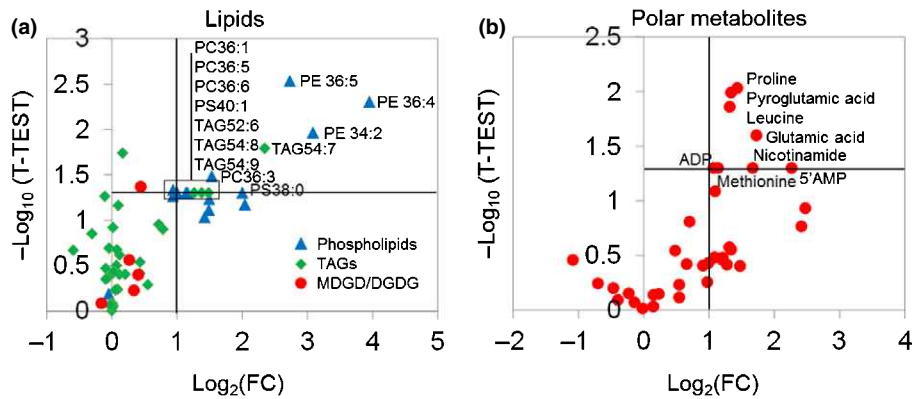
Fig. 4 Metabolome composition of Arabidopsis stress granules (SGs). (a, b) Volcano plot representation of the lipid and polar metabolite accumulation measured in the SGs isolated from heat/dark-treated vs control seedlings. Black lines indicate two-fold enrichment and a *P*-value of 0.05. Raw data can be found in Supporting Information (Tables S2, S3).
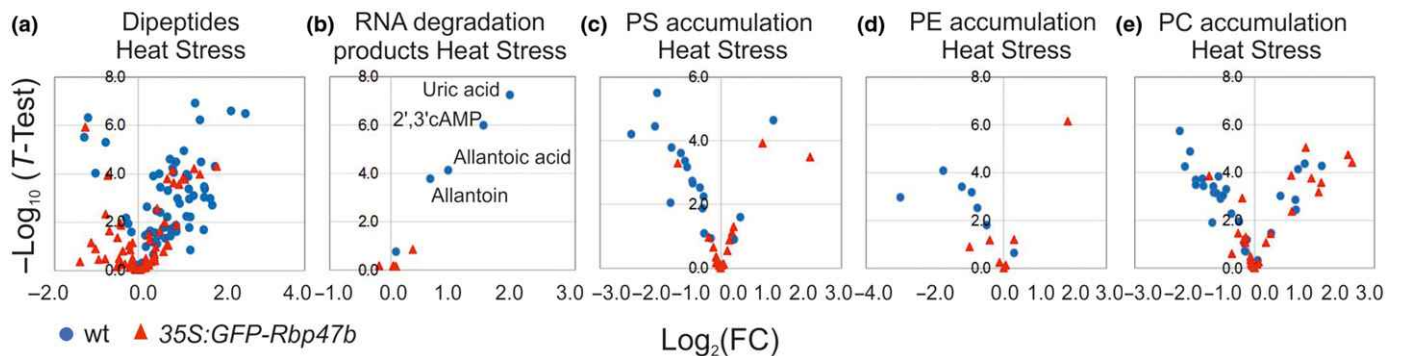
Fig. 5 Metabolic response of wild-type (WT) and *35S:GFP−Rbp47b* seedlings to a heat/dark stress. Volcano plot representation of (a) the dipeptides, (b) RNA degradation products and (c–e) lipids accumulation measured in the heat/dark-treated vs control in WT and *35S:GF−Rbp47b* seedlings. Data are the mean of replicates (*n* = 3 or 4). Replicates are from the same experiment.

Arabidopsis by investigating Rbp47b protein interactors in unstressed cells using a TAP protocol. Rbp47b protein was fused to a tandem affinity tag and expressed in Arabidopsis cell cultures. Affinity purification using IgG antibodies was followed by a specific elution using the TEV protease cleavage site. Empty vector control lines were used to correct for false positives. After a stringent analysis, we identified 22 proteins enriched in the Rbp47b pull-down when compared with the empty vector control (two-fold enrichment). Five proteins were removed from the final list based on their plastid or mitochondrial localisation that made them likely false positives (Table S5). As anticipated, among the identified proteins, we found known or predicted components of the SGs. These were almost exclusively RNA-binding proteins, the Rbp47b paralog Rbp47c, polyadenylate-binding proteins (PAB2, PAB4, PAB5 and PAB8), evolutionarily conserved C-terminal region proteins (ECT2 and ECT4), eukaryotic initiation factor 4A-III (EIF4A-III), and RNA/DNA helicase UAP56b (Fig. 6a). Importantly, seven of the identified RNA-binding proteins (Rbp47b, PAB2, PAB4, PAB5, PAB8, ECT2, and ECT4) contain the prion-like domain (Fig. 6b; Tables S5, S6) required for SG aggregation, and therefore can be seen as integral components of the SGs (SG core).

Discussion

In this study, we present the proteome-wide analysis of SG composition in plants and provide a first report of the metabolome analysis of SGs in any living organism. Similar to the SGs of humans and yeast (Jain *et al.*, 2016), Arabidopsis SG cores withstood biochemical purification via a series of differential centrifugations followed by AP, rendering them for proteomics and metabolomics analysis.

Several central conclusions can be drawn from our study. First, SG assembly and dynamics appears to be conserved across living organisms. A significant proportion of the plant SG proteome is evolutionarily conserved, as 28% of the identified proteins have a homolog present in either yeast or human SGs. These are proteins involved in SG assembly and dynamics, enriched in RNA-binding, prion-like, and ATPase regions. We retrieved elongation initiation factors, chaperones, and a variety of RNA-binding proteins. In the current model (Protter & Parker, 2016), SG assembly starts when mRNPs that are stalled in translation initiate complex formation with RNA-binding proteins. Therefore, mRNAs can be seen as a scaffold for multiple RNA-binding proteins that would either self-assemble or recruit additional proteins through protein−protein interactions. The prion-like domain
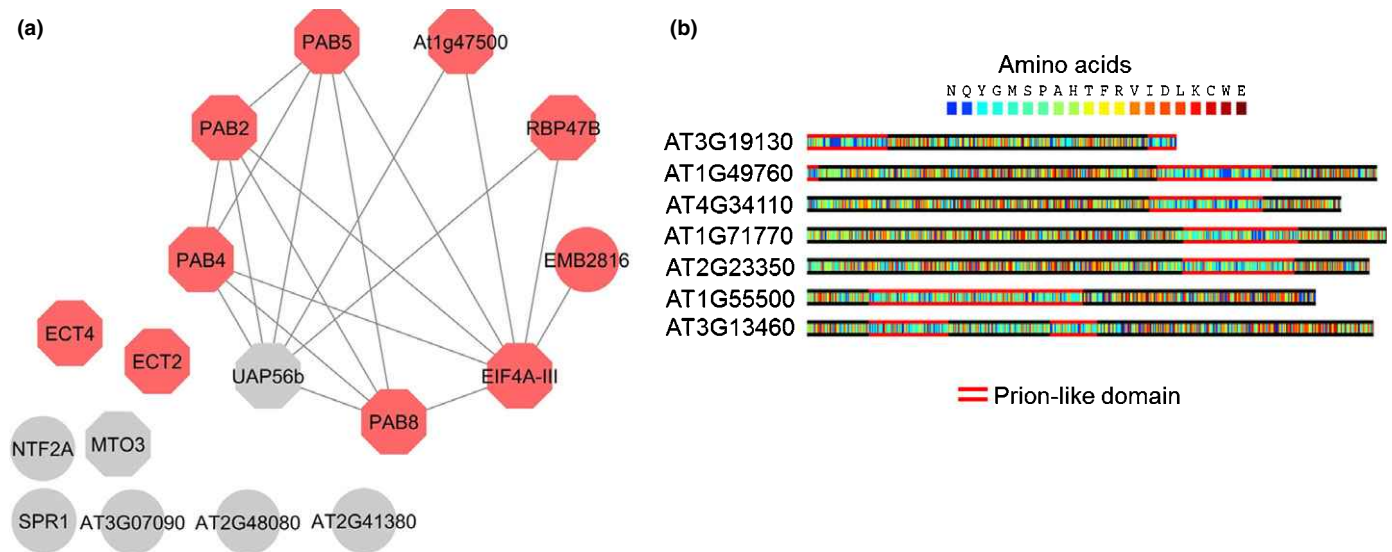
Fig. 6 Rbp47b protein interaction network. (a) Rbp47b protein interactors identified in the TAP experiment were visualised using Cytoscape. Nodes represent stress granule (SG) proteins; edges were imported from the STRING database using experimental, database, and literature evidence (score set at 0.4). Red shading indicates RNA binding, while octagonal shapes indicate SG association. (b) Prion-like domain visualisation based on the positive CORE score.

found in 12 of the SG RNA-binding proteins identified in our study is considered to be particularly important for the assembly of SGs (Gilks *et al.*, 2004; Weber *et al.*, 2008). Other key RNA-binding proteins observed in the Arabidopsis SGs are the TUDOR domain nucleases TSN1 and TSN2 that mediate connections to the cytoskeleton (Gutiérrez-Beltrán *et al.*, 2015). Once assembled, the SGs remain highly dynamic, allowing for fast exchange of components followed by rapid disassembly when the stress is alleviated. A prominent role in the regulation of SG dynamics has been assigned to ADP and to the ATP remodeling complexes, which we also found in our study (Jain *et al.*, 2016; Protter & Parker, 2016). These are chaperones (TCP-1 complex and heat shock proteins) as well as RNA/DNA helicases. Chaperones may additionally prevent misfolding of proteins concentrated in the SGs.

In line with recent results based on human cell lines (Markmiller *et al.*, 2018; Youn *et al.*, 2018), our data also point to the presence of a preexisting interaction network between core SG proteins that normally occurs in unstressed cells. The TAP experiments using Rbp47b as bait and in the unstressed cells revealed a list of interactors with well known associations with Arabidopsis SGs. Six of the identified proteins, analogously to Rbp47b, were characterised by the presence of the RNA-binding and prion-like regions that are essential for SG formation. Among these were recently described members of the evolutionarily conserved C-terminal region family, ECT2 and ECT4 (Scutenaire *et al.*, 2018), which bind specifically to RNAs containing methylations at position N6 of internal adenosines. Citing: 'Although SGs appear to form *de novo* in response to stress, their emergence represents a moderate and transient shift in a tightly controlled equilibrium of protein−protein and protein−RNA interactions.' (Markmiller *et al.*, 2018)

Our proteomics analysis also revealed the presence of multiple stress-related proteins in the Arabidopsis SGs. Protein

sequestration in SGs has been proposed to regulate the amounts of active protein (Jain *et al.*, 2016; Protter & Parker, 2016). This scenario is particularly interesting in relation to signaling proteins such as receptors, kinases and transcriptional regulators. To illustrate this point, in yeast, TORC1, a central protein kinase involved in the regulation of cell growth, is sequestered into SGs during heat stress and is maintained there in an inactive state. During heat recovery, the SGs disassemble and TORC1 is reactivated, thereby contributing to growth restoration (Takahara & Maeda, 2012). Here, we propose a similar mechanism involving SGs for cell-cycle arrest occurring in plants subjected to stress (Skirycz *et al.*, 2011). One of the proteins we detected in purified SGs was CDKA;1, the main driver of cell-cycle progression (Nowack *et al.*, 2012). CDKA;1 activity rapidly decreases in response to abiotic stress conditions, coinciding with cell-cycle arrest and subsequent growth suppression (West *et al.*, 2004; Jang *et al.*, 2005; Skirycz *et al.*, 2011). The mechanism responsible for this reduction in CDKA;1 activity is not well understood. We propose that stress leads to the sequestration of CDKA;1 into the SGs, where it is maintained in an inactive state. During stress recovery, the SGs disassemble and CDKA;1 is released to reinitiate cell proliferation. Presumably, CDKA;1 would be recruited to the SGs by an interaction with an RNA-binding protein and, in fact, Rbp45a was reported as a putative interaction partner for CDKA;1 (Van Leene *et al.*, 2007). Interestingly, homologues of CDKA;1 have been also found in yeast and mammalian SGs, suggesting an evolutionarily conserved mechanism for cell-cycle regulation (Jain *et al.*, 2016). In addition to CDKA;1 our study identified many more stress-related proteins localizing into SGs, such e.g. mitogen activated MKK5 and MPK3 kinases, SNRK 2.1 kinase and ethylene biosynthetic enzymes.

We speculate that SGs sequestration of the stress-related proteins might play two different roles. First, for TORC1 and CDKA;1 to temporally inactivate a regulatory protein. Such

mechanism could be relevant, for example, for translationally controlled tumour protein (TCTP) an upstream regulator of the TOR kinase and similar to CDKA;1 involved in a growth regulation. Second, due to high local concentration of components, SGs accumulation may favor the formation of biologically active complexes (Protter & Parker, 2016). This scenario was suggested to be particularly relevant for the metabolic enzymes.

We also showed that SGs are sites of metabolite accumulation. We hypothesise that metabolites are recruited to the SGs via protein–small molecule interactions. In support of this idea, the SG proteome contained numerous putative lipid-binding proteins (primarily from the Bet v 1 superfamily (Radauer et al., 2008) as well as proteins predicted to have amino acid- and nucleotide-binding properties. If metabolite sequestration within the SGs has a biological function needs to be investigated. One hypothesis is that, at least for some small molecules, this sequestration in the SGs would have a similar function to the sequestration of mRNAs and proteins, that is it is a way to regulate the active metabolite pool. To test this hypothesis it would be necessary to quantify absolute levels of metabolites sequestered into SGs in relation to a total cellular pool. An alternative hypothesis is based on the observation that small molecule binding increases protein thermostability (Mateus et al., 2016), and therefore may help to keep proteins in the folded state. Along similar lines, proline that accumulates in SGs was shown to activate molecular chaperones and by doing so may prevent misfolding of proteins concentrated in the SGs (Diamant et al., 2001).

Taken together, our results indicate the presence of a preexisting SG protein interaction network, an evolutionary conservation of the proteins involved in SG assembly and dynamics and an important role for SGs in moderation of stress responses by selective storage of proteins and metabolites. We anticipate that the nature and severity of stress conditions, the developmental stage and/or the organ identity will affect the exact proteome and metabolome composition, therefore resulting in a specific stress response.

Acknowledgements

Author contributions

AS: devised the experimental strategy, analysed metabolite data, supervised the project, and wrote the manuscript; MK: devised the experimental strategy, optimised the SG isolation protocol, performed confocal microscopy, analysed proteomics data, and assisted in writing the manuscript; SS: helped with SG isolation, and prepared metabolite and protein samples; ML: assisted with control AP experiments using 35S:GFP and WT material; JCM performed the dot-blot experiment; EL: assisted with metabolite and protein extraction; JS: performed TAP experiments; KS and AS: constructed the functional CDKA;1−mVenus reporter and provided the corresponding transgenic line; MG: was in charge of running proteomics and data deposition; EMS: performed the RHM1−GFP localisation experiment.

ORCID

Monika Kosmacz https://orcid.org/0000-0002-0295-0638
Juan C. Moreno https://orcid.org/0000-0001-9722-5262
Arp Schnittger https://orcid.org/0000-0001-7067-0091
Aleksandra Skirycz https://orcid.org/0000-0002-7627-7925
Kostika Sofroni https://orcid.org/0000-0001-8648-4648

References

Apel K, Hirt H. 2004. Reactive oxygen species: metabolism, oxidative stress, and signal transduction. Annual Review of Plant Biology 55: 373–399.

Apweiler R, Bairoch A, Wu CH, Barker WC, Boeckmann B, Ferro S, Gasteiger E, Huang H, Lopez R, Magrane M et al. 2004. UniProt: the Universal Protein knowledgebase. Nucleic Acids Research 32: D115–D119.

Asai T, Tena G, Plotnikova J, Willmann MR, Chiu WL, Gomez-Gomez L, Boller T, Ausubel FM, Sheen J. 2002. MAP kinase signalling cascade in Arabidopsis innate immunity. Nature 415: 977–983.

Berkowitz O, Jost R, Pollmann S, Masle J. 2008. Characterization of TCTP, the translationally controlled tumor protein, from Arabidopsis thaliana. Plant Cell 20: 3430–3447.

Chantarachot T, Bailey-Serres J. 2018. Polysomes, stress granules, and processing bodies: a dynamic triumvirate controlling cytoplasmic mRNA fate and function. Plant Physiology 176: 254–269.

Collier NC, Heuser J, Levy MA, Schlesinger MJ. 1988. Ultrastructural and biochemical-analysis of the stress granule in chicken-embryo fibroblasts. Journal of Cell Biology 106: 1131–1139.

Cox J, Mann M. 2008. MaxQuant enables high peptide identification rates, individualized p.p.b.-range mass accuracies and proteome-wide protein quantification. Nature Biotechnology 26: 1367–1372.

Diamant S, Eliahu N, Rosenthal D, Goloubinoff P. 2001. Chemical chaperones regulate molecular chaperones in vitro and in cells under combined salt and heat stresses. Journal of Biological Chemistry 276: 39586–39591.

Dissmeyer N, Nowack MK, Pusch S, Stals H, Inze D, Grini PE, Schnittger A. 2007. T-loop phosphorylation of Arabidopsis CDKA;1 is required for its function and can be partially substituted by an aspartate residue. Plant Cell 19: 972–985.

Giavalisco P, Li Y, Matthes A, Eckhardt A, Hubberten HM, Hesse H, Segu S, Hummel J, Kohl K, Willmitzer L. 2011. Elemental formula annotation of polar and lipophilic metabolites using ^{13}C, ^{15}N and ^{34}S isotope labelling, in combination with high-resolution mass spectrometry. The Plant Journal 68: 364–376.

Gilks N, Kedersha N, Ayodele M, Shen L, Stoecklin G, Dember LM, Anderson P. 2004. Stress granule assembly is mediated by prion-like aggregation of TIA-1. Molecular Biology of the Cell 15: 5383–5398.

Gutiérrez-Beltrán E, Moschou PN, Smertenko AP, Bozhkov PV. 2015. Tudor staphylococcal nuclease links formation of stress granules and processing bodies with mRNA catabolism in Arabidopsis. Plant Cell 27: 926–943.

Halkier BA, Gershenzon J. 2006. Biology and biochemistry of glucosinolates. Annual Review of Plant Biology 57: 303–333.

Hoyle NP, Castelli LM, Campbell SG, Holmes LE, Ashe MP. 2007. Stress-dependent relocalization of translationally primed mRNPs to cytoplasmic

granules that are kinetically and spatially distinct from P-bodies. *Journal of Cell Biology* 179: 65–74.

Jain S, Wheeler JR, Walters RW, Agrawal A, Barsic A, Parker R. 2016. ATPase-modulated stress granules contain a diverse proteome and substructure. *Cell* 164: 487–498.

Jang SJ, Shin SH, Yee ST, Hwang B, Im KH, Park KY. 2005. Effects of abiotic stresses on cell cycle progression in tobacco BY-2 cells. *Molecules and Cells* 20: 136–141.

Jung HW, Tschaplinski TJ, Wang L, Glazebrook J, Greenberg JT. 2009. Priming in systemic plant immunity. *Science* 324: 89–91.

Kedersha N, Chen S, Gilks N, Li W, Miller IJ, Stahl J, Anderson P. 2002. Evidence that ternary complex (eIF2-GTP-tRNA^{iMet}-deficient preinitiation complexes are core constituents of mammalian stress granules. *Molecular Biology of the Cell* 13: 195–210.

Kedersha NL, Gupta M, Li W, Miller I, Anderson P. 1999. RNA-binding proteins TIA-1 and TIAR link the phosphorylation of eIF-2 alpha to the assembly of mammalian stress granules. *Journal of Cell Biology* 147: 1431–1441.

Kosmacz M, Luzarowski M, Kerber O, Leniak E, Gutiérrez-Beltrán E, Moreno JC, Gorka M, Szlachetko J, Veyel D, Graf A *et al.* 2018. Interaction of 2′,3′-cAMP with Rbp47b plays a role in stress granule formation. *Plant Physiology* 177: 411–421.

Kuhn BM, Geisler M, Bigler L, Ringli C. 2011. Flavonols accumulate asymmetrically and affect auxin transport in Arabidopsis. *Plant Physiology* 156: 585–595.

Lancaster AK, Nutter-Upham A, Lindquist S, King OD. 2014. PLAAC: a web and command-line application to identify proteins with prion-like amino acid composition. *Bioinformatics* 30: 2501–2502.

Lee MW, Yang Y. 2006. Transient expression assay by agroinfiltration of leaves. *Methods in Molecular Biology* 323: 225–229.

Lorkovic ZJ, Wieczorek Kirk DA, Klahre U, Hemmings-Mieszczak M, Filipowicz W. 2000. RBP45 and RBP47, two oligouridylate-specific hnRNP-like proteins interacting with poly(A)$^+$ RNA in nuclei of plant cells. *RNA* 6: 1610–1624.

Luzarowski M, Kosmacz M, Sokolowska E, Jasinska W, Willmitzer L, Veyel D, Skirycz A. 2017. Affinity purification with metabolomic and proteomic analysis unravels diverse roles of nucleoside diphosphate kinases. *Journal of Experimental Botany* 68: 3487–3499.

Markmiller S, Soltanieh S, Server KL, Mak R, Jin W, Fang MY, Luo EC, Krach F, Yang D, Sen A *et al.* 2018. Context-dependent and disease-specific diversity in protein interactions within stress granules. *Cell* 172: 590–604. e513.

Mateus A, Maatta TA, Savitski MM. 2016. Thermal proteome profiling: unbiased assessment of protein state through heat-induced stability changes. *Proteome Science* 15: 13.

Matsuki H, Takahashi M, Higuchi M, Makokha GN, Oie M, Fujii M. 2013. Both G3BP1 and G3BP2 contribute to stress granule formation. *Genes to Cells* 18: 135–146.

Merkulova EA, Guiboileau A, Naya L, Masclaux-Daubresse C, Yoshimoto K. 2014. Assessment and optimization of autophagy monitoring methods in Arabidopsis roots indicate direct fusion of autophagosomes with vacuoles. *Plant & Cell Physiology* 55: 715–726.

Merret R, Descombin J, Juan YT, Favory JJ, Carpentier MC, Chaparro C, Charng YY, Deragon JM, Bousquet-Antonelli C. 2013. XRN4 and LARP1 are required for a heat-triggered mRNA decay pathway involved in plant acclimation and survival during thermal stress. *Cell Reports* 5: 1279–1293.

Murashige T, Skoog F. 1962. A revised medium for rapid growth and bio assays with tobacco tissue cultures. *Physiologia Plantarum* 15: 473–497.

Nakagawa T, Suzuki T, Murata S, Nakamura S, Hino T, Maeo K, Tabata R, Kawai T, Tanaka K, Niwa Y *et al.* 2007. Improved Gateway binary vectors: high-performance vectors for creation of fusion constructs in transgenic analysis of plants. *Bioscience, Biotechnology, and Biochemistry* 71: 2095–2100.

Nover L, Scharf KD, Neumann D. 1983. Formation of cytoplasmic heat shock granules in tomato cell cultures and leaves. *Molecular and Cellular Biology* 3: 1648–1655.

Nowack MK, Harashima H, Dissmeyer N, Zhao X, Bouyer D, Weimer AK, De Winter F, Yang F, Schnittger A. 2012. Genetic framework of cyclin-dependent kinase function in Arabidopsis. *Developmental Cell* 22: 1030–1040.

Nowack MK, Shirzadi R, Dissmeyer N, Dolf A, Endl E, Grini PE, Schnittger A. 2007. Bypassing genomic imprinting allows seed development. *Nature* 447: 312–315.

Protter DS, Parker R. 2016. Principles and properties of stress granules. *Trends in Cell Biology* 26: 668–679.

Radauer C, Lackner P, Breiteneder H. 2008. The Bet v 1 fold: an ancient, versatile scaffold for binding of large, hydrophobic ligands. *BMC Evolutionary Biology* 8: 286.

Rappsilber J, Ishihama Y, Mann M. 2003. Stop and go extraction tips for matrix-assisted laser desorption/ionization, nanoelectrospray, and LC/MS sample pretreatment in proteomics. *Analytical Chemistry* 75: 663–670.

Scutenaire J, Deragon JM, Jean V, Benhamed M, Raynaud C, Favory JJ, Merret R, Bousquet-Antonelli C. 2018. The YTH domain protein ECT2 is an m^{6}A reader required for normal trichome branching in Arabidopsis. *Plant Cell* 30: 986–1005.

Shannon P, Markiel A, Ozier O, Baliga NS, Wang JT, Ramage D, Amin N, Schwikowski B, Ideker T. 2003. Cytoscape: a software environment for integrated models of biomolecular interaction networks. *Genome Research* 13: 2498–2504.

Skirycz A, Claeys H, De Bodt S, Oikawa A, Shinoda S, Andriankaja M, Maleux K, Eloy NB, Coppens F, Yoo SD *et al.* 2011. Pause-and-stop: the effects of osmotic stress on cell proliferation during early leaf development in Arabidopsis and a role for ethylene signaling in cell cycle arrest. *Plant Cell* 23: 1876–1888.

Sorenson R, Bailey-Serres J. 2014. Selective mRNA sequestration by OLIGOURIDYLATE-BINDING PROTEIN 1 contributes to translational control during hypoxia in Arabidopsis. *Proceedings of the National Academy of Sciences, USA* 111: 2373–2378.

Szklarczyk D, Santos A, von Mering C, Jensen LJ, Bork P, Kuhn M. 2016. STITCH 5: augmenting protein-chemical interaction networks with tissue and affinity data. *Nucleic Acids Research* 44: D380–D384.

Takahara T, Maeda T. 2012. Transient sequestration of TORC1 into stress granules during heat stress. *Molecular Cell* 47: 242–252.

Umate P. 2011. Oxysterol binding proteins (OSBPs) and their encoding genes in Arabidopsis and rice. *Steroids* 76: 524–529.

Van Leene J, Stals H, Eeckhout D, Persiau G, Van De Slijke E, Van Isterdael G, De Clercq A, Bonnet E, Laukens K, Remmerie N *et al.* 2007. A tandem affinity purification-based technology platform to study the cell cycle interactome in Arabidopsis thaliana. *Molecular and Cellular Proteomics* 6: 1226–1238.

Veyel D, Kierszniowska S, Kosmacz M, Sokolowska EM, Michaelis A, Luzarowski M, Szlachetko J, Willmitzer L, Skirycz A. 2017. System-wide detection of protein-small molecule complexes suggests extensive metabolite regulation in plants. *Scientific Reports* 7: 42387.

Vizcaino JA, Csordas A, Del-Toro N, Dianes JA, Griss J, Lavidas I, Mayer G, Perez-Riverol Y, Reisinger F, Ternent T *et al.* 2016. 2016 update of the PRIDE database and its related tools. *Nucleic Acids Research* 44: 11033.

Weber C, Nover L, Fauth M. 2008. Plant stress granules and mRNA processing bodies are distinct from heat stress granules. *Plant Journal* 56: 517–530.

Weimer AK, Nowack MK, Bouyer D, Zhao X, Harashima H, Naseer S, De Winter F, Dissmeyer N, Geldner N, Schnittger A. 2012. Retinoblastoma related1 regulates asymmetric cell divisions in Arabidopsis. *Plant Cell* 24: 4083–4095.

West G, Inze D, Beemster GT. 2004. Cell cycle modulation in the response of the primary root of Arabidopsis to salt stress. *Plant Physiology* 135: 1050–1058.

Wheeler JR, Jain S, Khong A, Parker R. 2017. Isolation of yeast and mammalian stress granule cores. *Methods* 126: 12–17.

Youn JY, Dunham WH, Hong SJ, Knight JDR, Bashkurov M, Chen GI, Bagci H, Rathod B, MacLeod G, Eng SWM *et al.* 2018. High-density proximity mapping reveals the subcellular organization of mRNA-associated granules and bodies. *Molecular Cell* 69: 517–532. e511.

Zhao X, Harashima H, Dissmeyer N, Pusch S, Weimer AK, Bramsiepe J, Bouyer D, Rademacher S, Nowack MK, Novak B *et al.* 2012. A general G1/S-phase cell-cycle control module in the flowering plant *Arabidopsis thaliana*. *PLoS Genetics* 8: e1002847.

171

Supporting Information

Additional Supporting Information may be found online in the Supporting Information section at the end of the article.

Fig. S1 Dot-blot analysis of Rbp47b–GFP protein levels in the control and heat/dark-treated seedlings used for SGs isolation.

Fig. S2 Localisation of the GFP protein in the control and dark/heat-treated seedlings.

Fig. S3 Localisation of the RHM1–GFP protein in the control and dark/heat-treated seedlings.

Table S1 List of SGs localised proteins based on the two-fold enrichment in the SGs isolate (AP beads) from the heat-treated vs control seedlings.

Table S2 Lipidomics analysis of the SGs isolate (AP beads) from the heat-treated vs control seedlings.

Table S3 Metabolomics analysis of the SGs isolate (AP beads) from the heat-treated vs control seedlings.

Table S4 Polar and lipid metabolites measured in the starting WT and *35S:GFP–Rbp47b* plant material.

Table S5 List of Rbp47b interactors.

Table S6 Prion-like domain analysis in both experiments.

Please note: Wiley Blackwell are not responsible for the content or functionality of any Supporting Information supplied by the authors. Any queries (other than missing material) should be directed to the *New Phytologist* Central Office.

About *New Phytologist*

- *New Phytologist* is an electronic (online-only) journal owned by the New Phytologist Trust, a **not-for-profit organization** dedicated to the promotion of plant science, facilitating projects from symposia to free access for our Tansley reviews and Tansley insights.

- Regular papers, Letters, Research reviews, Rapid reports and both Modelling/Theory and Methods papers are encouraged. We are committed to rapid processing, from online submission through to publication 'as ready' via *Early View* – our average time to decision is <26 days. There are **no page or colour charges** and a PDF version will be provided for each article.

- The journal is available online at Wiley Online Library. Visit **www.newphytologist.com** to search the articles and register for table of contents email alerts.

- If you have any questions, do get in touch with Central Office (np-centraloffice@lancaster.ac.uk) or, if it is more convenient, our USA Office (np-usaoffice@lancaster.ac.uk)

- For submission instructions, subscription and all the latest information visit **www.newphytologist.com**

3.2 Towards the quantification of cell cycle progression by the use of live cell imaging in Arabidopsis roots

3.2.1 Introduction

Visualization of cell cycle progression is beneficial to understand how cells divide and modify their growth in response to environmental conditions. The choice of a complementing set of fluorescent reporter lines is crucial to precisely follow the spatiotemporal changes during cell cycle progression using live cell imaging. One of the most studied cell cycle markers in plants are the B1-type cyclins (CYCB1;1 and CYCB1;2) and the plant-specific B2-type cyclin-dependent kinase (CDKB;2) (Colón-Carmona et al., 1999; Iwata et al., 2011; Marhava et al., 2019). CDKB;2-cyclin complexes progressively accumulate in the cytoplasm throughout G2/M phase, thus making them often used markers to monitor the length of G2/M (Marhava et al., 2019). On the other hand, live imaging of the G1/S phase appears to be more challenging. Good candidates, due to elevated transcript levels at G1, are the D-type cyclins and histones (Takahashi et al., 2002; Okada et al., 2005). However, recent studies have shown that their proteolysis is not linked to a certain cell cycle phase and hence as fluorescent protein fusions they are not suitable as markers of G1/S phase (Boudolf et al., 2009). Interestingly, Ctd1, a loading factor that enables the MCM helicase to associate with DNA replication origins, was exploited as new cell cycle marker, accumulating specifically at S/G2 phase (Yin et al., 2014). Additionally, S phase dynamics were dissected in detail in live cell imaging by following the proliferating cell nuclear antigen (PCNA), which shows whole nuclear localization at G1 that changes first to a dotted (fine grained spots) and then to a speckled (larger spots) pattern, thus distinguishing early and late S phase, respectively (Yokoyama et al., 2016).

To monitor cell cycle dynamics of specific plant cells *in planta* in contrast to cultured cells, the time-lapse microscopy set-up has to be adapted to tissue-specific requirements allowing the follow-up of the entire cycle of a cell of interest, as part of an entire tissue. One approach, was the use of a confocal microscope equipped with a long distance water-dipping lens to study the cell cycle of rapidly dividing cells in the shoot apical meristem (Hamant et al., 2019; Grandjean et al., 2004). This method, combined with fluorescent protein marker lines, allowed the analysis of cell division

and differentiation under normal conditions as well as under several drug treatments i.e. oryzalin, aphidicolin and hydroxyurea (Grandjean et al., 2004). Later on, the same technique was modified to follow meiocytes within anthers (Prusicki et al., 2019) and recently live imaging of entire flowers in 3D for more then 72h, albeit at a lower magnification/resolution, was successfully achieved using light sheet microscopy (Valuchova et al., 2020). These microscope setups in combination with a large panel of fluorescent reporter lines allowed the establishment of a time course describing the development of Arabidopsis male meiocytes (Prusicki et al., 2019) and furthermore the analysis of diverse aspects of male and female germline differentiation (Valuchova et al., 2020).

However, the meiotic cell cycle program is to some extend special as it leads to daughter cells with half of the genetic material which then need to switch to a mitotic cell cycle program for gametophyte development. Additionally the entry into the meiotic cell cycle and the definition of a meiotic G1 phase in plants is poorly understood. Therefore the here described endeavour to establish additional markers of cell cycle progression for *in tissue* live cell imaging was first done with a more easily accessible system of mitotically dividing cells, the root tip. The aim was to get a good spatiotemporal recording of different markers in a regular mitotic cell cycle before switching to the more complex meiotic cell cycle. Previous studies have already monitored *in vivo* cell cycle progression in epidermal root cells using a classical horizontal confocal microscope (Campilho et al., 2006; Yin et al., 2014). However, in all these studies the time of observation under the microscope did not exceed 12h, due to the incompatibility of a physiological vertical root growth with a horizontal microscope setup. To overcome this issue, in this study we used a vertical confocal microscope setup (for more see material & methods and (Wangenheim et al., 2017)) in combination with different fluorescent reporter constructs i.e. PCNA as nuclear marker and CYCB3;1 and tubulin as cytosolic markers to monitor cell cycle progression in root epidermal cells and established a landmark system to dissect stages and sub-stages of mitotically dividing cells.

3.2.2 Material and methods

3.2.2.1 Plant material and growth conditions

The *Arabidopsis thaliana* plants used in this study were all derived from the Columbia (Col-0) ecotype. The fluorescent reporter lines PCNA:RFP and RFP:TUA5 were previously described (Yokoyama et al., 2016) and (Prusicki et al., 2019) respectively. CYCB3;1:GFP reporter line is described in Chapter 1 and SMC1:mVenus was kindly provided by Shinichiro Komaki (unpublished line).

All seeds were surface-sterilized with chloride gas, sown on MS plates and stored 2 days at 4°C in the dark for stratification. For germination, plates were transferred to long-day conditions (16h day/8h night at 22°). After germination, plants were transferred to soil and grown under long-day conditions.

3.2.2.2 Confocal microscopy

Still images of root sections were acquired using a Zeiss LSM 880 confocal microscope and ZEN 2.3 SP1 software (Carl Zeiss GmbH, Oberkochen, Germany). Pictures were captured with a 40X water immersion objective. mEGFP was exited at 488 nm and detected at a wave length between 495-560 nm and TagRFP was exited at 561 nm and detected at 570-650 nm.

Time lapses were acquired using a microscope body (Zeiss Axio Observer) rotated 90° with the scan head of a Zeiss LSM 700 confocal microscope as described by (Wangenheim et al., 2017) (Figure 1A). 5 days old Arabidopsis seedlings were put in a chamber containing ½ MS medium with 1.2% agar and covered carefully with a coverslip (Figure 1B). Up to 8 seedlings were imaged simultaneously within 24h using the Plan-Apochromat 20x/0.8 air objective lens. mEGFP was exited at 488 nm and detected at a wave length between 495-560 nm and TagRFP was exited at 561 nm and detected at 570-650 nm. Additionally, a combination of a specific illumination system with the rotational stage allowed stable tracking of root growth. The illumination system was composed of five pairs of red and blue LEDs (for more specifications see (Wangenheim et al., 2017). Simultaneously, the TipTracker program allowed the online tip tracking and the correction of moving positions due to root growth (Figure 1B). Room temperature and sample temperature were controlled and stabilized at 18°.
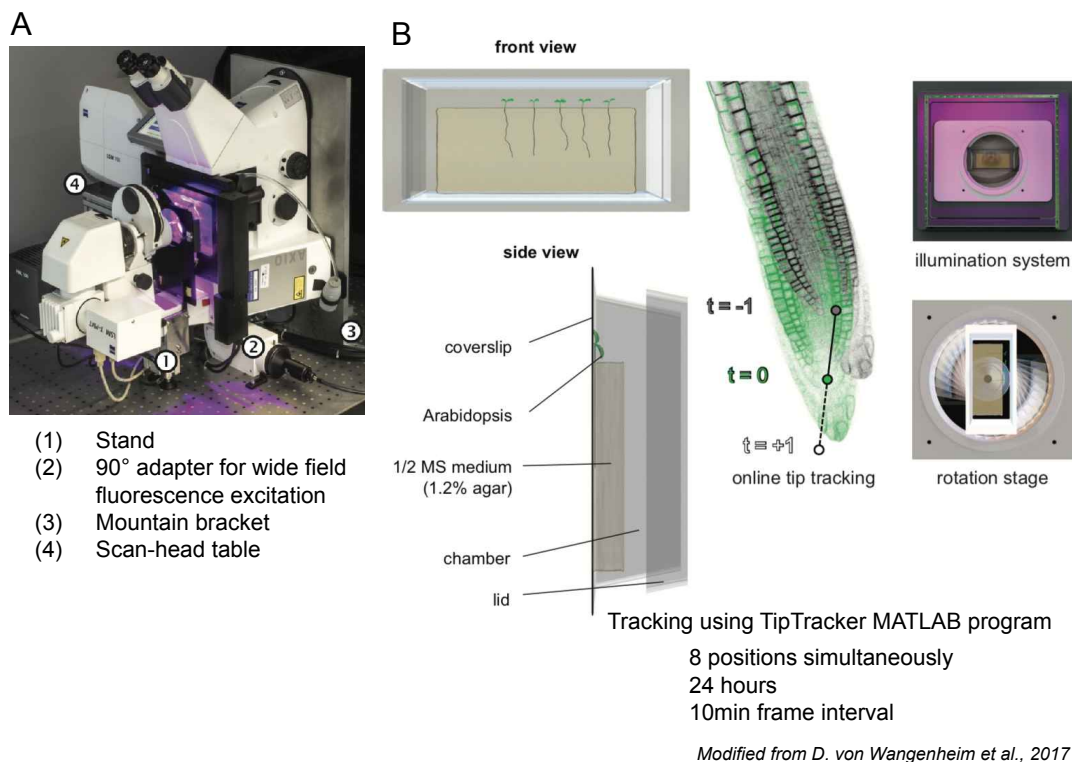
Figure 1: *Overview of the vertical microscope setup. (A) Photograph of the microscope body (Zeiss Axio Observer) rotated by 90° and mounted to an optical table together with the scan head (Zeiss LSM 700). (B) Schematic representation of roots growing vertically in chambered coverslips between the coverglass and the agar. The combination of a specific illumination system and the rotation stage together with the online tip tracking allowed the stable imaging of vertically growing root tips. This figure was modified from Wangenheim et al., 2017.*

3.2.3 Results

3.2.3.1 Combination of nuclear and cytosolic markers to monitor cell cycle progression

To explore the dynamics of cell cycle progression we generated plant lines expressing different combinations of reporter constructs. Either we combined one construct expressed in the nucleus with one in the cytosol or we used two different cytoplasmic markers in parallel. Then we monitored the expression pattern of the marker proteins for at least 24h in root epidermal cells.

The first double reporter line carried the combination of PCNA, a nuclear marker, with the CYCB3;1 marker. Conventional confocal laser scanning micrographs (stills) revealed different localization patterns of these reporters in different cells (Figure 2).

PCNA:RFP x CYCB3;1:GFP
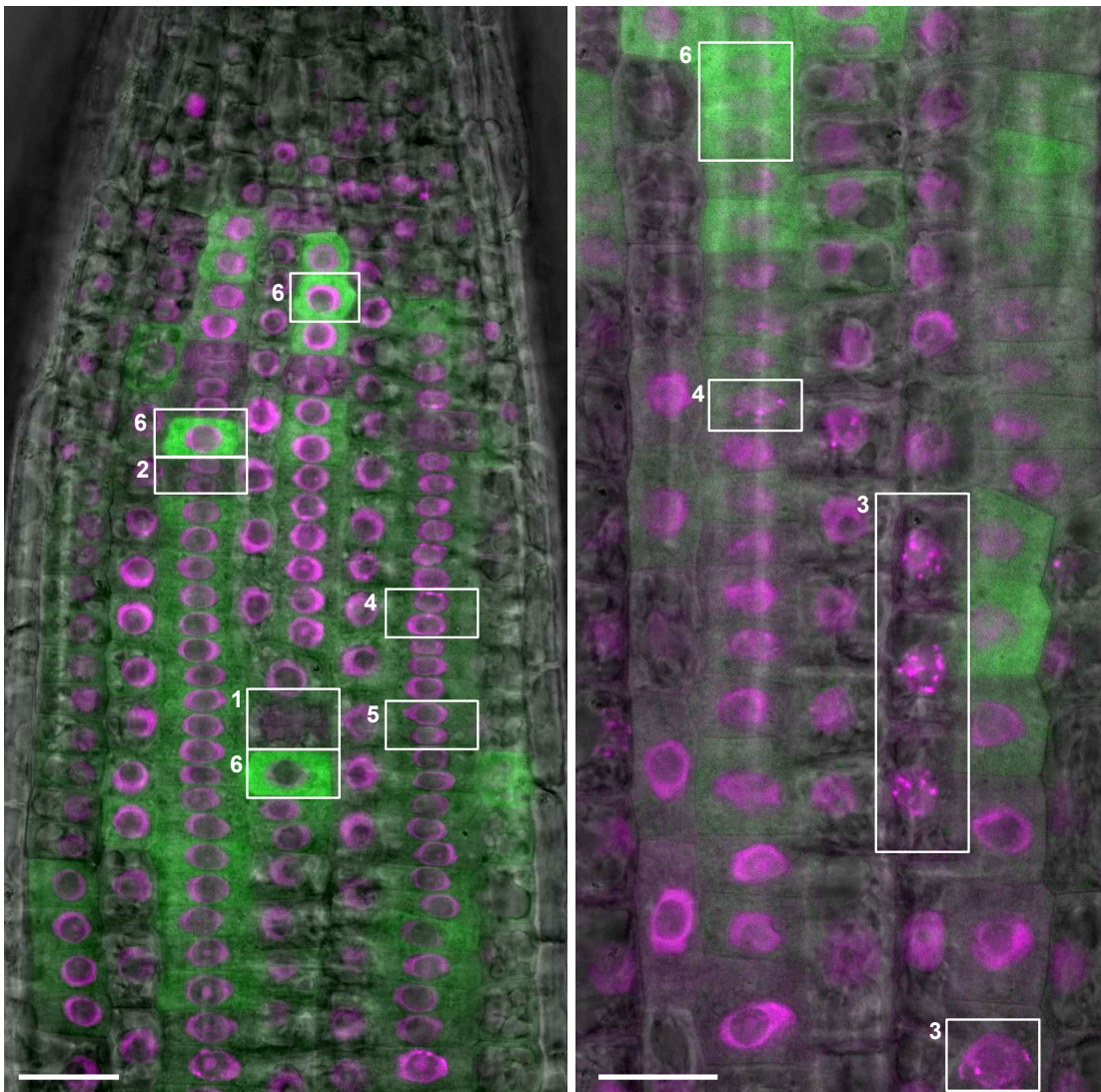
Figure 2: Confocal laser scanning micrographs going through one section of a root showing the localization of PCNA:RFP and CYCB3;1:GFP. The white rectangles highlight (1) absence of both PCNA and CYCB3;1, (2) diffuse nuclear localization of PCNA but absence of CYCB3;1, (3) Speckled pattern of PCNA, (4) 2-3 dots and diffuse PCNA in the nucleus and low expression of CYCB3;1 in the cytosol, (5) diffuse nuclear localization of PCNA and low cytoplasmic expression of CYCB3;1, (6) diffuse and low nuclear localization of PCNA and high accumulation of CYCB3;1 in the cytoplasm. Scale bar 10µm.

We observed cells in which both reporter constructs were not expressed (Figure 2(1)) or cells having only a very diffuse localization of PCNA (Figure 2(2)). In some cells PCNA showed a speckled pattern (Figure 2(3)) while in other cells only 2-3 dots remained (Figure 2(4)). From this localization pattern it is difficult to distinguish between early and late S phase events in comparison with the description by (Yokoyama et al., 2016) showing clear differences between early S (dotted pattern)

177

and late S (specked pattern) (Figure S1). Further, we found cells in which PCNA remained diffuse in the nucleus, but CYCB3;1 showed either a low accumulation in the cytoplasm (Figure 2(5)) or was highly expressed (Figure 2(6)). As most B-type cyclins accumulate during G2, we speculated that the period of CYCB3;1 accumulation could indeed indicate the G2 stage which is consistent with the shape of the nucleus and the diffuse nuclear staining of PCNA.

To confirm this hypothesis, we next performed live cell imaging of PCNA and CYCB3;1 (Figure 3A from Video 1) using the vertical microscope system described in material and methods. We confirmed the timing of CYCB3;1 accumulation (Video 1) with respect to the speckled localization of PCNA (Video2). CYCB3;1 accumulation started after S phase, as revealed by the transition from speckled to diffuse pattern of PCNA and continued for at least 12 hours until a spindle-like localization of CYCB3;1 was observed (Figure 3A,B and Video 1). The accumulation pattern of CYCB3;1 was progressive: low in the beginning and reaching the maximum shortly before the spindle-like localization. These data suggest that CYCB3;1 can be used to monitor the length of G2 and in combination with PCNA the full cell cycle progression can be staged as described below (Figure 3C):

Early G1 → absence of PCNA and CYCB3;1

G1→ PCNA diffuse in the nucleus and absence of CYCB3;1

S phase → speckled pattern of PCNA and absence of CYCB3;1

Early G2 → diffuse PCNA and low accumulation of CYCB3;1

Late G2 → diffuse PCNA and high accumulation of CYCB3;1

M → spindle localization of CYCB3;1
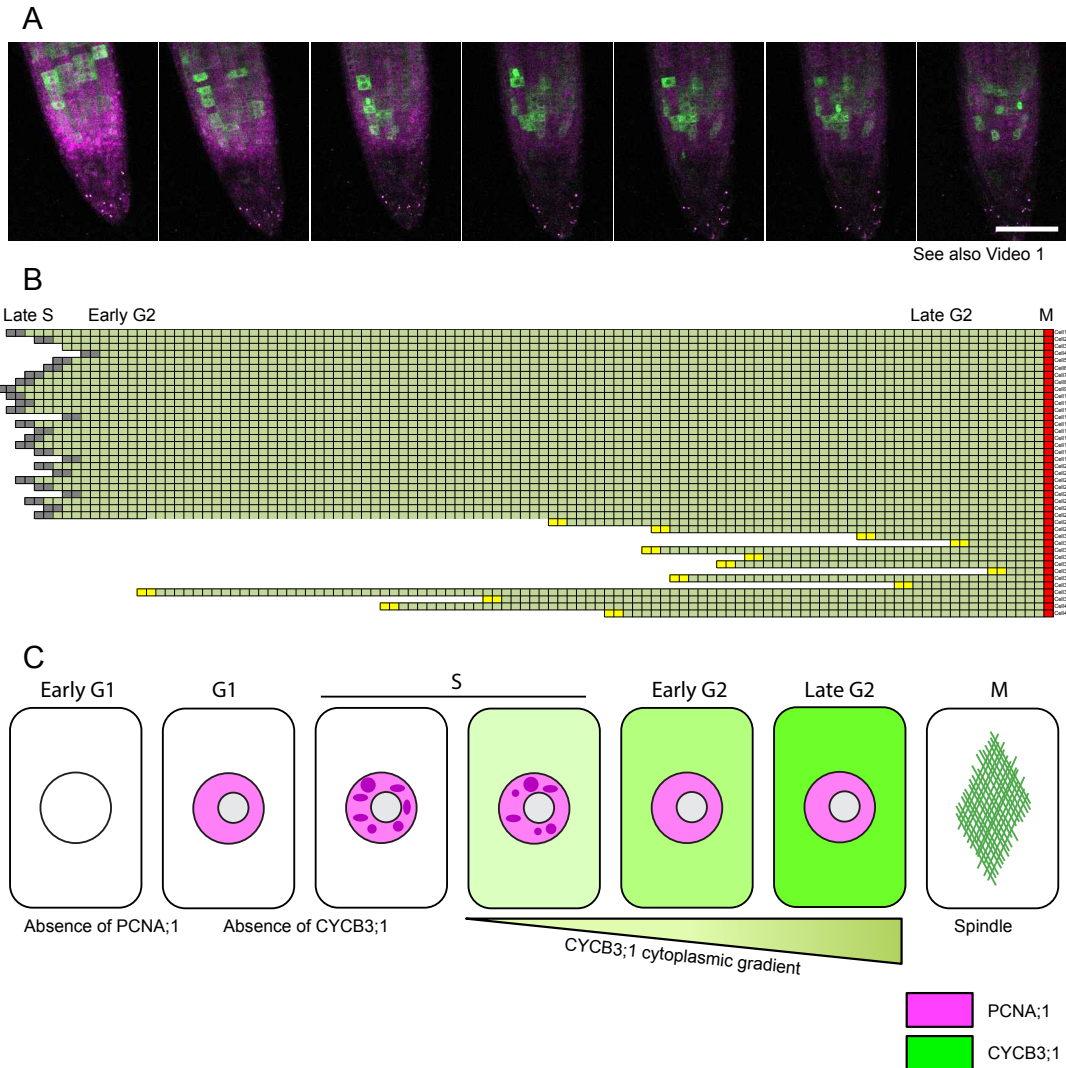
See also Video 1

Figure 3: *Analysis of cell cycle progression in root epidermal cells (A, see also Video 1). Confocal laser scanning micrographs of root cells expressing PCNA:RFP (magenta) and CYCB3;1:GFP (green) at different time points of cell cycle progression. Scale bar 100μm (B) Time course analysis of CYCB3;1 cytoplasmic accumulation during G2. Every line represents a single cell undergoing a cell cycle and every square represents an 8 min interval, S phase (grey squares), G2 (green square) and M phase (red square). Yellow squares represent the initial time points of cells that were between S and M at the beginning of live cell imaging. Data were aligned by taking the spindle formation at M phase as the end point. (C) Cartoons, based on stills and live imaging experimental data summarizing the localization pattern of CYCB3;1 (green) and PCNA (magenta) throughout the cell cycle.*

Next, we analysed other double reporter combinations. The concomitant expression of CYCB3;1 and tubulin confirmed the spindle localization of CYCB3;1 at M phase (Figure 4A,B and Video3). Additionally the four typical microtubule arrays during the mitotic cell cycle could be observed: cortical microtubules throughout G1, S and early G2 phase; the preprophase band at late G2; nuclear envelope breakdown and

spindle at early M and phragmoplast at late M phase (Figure 3B, 5B and Video 3). The localization pattern of SMC1 (Structural Maintenance of Chromosome), as part of the cohesion complex together with PCNA or tubulin did not give additional information about the cell cycle staging as the signal remained diffused in the nucleus without showing any particular structures (Figure 5 and Video 4). However the signal intensity of SMC1 was not homogenous within different cells and these changes could potentially be addressed in the future.
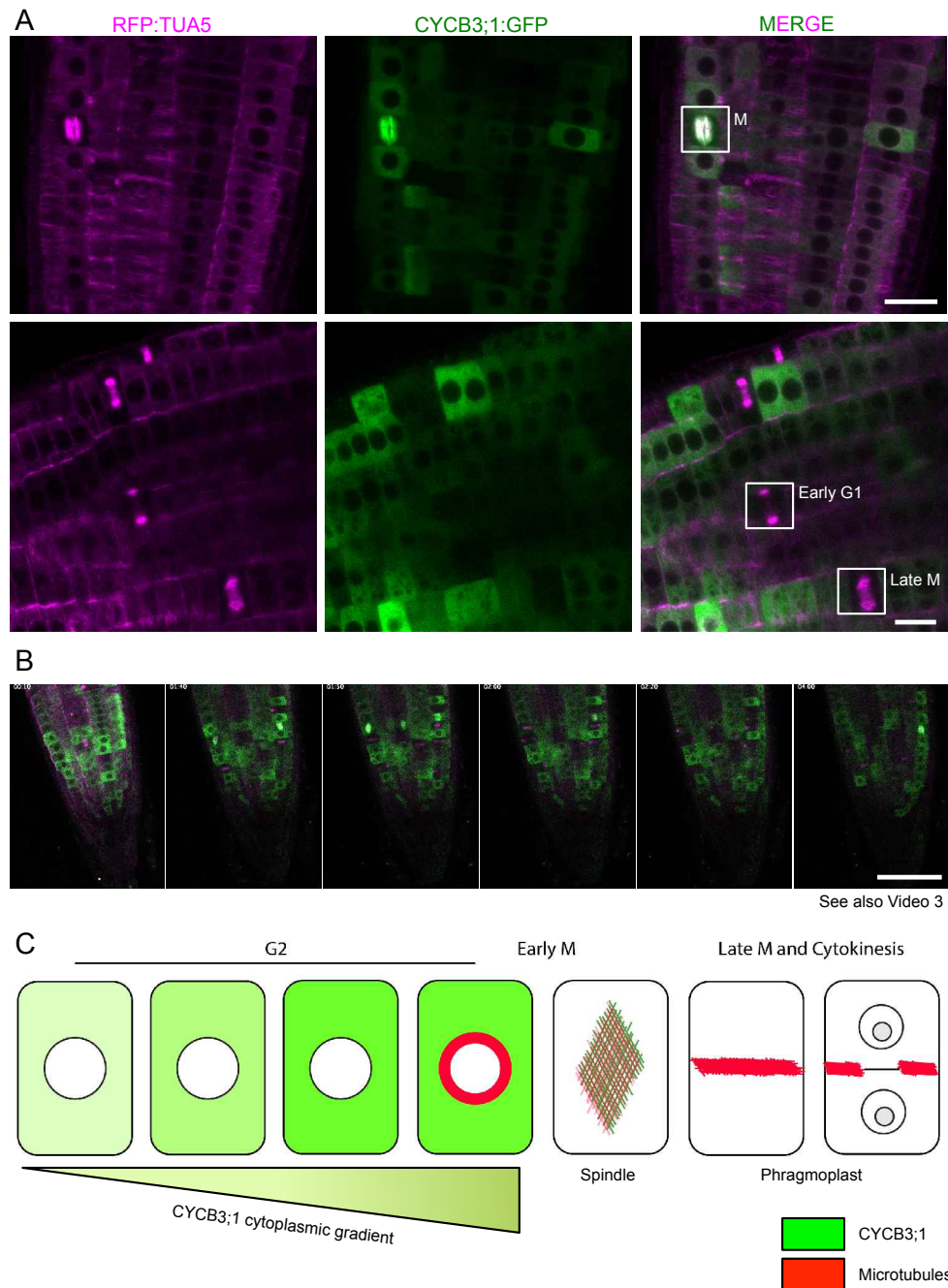
Figure 4: *Analysis of cell cycle progression in roots using tubulin and CYCB3;1. (A) Confocal laser scanning micrographs of root cells expressing RFP:TUA5 in magenta and CYCB3;1in green. Note the*

cortical microtubule array in the majority of cells. The spindle and phragmolpast are highlighted by the white squares. Scale bar 10µm. (B from Video 3) Overview of root tips at successive time points showing cells in different cell cycle phases, tubulin in magenta and CYCB3;1 in green. Scale bar 100µm. (C) Cartoons, based on stills and live imaging experimental data summarizing the localization pattern of CYCB3;1 (green) and TUA5 (red) throughout the cell cycle.
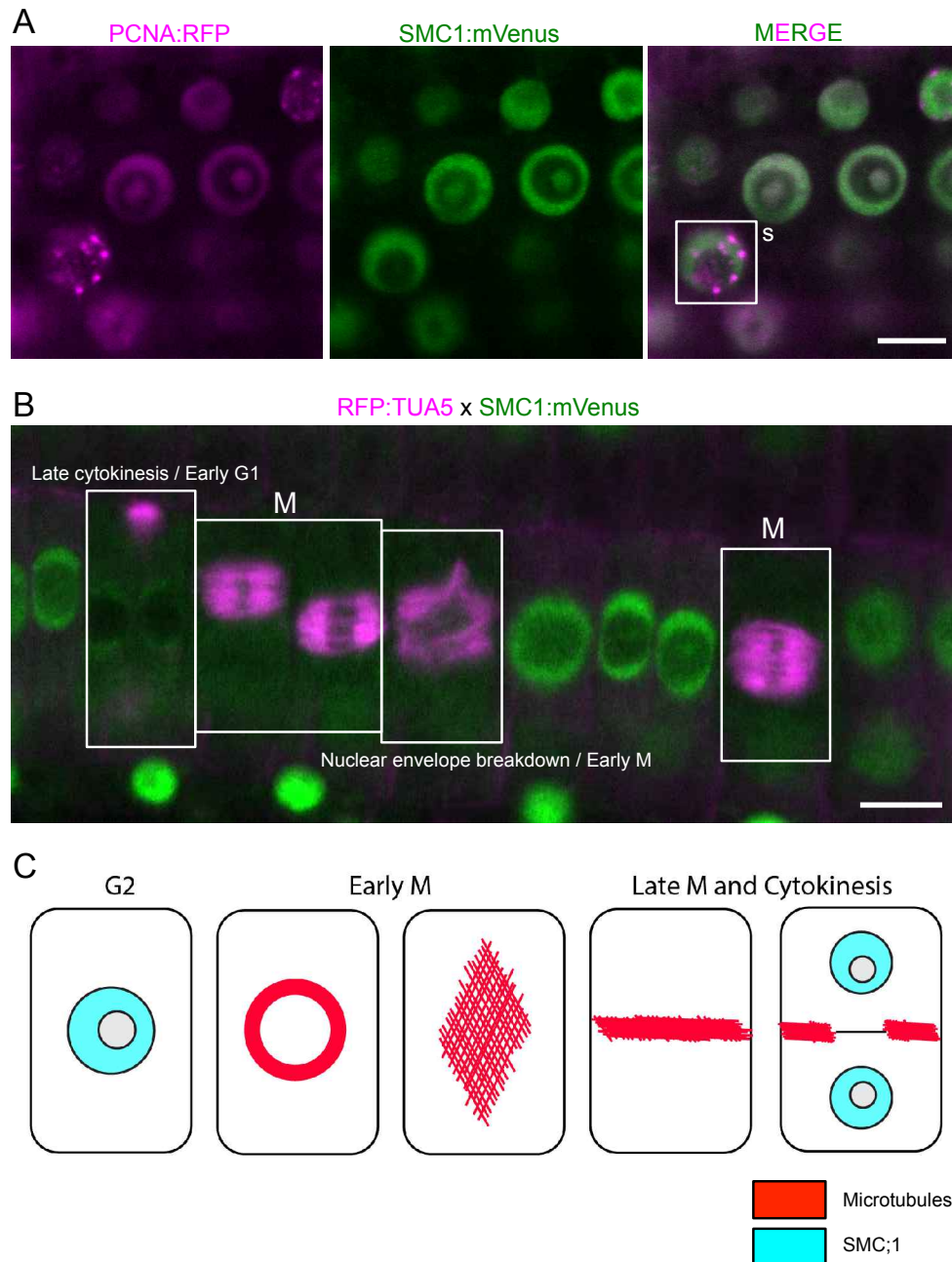
Figure 5: *Confocal laser scanning micrographs of root cells expressing (A) PCNA:RPF (magenta) and SMC1:mVenus (green) (B) RFP:TUA5 (magenta) and SMC1:mVenus (green). In (A) the white box represents a cell in S phase and in (B) from left to right the white boxes highlight cells at late cytokinesis/early G1, early M phase spindles and nuclear envelope breakdown. (C) Cartoons based on stills and live imaging experimental data summarizing the localization pattern of SMC1 (cyan) and TUA5 (red) throughout the cell cycle.*

3.2.4 Discussion

A precise dissection of the cell cycle relies on the choice of fluorescent reporter constructs and their dynamics over time. In this study, we attempted to establish a landmark system to monitor the different cell cycle stages in Arabidopsis roots. Among the combinations analysed, CYCB3;1 and PCNA together could differentiate the four stages of cell cycle: speckled PCNA for S phase, accumulation pattern of CYCB3;1 for G2, spindle localization of CYCB3;1 for M and absence of both reporters for G1. However, as these results are preliminary it is important in the future to increase the number of cells/roots for each reporter line combination to further validate the changes in localization observed over the entire cell cycle.

An important issue during the live cell imaging was the stability of the PCNA signal, i.e. its high bleaching over time. Please note that for live cell imaging we used a 20x air objective, thus limiting the resolution and making impossible to distinguish between dotted and speckled localization of PCNA as described by (Yokoyama et al., 2016) (Figure S1). One of the limitations of the vertical system is the impossibility to use liquid-immersion objectives as the liquid drop slides down due to gravity. The use of a special viscous solution, which is highly gravity-resistant, is already being developed to overcome the resolution issue. Additionally we could exchange the fluorophore of PCNA from TagRFP to a less bleachable fluorophore i.e. mVenus or mTurquoise2. Together this could allow a better dissection between early and late S phase in live cell imaging. Furthermore, work from Umeda lab demonstrated that CDT1 (replication licensing factor CDC10 Target1) could be an effective S phase marker (Yin et al., 2014). We could additionally use this marker together with CYCB3;1 to better asses the beginning of S phase.

The accumulation pattern of CYCB3;1 throughout G2 is of particular interest. We could better characterize this accumulation in a more quantitative manner by measuring the protein concentration within one cell using FCS (Fluorescence Correlation Spectrometry). If the same accumulation profile is present throughout all epidermal root cells, we could define a "G2 standard time", similarly to previous work from the Ellenberg lab defining a mitotic standard time as prerequisite for establishing an atlas of human cell division (Cai et al., 2018). Once the G2 standard time is defined we could compare the relative duration of different cell cycle phases of cells within different tissues, or compare wt with mutants displaying developmental defects or normal growth conditions with drug treatments or stress conditions.

As a long time goal, we would like to define a robust landmark system including regulators of plant development i.e. Cdks, cohesion proteins and many others to study the differences in cell cycle timing between different cell types and establish an atlas of plant cell division varieties in Arabidopsis.
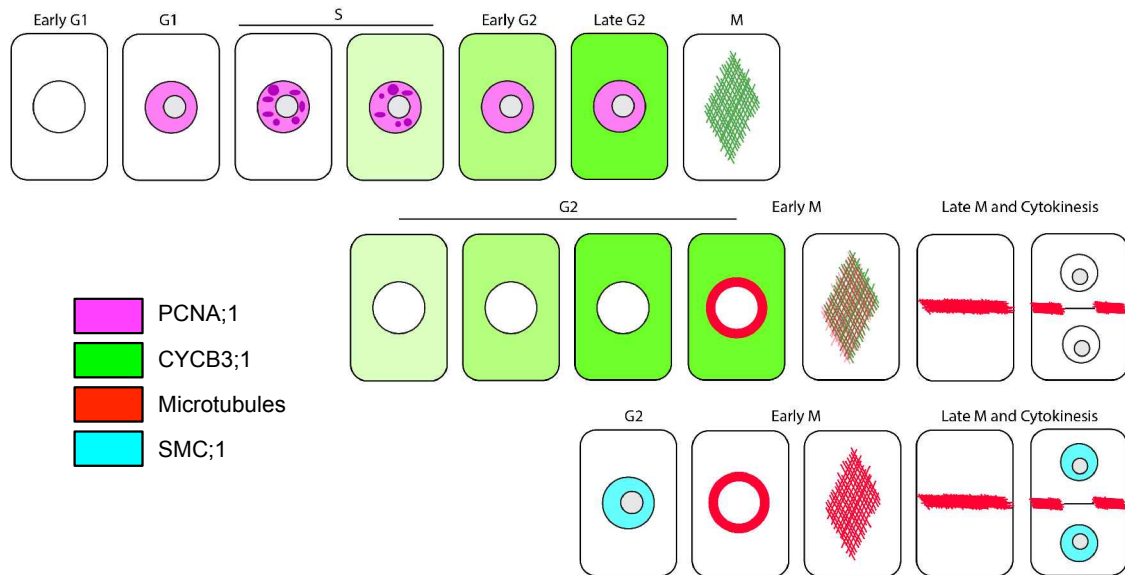
Summary of reporter constructs described in this chapter and their respective localization throughout cell cycle based on stills and live imaging experimental data.

3.2.5 References

Boudolf, V., T. Lammens, J. Boruc, J. Van Leene, H. Van Den Daele, S. Maes, G. Van Isterdael, E. Russinova, E. Kondorosi, E. Witters, G. De Jaeger, D. Inzé, and L. De Veylder. 2009. CDKB1;1 Forms a Functional Complex with CYCA2;3 to Suppress Endocycle Onset. *Plant Physiol.* 150:1482–1493. doi:10.1104/pp.109.140269.

Cai, Y., M.J. Hossain, J.-K. Hériché, A.Z. Politi, N. Walther, B. Koch, M. Wachsmuth, B. Nijmeijer, M. Kueblbeck, M.M. Kavur, R. Ladurner, S. Alexander, J.-M. Peters, and J. Ellenberg. 2018. Experimental and computational framework for a dynamic protein atlas of human cell division. *Nature.* 561:411–415. doi:10.1038/s41586-018-0518-z.

Campilho, A., B. Garcia, H. v d Toorn, H. v Wijk, A. Campilho, and B. Scheres. 2006. Time-lapse analysis of stem-cell divisions in the Arabidopsis thaliana root meristem. *Plant J.* 48:619–627. doi:10.1111/j.1365-313X.2006.02892.x.

Colón-Carmona, A., R. You, T. Haimovitch-Gal, and P. Doerner. 1999. Spatio-temporal analysis of mitotic activity with a labile cyclin–GUS fusion protein. *Plant J.* 20:503–508. doi:10.1046/j.1365-313x.1999.00620.x.

Grandjean, O., T. Vernoux, P. Laufs, K. Belcram, Y. Mizukami, and J. Traas. 2004. In Vivo Analysis of Cell Division, Cell Growth, and Differentiation at the Shoot Apical Meristem in Arabidopsis. *Plant Cell.* 16:74–87. doi:10.1105/tpc.017962.

Hamant, O., P. Das, and A. Burian. 2019. Time-Lapse Imaging of Developing Shoot Meristems Using A Confocal Laser Scanning Microscope. *In* Plant Cell Morphogenesis: Methods and Protocols. F. Cvrčková and V. Žárský, editors. Springer, New York, NY. 257–268.

Iwata, E., S. Ikeda, S. Matsunaga, M. Kurata, Y. Yoshioka, M.-C. Criqui, P. Genschik, and M. Ito. 2011. GIGAS CELL1, a Novel Negative Regulator of the Anaphase-Promoting Complex/Cyclosome, Is Required for Proper Mitotic Progression and Cell Fate Determination in Arabidopsis[W]. *Plant Cell.* 23:4382–4393. doi:10.1105/tpc.111.092049.

Marhava, P., L. Hoermayer, S. Yoshida, P. Marhavý, E. Benková, and J. Friml. 2019. Re-activation of Stem Cell Pathways for Pattern Restoration in Plant Wound Healing. *Cell.* 177:957-969.e13. doi:10.1016/j.cell.2019.04.015.

Okada, T., M. Endo, M.B. Singh, and P.L. Bhalla. 2005. Analysis of the histone H3 gene family in Arabidopsis and identification of the male-gamete-specific variant AtMGH3. *Plant J. Cell Mol. Biol.* 44:557–568. doi:10.1111/j.1365-313X.2005.02554.x.

Prusicki, M.A., E.M. Keizer, R.P. van Rosmalen, S. Komaki, F. Seifert, K. Müller, E. Wijnker, C. Fleck, and A. Schnittger. 2019. Live cell imaging of meiosis in Arabidopsis thaliana. *eLife.* 8. doi:10.7554/eLife.42834.

Takahashi, S., T. Ono, Y. Ishiwata, and T. Kuroda. 2002. Breathing modes, body positions, and suprahyoid muscle activity. *J. Orthod.* 29:307–313; discussion 279. doi:10.1093/ortho/29.4.307.

Valuchova, S., P. Mikulkova, J. Pecinkova, J. Klimova, M. Krumnikl, P. Bainar, S. Heckmann, P. Tomancak, and K. Riha. 2020. Imaging plant germline differentiation within Arabidopsis flowers by light sheet microscopy. *eLife*. doi:10.7554/eLife.52546.

Wangenheim, D. von, R. Hauschild, M. Fendrych, V. Barone, E. Benková, and J. Friml. 2017. Live tracking of moving samples in confocal microscopy for vertically grown roots. *eLife*. doi:10.7554/eLife.26792.

Yin, K., M. Ueda, H. Takagi, T. Kajihara, S.S. Aki, T. Nobusawa, C. Umeda-Hara, and M. Umeda. 2014. A dual-color marker system for in vivo visualization of cell cycle progression in Arabidopsis. *Plant J.* 80:541–552. doi:10.1111/tpj.12652.

Yokoyama, R., T. Hirakawa, S. Hayashi, T. Sakamoto, and S. Matsunaga. 2016. Dynamics of plant DNA replication based on PCNA visualization. *Sci. Rep.* 6:1–9. doi:10.1038/srep29657.

3.2.6 Appendix

3.2.6.1 Supplementary Figures
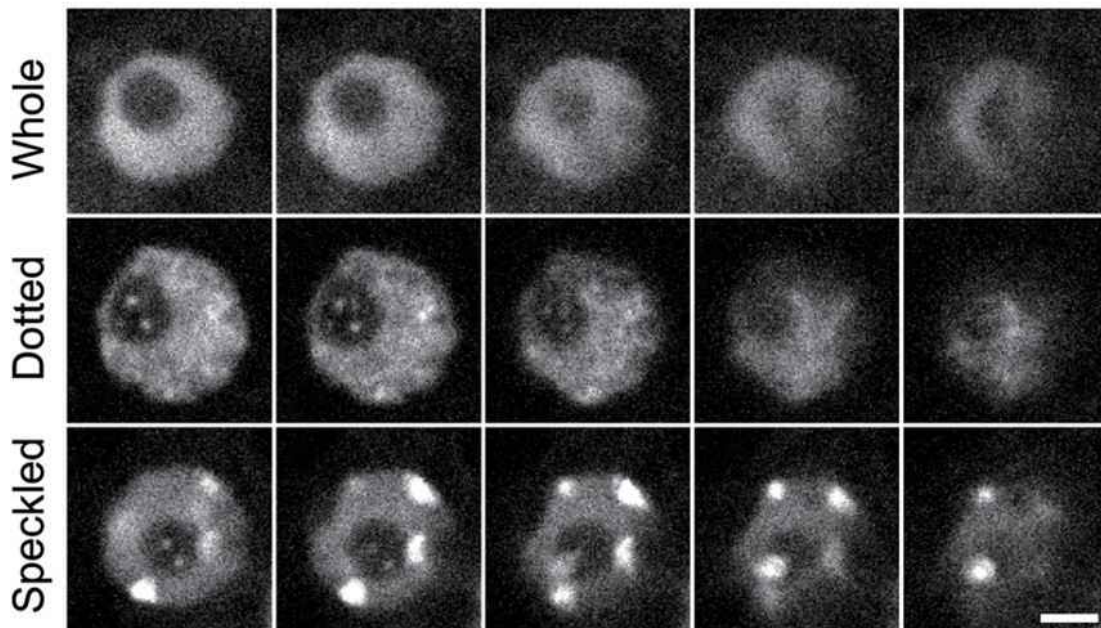
Figure S1: *Comparison between dotted (early S) and specked (late S) pattern of PCNA in the root meristematic zone. Figure taken from (Yokoyama et al., 2016).*

3.2.6.2 Video legends

Video 1: Time course of root cells expressing CYCB3;1 in green and in magenta merged with the bright field in grey at the right panel. Time format (h:min). See also Figure 3A.

Video 2: Time course of root cells expressing PCNA highlighted in white. Note the dotted PCNA signal of cells in S-phase. Time format (h:min).

Video 3: Time course of root cells expressing CYCB3;1 in green and tubulin in magenta, merged with the bright field in grey at the right panel. Time format (h:min). See also Figure 4B.

Video 4: Time course of root cells expressing SMC1 in green and PCNA in magenta. Time format (h:min).

Publications and presentations

Publications

CDKD-dependent activation of CDKA;1 controls microtubule dynamics and cytokinesis during meiosis

Sofroni K, Takatsuka H, Yang C, Dissmeyer N, Komaki S, Hamamura Y, Böttger L, Umeda M, Schnittger A.

Journal of Cell Biology, 2020

The Arabidopsis Cdk1/Cdk2 homolog CDKA;1 controls chromosome axis assembly during plant meiosis

Yang C, **Sofroni K**, Wijnker E, Hamamura Y, Carstens L, Harashima H, Stolze SC, Vezon D, Chelysheva L, Orban-Nemeth Z, Pochon G, Nakagami H, Schlögelhofer P, Grelon M, Schnittger A.

EMBO Journal, 2020

SWITCH 1/DYAD is a WINGS APART-LIKE antagonist that maintains sister chromatid cohesion in meiosis

Yang C, Hamamura Y, **Sofroni K**, Böwer F, Stolze SC, Nakagami H, Schnittger A.

Nature Communications, 2019

Protein and metabolite composition of Arabidopsis stress granules

Kosmacz M, Gorka M, Schmidt S, Luzarowski M, Moreno JC, Szlachetko J, Leniak E, Sokolowska EM, **Sofroni K**, Schnittger A, Skirycz A.

New Phytologist, 2019

The retinoblastoma homolog RBR1 mediates localization of the repair protein RAD51 to DNA lesions in Arabidopsis

Biedermann S, Harashima H, Chen P, Heese M, Bouyer D, **Sofroni K**, Schnittger A.

EMBO Journal, 2017

Oral presentations

11th International PhD School in Plant Development. 10-12 October 2018, Retzbach, Germany
Presentation title: "Control of Meiotic Progression Through Cyclin-Dependent Kinase Complexes"
Prize: Best Oral Presentation

Gordon Research Seminar: Mechanisms and regulation of gametogenesis through meiosis. 9-10 June 2018, New London, USA
Presentation title: "Control of Meiotic Progression Through Cyclin-Dependent Kinase Complexes"

Poster presentations

EMBL Conference: From images to knowledge with ImageJ and friends. 6-8 December 2018, Heidelberg, Germany

11th International PhD School in Plant Development. 10-12 October 2018, Retzbach, Germany

Gordon Research Conference: Molecular mechanisms and regulation of meiosis across species. 10-15 June 2018, New London, USA
Prize: Best Poster

The students and postdocs meiosis workshop. 19-20 September 2016, Montpellier, France

Microscopy Congress: Utilizing microscopical technologies as a tool for progressing medical research. 30 November – 1st December 2015, London, UK

Eidesstattliche Versicherung / Declaration on Oath

Hiermit erkläre ich an Eides statt, dass ich die vorliegende Dissertationsschtift selbst une keine anderen als die angegebenen Quellen und Hilfsmittel benutzt habe.

I hereby declare, on oath, that I have written the present dissertation by my own and have not used other then the acknowledged resources and aids.

Hamburg, den   Unterschrift

Declarations of contributions

I hereby declare that all results shown in this thesis are obtained by my own, except from the ones indicated in the respective figure legends in Chapter 1 and the published papers in Chapter 2 and 3. Here I summarize the contributions from collaborators in Chapter 1 and my contributions to the published papers presented in Chapter 2 and 3.

In **Chapter 1:**

- Hirotomo Takatsuka generated the *CDKD;1*, *CDKD;2* and *CDKD;3* reporter lines
- Chao Yang generated the *CYCB3;1* reporter line and performed the kinase assays of CDKA;1 and CYCB3;1 in Figure 8C
- Nico Dissmeyer generated the *VFD cdka;1* construct and performed the kinase assays of *VF cdka;1* and *VFD cdka;1* in Figure 3D
- Shinichiro Komaki generated the *MAP65-3* reporter line
- Lev Böttger performed and analysed the root growth assay in Figure S5A

In **Chapter 2.1**, my contribution is summarized below:

- Generation, cytological and phenotypical characterization of the functional reporter line $Pro_{CDKA;1}CDKA;1:mVenus$ (Figure EV1A-C)
- Localization pattern of CDKA;1 together with tubulin during meiosis (Figure 1A) and quantitative analysis of the signal distribution of the nuclear versus cytoplasmic fraction of CDKA;1:mVenus during prophase I, revealed by live cell imaging (Figure 1B and Movie EV1)
- Chromosome spreads of the hypomorphic *cdka;1* mutant $CDKA;1^{T161D}$ in *cdka;1* mutant background (Figure 1D second row)

In **Chapter 2.2**, my contribution is summarized below:

- Cytological characterization of the de-phosphomimetic $SWI1^{13A}$ mutant, in which the Cdk-mediated phosphorylated amino acid 13 was exchanged with a hydrophobic amino acid. I performed the chromosome spreads analysis of $SWI^{13A}:GFP$ compared to wildtype and double *wapl1 wapl2*

mutants (Figure 8A) and immunolocalization of *SWI1^{13A}:GFP* in wild-type plants (Figure S8b).

- Contribution to the immunolocalization analysis of REC8:GFP during prophase I in wildtype, *swi1-2* and *swi1-4* mutants (Figure S7)

- Chromosome spreads analysis of SWI1:GFP line #2 in *swi1-2* (Figure S2f), ASY3:RFP line #1 in *asy3* (Figure S3d), SWI1:RFP line #1 in *swi1-2* (Figure 5d) and *SWI1^{13A}:GFP*/WT plants (Figure S12)

In **Chapter 3.1**, I provided the functional reporter line of CDKA;1:mVenus.

In **Chapter 3.2**, Monika Hrtyan (IST Vienna) helped with the image processing of root growth imaging.

Kostika Sofroni   **Prof. Dr. Arp Schnittger**

                                                                                       (Thesis supervisor)

Acknowledgements

A long marathon consists on a persistent everyday preparation and on the capacity in improving, challenging and surpassing your own fears and limits to achieve the final goal: not necessarily winning the marathon but proudly touching the finish line. The road is long and painful, with up and downs, achievements, frustration, rewards but what remains in the end is the feeling of giving your best, giving everything you could, whatever the final destination was in the end. And it's not truly an end but a new road, another challenge and goal to achieve that opens up. Going through this long road or this marathon would have never been possible without the support of people that always encouraged and pushed me to the limits in giving the best of me.

First, I would like to thank my mentor and supervisor Prof. Arp Schnittger who believed in me since I started the scientific road, 8 years ago at my bachelor thesis in his lab in Strasbourg. He gave me the very first spark in loving science, cell cycle and microscopy. He supported my ideas and work throughout the PhD and I am really grateful having him as an amazing source of motivation and inspiration.

Many thanks go to Dr. Magdalena Weingartner who kindly accepted to review and examine the final dissertation.

Special thanks go to Dr. Maren Heese, for her feedback, critical reading and discussions on my overall results during the PhD thesis.

When I started my PhD in Hamburg, I didn't find only a working group, but also a huge family that provided me continuous technical, scientific and emotional support. I would like to thank here all present and past members of the Schnittger group: Chao, Gaetan, Maria, Vanesa, Shini, Viola, Marti, Joke, Yuki, Franzi, Mariana, Oscar, Dagmar, Reinhold, Lucas, Max, Poyu, Felix and Katja. Over time our lab became so big that I might miss many names here so again many thanks to all of you. Special thanks go to two of the students I supervised: Frederike and Lev for their help and contribution to my work. Many thanks to Susanne and Maren Roeper for the administrative support in completing my thesis.

I would like to thank two of our collaborators at IST Vienna, Jiri Friml and Monika Hrtyan for giving me the opportunity to perform live cell imaging in their recently developed vertical microscope system.

Thank you Yuki, for your amazing help in microscopy techniques and image analysis. I feel so lucky to have your feedback and scientific expertise in microscopy.

My life in Hamburg wouldn't have been the same without the weekend brunches, afternoon games, picnics, concerts, night-outs, European weekend trips and many other social events with Gaetan, Vanesa, Maria, Joke, Marti and Yuki. Thank you Jacob for your everyday support and for giving me the possibility to escape science and realize that other things are happening outside the lab.

A final and very special thank is for my family who supported and believed in me during all my university studies. I would like to dedicate this entire work to my grandfather, the greatest source of inspiration to me and the first one, who traced in me the love for discovering nature and science.